

The Influence of Sulfides on Localized Corrosion of Mild Steel

A dissertation presented to
the faculty of
the Russ College of Engineering and Technology of Ohio University

In partial fulfillment
of the requirements for the degree
Doctor of Philosophy

Bruce N. Brown

December 2013

© 2013 Bruce Brown. All Rights Reserved.

This dissertation titled
The Influence of Sulfides on Localized Corrosion of Mild Steel

by

BRUCE N. BROWN

has been approved for

the Department of Chemical and Biomolecular Engineering

and the Russ College of Engineering and Technology by

Khairul Alam

Professor of Mechanical Engineering

Dennis Irwin

Dean, Russ College of Engineering and Technology

ABSTRACT

BROWN, BRUCE N., Ph.D., December 2013, Chemical Engineering

The Influence of Sulfides on Localized Corrosion of Mild Steel

Director of Dissertation: Khairul Alam

Understanding the mechanisms that lead to localized corrosion in oil and gas pipeline is of great interest to corrosion engineers worldwide. The objective of this study is to examine the phenomena of localized corrosion in upstream oil and gas industry pipelines which operate under slightly sour conditions due to an H₂S/CO₂ environment. Experimental studies have been carried out to identify the parameters with the most influence on the likelihood of localized corrosion. It is shown that the solution bulk pH, concentrations of carbonates, concentration of sulfides, and the ionic strength of the solution are the major factors for localized corrosion. The flow temperature, and saturation values for both iron sulfide and iron carbonate were also identified as important parameters affecting the corrosion process. The experimental data were then analyzed and used to develop a correlation to relate these parameters to the likelihood of localized corrosion in mild steel pipelines.

ACKNOWLEDGMENTS

I wish to express my sincere gratitude to several people who have given me the insight and perspective to complete this body of work. My first expression of gratitude must be given to Dr. Srdjan Nešić who has been my mentor for over 10 years and has given me guidance to learn and to teach research fundamentals to many other graduate students as part of the corrosion research at Ohio University. You have added to my enjoyment of teaching others and taught me quite a bit along the way. Thank you. I also need to express my gratitude to Dr. Marc Singer who has been a helpful lab partner during sample installation and removal procedures from the large scale system, a good person to share an office with for those times when I just needed to discuss sour corrosion with a fellow engineer, and a great friend whose friendly wager as to “who would get their PhD first” got us both to the outcome we desired. Thank you, my friend.

Furthermore, the group of staff and student researchers who have been researching and discussing sour corrosion at the Institute for many years that have added to our knowledge: Dr. Yoon-Seok Choi, Dr. Wei Sun, Dr. Kun-Lin John Lee, Yougui Zheng, and Jing Ning. I would also like to thank the full support staff at the Institute for their dedicated work and assistance during my PhD. I am also indebted to Steve Smith, who I consider a good friend that has always been a fantastic encyclopedia of information related to corrosion seen in the laboratory and field conditions. Having your assistance as an adjunct professor for the Institute for many years has been a huge benefit for our sour research program. Last but not least, I need to thank my advisor, Dr. Khairul Alam, for his dedication, multiple reviews, and persistence that this document you have in your hands is the best it can be.

DEDICATION

To

Debi, Lindsay, and Garret Brown

(my family)

TABLE OF CONTENTS

Abstract.....	3
Acknowledgments.....	4
Dedication.....	5
List of Tables	9
List of Figures.....	12
Chapter 1: Introduction.....	41
Chapter 2: Background and Objectives	47
Introduction.....	47
Focus on Localized Corrosion	47
Effect of the Corrosion Product Layer on Localized Corrosion Mechanisms.....	52
Objectives and Rationale for the Study	56
Chapter 3: Experimental Method.....	59
Experimental Parameters	59
Calculation of Environmental Conditions	62
Corrosion Measurement and Analysis Procedures	80
Definition of Localized Corrosion	88
Chapter 4: Experimental Results	91

Introduction.....	91
Effect of Iron Carbonate and Iron Sulfide Saturation Values.....	92
Effect of a Higher Ionic Strength Solution at pH 6	137
Effect of a Decrease in Solution pH	156
Effect of a Lower Ionic Strength Solution and Lower pH_2S at pH 5	194
Effect of a Decrease in pCO_2	220
Effect of a Decrease in Temperature	246
Effect of the Presence of Acetic Acid.....	285
Chapter 5: Prediction of Localized Corrosion	305
Experimental Data Set	305
Relationship of Parameters to the Likelihood of Localized Corrosion.....	306
Analysis of the Data Set.....	312
Prediction Model for Localized Corrosion	315
Verification of Model	320
Chapter 6: Discussion and Conclusions.....	325
Introduction.....	325
Discussion.....	325
Conclusions.....	335
Future work.....	336
References.....	338

Appendix A: ANOVA of Dataset	346
Appendix B. NACE 2002 Conference Paper No. 02502.....	347

LIST OF TABLES

Table 1. Ions and Aqueous Species Possible in an H ₂ S/CO ₂ System. ²¹	55
Table 2. List of Parameters Tested in the Large Scale H ₂ S Flow Loop	58
Table 3. Specifications of the Hydrogen Sulfide large scale flow loop.....	62
Table 4. Variation in pCO ₂ /pH ₂ S ratio to maintain an equal source of hydrogen ions from sulfide species and carbonate species at pH 4.5, 5, & 6 with 8 bar pCO ₂ at 60°C....	71
Table 5. Material Analysis of X65 pipeline material used vs. requirements of standard.	82
Table 6. Experiments 1, 2, 3, & 4 – Change in Saturation Values	93
Table 7. Controlled Parameters for S(FeS) ≈ (25%)[S(FeCO ₃)].	95
Table 8. Controlled Parameters for S(FeS) ≈ (15%)[S(FeCO ₃)].	103
Table 9. Controlled Parameters for S(FeS) ≥ S(FeCO ₃).....	109
Table 10. Controlled Parameters for S(FeS) ≈ 10[S(FeCO ₃)]	120
Table 11. Experiments 5 & 6: higher ionic strength, two partial pressures of H ₂ S	138
Table 12. Controlled Parameters for High Sodium Chloride Test at 1 mbar pH ₂ S.....	139
Table 13. Controlled Parameters for High Sodium Chloride Test at 10 mbar pH ₂ S.....	146
Table 14. Experiments 9 & 12: change in pH.....	157
Table 15. Controlled Parameters for Effect of Corrosion Product Layer test at 10 mbar pH ₂ S and 10 wt% NaCl.	158
Table 16. Exp 12. Controlled Parameters for Effect of pH test at 10 mbar pH ₂ S and 10 wt% NaCl.....	172

Table 17. The range of S(FeS) calculated for experiments at 60°C, 7.7 bar pCO ₂ , 10 mbar pH ₂ S.....	182
Table 18. Statistics for comparison of two weight loss samples: 21 days , 60°C, pCO ₂ = 7.7 bar, pH ₂ S = 10 mbar, 10 wt.% NaCl, multiphase flow.....	188
Table 19. Experiments 7 & 8: decreased ionic strength, lower pH ₂ S.....	195
Table 20. Controlled Parameters for Effect of pH test at 10 mbar pH ₂ S and 1 wt% NaCl.	196
Table 21. Controlled Parameters for Effect of pH test at 1 mbar pH ₂ S and 1 wt% NaCl.	207
Table 22. Test Matrix for Experiment 10 & 11 with changes in pCO ₂ , Temperature, Flow, [NaCl], & pH ₂ S.....	221
Table 23. Controlled Parameters for Effect of Corrosion Product Layer test at 14 mbar pH ₂ S and 1 wt% NaCl.	222
Table 24. Controlled Parameters for Effect of Corrosion Product Layer test at 4 mbar pH ₂ S and 1 wt% NaCl.	234
Table 25. Test Matrix – Effect of a Decrease in Temperature.....	247
Table 26. Exp 13. Controlled Parameters for the Effect of Temperature at 2.8 bar pCO ₂ , and 100 mbar pH ₂ S.....	248
Table 27. Exp 14. Controlled Parameters for Effect of Higher pH ₂ S at 40°C.....	266
Table 28. Exp 15. Controlled Parameters for Effect of 100 ppm Free HAc.....	286
Table 29. Weight Loss Data Before and After Addition of 100 ppm Free HAc.	291

Table 30. Descriptive Statistics of H ₂ S/CO ₂ Sample Data Set (N = 78)	306
Table 31. Environmental conditions for eight experiments at 1 wt% NaCl that involve a change in pCO ₂ for comparison.....	310
Table 32. Determination of Likelihood of Localized Corrosion from Sample Analysis	314
Table 33. Definition of parameters used for correlation with calculated coefficients....	316
Table 34. Referenced Research from IFE, Norway	321
Table 35. Referenced Research from ICMT, USA (NACE 2007)	324

LIST OF FIGURES

Figure 1. Definition of focus area for localized attack or localized corrosion, termed the “gray zone.” ¹	42
Figure 2. Definition of an active pit under conditions subject to localized corrosion. ² ...	43
Figure 3. Layered structure of Mackinawite with the unit cells shown as lines between the layers. Iron molecules (Fe) are indicated as small orange spheres and sulfur molecules (S) are indicated by the larger yellow spheres.....	53
Figure 4. Representation of charge separation by the mackinawite layer ²⁰	54
Figure 5. Schematic of the Hydrogen Sulfide large scale flow loop. Full dimensions are 29 m (95 ft) in length and 3.6 m (12 ft) in width.....	61
Figure 6. Relationship between the solubility constants for CO ₂ (K _{sol}) and H ₂ S (K _{h2s,sol}) at operating conditions from 40°C to 80°C.	65
Figure 7. Relationship between the dissociation constants for H ₂ CO ₃ (K _{ca}) and H ₂ S _(aq) (K _{a,1(H2S)}) for the temperature range of 40°C to 80°C.....	70
Figure 8. Pourbaix diagrams representing corrosion products formed at near saturation conditions for both iron carbonate and iron sulfide at (A) 1 mbar and (B) 5 mbar pH ₂ S, respectively (60°C, 7.7bar pCO ₂ , pH 6, 1 ppm [Fe ²⁺]). (Eh-pH diagrams from GWB ³⁶).....	75

- Figure 9. Pourbaix diagram representing corrosion products formed at near saturation conditions for both iron carbonate and iron sulfide (60°C, 7.7bar pCO₂, pH 6, 1 ppm Fe⁺⁺, 0.001 bar pH₂S and 0.005 bar pH₂S). (Eh-pH diagram from GWB³⁶)..... 76
- Figure 10. Pourbaix diagrams calculated from potential/pH program (VB version) showing that an increase in pH₂S from 0.1 mbar (A) to 1.0 mbar (B) will change the favored corrosion product from FeCO₃ (pink color) to pyrrhotite (white color). (60°C, 8 bar pCO₂, 1 ppm Fe⁺⁺) 79
- Figure 11. Pourbaix diagram calculated from potential/pH program (VB version) showing that an increase up to 24 mbar pH₂S is needed to make mackinawite (purple color) the favored corrosion product over FeCO₃. (60°C, 8 bar pCO₂, 1 ppm Fe⁺⁺) 80
- Figure 12. Micrograph image of API 5L X65 pipeline material used in this study. (Provided by Chevron Corporation.)⁴⁸ 83
- Figure 13. Variations of iron and hydrogen sulfide concentrations with time. (60°C, 0.77 MPa CO₂, pH 6, H₂S gas phase concentration = 20 ± 7 ppm) 96
- Figure 14. Calculated values of iron sulfide and iron carbonate saturation. (60°C, 0.77 MPa CO₂, pH 6, pH₂S = 0.00015 bar ± 0.00005 bar)..... 96
- Figure 15. Corrosion rate measurements by LPR and X65 WL values. (60°C, 0.77 MPa CO₂, pH 6, V_{sg} = 3m/s, V_{sl} = 1m/s, pH₂S = 0.15 mbar ± 0.05 mbar)..... 97
- Figure 16. Visual examination of weight loss samples as removed from experiment. (60°C, 0.77 MPa CO₂, pH 6, V_{sg} = 3m/s, V_{sl} = 1m/s, pH₂S = 0.15 mbar ± 0.05 mbar)..... 98

- Figure 17. Top view, metallurgical microscope image, of multiphase weight loss sample after 20 day exposure to conditions; shown without corrosion product layer. (60°C, 0.77 MPa CO₂, pH 6, V_{sg} = 3m/s, V_{sl} = 1m/s, pH₂S = 0.15 mbar ± 0.05 mbar) 99
- Figure 18. Single Phase, 30 Day Exposure, From SEM cross section: 73µm and 85µm pit depth, Localized Corrosion by max depth: 3.3 mm/yr, General Corrosion by wt loss: 0.89 mm/yr, Pitting Factor: 3.7..... 100
- Figure 19. Sample weight loss comparison. (60°C, 0.77 MPa CO₂, pH 6, V_{sg} = 3m/s, V_{sl} = 1m/s, pH₂S = 0.15 mbar ± 0.05 mbar, 10, 20, & 30 days) 101
- Figure 20. SEM and Backscatter cross-sectional analysis of X65 sample from 30 day exposure to multiphase flow conditions shows pit growth under the corrosion product layer. (60°C, 0.77 MPa CO₂, pH 6, V_{sg} = 3m/s, V_{sl} = 1m/s, pH₂S = 0.15 mbar ± 0.05 mbar)(227)..... 101
- Figure 21. SEM image of corrosion product layer after 30 days in multiphase flow. Note the polish marks still visible across the surface. (60°C, 0.77 MPa CO₂, pH 6, V_{sg} = 3m/s, V_{sl} = 1m/s, pH₂S = 0.15 mbar ± 0.05 mbar) 102
- Figure 22. Variations of iron and hydrogen sulfide concentrations with time. (60°C, 7.7bar pCO₂, pH 6, 0.00012 bar ± 0.00004 bar pH₂S) 104
- Figure 23. Calculated values of iron sulfide and iron carbonate saturation. (60°C, 7.7 bar pCO₂, pH 6, 0.00012 bar pH₂S)..... 104

Figure 24. Corrosion rates in multiphase flow (MP) and single phase flow (SP) as measured by polarization resistance (LPR) and weight loss (WL). (60°C, 0.77 MPa CO ₂ , pH 6, p _{H₂S} = 0.00012 bar ± 0.00004 bar)	105
Figure 25. Visual examination of weight loss samples as removed from experiment. (60°C, 0.77 MPa CO ₂ , pH 6, p _{H₂S} = 0.00012 bar ± 0.00004 bar)	106
Figure 26. SEM surface analysis of multiphase flow sample of X65 after 10 days exposure (60°C, 0.77 MPa CO ₂ , pH 6, p _{H₂S} = 0.00012 bar ± 0.00004 bar).	107
Figure 27. Cross sectional analysis of multiphase WL sample of X65 after 30 day exposure. Corrosion product is approximately 28 to 30 μm thick. (100X metallurgical microscope, 60°C, 0.77 MPa CO ₂ , p _{H₂S} = 0.00012 bar ± 0.00004 bar).	107
Figure 28. Iron concentration and H ₂ S partial pressure. (60°C, 0.77 MPa CO ₂ , pH 6, H ₂ S gas phase concentration = 120 ± 10 ppm)	110
Figure 29. Saturation Values for Iron Carbonate and Iron Sulfide. (60°C, 0.77 MPa CO ₂ , pH 6, p _{H₂S} = 1.2 mbar ± 0.1 mbar).....	110
Figure 30. Polarization resistance measurements for single phase and multiphase flow showing a conductive layer was deposited on the SP probe giving false readings.	111
Figure 31. LPR and WL sample corrosion rate measurements. (60°C, 0.77 MPa CO ₂ , pH 6, p _{H₂S} = 1.2 mbar ± 0.1 mbar).....	112

- Figure 32. Visual examination of weight loss samples as removed from experiment for 10 day and 15 day exposure times. (60°C, 0.77 MPa CO₂, pH 6, pH₂S = 1.2 mbar ± 0.1 mbar)..... 114
- Figure 33. SEM and Backscatter images of surface layers developed in single phase flow (SP) after 10 day exposure to conditions. (60°C, 0.77 MPa CO₂, pH 6, pH₂S = 1.2 mbar ± 0.1 mbar). 115
- Figure 34. SEM and Backscatter images of surface layers developed in multiphase flow (MP) after 10 day exposure to conditions. (60°C, 0.77 MPa CO₂, pH 6, pH₂S = 1.2 mbar ± 0.1 mbar). 115
- Figure 35. Visual examination of weight loss sample removed from multiphase flow after 25 days as used for cross sectional analysis. (60°C, 0.77 MPa CO₂, pH 6, pH₂S = 1.2 mbar ± 0.1 mbar). 116
- Figure 36. Experiment 3: Cross section of multiphase X65(2) coupon after 25 day exposure (60°C, 0.77 MPa CO₂, pH 6, pH₂S = 1.2 mbar ± 0.1 mbar, 25 day exposure). (next to metal surface) layer #1: 60 µm, layer #2: 60 µm, and layer #3: 30 µm. Layer #1 EDS is [32.4% Fe, 0.0% S, 13.4% C, 26.5% O], the interface between layer #1 and layer #2 EDS is [35.4% Fe, 12.9% S, 14.0% C, 9.5% O], and the EDS of layer #2 is [31.2% Fe, 15.0% S, 20.8% C, 11.2% O]..... 117
- Figure 37. Visual examination of weight loss samples after Clarke solution procedures to remove the corrosion product layer; samples cut in half have undergone cross section analysis. (60°C, 0.77 MPa CO₂, pH 6, pH₂S = 1.2 mbar ± 0.1 mbar)..... 118

- Figure 38. Variations of iron and hydrogen sulfide concentrations with time. (60°C , $P_{\text{total}} = 8 \text{ bar}$, $0.01 \text{ bar} \pm 0.001 \text{ bar pH}_2\text{S}$ [1000 ppm]) 121
- Figure 39. Comparison of Saturation values for iron carbonate (FeCO_3) and iron sulfide (FeS). (60°C , $P_{\text{total}} = 8 \text{ bar}$, $0.01 \text{ bar} \pm 0.001 \text{ bar pH}_2\text{S}$ [1000ppm], 1 wt% NaCl).. 122
- Figure 40. Comparison of Corrosion rates measured by linear polarization and weight loss coupons. SP – Single Phase, MP – Multiphase (60°C , $P_{\text{total}} = 8 \text{ bar}$, $0.01 \text{ bar} \pm 0.001 \text{ bar pH}_2\text{S}$ [1000ppm], 1 wt% NaCl)..... 122
- Figure 41. Cross section with calculation of general corrosion rate vs. localized corrosion rate for multiphase flow sample after 10 days exposure. (60°C , $P_{\text{total}} = 8 \text{ bar}$, $0.01 \text{ bar} \pm 0.001 \text{ bar pH}_2\text{S}$ [1000ppm], 1 wt% NaCl)..... 124
- Figure 42. Visual examination of weight loss samples as removed from experiment. (60°C , $P_{\text{total}} = 8 \text{ bar}$, $0.01 \text{ bar} \pm 0.001 \text{ bar pH}_2\text{S}$ [1000ppm], 1 wt% NaCl)..... 124
- Figure 43. Visual examination of weight loss samples after Clarke solution procedures to remove the corrosion product layer; samples cut in half have undergone cross section analysis. (60°C , $P_{\text{total}} = 8 \text{ bar}$, $0.01 \text{ bar} \pm 0.001 \text{ bar pH}_2\text{S}$ [1000ppm], 1 wt% NaCl) 125
- Figure 44. Backscatter SEM image of corrosion product layer showing circular pattern observed in many locations on multiphase flow sample after 10 days exposure. (60°C , $P_{\text{total}} = 8 \text{ bar}$, $0.01 \text{ bar} \pm 0.001 \text{ bar pH}_2\text{S}$ [1000ppm], 1 wt% NaCl)..... 126

- Figure 45. Visual example of layer breakdown and localized corrosion from SEM cross section analysis of multiphase flow sample after 10 days exposure. (60°C, $P_{\text{total}} = 8$ bar, 0.01 bar \pm 0.001 bar pH₂S [1000ppm], 1 wt% NaCl) 126
- Figure 46. EDS composition of locations within the localized corrosion. (60°C, $P_{\text{total}} = 8$ bar, 0.01 bar \pm 0.001 bar pH₂S [1000ppm], 1 wt% NaCl, multiphase flow, 10 days)
The bright circular region in the figure is due to an air bubble captured under the layer during epoxy coating of the sample for cross sectioning. 128
- Figure 47. Region of layer exfoliation. (60°C, $P_{\text{total}} = 8$ bar, 0.01 bar \pm 0.001 bar pH₂S [1000ppm], 1 wt% NaCl, multiphase flow, 10 days) 129
- Figure 48. Upper layer of corrosion product – fluffy mackinawite. (60°C, $P_{\text{total}} = 8$ bar, 0.01 bar \pm 0.001 bar pH₂S [1000ppm], 1 wt% NaCl, multiphase flow, 10 days) ... 130
- Figure 49. Surface layer failure and corrosion product layer thickness by cross section analysis for an X65 sample from single phase after 16 days exposure. (60°C, $P_{\text{total}} = 8$ bar, 0.01 bar \pm 0.001 bar pH₂S [1000ppm], 1 wt% NaCl) 132
- Figure 50. SEM and EDS analysis of the corrosion product layer outside and inside a surface layer failure from single phase flow after 16 days exposure. (60°C, $P_{\text{total}} = 8$ bar, 0.01 bar \pm 0.001 bar pH₂S [1000ppm], 1 wt% NaCl) 133
- Figure 51. SEM and Backscatter images of surface layer failure for an X65 sample from multiphase after 26 days exposure. (60°C, $P_{\text{total}} = 8$ bar, 0.01 bar \pm 0.001 bar pH₂S [1000ppm], 1 wt% NaCl) 134

Figure 52. SEM and Backscatter images from cross sectional analysis of a surface layer failure for an X65 sample from multiphase after 26 days exposure. (60°C, $P_{\text{total}} = 8$ bar, 0.01 bar \pm 0.001 bar pH_2S [1000ppm], 1 wt% NaCl)	135
Figure 53. SEM and EDS analysis of a general surface area of corrosion product from an X65 sample in multiphase flow after 26 days exposure. (60°C, $P_{\text{total}} = 8$ bar, 0.01 bar \pm 0.001 bar pH_2S [1000ppm], 1 wt% NaCl).....	135
Figure 54. Experiment 5: Comparison of supersaturation values for iron carbonate (FeCO_3) and iron sulfide (FeS). (60°C, $P_{\text{total}} = 8$ bar, $\text{pH}_2\text{S} = 0.001$ bar [100ppm], 10wt% NaCl).	140
Figure 55. Experiment 5: Comparison of Corrosion rates measured by linear polarization (LPR) and weight loss (WL) coupons. SP – Single Phase (60°C, $P_{\text{total}} = 8$ bar, $\text{pH}_2\text{S} = 0.001$ bar [100ppm], 10wt% NaCl).	141
Figure 56. Experiment 5: Surface layer from influence of pH_2S and NaCl solution. (60°C, $P_{\text{total}} = 8$ bar, $\text{pH}_2\text{S} = 0.001$ bar [100ppm], 10wt% NaCl).	142
Figure 57. Experiment 5: Surface layer from influence of pH_2S and NaCl solution. (60°C, $P_{\text{total}} = 8$ bar, $\text{pH}_2\text{S} = 0.001$ bar [100ppm], 10wt% NaCl).	143
Figure 58. Surface features in cross sectional analysis of X65 sample from Single Phase flow after 31 day exposure to system conditions. (60°C, $P_{\text{total}} = 8$ bar, $\text{pH}_2\text{S} = 0.001$ bar [100ppm], 10wt% NaCl).	144

Figure 59. Surface features from SEM analysis of an X65 sample from Single Phase flow after 31 days exposure to system conditions. (60°C, $P_{\text{total}} = 8$ bar, $p\text{H}_2\text{S} = 0.001$ bar [100ppm], 10wt% NaCl).	144
Figure 60. Bar chart comparison of WL general corrosion rate and IFM measured penetration rate for both sets of samples from Experiment 3 and Experiment 5. (60°C, $P_{\text{total}} = 8$ bar, $p\text{H}_2\text{S} = 0.001$ bar [100ppm], 10wt% NaCl).....	145
Figure 61. Experiment 6: partial pressures of CO_2 and H_2S vs. time.	147
Figure 62. Experiment 6: pH and $[\text{Fe}^{++}]$ vs. time	147
Figure 63. Experiment 6: Multiphase, 10 days, 60°C, $p\text{CO}_2 = 7.7$ bar, pH 6.0, 10 mbar H_2S , 10 wt% NaCl.....	149
Figure 64. Experiment 6: IFM surface imaging of X65 coupon exposed for 30 days in single phase flow for conditions: 60°C, $p\text{CO}_2 = 7.7$ bar, pH 6.0, 1.0 mbar H_2S , 10 wt% NaCl.....	150
Figure 65. Experiment 6: IFM surface imaging of X65 coupon exposed for 30 days in single phase flow for conditions: 60°C, $p\text{CO}_2 = 7.7$ bar, pH 6.0, 1.0 mbar H_2S , 10 wt% NaCl.....	151
Figure 66. SEM cross sectional analysis of X65 coupon exposed for 20 days in single phase flow for conditions: 60°C, $p\text{CO}_2 = 7.7$ bar, pH 6.0, 1.0 mbar H_2S , 10 wt% NaCl.....	152
Figure 67. Corrosion rate vs location (SP – single phase, MP – multiphase), 60°C, $p\text{CO}_2 = 7.7$ bar, pH 6.0, 10.0 mbar H_2S , 10 wt% NaCl.....	153

Figure 68. Partial pressure measurements of CO ₂ and H ₂ S during the experiment of 60°C, pH 5, pCO ₂ = 7.7 bar, pH ₂ S = 10 mbar, 10 wt% NaCl	159
Figure 69. Single phase weight loss corrosion rate and penetration rate for samples in 60°C, pH 5, pCO ₂ = 7.7 bar, pH ₂ S = 10 mbar, 10 wt% NaCl	160
Figure 70. Multiphase weight loss corrosion rate and penetration rate for samples in 60°C, pH 5, pCO ₂ = 7.7 bar, pH ₂ S = 10 mbar, 10 wt% NaCl	160
Figure 71. Exp 9. Pitting ratio for single phase and multiphase weight loss coupons in 60°C, pH 5, pCO ₂ = 7.7 bar, pH ₂ S = 10 mbar, 10 wt% NaCl	161
Figure 72. Exp 9. Multiphase weight loss sample taken from 60°C, pH 5, pCO ₂ = 7.7 bar, pH ₂ S = 10 mbar, 10 wt% NaCl after 7 days' exposure.	162
Figure 73. Exp 9. Multiphase weight loss sample taken from 60°C, pH 5, pCO ₂ = 7.7 bar, pH ₂ S = 10 mbar, 10 wt% NaCl after 7 days' exposure.	162
Figure 74. Exp 9. IFM analysis from multiphase flow sample showing the single localized corrosion location. Multiphase weight loss sample taken from 60°C, pH 5, pCO ₂ = 7.7 bar, pH ₂ S = 10 mbar, 10 wt% NaCl after 7 days' exposure.	163
Figure 75. Exp 9. Multiphase WL sample, 15 days, with layer. Multiphase weight loss sample taken from 60°C, pH 5, pCO ₂ = 7.7 bar, pH ₂ S = 10 mbar, 10 wt% NaCl. .	164
Figure 76. Exp 9. IFM of multiphase WL sample, 15 days, without layer. Multiphase weight loss sample taken from 60°C, pH 5, pCO ₂ = 7.7 bar, pH ₂ S = 10 mbar, 10 wt% NaCl.	165

- Figure 77. Exp 9. SEM and EDS of sample taken from multiphase flow after 22 days.
 Multiphase weight loss sample taken from 60°C, pH 5, pCO₂ = 7.7 bar, pH₂S = 10 mbar, 10 wt% NaCl. 166
- Figure 78. Exp 9. IFM image of the whole cross-section of the multiphase sample taken at 22 days. Multiphase weight loss sample taken from 60°C, pH 5, pCO₂ = 7.7 bar, pH₂S = 10 mbar, 10 wt% NaCl..... 167
- Figure 79. Exp 9. SEM composite image of Multiphase weight loss sample taken from 60°C, pH 5, pCO₂ = 7.7 bar, pH₂S = 10 mbar, 10 wt% NaCl. Arrow locations 1 & 2 were analyzed by EDS. Both locations show a higher chloride content than was observed elsewhere on the same sample. 168
- Figure 80. Exp 9. Sample surface after removal from H₂S system after 22 days exposure in multiphase flow. 60°C, pH 5, pCO₂ = 7.7 bar, pH₂S = 10 mbar, 10 wt% NaCl. 170
- Figure 81. Exp 9. Cross section of multiphase sample taken after 22 days exposure. 60°C, pH 5, pCO₂ = 7.7 bar, pH₂S = 10 mbar, 10 wt% NaCl. (Sample mass loss = 3.27g, Corrosion rate calculation = 9.4 mm/yr. Uniform corrosion loss of substrate would be 530µm.)..... 170
- Figure 82. Exp 12. Partial pressures of CO₂ and H₂S for pH 4.0 experiment. 173
- Figure 83. Exp 12. General corrosion rates for 60°C, pCO₂ = 7.7 bar, pH₂S = 10 mbar, 10 wt.% NaCl. pH 4.5..... 174

- Figure 84. Exp 12. General corrosion (squares), as well as “localized” corrosion from IFM (single sided error bars), from weight loss of samples exposed to single phase flow in 60°C, $p\text{CO}_2 = 7.7$ bar, $p\text{H}_2\text{S} = 10$ mbar, 10 wt.% NaCl. pH 4.5. 174
- Figure 85. Exp 12. General corrosion (triangles), as well as “localized” corrosion from IFM (single sided error bars), rates from weight loss samples exposed to multiphase flow in 60°C, $p\text{CO}_2 = 7.7$ bar, $p\text{H}_2\text{S} = 10$ mbar, 10 wt.% NaCl. pH 4.5. 175
- Figure 86. Exp 12. Pitting ratio for weight loss samples exposed in 60°C, $p\text{CO}_2 = 7.7$ bar, $p\text{H}_2\text{S} = 10$ mbar, 10 wt.% NaCl. pH 4.5. 175
- Figure 87. Exp 12. Analysis of WL sample exposed in 60°C, $p\text{CO}_2 = 7.7$ bar, $p\text{H}_2\text{S} = 10$ mbar, 10 wt% NaCl, multiphase flow, 7 days. 178
- Figure 88. Exp 12. Sample #51. Analysis of WL sample exposed in 60°C, $p\text{CO}_2 = 7.7$ bar, $p\text{H}_2\text{S} = 10$ mbar, 10 wt% NaCl, single phase flow, for 7 days. pH 4.5. General Corrosion rate = 10.8 mm/yr; pit penetration rate = 36.3 mm/yr; Ratio = 3.4; Layer weight = 0.9 grams; multiple smaller pits of ~150 μm (8 mm/yr) were observed. . 181
- Figure 89. Exp 12. Analysis of corrosion product layer thickness for two WL samples exposed in 60°C, $p\text{CO}_2 = 7.7$ bar, $p\text{H}_2\text{S} = 10$ mbar, 10 wt.% NaCl, multiphase phase flow, for 7 and 14 days. 183
- Figure 90. Exp 12. Direct comparison of corrosion product layer thickness for two WL samples exposed in 60°C, $p\text{CO}_2 = 7.7$ bar, $p\text{H}_2\text{S} = 10$ mbar, 10 wt.% NaCl, multiphase phase flow, for 7 and 14 days. 184

- Figure 91. Exp 12. Comparison of weight loss samples: 21 days , 60°C, $p\text{CO}_2 = 7.7$ bar, $p\text{H}_2\text{S} = 10$ mbar, 10 wt.% NaCl, multiphase flow..... 187
- Figure 92. Comparison of weight loss general corrosion rates for pH 4.5, pH 5.0 and pH 6.0 (60°C, $p\text{CO}_2 = 7.7$ bar, $p\text{H}_2\text{S} = 10$ mbar, 10 wt.% NaCl). 189
- Figure 93. Localized corrosion rates measured by IFM. Shown for testing conducted at pH 4.5, pH 5.0 & pH 6.0 in the multi-week experiment under the same test conditions (60°C, $p\text{CO}_2 = 7.7$ bar, $p\text{H}_2\text{S} = 10$ mbar, 10 wt.% NaCl)..... 189
- Figure 94. Comparison of general and localized corrosion for single phase flow and multiphase flow at pH 4.5, pH 5.0, & pH 6.0 for a 1 week exposure under the same test conditions (60°C, $p\text{CO}_2 = 7.7$ bar, $p\text{H}_2\text{S} = 10$ mbar, 10 wt.% NaCl). 190
- Figure 95. Comparison of general and localized corrosion for single phase flow and multiphase flow at pH 4.5, pH 5.0 & pH 6.0 for a 2 week exposure under the same test conditions (60°C, $p\text{CO}_2 = 7.7$ bar, $p\text{H}_2\text{S} = 10$ mbar, 10 wt.% NaCl). 191
- Figure 96. Comparison of general and localized corrosion for single phase flow and multiphase flow at pH 4.5, pH 5.0 & pH 6.0 for a 3 week exposure under the same test conditions (60°C, $p\text{CO}_2 = 7.7$ bar, $p\text{H}_2\text{S} = 10$ mbar, 10 wt.% NaCl). 192
- Figure 97. Exp 8: As measured concentrations of hydrogen sulfide and iron ions with pH. Information necessary to calculate saturation values of iron sulfide and iron carbonate. (60°C, 7.7 bar $p\text{CO}_2$, 10 mbar $p\text{H}_2\text{S}$, 1wt% NaCl, pH 5)..... 197

Figure 98. Exp 8: Single phase and Multiphase weight loss corrosion rate (bar) and penetration rate measurement (vertical error bar). (60°C, 7.7 bar pCO ₂ , 10 mbar pH ₂ S, 1wt% NaCl, pH 5).....	198
Figure 99. Exp 8: Corrosion product layer mass loss after Clarke solution cleaning of single phase (SP) and multiphase (MP) samples. (60°C, 7.7 bar pCO ₂ , 10 mbar pH ₂ S, 1wt% NaCl, pH 5)	199
Figure 100. Examples of corrosion product layers formed at in multiphase flow after 14 days and in single phase flow after 21 days at 60°C, 7.7 bar pCO ₂ , 10 mbar pH ₂ S, 1wt% NaCl, pH 5. (BEC images at 50X magnification and SEM images at 400X magnification.).....	200
Figure 101. SEM images of surface (a) and cross-section (b) for X65 sample #12 after 21 day exposure to single phase H ₂ S system conditions of 60°C, 7.7 bar pCO ₂ , 10 mbar pH ₂ S, 1 m/s V _{sl}	201
Figure 102. SEM images of surface (a) and cross-section (b) for X65 sample #15 after 21 day exposure to multiphase H ₂ S system conditions of 60°C, 7.7 bar pCO ₂ , 10 mbar pH ₂ S, 1 m/s V _{sl} . (196 μm in 21 days = 3.4 mm/yr).....	202
Figure 103. Aspects of analysis for X65 weight loss sample after 21 day exposure in H ₂ S flow loop. (Single phase, 60°C, 7.7 bar pCO ₂ , 10 mbar pH ₂ S, pH 5, 1 m/s V _{sl}).....	204
Figure 104. SEM images at increased magnification of local corrosion product failure from Figure 103b. (Sample 11, 21 days, with corrosion product layer, single phase, 60°C, 7.7 bar pCO ₂ , 10 mbar pH ₂ S, pH 5, 1 m/s V _{sl})......	205

Figure 105. Spot EDS of materials observed in center of local corrosion product failure from Figure 103b. (Sample 11, 21 days, with corrosion product layer, single phase, 60°C, 7.7 bar pCO ₂ , 10 mbar pH ₂ S, pH 5, 1 m/s V _{sl}).....	206
Figure 106. Exp 7: As measured concentrations of hydrogen sulfide and iron ions with pH. Information necessary to calculate saturation values of iron sulfide and iron carbonate. (60°C, 7.7 bar pCO ₂ , 1 mbar pH ₂ S, 1wt% NaCl, pH 5).....	208
Figure 107. Exp 7: Single phase and Multiphase weight loss corrosion rate (bar) and penetration rate measurement (vertical error bar). (60°C, 7.7 bar pCO ₂ , 1 mbar pH ₂ S, 1wt% NaCl, pH 5)	209
Figure 108. Exp 7: Corrosion product layer mass loss after Clarke solution cleaning of single phase (SP) and multiphase (MP) samples. (60°C, 7.7 bar pCO ₂ , 1 mbar pH ₂ S, 1wt% NaCl, pH 5)	210
Figure 109. SEM images of surface (a) and cross-section (b) for X65 sample #04 after 21 day exposure to multiphase H ₂ S system conditions of 60°C, 7.7 bar pCO ₂ , 0.1 mbar pH ₂ S, 1 m/s V _{sl} , 3 m/s V _{sg}	212
Figure 110. SEM images of surface (a) and cross-section (b) for X65 sample #02 after 21 day exposure to single phase H ₂ S system conditions of 60°C, 7.7 bar pCO ₂ , 0.1 mbar pH ₂ S, 1 m/s V _{sl}	213
Figure 111. Polish marks visible in SEM image of the corrosion product layer for X65 sample #02 as lines from the upper left to the lower right. A portion of Figure 110(a) is magnified to match the physical measurement shown in Figure 109(a).....	214

- Figure 112. Exp 7: Picture of weight loss sample plus IFM surface imaging of X65 coupon exposed for 21 days in single phase flow for conditions: 60°C, pH 5.0, pCO₂ = 7.7 bar, 1.0 mbar H₂S, 1 wt% NaCl. (General corrosion rate was calculated from Sample #3.) 215
- Figure 113. SEM image evidence of an upper corrosion product layer different from the underlying corrosion product layer after 21 days on four samples exposed to H₂S system conditions of 60°C, 7.7 bar pCO₂, 0.1 mbar pH₂S, 1 m/s V_{sl}, 3 m/s V_{sg}..... 216
- Figure 114. IFM images and analysis of the corrosion product layer on sample #06 showing (a) open pit failures up to 245 μm in depth [1.2 & 1.0 mm diameter, L to R] and (b) a partial layer failure with a raised corrosion product layer [1.3 mm diameter]..... 217
- Figure 115. Partial pressure measurements for 60°C, pH 6, pCO₂ = 2.8 bar, pH₂S = 10 mbar, 1 wt% NaCl experiment 222
- Figure 116. Single phase corrosion rate measurements. Weight loss + IFM for penetration rates. X65 steel, 60°C, pH 6, pCO₂ = 2.8 bar, pH₂S = 10 mbar, 1 wt% NaCl 223
- Figure 117. Multiphase corrosion rate measurements. Weight loss + IFM for penetration rates. X65 steel, 60°C, pH 6, pCO₂ = 2.8 bar, pH₂S = 10 mbar, 1 wt% NaCl 224
- Figure 118. Pitting ratio for single phase and multiphase X65 steel weight loss coupons in 60°C, pH 6, pCO₂ = 2.8 bar, pH₂S = 10 mbar, 1 wt% NaCl 225
- Figure 119. Exp 10. SEM / EDS analysis 14 day WL sample, iron sulfide corrosion product layer cover, 60°C, pH 6, pCO₂ = 2.8 bar, pH₂S = 10 mbar, 1 wt% NaCl . 226

- Figure 120. Exp 10. SEM / EDS analysis 14 day WL sample, iron carbonate dominated corrosion product “under” iron sulfide, 60°C, pH 6, pCO₂ = 2.8 bar, pH₂S = 10 mbar, 1 wt% NaCl..... 226
- Figure 121. Exp 10. SEM / EDS analysis, Multiphase flow WL sample 14 days, iron sulfide exterior, iron carbonate interior, 60°C, pH 6, pCO₂ = 2.8 bar, pH₂S = 10 mbar, 1 wt% NaCl 227
- Figure 122. Exp 10. IFM analysis with corrosion product removed, 14 day sample, single phase flow, 60°C, pH 6, pCO₂ = 2.8 bar, pH₂S = 10 mbar, 1 wt% NaCl..... 227
- Figure 123. Exp 10. SEM of iron carbonate crystals, Multiphase flow WL sample 14 days, iron sulfide exterior, iron carbonate interior, 60°C, pH 6, pCO₂ = 2.8 bar, pH₂S = 10 mbar, 1 wt% NaCl 228
- Figure 124. Exp 10. IFM of sample WITH corrosion product layer showing growth and failure leading to localized corrosion, Multiphase flow WL sample 14 days, 60°C, pH 6, pCO₂ = 2.8 bar, pH₂S = 10 mbar, 1 wt% NaCl 229
- Figure 125. Exp 10. IFM of sample WITHOUT corrosion product layer showing growth and failure leading to localized corrosion, Multiphase flow WL sample 14 days, 60°C, pH 6, pCO₂ = 2.8 bar, pH₂S = 10 mbar, 1 wt% NaCl 230
- Figure 126. Exp 10. SEM of iron sulfide layer growth, Single phase flow, 21 days, 60°C, pH 6, pCO₂ = 2.8 bar, pH₂S = 10 mbar, 1 wt% NaCl 231
- Figure 127. Exp 10. Close up image for SEM of iron sulfide layer growth, Single phase flow, 21 days, 60°C, pH 6, pCO₂ = 2.8 bar, pH₂S = 10 mbar, 1 wt% NaCl..... 231

- Figure 128. Exp 10. IFM analysis of sample WITHOUT corrosion product layer, Single phase flow, 21 days, 60°C, pH 6, pCO₂ = 2.8 bar, pH₂S = 10 mbar, 1 wt% NaCl . 232
- Figure 129. SEM cross-section analysis view of localized corrosion, Single phase flow, 21 days, 60°C, pH 6, pCO₂ = 2.8 bar, pH₂S = 10 mbar, 1 wt% NaCl, Thin adherent layer, (10 mm) with ‘fluffy mackinawite’ on top, failed as seen by the loss of material under the layer. 233
- Figure 130. Exp 10. Close up view of SEM cross-section analysis view of localized corrosion, Single phase flow, 21 days, 60°C, pH 6, pCO₂ = 2.8 bar, pH₂S = 10 mbar, 1 wt% NaCl, Fluffy mackinawite seen on top of corrosion product buildup, possible fracture in layer..... 233
- Figure 131. Partial pressure measurements for 21 day experiment with lower partial pCO₂, lower partial pH₂S, lower temperature, lower pH, lower flow rate, 40°C pH 5, 2.9 bar pCO₂, 4 mbar pH₂S..... 235
- Figure 132. Single phase corrosion rate measurements. Weight loss + IFM for penetration rates. X65 steel, 40°C, pH 5, pCO₂ = 2.8 bar, pH₂S = 4 mbar, 1 wt% NaCl 236
- Figure 133. Stratified flow corrosion rate measurements. Weight loss + IFM for penetration rates. X65 steel, 40°C, pH 5, pCO₂ = 2.8 bar, pH₂S = 4 mbar, 1 wt% NaCl..... 236
- Figure 134. Pitting ratio for single phase and stratified flow X65 steel weight loss coupons in 40°C, pH 5, pCO₂ = 2.8 bar, pH₂S = 4 mbar, 1 wt% NaCl..... 237

Figure 135. Exp 11. Local layer failures found after 7 day exposure, Single phase flow, 40°C, pH 5, pCO ₂ = 2.8 bar, pH ₂ S = 4 mbar, 1 wt% NaCl	238
Figure 136. Exp 11. Close up of local corrosion product layer failure found after 7 day exposure, Single phase flow, 40°C, pH 5, pCO ₂ = 2.8 bar, pH ₂ S = 4 mbar, 1 wt% NaCl.....	238
Figure 137. Exp 11. SEM / EDS of WL sample, corrosion product layer showing polish marks of original corrosion product, 7 days, 40°C, pH 5, pCO ₂ = 2.8 bar, pH ₂ S = 4 mbar, 1 wt% NaCl	239
Figure 138. Exp 11. IFM of WL sample WITHOUT corrosion product layer. stratified flow, 40°C, pH 5, pCO ₂ = 2.8 bar, pH ₂ S = 4 mbar, 1 wt% NaCl, 7 days.....	240
Figure 139. Exp 11. Two separate examples of corrosion product layer failure from stratified flow, 21 days, 40°C, pH 5, pCO ₂ = 2.8 bar, pH ₂ S = 4 mbar, 1 wt% NaCl	241
Figure 140. Exp 11. IFM of WL sample WITHOUT corrosion product layer, 21 days, stratified flow, 40°C, pH 5, pCO ₂ = 2.8 bar, pH ₂ S = 4 mbar, 1 wt% NaCl.....	241
Figure 141. Exp 11. Corrosion product layer, 21 days, single phase flow, 40°C, pH 5, pCO ₂ = 2.8 bar, pH ₂ S = 4 mbar, 1 wt% NaCl	242
Figure 142. Exp 11. Iron sulfide corrosion product layer, 21 days, single phase flow, 40°C, pH 5, pCO ₂ = 2.8 bar, pH ₂ S = 4 mbar, 1 wt% NaCl	243
Figure 143. Exp 11. “Lettuce Leaf Mackinawite,” Corrosion product layer, 21 days, single phase flow, 40°C, pH 5, pCO ₂ = 2.8 bar, pH ₂ S = 4 mbar, 1 wt% NaCl	243

Figure 144. Exp 11. Iron sulfide corrosion product layer, same sample, different location, 21 days, single phase flow, 40°C, pH 5, pCO ₂ = 2.8 bar, pH ₂ S = 4 mbar, 1 wt% NaCl	244
Figure 145. Exp 11. IFM analysis without corrosion product layer, 21 days, single phase flow, 40°C, pH 5, pCO ₂ = 2.8 bar, pH ₂ S = 4 mbar, 1 wt% NaCl.....	244
Figure 146. General corrosion (squares), as well as “localized” corrosion from IFM (single sided error bars), from weight loss of samples exposed to single phase flow in 25°C, pCO ₂ = 2.8 bar, pH ₂ S = 100 mbar, 1 wt.% NaCl.	249
Figure 147. General corrosion (triangles), as well as “localized” corrosion from IFM (single sided error bars), rates from weight loss samples exposed to multiphase flow in 25°C, pCO ₂ = 2.8 bar, pH ₂ S = 100 mbar, 1 wt.% NaCl.	250
Figure 148. Pitting ratio for weight loss samples exposed in 25°C, pCO ₂ = 2.8 bar, pH ₂ S = 100 mbar, 1 wt.% NaCl.	250
Figure 149. Corrosion product layer growth vs. time. 25°C, pCO ₂ = 2.8 bar, pH ₂ S = 100 mbar, 1 wt.% NaCl.	251
Figure 150. Scaling Tendency for 25°C, pCO ₂ = 2.8 bar, pH ₂ S = 100 mbar, 1 wt.% NaCl.	252
Figure 151. SEM images of corrosion product on sample from single phase after 7 days exposure to conditions, 25°C, pH 5, pCO ₂ = 2 bar, pH ₂ S = 100 mbar, 1 wt% NaCl solution. Images show corrosion product has multiple layers (a) and the upper layer shows original polish marks (b).....	254

- Figure 152. SEM images of corrosion product on sample from single phase after 7 days exposure to conditions, 25°C, pH 5, pCO₂ = 2 bar, pH₂S = 100 mbar, 1 wt% NaCl solution. Images show a location where the corrosion product layer failed in situ (a) and corrosion product growth filled the area (b). 254
- Figure 153. EDS analysis of corrosion product layer surface features. 25°C, pH 5.0, pCO₂ = 2.8 bar, pH₂S = 100 mbar, 1 wt.% NaCl, 7 days..... 255
- Figure 154. Single phase, 7 days exposure to (25°C); Sample “as removed” on left, IFM image of surface both with the corrosion product layer (middle) and without the corrosion product layer (right)..... 257
- Figure 155. Single phase flow, 21 days, corrosion product layer. SEM image on the left at 100x magnification shows the surface topography covered with iron sulfide. On the right side, increasing the magnification of the SEM image to 400x shows the ‘polish marks’ visible in the substrate below the precipitation. 258
- Figure 156. EDS analysis of surface precipitate (left) and substrate material (right) after 21 day exposure to conditions, 25°C, pH 5, pCO₂ = 2 bar, pH₂S = 100 mbar, 1 wt% NaCl solution. 258
- Figure 157. EDS analysis comparison of the precipitate to the substrate in (left) linear scale and (right) log scale on the y-axis after 21 day exposure to conditions, 25°C, pH 5, pCO₂ = 2 bar, pH₂S = 100 mbar, 1 wt% NaCl solution..... 260

- Figure 158. Single phase, 21 days exposure to 25°C; Sample “as removed” on left, IFM image of surface both with the corrosion product layer (middle) and without the corrosion product layer (right)..... 261
- Figure 159. SEM images of corrosion product on sample from multiphase flow after 7 days exposure to conditions, 25°C, pH 5, pCO₂ = 2 bar, pH₂S = 100 mbar, 1 wt% NaCl solution. Images show corrosion product has multiple layers of slightly different composition in backscatter analysis (a) and upper layer shows original polish marks (b). 262
- Figure 160. Corrosion product layer has two components. The top layer shows the polish marks (left side image), while the bottom layer could be described as the remaining carbide layer or an iron depleted substrate. Multiphase flow, 7 days’ exposure to conditions, 25°C, pH 5, pCO₂ = 2 bar, pH₂S = 100 mbar, 1 wt% NaCl solution.... 262
- Figure 161. Multiphase, 7 days exposure to 25°C; Sample “as removed” on left, IFM image of surface both with the corrosion product layer (middle) and without the corrosion product layer (right)..... 263
- Figure 162. Thin layer, top layer failure. Multiphase 21 days, thin layer, top layer failure. Polish marks are still visible. Multiphase flow after 21 days exposure to conditions, 25°C, pH 5, pCO₂ = 2 bar, pH₂S = 100 mbar, 1 wt% NaCl solution. 264
- Figure 163. Multiphase, 21 days exposure to 25°C; Sample “as removed” on left, IFM image of surface both with the corrosion product layer (middle) and without the corrosion product layer (right)..... 265

Figure 164. General corrosion (squares), as well as “localized” corrosion from IFM (single sided error bars), from weight loss of samples exposed to single phase flow in 40°C, pCO ₂ = 2.8 bar, pH ₂ S = 100 mbar, 1 wt.% NaCl, pH 5.0 for 7, 14 and 21 days exposure.....	267
Figure 165. General corrosion (squares), as well as “localized” corrosion from IFM (single sided error bars), from weight loss of samples exposed to multiphase flow in 40°C, pCO ₂ = 2.8 bar, pH ₂ S = 100 mbar, 1 wt.% NaCl, pH 5.0 for 7, 14 and 21 days exposure.....	267
Figure 166. Pitting ratio for weight loss samples exposed in 40°C, pCO ₂ = 2.8 bar, pH ₂ S = 100 mbar, 1 wt.% NaCl.....	268
Figure 167. Corrosion product layer growth vs. time. 40°C, pCO ₂ = 2.8 bar, pH ₂ S = 100 mbar, 1 wt.% NaCl.....	269
Figure 168. Scaling Tendency for 40°C, pCO ₂ = 2.8 bar, pH ₂ S = 100 mbar, 1 wt.% NaCl.....	269
Figure 169. SEM images of corrosion product on sample from single phase after 7 days exposure to conditions, 40°C, pH 5, pCO ₂ = 2.8 bar, pH ₂ S = 100 mbar, 1 wt% NaCl solution. Images show a failure area in the corrosion product layer (left), but no polish marks can be seen on the surface next to a failure location (right).....	270
Figure 170. EDS analysis of the corrosion product found on the surface (left) and in the failure location (right) shown in Figure 169.....	271

- Figure 171. Single phase, 7 days exposure to 40°C; Sample “as removed” on left, IFM image of surface both with the corrosion product layer (middle) and without the corrosion product layer (right)..... 272
- Figure 172. Corrosion product shown in two different magnifications for emphasis that failure of the layer occurred in situ (left) and a closer view of the crystalline surface features..... 273
- Figure 173. Higher magnification and EDS analysis of crystal structures found on the corrosion product surface. 21 days exposure to conditions, 40°C, pH 5, pCO₂ = 2.8 bar, pH₂S = 100 mbar, 1 wt% NaCl solution, single phase flow..... 273
- Figure 174. Corrosion product and polish marks observed after 21 days exposure to conditions in single phase flow, 40°C, pH 5, pCO₂ = 2.8 bar, pH₂S = 100 mbar, 1 wt% NaCl solution..... 274
- Figure 175. Single phase, 21 days exposure to 40°C; Sample “as removed” on left, IFM image of surface both with the corrosion product layer (middle) and without the corrosion product layer (right)..... 275
- Figure 176. Layer failure (ex situ); polish marks visible on corrosion product layer. ... 276
- Figure 177. Multiphase flow, 7 days exposure to 40°C; Sample “as removed” on left, IFM image of surface both with the corrosion product layer (middle) and without the corrosion product layer (right)..... 277

- Figure 178. Similar areas of corrosion initiation at 7 days (left) and at 14 days (right) exposure to conditions 40°C, pH 5, pCO₂ = 2.8 bar, pH₂S = 100 mbar, 1 wt% NaCl solution. 278
- Figure 179. Corrosion product layer fractured after drying procedures showing a top layer that was intact in many areas with polish marks still visible. 21 days, 40°C, pH 5, pCO₂ = 2.8 bar, pH₂S = 100 mbar, 1 wt% NaCl solution 279
- Figure 180. Multiphase flow, 21 days exposure to 40°C; Sample “as removed” on left, IFM image of surface both with the corrosion product layer (middle) and without the corrosion product layer (right)..... 280
- Figure 181. Surface layer failure assumed to occur ex situ (left) and magnified image of the area that would have been under that failed layer (right) indicates iron carbonate growth occurred beneath an iron sulfide layer. Multiphase flow, 21 days, 40°C, pH 5, pCO₂ = 2.8 bar, pH₂S = 100 mbar, 1 wt% NaCl solution. 281
- Figure 182. EDS analysis of crystal structure found in area under failed surface layer (Figure 181) shows only components consistent with iron carbonate. Multiphase flow, 21 days, 40°C, pH 5, pCO₂ = 2.8 bar, pH₂S = 100 mbar, 1 wt% NaCl solution. 281
- Figure 183. Cross section showing corrosion occurring underneath a thin corrosion product layer (lifted). Multiphase flow, 21 days, 40°C, pH 5, pCO₂ = 2.8 bar, pH₂S = 100 mbar, 1 wt% NaCl solution. 282

Figure 184. EDS analysis shows lower sulfur content underneath the “lifted” thin layer. Multiphase flow, 21 days, 40°C, pH 5, pCO ₂ = 2.8 bar, pH ₂ S = 100 mbar, 1 wt% NaCl solution.	283
Figure 185. Measured test parameters: pH and Temperature for 21 days, 60°C, pH 6, pCO ₂ = 7.7 bar, pH ₂ S = 10 mbar, 1 wt% NaCl solution with 100 ppm free acetic acid added at day 10.	287
Figure 186. Measured test parameters: corrosion rate and corrosion potential for 60°C, pH 6, pCO ₂ = 7.7 bar, pH ₂ S = 10 mbar, 1 wt% NaCl solution with 100 ppm free acetic acid added at day 10.	288
Figure 187. WL coupon after 10 days exposure to conditions in single phase flow.	289
Figure 188. WL samples after 10 days exposure to initial conditions in multiphase flow.	290
Figure 189. EDS analysis of the single phase coupon exposed for 10 days shows a sulfide dominant layer (left) that is also repeatable for each of the various shaped surface morphologies (right).	292
Figure 190. WL coupon after 10 days exposure to conditions with HAc in single phase flow.	293
Figure 191. WL coupon after 10 days exposure to conditions with HAc in multiphase flow.	294
Figure 192. WL coupon after 10 days exposure to conditions with HAc in multiphase flow. Cross section with corrosion product layer.	295

Figure 193. WL coupon “A” after 20 days exposure to the full test conditions in single phase flow.....	296
Figure 194. WL coupon “B” after 20 days exposure to the full test conditions in single phase flow.....	297
Figure 195. WL coupon after 20 days exposure to conditions with HAc in single phase flow. Cross section with corrosion product layer.	298
Figure 196. EDS analysis of localized corrosion found in cross section of WL coupon after 20 days exposure to conditions with HAc in single phase flow; material below original surface.	299
Figure 197. EDS analysis of localized corrosion found in cross section of WL coupon after 20 days exposure to conditions with HAc in single phase flow; material above original surface.	300
Figure 198. EDS analysis of localized corrosion found in cross section of WL coupon after 20 days exposure to conditions with HAc in single phase flow; material above original surface.	300
Figure 199. WL coupon after 20 days exposure to the full test conditions in multiphase flow.....	302
Figure 200. WL corrosion rate data comparison for all coupons from single phase (SP), multiphase (MP), first 10 days (No HAc), second 10 days (HAc), and full test.	303
Figure 201. WL pitting ratio comparison for all coupons from single phase (SP), multiphase (MP), first 10 days (No HAc), second 10 days (HAc), and full test.	303

Figure 202. Environmental parameters plotted on an arbitrary axis for 80 analyzed weight loss samples (x-axis) sorted by temperature, pH, and sodium chloride concentration (M_NaCl represents ionic strength, Total_CO ₂ represents the sum of [H ₂ CO ₃]+[HCO ₃ ⁻], Total_H ₂ S represents the sum of [H ₂ S] _{aq} +[HS ⁻].	312
Figure 203. Addition of Pitting Ratio data to the environmental parameter set.	313
Figure 204. Likelihood of localized corrosion sorted with respect to temperature, pH, sodium chloride concentration, pCO ₂ , and pH ₂ S.	315
Figure 205. Correlation between measured and calculated values for likelihood for localized corrosion.	317
Figure 206. Direct comparison of measured and calculated likelihood for localized corrosion under the tested conditions.	318
Figure 207. Comparison of the measured maximum pitting ratio for 78 test samples to the measured and calculated values for likelihood of localized corrosion.	318
Figure 208. Graphic representation of the concentration of species as diffused through an initial corrosion product layer in an H ₂ S/CO ₂ environment that is 25% of its final thickness.	331
Figure 209. Graphic representation of the concentration of species, [H ₂ S] _(aq) , [H ₂ CO ₃], and [Fe ²⁺], as diffused through an initial corrosion product layer in an H ₂ S/CO ₂ environment that is only 50% of its final thickness.	332

Figure 210. Graphic representation of the concentration of species, $[\text{H}_2\text{S}]_{(\text{aq})}$, $[\text{H}_2\text{CO}_3]$,
and $[\text{Fe}^{2+}]$, as diffused through a corrosion product layer in an $\text{H}_2\text{S}/\text{CO}_2$ environment
that is fully developed..... 333

CHAPTER 1: INTRODUCTION

Localized corrosion in its worst form as related to pipelines in the upstream oil and gas industry represents a non-uniform loss of metal from the pipe wall which can lead to a loss of containment. Pipelines designed to withstand 50 years of operation under a “worst case” general corrosion rate may fail after a few months of operation due to localized corrosion. Loss of containment from a pipeline failure is a costly event as it would cause an emergency shutdown in the production of oil and/or gas, an emergency repair of the pipeline, and probably an environmental clean-up at the leak site. In an effort to minimize pipeline failures and loss of containment, companies around the world in the oil and gas industry sponsor research programs focused on better prediction methods and better mitigation methods of localized corrosion.

Research is conducted at the Institute for Corrosion and Multiphase Technology (ICMT) in an effort to define and characterize localized corrosion in upstream oil and gas pipelines. The first definition of the focus area for localized attack as related to CO₂ corrosion was provided in 2003¹. Three areas, graphically shown in Figure 1, provide a simplistic explanation of the likelihood of localized corrosion based upon the presence of a corrosion product layer. An uninhibited mild steel pipeline in an environment where no corrosion product layer would form would have a high uniform corrosion rate with no localized corrosion expected. An uninhibited mild steel pipeline in an environment where a fully developed corrosion product layer would be maintained on the metal surface to provide protection against corrosion would not be expected to develop localized

corrosion. But, the “gray zone,” as it was termed, is where a partially protective iron carbonate layer on the surface of the carbon steel provides the opportunity for anodic and cathodic sites to be developed, thus propagating localized corrosion through galvanic corrosion.

No Layer	Partially Protective Layer	Fully Protective Layer
High Uniform Attack No Localized Corrosion	Low/High Corrosion Attack Localized Corrosion	Low Uniform Attack No Localized Corrosion

Figure 1. Definition of focus area for localized attack or localized corrosion, termed the “gray zone.”¹

Having experimental conditions in the “gray zone” has been seen to facilitate propagation of localized corrosion² independent of the method of localized corrosion initiation. A full coverage of an iron carbonate layer on a mild steel surface will cause an increase in the electrochemical potential of the metal substrate. But any damage to that iron carbonate layer in an environment that is not highly saturated with iron carbonate would expose the metal substrate which would have the original electrochemical potential of bare steel in the environmental conditions, and this difference in potential is the basis for the initiation of localized corrosion as portrayed in Figure 2.

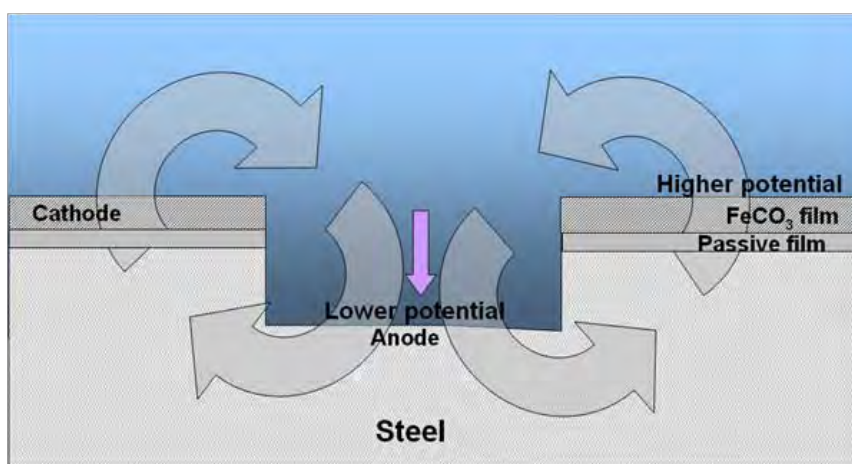


Figure 2. Definition of an active pit under conditions subject to localized corrosion.²

Continued efforts in the characterization of localized corrosion related to internal corrosion of upstream oil and gas pipelines also needs to include ‘sour’ conditions, or environments containing both CO₂ and H₂S. Research focused on sour corrosion at the ICMT have provided a wealth of information related to testing CO₂ corrosion in the presence of trace amounts of H₂S³, to mechanistic modeling of CO₂ corrosion of mild steel in the presence of H₂S⁴, and to the understanding the kinetics of scale formation in CO₂/H₂S corrosion⁵. These projects have focused on defining the mechanisms related to general corrosion in a sour environment which provide the basis for further research focused on localized corrosion in a sour environment.

Experiments in a large scale flow loop were used to establish the effects of low concentrations of H₂S in a CO₂ environment on the corrosion rates of mild steel under non-film forming conditions by Brown³ in 2004. Environmental conditions in this previous research exposed C1018 and X65 mild steel samples to a synthetic seawater

solution at pH 4 with gas phase concentrations of H₂S from 3 ppm to 100 ppm (2 Pa to 79 Pa) in a CO₂ saturated system at 7.9 bar (100 psig) total pressure at temperatures of either 60°C or 80°C. It was found that the addition of trace amounts of H₂S to a CO₂ saturated environment retarded the general corrosion rate over a 4 day period of time as compared to a pure CO₂ environment with corrosion mechanisms related to adsorption and surface reaction.⁶

The first mechanistic model related to trace amounts of H₂S in a CO₂ saturated environment included definitions for an initial adsorbed layer of iron sulfide (FeS) and for the precipitation of a corrosion product related to bulk solution conditions was developed by Lee⁴ in 2004. The initial adsorbed layer of FeS on a metal surface is modeled by a Langmuir type adsorption isotherm which simulates an immediate reduction in corrosion rate based on limiting the mass transfer of species from the bulk solution to the metal surface. The subsequent formation of iron sulfide and iron carbonate corrosion product relies on the prediction of solution chemistry at the metal surface and then uses two principle mechanisms of precipitation and undermining. These mechanisms determine the kinetics of growth and resulting morphology of the corrosion product layer while always taking into account the mass transfer limitation due to the initial FeS layer.

The kinetics of iron carbonate and iron sulfide scale formation in CO₂/H₂S corrosion were further modeled by Sun⁵ in 2006. Based on Sun's H₂S/N₂ corrosion research, the growth of the corrosion product layer is defined by the diffusion of species which occurs after the formation of a mackinawite (FeS) scale as the first layer on the

steel surface (Lee⁴). The growth of the corrosion product layer is defined by two processes: (i) the outward diffusion of ferrous ions through the corrosion product layer which is consistent with the electrochemical iron dissolution mechanism and with the growth of mackinawite at the outer film/solution boundary, and, (ii) the inward diffusion of species through the corrosion product layer which leads to the direct reduction of H₂S and mackinawite formation at the inner film/metal substrate boundary. This scenario provides mechanisms for observations of void spaces near the metal surface and corrosion product layers that are weak and prone to spalling. For H₂S/CO₂ corrosion, Sun⁵ defines an H₂S corrosion rate based on the presence of CO₂, where the mackinawite scale always forms as the first layer on the steel surface and iron carbonate crystals may precipitate in the outer mackinawite scale. Since the research observations in which iron carbonate crystals were formed in these H₂S/CO₂ corrosion studies was based on short term experiments (up to 4 days) at 80°C with an iron carbonate saturation value greater than 300 and the ratio of total sulfides to total carbonates less than 5%, Sun's model may be valid only for a narrow range of conditions; more research is required to expand and validate the model over a larger range of conditions.

Therefore, the goals for this research on the nature of sulfides and their effect on corrosion are threefold: (i) to design and carry out experiments that delineate the effect of multiple parameters on the rate of localized corrosion over a wide range of parameter values for an H₂S/CO₂/H₂O/Fe system, (ii) to analyze the experimental data to develop a

correlation to predict the likelihood of localized corrosion in sour systems, and (iii) to identify the parameters for developing a mechanistic model for localized corrosion.

This dissertation is organized in the following manner: Chapter 2 summarizes the current state of relevant research for localized corrosion in pipelines and establishes the objectives and rationale of the present research. Chapter 3 describes the design of the corrosion experiment, the thermodynamic equilibrium calculations of the system, and the experimental methods used in operation of the system and analysis of results. Chapter 4 contains the experimental results from 15 different experiments which cover 7 different topics. Chapter 5 contains the statistics of the data used for the model, the model for prediction of localized corrosion in an $\text{H}_2\text{S}/\text{CO}_2/\text{H}_2\text{O}/\text{Fe}$ system, the influence of each parameter used in the calculation, and verification of the model. Chapter 6 contains a discussion on the relationship between the growth of the corrosion product layer and localized corrosion, the conclusions drawn from the research, and guidelines for future research.

CHAPTER 2: BACKGROUND AND OBJECTIVES

Introduction

There is an increased focus on hydrogen sulfide influenced corrosion in the oil and gas industry that stems from the fact that pipeline leaks and failures caused by localized corrosion occur more frequently when H₂S is present.⁷ New production wells are being drilled deeper and most (if not all) are sour (containing H₂S) and older wells that have been influenced by enhanced production procedures can easily be contaminated with organic matter that will eventually make a previously sweet reservoir (containing only CO₂) become sour.⁸ Because of these issues, research in this field of study is necessary to provide an understanding of the corrosion mechanisms which will aid in improving methods for corrosion control.

Focus on Localized Corrosion

To provide a better understanding of the terminology used in the following research, a more detailed definition for localized corrosion is needed. Corrosion is an undesirable deterioration of a material that will eventually compromise the attributes of that material until a failure occurs. Detailed discussions about the global definitions of corrosion can be found in many textbooks^{9, 10, 11} including definitions similar to those used with the context of the current research which are all related to internal corrosion of mild steel pipelines or tubing materials in the upstream oil and gas industry. There are different forms of metallic corrosion which can be related to the mechanisms of the metal

loss (general corrosion, localized corrosion, mechanically assisted corrosion, etc.) and each of these forms is further defined by several distinct types of corrosion that have been observed. Localized corrosion is observed when certain areas of the surface deteriorate faster than other areas and usually results from the breakdown of a partially protective corrosion product layer. The most common type of localized corrosion is pitting corrosion.¹⁰ Pitting corrosion is observed as a highly localized deterioration of the metal surface that is much greater than the general corrosion rate on the surrounding surface area. Initiation of pitting corrosion occurs when a defect or discontinuity in a corrosion product layer allows a small surface area on the metal substrate to become anodic with respect to the larger surrounding surface area of the same metal substrate in a conductive, corrosive solution.

Propagation or growth of the pit may be related to the general corrosion rate of the bare metal surface or accelerated by the galvanic effect between a large cathode area and a small anode, but must be much greater than the general corrosion rate of the overall metal surface. Although many examples of localized corrosion reviewed throughout the current research fit the description of pitting corrosion, experiments were not designed to elucidate the mechanisms of pit initiation and pit propagation, but were focused on identifying the environmental parameters with the most influence on the likelihood of localized corrosion. Therefore the terminology used in reviewing and modeling the experimental results will be the more generic form, localized corrosion rather than the more specific type, pitting corrosion.

Localized corrosion in pipelines carrying definable concentrations of H₂S has been linked to the iron sulfide corrosion products that develop. Although the effects of H₂S on CO₂ corrosion which lead to this type of localized corrosion are not entirely understood, it has been speculated that adsorbed sulfide species and/or sulfide layers influence the local acceleration of mild steel corrosion through a catalytic or a galvanic effect.¹² H₂S and ferrous ions have been confirmed to have extremely fast reaction kinetics, able to create a thin protective layer in a matter of minutes.⁴ The initial layer covers the metal surface so well that corrosion prediction models must be based on mass transfer because of initial corrosion product formation.^{13,14} The current understanding in the corrosion community is that the presence of H₂S can develop a variety of iron sulfide corrosion products, over time, depending on the environmental conditions which directly influence localized corrosion, but the environmental conditions leading to the build-up of these poorly protective iron sulfide layers as well as the main causes and mechanisms of severe pitting (>5-10mm/yr) in sour gas conditions remain unknown.⁷

In a review of oilfield corrosion related to H₂S, Smith *et al.*¹⁵ stated that, even though there is over 60 years of H₂S related corrosion research work, much of the research can be confusing and contradictory because iron sulfide chemistry is complex and seemingly minor changes in environmental conditions can lead to dramatically different results. With formal names such as mackinawite, pyrrhotite, and troilite, these iron sulfide corrosion products are semiconductive, weak in adherence, have a range of compositions from iron-deficient to iron-rich, and are all thought to have a different

effect on mild steel corrosion. The interest in understanding the effect of H₂S on corrosion of mild steel stems from the fact that the corrosion product formed has a greater tendency to develop localized corrosion, which can be magnitudes greater than the general corrosion observed throughout the same system.^{16,17}

Sun *et al.*¹³ reported that the corrosion products formed in a CO₂/H₂S system depend on the competitiveness of the iron carbonate and iron sulfide formed. With mackinawite as the predominant iron sulfide, the precipitation rate of the corrosion product layer increased with the increase of H₂S concentration, but decreased over time as the mass transfer rate of species decreased due to the increased thickness of the corrosion product layer. They concluded that iron sulfide scale was formed mainly by Fe²⁺ released from the steel surface by corrosion and not from Fe²⁺ in the bulk solution. This is an important statement because it directly connects the corrosion rate with the growth rate of corrosion product scale in the presence of H₂S. In the same study, they found that the initial corrosion rate of mild steel increased with the partial pressure of H₂S at low concentrations, but the overall corrosion rate was found to decrease with an increase in the amount of time the mild steel was exposed to the tested conditions.

Lee and Nešić¹⁸ investigated the initial reaction of mild steel with trace amounts of H₂S and determined that a Frumkin-type adsorption isotherm is successful in modeling the surface coverage by mackinawite. Mackinawite formed immediately on the electrode surface and even though it was not visible by the naked eye, XPS analysis confirmed the

presence of mackinawite (FeS_{1-x}) on the electrode surface under these experimental conditions.

Brown and Nešić¹⁶ studied corrosion product layer development in a $\text{CO}_2/\text{H}_2\text{S}$ system under conditions with varied iron sulfide and iron carbonate saturation values. They concluded that these values are important in defining layer morphology and corrosion rate prediction, but are not direct indicators for predicting localized corrosion. Precipitated corrosion product layers were observed to decrease the effect of flow on corrosion by decreasing the mass transfer rate of species to the metal surface, but increased the likelihood of localized corrosion.

In her dissertation, the corrosion model developed by Sun⁵ related the corrosion products formed in a $\text{H}_2\text{S}/\text{N}_2$ system to flow and found that the corrosion product retained on the steel surface was dependant on both the scale formation rate and the scale damage rate. The scale formation rate is a function of both the corrosion rate and precipitation rate. The scale damage rate is a calculation related to both mechanical removal and chemical removal of the corrosion product layer. Experimental data were used to develop an empirical correlation for the scale damage rate (SDR) in the form of a linear expression with respect to the calculated corrosion rate (CR):

$$SDR = 0.5 * CR \quad (1)$$

Although this correlation has been sufficient to develop the general corrosion prediction model, more research is necessary to develop an understanding of corrosion mechanisms in order to model the relationship of the corrosion product layer to localized corrosion.

Effect of the Corrosion Product Layer on Localized Corrosion Mechanisms

Dissolved and dissociated species from H₂S have been confirmed to have extremely fast reaction kinetics with iron and ferrous ions, able to create a thin ferrous sulfide layer on a mild steel surface that reduces the general corrosion rate in a matter of minutes. This first corrosion product layer covers the metal surface so well that corrosion prediction models must be based on mass transfer.^{13,14}

Many researchers have been trying to understand how the corrosion product layer that develops when H₂S is present leads to localized corrosion of mild steel and understand the corrosion mechanisms involved. The ferrous sulfide or mackinawite corrosion product has been characterized to have a layered structure which will allow species migration. Wolthers *et al.*¹⁹ have hypothesized that the structure of mackinawite is large enough to allow water molecules to be incorporated into the lattice during its formation. He reports that the tetragonal structure of the mackinawite unit cell (Figure 3) has dimensions ($a = b = 367.35$ pm, $c = 503.28$ pm) that are sufficiently far apart for species to reside or diffuse “between the sheets”.

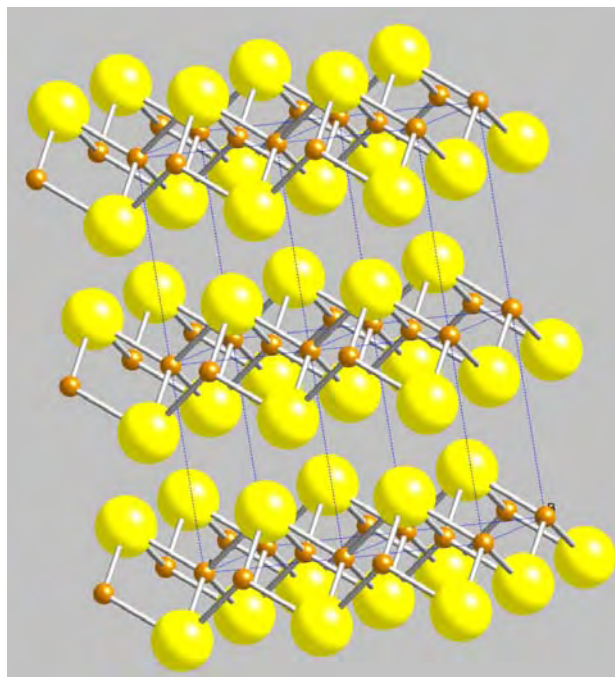


Figure 3. Layered structure of Mackinawite with the unit cells shown as lines between the layers. Iron molecules (Fe) are indicated as small orange spheres and sulfur molecules (S) are indicated by the larger yellow spheres.[†]

Zhao *et al.*²⁰ have shown that the ferrous sulfide layer can have a difference in electrical potential between the interior and exterior of the layer that will lead to ion-selectivity. In tests using two Plexiglas cells separated by a cellulose layer, ferrous sulfide was grown on the cellulose layer and the membrane potential measured in relation to a difference in sodium chloride concentration across the layer. They found that the potential of the cellulose sheet alone is seen to be small enough to be neglected, but a large potential difference is observed when the surface of the cellulose is covered with a ferrous sulfide layer. This is an important characteristic for understanding the

[†] Provided by Dr. D. Young from Crystal Maker® Software, 2010.

mechanisms related to the formation and breakdown of the iron sulfide layer that leads to localized corrosion.

The cation-selective interior of the mackinawite layer aids in cation (Fe^{2+}) migration from the metal surface into the layer while the anion-selective exterior of the layer aids anions (HS^- , S^{2-} , HCO_3^- , CO_3^{2-} , Cl^-) migrating from the bulk solution into the layer. A representation of the separation of charges across the mackinawite layer envisioned by Zhao *et al.*²⁰ is shown Figure 4.

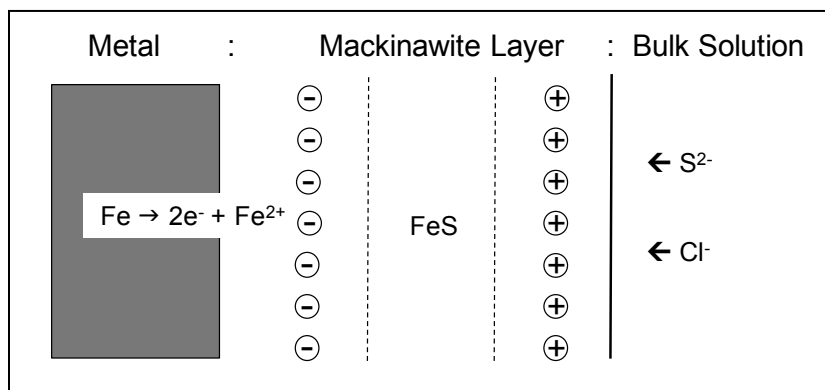


Figure 4. Representation of charge separation by the mackinawite layer²⁰

The relative sizes of the cations and anions, given in Table 1, are less than the unit cell size given for mackinawite, so that migration into the layer is highly likely. The ferrous ions react with sulfide ions within the corrosion product layer during the migration process, building the corrosion product layer from within. This process would lead to local areas of failure in corrosion product layer by promoting internal stresses within the corrosion product layer (previously modeled by Sun⁵).

Table 1. Ions and Aqueous Species Possible in an H₂S/CO₂ System.²¹

Ions	Ionic radius	Ions	Ionic radius
H ⁺	25 pm	Cl ⁻	167 pm
Fe ²⁺	77 pm	S ²⁻	170 pm
Na ⁺	116 pm	HS ⁻	191 pm
O ²⁻	126 pm	HCO ₃ ⁻	207 pm

In the opinion of Zhao *et al.*²⁰ the anion-selective exterior layer of the corrosion product would help Cl⁻ ions migrate from the bulk solution. But with no reaction in the ferrous sulfide layer, the Cl⁻ ions will reach the metal surface, leading to Cl⁻ enrichment under the precipitate. A mechanism related to the breakdown of a passive layer by chlorides leading to pit nucleation²² is undefined and may not prove to be the cause or initiator for localized corrosion on mild steels. But the indication that the structure of the mackinawite layer would allow limited diffusion of bulk solution species while promoting ion exchange within the layer sets the stage for a localized corrosion prediction model that can incorporate these mechanisms.

There is only a limited volume of research available in literature that describes the corrosion mechanism and the corrosion reactions that result in the formation iron sulfide corrosion products in aqueous corrosion systems, especially at temperatures below 100°C. The few experimental studies^{12,23, 24, 25} that have been published in open literature are limited to autoclaves and glass cells. H₂S concentrations of a few parts per million (ppm) in nitrogen gas have been observed to decelerate the corrosion rate at temperatures between 20°C and 60°C. This type of layer has been seen on mild steel samples where the

mixture of a few ppm H₂S into a CO₂ gas-purged, brine-filled, 2-liter glass cell greatly decreased the corrosion rates of the pre-corroding samples²³. Ikeda *et al.*²⁴ have shown contradictory results related to low concentrations of H₂S (<30 ppm) in a CO₂ saturated solution that accelerated the corrosion rate significantly, but the effect seems questionable and may be related to the small initial mass of H₂S added to the experiment fully reacting away in a closed autoclave; this phenomena decreased dramatically at higher H₂S concentrations (>30 ppm) and higher temperatures (>80°C) when a protective layer forms²⁴. The development of a more protective layer at higher temperatures (80°C to 100 °C) is also in agreement with studies by Valdes *et al.*²⁵. These observations lead one to believe that the mechanisms of corrosion in the presence of H₂S and CO₂ can be directly related to the characteristics of the corrosion product layer and its process of formation.

Objectives and Rationale for the Study

Objectives

The objectives for this research on the nature of sulfides and their effect on corrosion are:

- (i) To design and carry out experiments that delineate the effect of multiple parameters on the rate of localized corrosion over a wide range of parameter values for an H₂S/CO₂/H₂O/Fe system,
- (ii) To analyze the experimental data to develop a correlation to predict the likelihood of localized corrosion in sour systems, and
- (iii) To identify key parameters for developing a mechanistic model for localized corrosion.

Rationale

The rationale related to the conducted research is threefold, similar to the objectives:

(i) There is a need for more research to be conducted in large scale systems on H₂S/CO₂ corrosion to gain more understanding of localized corrosion mechanisms involved in sour corrosion. A large scale system was used so that the physics of the flow are similar to those found in the oil and gas industry pipelines.²⁶ The experimental conditions used in this study focused on a “slightly sour” corrosion environment with CO₂ present and were chosen to develop only partially protective corrosion product layers. The partial pressures, temperatures, and pH were defined such that some experimental conditions tested would have the carbonic acid concentration dominant and some conditions tested would have the aqueous H₂S concentration dominant. The ranges of parameters studied are listed in Table 2. It should be noted that there are a limited number of large scale test facilities for sour corrosion research related to internal pipeline corrosion available to researchers across the world. Due to the nature of testing with a hazardous gas, most of the studies referred to in the literature are limited to autoclaves which are not able to produce the correct physics of the flow for the simulation of corrosion in multiphase slug flow.

(ii) A quantitative model relating localized corrosion in sour corrosion to the environmental parameters involved in the corrosion process does not currently exist in open literature. Understanding the mechanisms that lead to localized corrosion as related

to internal pipeline corrosion found in the upstream oil and gas industry is of great interest to corrosion engineers worldwide. Previous research reviewed from literature provides some of the supporting information for localized corrosion mechanisms related to the H₂S/CO₂/H₂O/Fe system, but this field of study is relatively new and there is still much to be learned.

(iii) A discussion of current research related to the corrosion product growth mechanisms in an H₂S/CO₂/H₂O/Fe system is needed to aid future researchers in understanding the key parameters involved.

Table 2. List of Parameters Tested in the Large Scale H₂S Flow Loop

Parameter	Description
Equipment	H ₂ S Flow Loop
Total pressure	3, 8 bar
Temperature	25°C, 40°C, 60°C
Test duration	10, 20, 30 days or 7, 14, 21 days
Solution	1 wt %, 10 wt% NaCl
pH	4.5, 5, & 6
Superficial Liquid Velocity (V_{sl})	0.1, 1 m/s
Superficial Gas Velocity (V_{sg})	0, 1, 3 m/s
pCO ₂	2.7, 2.9, 7.7 bar
pH ₂ S	0.25, 0.1, 1, 1.2, 4, 10, 100 mBar
Concentration of Free Acetic Acid, [HAc] [‡]	0, 100ppm

[‡] The abbreviation “HAc” is used to represent undissociated acetic acid. HAc in solution can act as another cathodic species in solution to provide protons (H⁺) for the electrochemical reaction and leave an inert acetate ion (Ac⁻) behind.

CHAPTER 3: EXPERIMENTAL METHOD

Experimental Parameters

In order to observe the desired corrosion product(s) and possible failure modes that would lead to localized corrosion, testing was conducted in a large scale system under controlled conditions, which included:

- Partial pressures of the acid gases (p_{H_2S}/p_{CO_2})
- Water chemistry parameters ($pH/CH_3COOH/Fe^{++}$)
- Temperature ($40^\circ C - 80^\circ C$)
- Flow regime (single phase flow vs. multiphase flow)
- Pipeline steel (API 5L X65)

The large scale H_2S flow loop provides a two-phase water/gas environment with a total volume of approximately 2000 liters with provisions for multiphase flow and single phase flow regimes in a 10.1 cm ID pipeline. The solution volume to sample surface area ratio is greater than 30:1 and temperature, pH, flow rates, and partial pressures of both gases can be controlled during testing. The large scale flow loop was used in order to correctly simulate the physics of pipe flow similar to that of upstream oil and gas pipelines while also providing a laboratory environment to monitor and control the parameters related to corrosion product development on mild steel. A full report ³ is available which fully describes the large-scale, multiphase flow loop used for the study of corrosion in sour gas environments.

Testing began with the attempt to create environmental conditions where the iron carbonate and iron sulfide saturation values were similar in an effort to observe competition between precipitation and corrosion product layer development from the two weak acids. The introduction of higher sodium chloride concentrations in further testing was used to lower the iron carbonate saturation value and because it is also thought to be an initiator of localized corrosion through the increased chloride content.²² A change in pH was used to increase or decrease the amount of corrosion product layer that was developed on the corroding surface to provide needed information on the corrosion product layers' effect on corrosion. A change in temperature was explored to observe if a change in the rate of reactions would greatly impact the type of corrosion or corrosion product layer developed. And the addition of acetic acid, a cathodic species which is known to influence the corrosion reaction, was tested to observe the effects on H₂S/CO₂ corrosion. Overall, the test topics conducted in this study are listed below in the order presented in Chapter 4: Experimental Results:

- Effect of Iron Carbonate and Iron Sulfide Saturation Values
- Effect of a Higher Ionic Strength Solution at pH 6
- Effect of a Decrease in Solution pH
- Effect of a Lower Ionic Strength Solution and Lower pH₂S at pH 5
- Effect of a Decrease in pCO₂
- Effect of a Decrease in Temperature
- Effect of the Presence of Acetic Acid

All experiments were conducted in the large scale H₂S system (Figure 5) so that testing is conducted in multiphase flow regimes that can be scaled up to similar to conditions observed in working pipelines.

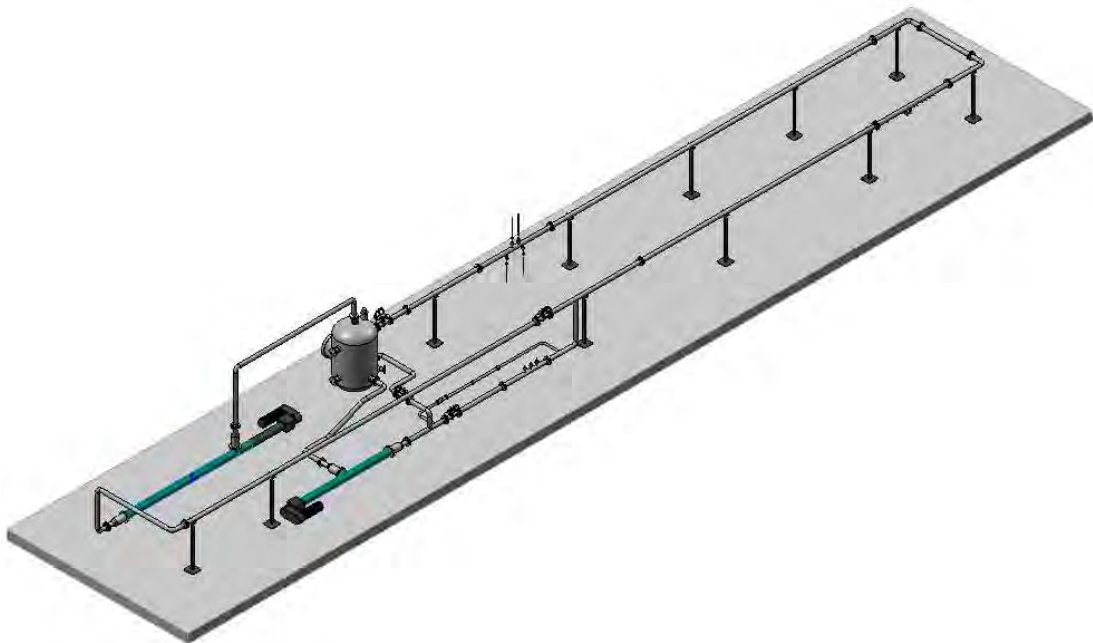


Figure 5. Schematic of the Hydrogen Sulfide large scale flow loop. Full dimensions are 29 m (95 ft) in length and 3.6 m (12 ft) in width.

The operating specifications for large scale equipment may change with time due to modifications of the equipment, so the current list is provided in Table 3. The full description of the large scale H₂S system with the original operating conditions was previously published²⁷ and is provided for review as Appendix B. Due to the cost of Hastelloy C-276 (UNS No. N10276), the pumps used for gas and liquid circulation in the H₂S system have wetted parts that are 316 stainless steel (UNS No. S31603). The

maximum p_{H_2S} that can be used in the H_2S system is due to recommended limitations²⁸ on 316 stainless steel.

Table 3. Specifications of the Hydrogen Sulfide large scale flow loop.

Parameter	Description
Liquid flow rates	0.5 m/s to 2.5 m/s
Gas flow rates	2.0 m/s to 10 m/s
Temperature range	40°C to 90°C
Pressure range	1 bar to 27 bar
Gas mixtures	N_2 , CO_2 , H_2S
Maximum p_{H_2S}	0.13 bar
Pipe internal diameter	10.1 cm (4 inches)
Liquid mixtures	deionized water, salt solutions, model oil
Instrumentation	superficial liquid and gas velocities, flow regime determination, corrosion rate, pH, and temperature

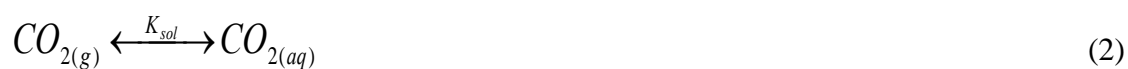
Calculation of Environmental Conditions

Chemical Reactions

In order to relate concentrations to partial pressures from field and laboratory measurements, a simple vapor-liquid equilibrium model is used. This $CO_2/H_2S/H_2O$ vapor-liquid equilibrium model for dilute aqueous solutions was made based upon a system with constant partial pressures of CO_2 and H_2S , such as large open systems or systems which receive input from a continuous source. The model is based on the vapor-liquid equilibria of gaseous species and the dissociation equilibria for dissolved species.

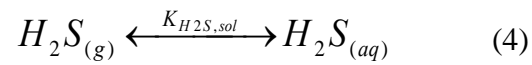
Since the environmental conditions at any point within a pipeline used in the oil and gas industry would have a continuous supply of fresh reservoir fluids and gases from the previous point upstream, calculations can be made using constant partial pressures of carbon dioxide and hydrogen sulfide to determine the environmental conditions at that point in the pipeline. It is assumed that the vapor-liquid equilibrium of the acid gases to the flowing solution is maintained at each point along the pipeline. Saturation of the fluids with the acid gases occurs in the reservoir at higher temperatures and pressures. As the temperature and pressure decrease during transport along the pipeline, the solution will remain saturated and be in equilibrium with the gas phase concentrations of CO₂ and H₂S. The equilibrium constants used for each equation are constant with respect to the reactant and product species in the reaction in order to determine equilibrium concentrations, but vary with temperature as it is understood that reaction rates are directly affected by temperature. Each equation for the vapor-liquid equilibrium of these acid gases is directly followed by the respective equation for the equilibrium constants used as shown in Equation (2) through Equation (15).

The concentration of CO₂ and H₂S in solution is a function of temperature and the respective partial pressure of the gases. The equilibrium constants are solubility constants used in a Henry's Law equation with units of molar/bar.



$$K_{sol} = \frac{14.5}{1.00258} \times 10^{-(2.27+5.65 \times 10^{-3}(T_F)-8.06 \times 10^{-6}(T_F^2)+0.075(I))} \quad (3)$$

with temperature (T_F) in Fahrenheit and ionic strength (I) in mol/L.



$$K_{H_2S,sol} = 10^{-0.71742672-0.012145427(T_C)+5.6659982 \times 10^{-5}(T_C^2)-8.1902716 \times 10^{-8}(T_C^3)} \quad (5)$$

with temperature (T_C) in Celsius.

By comparison of the solubility constants at operating conditions between 40°C and 80°C in Figure 6, it can be seen that H₂S is approximately 3 times more soluble than CO₂.

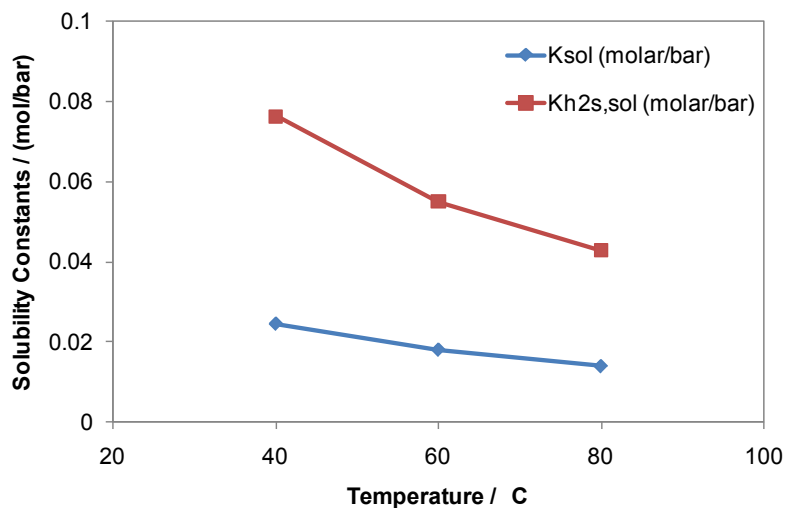


Figure 6. Relationship between the solubility constants for CO₂ (K_{sol}) and H₂S (K_{h2s,sol}) at operating conditions from 40°C to 80°C.

Once carbon dioxide dissolves in water, a hydration reaction occurs to produce carbonic acid. The hydration of carbon dioxide is considered the slow step in the dissolution process and is defined by a fixed dissociation constant, Equation (7)³¹ with molar units, which gives an approximate ratio of 388 mol CO_{2(aq)} for each mol of H₂CO₃ in solution.

Hydration of aqueous carbon dioxide to produce carbonic acid:



$$K_{hy} = 2.58 \times 10^{-3} \quad (7)$$

Carbonic acid, H_2CO_3 , then undergoes two dissociations to maintain the concentrations of bicarbonate ions and carbonate ions as related to the equilibrium conditions of the system. The equilibrium constants are dissociation constants with molar units for each in the following equations:

Dissociation of carbonic acid:



$$K_{ca} = 387.6 \times 10^{-6.41 - 1.594 \times 10^{-3}(T_F) + 8.52 \times 10^{-6}(T_F^2) - 3.07 \times 10^{-5}(p) - 0.4772(\sqrt{I}) + 0.1180(I)} \quad (9)$$

with temperature (T_F) in Fahrenheit, partial pressure of CO_2 (p) is in psia, and ionic strength (I) in mol/L.

Dissociation of bicarbonate ion:



$$K_{bi} = 10^{-(10.61 - 4.97 \times 10^{-3}(T_F) + 1.331 \times 10^{-5}(T_F^2) - 2.624 \times 10^{-5}(p) - 1.166(\sqrt{I}) + 0.3466(I))} \quad (11)$$

with temperature (T_F) in Fahrenheit, partial pressure of CO_2 (p) is in psia, and ionic strength (I) in mol/L.

When hydrogen sulfide dissolves in water, two dissociations also occur for the concentrations of bisulfide ions and sulfide ions as related to the equilibrium conditions of the system. The equilibrium constants are considered to be dissociation constants with molar units.

Dissociation of aqueous hydrogen sulfide:



$$K_{H_2S} = 10^{(782.43945 + 0.361261(T_K) - 1.6722 \times 10^{-4}(T_K^2) - \frac{20565.7315}{T_K} - 142.741722 \ln T_K)} \quad (13)$$

with temperature (T_K) in Kelvin.

Dissociation of the bisulfide ion:



$$K_{HS^-} = 10^{-(23.93 - 0.030446(T_K) + 2.4831 \times 10^{-5}(T_K^2))} \quad (15)$$

with temperature (T_K) in Kelvin.

Electrochemical Reactions

The corrosion of carbon steel in an aqueous solution can be defined by a set of reactions that use the transfer of electrons through the conductive media and the transfer of ions through solution. There is only one anodic reaction, which is the dissolution or loss of ferrous ions to the solution, but there can be several cathodic reactions which supply the current (transfer of electrons) to aid in the corrosion process.

The anodic dissolution of iron:



Accompanied by the possible cathodic reactions in a system with $CO_{2(aq)}$ and $H_2S_{(aq)}$:

Reduction of hydrogen ions:



Direct reduction of carbonic acid:



Direct reduction of hydrogen sulfide:



The reduction of hydrogen ions is considered the most important cathodic reaction in an acid solution ($\text{pH} < 4$)^{29, 30} and the rate limiting step in the reduction of hydrogen ions is the diffusion rate of H^+ ions from the bulk of the solution to the metal surface.^{30, Error! Bookmark not defined.} The two dissociation steps shown in Equation (8) and Equation (10) indicate that carbonic acid acts as a source of hydrogen ions or a buffering agent for the cathodic reduction reaction in Equation (17). Although the direct reduction of carbonic acid is suggested to be important in CO_2 influenced environments at intermediate pH values ($4 < \text{pH} < 6$)³⁰, the presence of carbonic acid may only act as a reservoir for hydrogen ions³². But the direct reduction of hydrogen sulfide on mild steel in an aqueous environment has been proven to occur⁶ and is an important reaction when considering the effect of the presence of H_2S on mild steel corrosion. The two dissociation steps for aqueous hydrogen sulfide are shown in Equation (12) and Equation (14) and indicate that $[H_2S]_{(aq)}$ can also act as a buffering agent for hydrogen ions. It should also be noted that the equilibrium concentrations of species in Equations (8) through (14) are dependent upon the pH of the system.

Some authors³³ have tried to use the carbon dioxide to hydrogen sulfide partial pressure ratio as an indicator for when corrosion would be dominated by either CO_2 or H_2S , but some quick calculations based on the solubility and hydration in the previous

equations above can show this to be a misnomer. Both carbonic acid, $[\text{H}_2\text{CO}_3]$, and aqueous hydrogen sulfide, $[\text{H}_2\text{S}]_{(\text{aq})}$, are weak acids in solution with their first and second dissociations dependent upon the solution pH as observed in Equations (8) through (14). Over the temperature range of 40°C to 80°C , the dissociation constant for H_2CO_3 is 500 to 1000 times greater than for $\text{H}_2\text{S}_{(\text{aq})}$ (Figure 7). According to this example, for every mol/liter of $[\text{HCO}_3^-]$ there are 10 thousand mol/liter of $[\text{H}_2\text{CO}_3]$ while for every mol/liter of $[\text{HS}^-]$ there are 10 million $[\text{H}_2\text{S}]_{(\text{aq})}$.

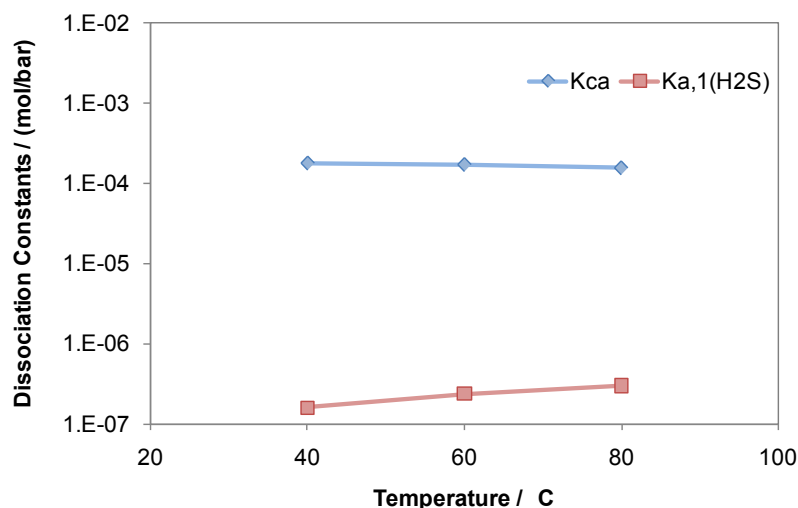


Figure 7. Relationship between the dissociation constants for H_2CO_3 (K_{ca}) and $\text{H}_2\text{S}_{(\text{aq})}$ ($K_{\text{a},1(\text{H}_2\text{S})}$) for the temperature range of 40°C to 80°C .

Assuming that carbonic acid, $[\text{H}_2\text{CO}_3]$, and aqueous hydrogen sulfide, $[\text{H}_2\text{S}]_{(\text{aq})}$, equally supply protons for the corrosion reaction, a direct comparison of their concentrations in solution can be done at a specific temperature. In a system with 8 bar

$p\text{CO}_2$ at 60°C , $[\text{H}_2\text{S}]_{(\text{aq})}$ is equivalent to $[\text{H}_2\text{CO}_3]$ when $p\text{H}_2\text{S}$ is only 7 millibar so that the ratio of $p\text{CO}_2/p\text{H}_2\text{S}$ is 1163. Even without considering the reaction kinetics of either species, this would seem to explain why H_2S is more dominant at seemingly high $p\text{CO}_2/p\text{H}_2\text{S}$ ratios.

Taking the bicarbonate ions, Equation (10), and bisulfide ions, Equation (14), into consideration as another source of hydrogen ions for the corrosion reaction, the solution pH also becomes a factor in the comparison. In a system with 8 bar $p\text{CO}_2$ and temperature of 60°C , the $p\text{CO}_2/p\text{H}_2\text{S}$ ratio is dramatically different based on a change in solution pH in order to make the concentration of carbonate species that can act as a source of hydrogen ions equal to the concentration of sulfide species that can act as a source of hydrogen ions (Table 4).

Table 4. Variation in $p\text{CO}_2/p\text{H}_2\text{S}$ ratio to maintain an equal source of hydrogen ions from sulfide species and carbonate species at pH 4.5, 5, & 6 with 8 bar $p\text{CO}_2$ at 60°C .

$p\text{CO}_2 = 8 \text{ bar}$ $T = 60^\circ\text{C}$	$\frac{[\text{H}_2\text{S}] + [\text{HS}^-]}{[\text{H}_2\text{CO}_3] + [\text{HCO}_3^-]}$	$\frac{[\text{H}_2\text{S}]}{[\text{H}_2\text{CO}_3]}$	$p\text{H}_2\text{S} /$ (bar)	$p\text{CO}_2/p\text{H}_2\text{S}$
pH 6	1	233.1	1.5	5.3
pH 5	1	26.4	0.17	46.0
pH 4.5	1	9.1	0.060	132.9
pH 4	1	3.5	0.023	347.8

This comparison shows that the $p\text{CO}_2/p\text{H}_2\text{S}$ ratio is not a good indicator to determine if CO_2 or H_2S is the dominant reactant of the system because the concentrations of species in solution that directly affect the corrosion reaction are dependent on the environmental conditions. Corrosion prediction models must rely on a good water chemistry model in order to correctly determine the correct mechanisms for the corrosion reaction.

Dissolution and Precipitation Reactions

The solubility of a species is written as a dissolution reaction. The two main species of interest in this research are iron carbonate and iron sulfide (mackinawite) as shown in Equations (20) and (21).

Iron carbonate dissolution:



Iron sulfide dissolution:



Because of the complexity in determining the parameters associated with iron sulfide dissolution, there are three expressions that have been used³⁴ in past research.

Only the most widely used method, the $[H^+, HS^-]$ based expression of Equation (21), will be used in this study.

The saturation value for iron carbonate, $S(FeCO_3)$, is calculated in Equation (22):

$$S(FeCO_3) = \frac{[Fe^{2+}][CO_3^{2-}]}{K_{sp}(FeCO_3)} \quad (22)$$

The solubility product for iron carbonate, Equation (23), is a function of temperature and the ionic strength of the solution:

$$K_{sp}(FeCO_3) = 10^{(-59.3498 - 0.041377(T_K) - 2.1963/(T_K) + 24.5724 * \text{Log}(T_K) + 2.5188(\sqrt{I}) - 0.657(I))} \quad (23)$$

with temperature (T_K) in Kelvin and ionic strength (I) in mol/L. ³⁴

The saturation value for mackinawite, $S(FeS)$, is calculated based on the H^+ and HS^- ions from Equation (21):

$$S(FeS) = \frac{[Fe^{2+}][HS^-]}{[H^+]K_{sp}(FeS)} \quad (24)$$

The solubility product for iron sulfide (mackinawite) is from Benning *et al.* ³⁵,

$$K_{sp}(FeS) = 10^{(2848.779/T_K - 6.347 + \log(K_{H_2S}))} \quad (25)$$

with temperature (T_K) in Kelvin and K_{H_2S} from Equation (13).

A comparison can now be made between the saturation values for iron sulfide (mackinawite) and iron carbonate (siderite) under the same environmental conditions.

Thermodynamic Equilibrium Calculations

Two software programs were used to review the aqueous thermodynamics in order to discuss the basis for the corrosion product expected in the experimental procedures. The E-pH diagrams (Pourbaix diagrams) shown in the following discussion were created from Geochemist's Workbench³⁶ or from a model developed in-house, which allows the user to investigate transition species such as mackinawite and greigite. The in-house model is based upon research completed at the ICMT for iron sulfide formation³⁷ and iron carbonate formation³⁸, both confirmed by comparisons with OLI Analyzer Studio³⁹ and written into a visual basic program using Microsoft Visual Studio 2010 based on a method by Fishtik⁴⁰. These programs will be referred to, respectfully, as GWB (Geochemist's Workbench program) and VB (visual basic program) in the following text. When using GWB, the assumption was also made to exclude hematite, goethite, magnetite, and troilite, as these species require the presence of oxygen to form under these conditions; these species are not considered in the VB version calculations.

Using the environmental conditions as tested near saturation for iron carbonate and iron sulfide (60°C, 7.7 bar pCO₂, pH 6, 1ppm Fe⁺⁺), Pourbaix diagrams developed

using GWB show that siderite (FeCO_3) is the favored corrosion product up to 5 mbar pH_2S , but FeS (pyrrhotite) is the favored corrosion product at 5 mbar pH_2S and above. The Pourbaix diagrams in Figure 8 show that a small change from 1 mbar pH_2S to 5 mbar pH_2S under the tested conditions is enough to change the more thermodynamically stable species from FeCO_3 (siderite) to FeS (pyrrhotite), respectively.

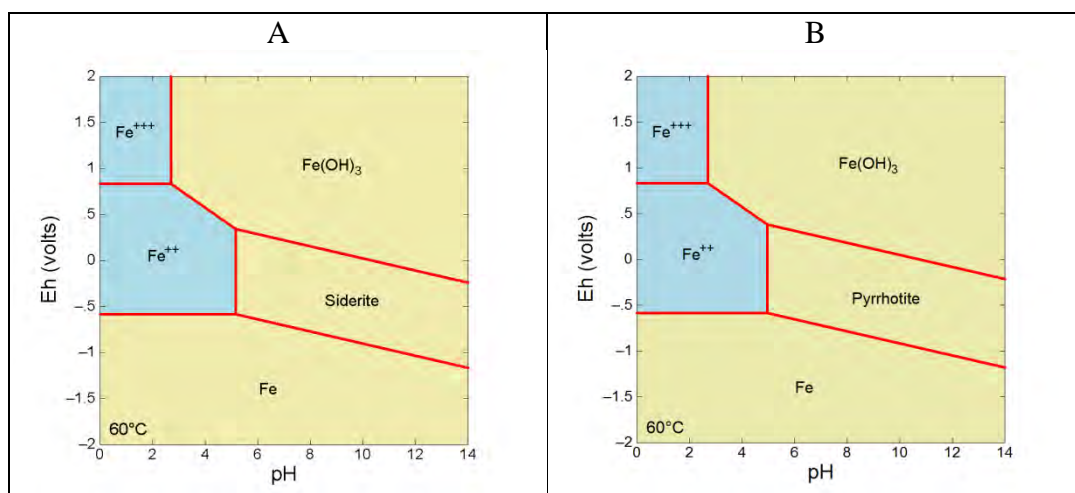


Figure 8. Pourbaix diagrams representing corrosion products formed at near saturation conditions for both iron carbonate and iron sulfide at (A) 1 mbar and (B) 5 mbar pH_2S , respectively (60°C, 7.7bar pCO_2 , pH 6, 1 ppm $[\text{Fe}^{2+}]$). (Eh-pH diagrams from GWB ³⁶)

This subtle change may be better understood in a Pourbaix diagram (Figure 9) which shows where FeCO_3 (siderite) is thermodynamically stable under the specified conditions, but the increase in pH_2S from 1 mbar to 5 mbar makes the reaction to iron sulfide preferred. It is understood that both reactions still occur and both corrosion products may be present due to reaction kinetics, but this is not visually accounted for in a Pourbaix diagram which depicts thermodynamic equilibrium.

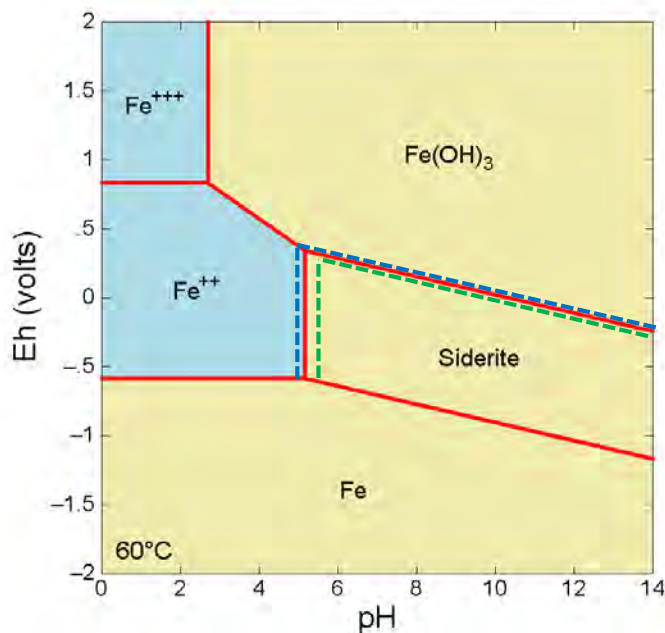
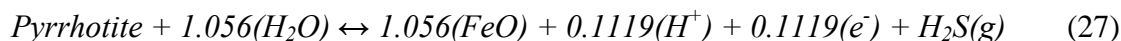


Figure 9. Pourbaix diagram representing corrosion products formed at near saturation conditions for both iron carbonate and iron sulfide (60°C, 7.7bar pCO₂, pH 6, 1 ppm Fe⁺⁺, 0.001 bar pH₂S and 0.005 bar pH₂S). (Eh-pH diagram from GWB³⁶)

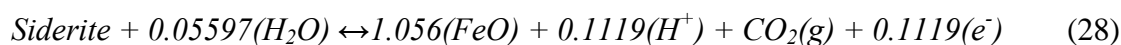
For reference, the equations used in GWB to determine whether the product or the reactant of Equation (26) is preferred are related by reaction with wüstite (FeO) while the program methodology used in VB relates each reaction to elemental iron (Fe). GWB states that the equilibrium in question is defined according to Equation (26):



For Pyrrhotite (FeS):



For Siderite (FeCO₃):



Using the general expression for the Gibbs free energy change of a chemical reaction,

$$\Delta G = \Delta G^0 + RT \sum_{i=1}^k \ln (c_i)^{n_i} \quad (29)$$

The equations used in VB determine the most stable species (lowest or most negative ΔG) at each pixel point in the diagram by use of matrix functions that require elemental iron (Fe) as the common species in the reaction equation for each species.⁴⁰

The reason for developing a separate E-pH program (VB) was to enable the inclusion of transitional species not usually provided in commercial E-pH programs and to have a usable model with no hidden features or unknown calculations. Mackinawite is considered to be a transitional species for pyrrhotite and should be included as a possible species in the E-pH diagram when conducting theoretical analysis. The VB version of the E-pH diagram was created to explore the conditions related to the transition from siderite

(FeCO₃) to pyrrhotite as the favored corrosion product including mackinawite in the calculations. When the option for pyrrhotite formation is chosen in the VB version, pyrrhotite becomes the more thermodynamically preferred species when the partial pressure of H₂S is 1 mbar (0.001 bar) or greater (Figure 10). The change from FeCO₃ to Pyrrhotite in the VB version actually occurs between 0.9 mbar and 1.0 mbar.

Investigation of when mackinawite becomes more thermodynamically stable than FeCO₃ requires the suppression of the pyrrhotite reaction in the VB program, but does not occur until the partial pressure of H₂S exceeds 23 mbar as seen in Figure 11. This is an indication that the $\Delta G_{\text{FeS(pyrrhotite)}}$ is approximately 25 times less than the $\Delta G_{\text{FeS(mackinawite)}}$ as compared to the ΔG_{FeCO_3} calculated for iron carbonate under the same environmental conditions.

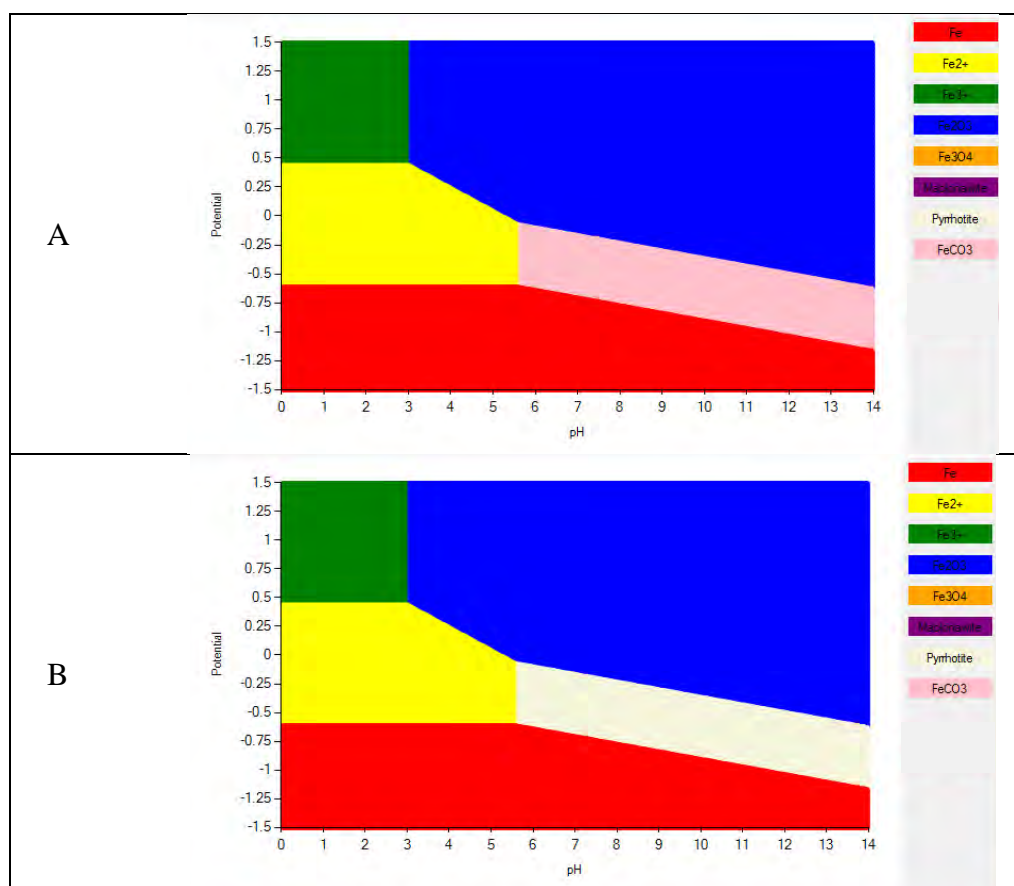


Figure 10. Pourbaix diagrams calculated from potential/pH program (VB version) showing that an increase in pH_2S from 0.1 mbar (A) to 1.0 mbar (B) will change the favored corrosion product from FeCO_3 (pink color) to pyrrhotite (white color). (60°C , 8 bar pCO_2 , 1 ppm Fe^{++})

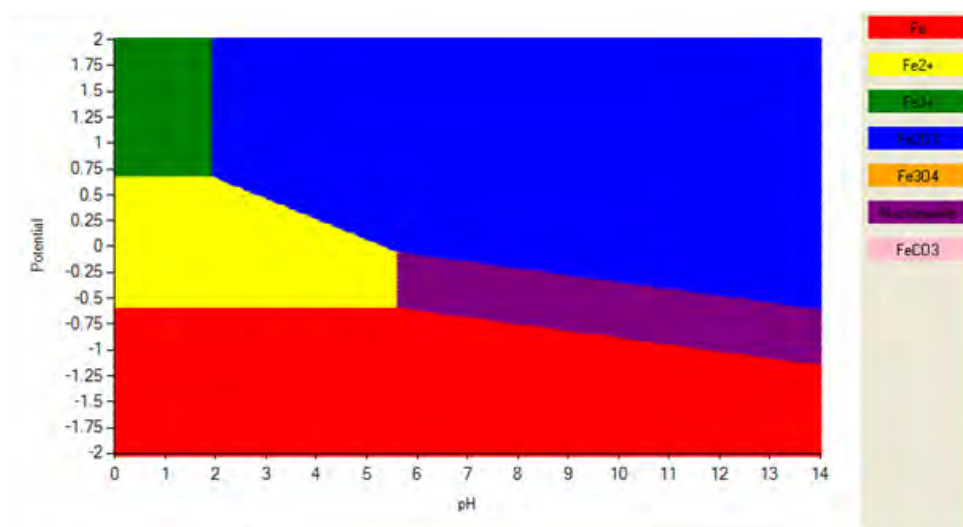


Figure 11. Pourbaix diagram calculated from potential/pH program (VB version) showing that an increase up to 24 mbar $p_{\text{H}_2\text{S}}$ is needed to make mackinawite (purple color) the favored corrosion product over FeCO_3 . (60°C , 8 bar p_{CO_2} , 1 ppm Fe^{++})

Corrosion Measurement and Analysis Procedures

Beginning Each Experiment

Well-Controlled Environmental Conditions

Environmental conditions for each test are defined prior to filling and de-oxygenation of the H_2S system. All additions to control or define the environmental conditions are completed before the material to be tested is inserted and exposed for testing. Flow rates and temperatures were always consistent within each experiment, but some additions of hydrogen sulfide were necessary during the longer term tests to maintain the desired ppm concentration; these usually occurred at H_2S partial pressures below 0.05 bar. With such a large system for testing, it is considered to be equivalent to an “open” system in which the conditions remain stable due to the excess amounts of the species involved in the corrosion reaction in relation to the surface area of the material

being corroded. These reactions are shown as Equation (2) through Equation (24) in the section titled Calculation of Environmental Conditions.

Definition of X65 Pipeline Material

Experimentation was conducted on API 5L X65 mild steel which is a commonly used type of pipeline steel in upstream oil and gas transportation.⁴¹ All samples were machined from a single pipeline with an outer diameter of 13 inches and a wall thickness of 1.5 inches. Pipeline materials designated as X65 can vary a few weight percent in composition and may have different heat treatments as the X65 designation only refers to minimum yield strength.⁴² The strength of a material is characterized as the force per unit area required to deform the material to 0.002 plastic strain (0.2% yield strength), or to deform the material to complete failure (ultimate tensile strength). The minimum yield strength for API 5L X65 is 65 ksi and the ultimate tensile strength is 77 ksi.⁴³

The X65 steel used in this research is a quenched and tempered alloy and its chemical composition was analyzed by Laboratory Testing, Inc., Hatfield, PA.⁴⁴ The results of elemental analysis obtained by direct reading atom emissions spectroscopy⁴⁴ are shown in Table 5. The restrictions applied in the API 5L X65 standard⁴³ only include carbon, manganese, phosphorus, sulfur, and titanium content which are also listed in Table 5.

Table 5. Material Analysis of X65 pipeline material used vs. requirements of standard.

Element	Wt% in X65	Wt% standard API 5L X65	Element	Wt% in X65	Wt% standard API 5L X65
Al	0.032		Ni	0.36	
As	0.008		P	0.009	< 0.03
B	0.001		Pb	<0.001	
C	0.13	< 0.28	S	0.009	< 0.03
Ca	0.002		Sb	0.009	
Co	0.007		Si	0.26	
Cr	0.14		Sn	0.007	
Cu			Ta	<0.001	
Mn	1.16	<1.40	Ti	<0.001	< 0.06
Mo	0.16		V	0.047	
Nb	0.017		Zr	<0.001	

Because of the low carbon content, martensite is generally not expected in the quenched and tempered alloy. A metallurgical evaluation on this X65 material conducted at the ICMT in 2003 found “a finer microstructure, where grain boundaries are not well defined. Even at a magnification of 1000X, the identification of the dark areas of pearlite could not be confirmed. Iron carbide could be distributed in spheroidized form instead of a lamellar arrangement.”⁴⁵ Studies of this alloy have shown that martensite can form in fine grained X65 steel⁴⁶ or under certain quenching conditions.⁴⁷ A micrograph of the sample surface is shown in Figure 12.

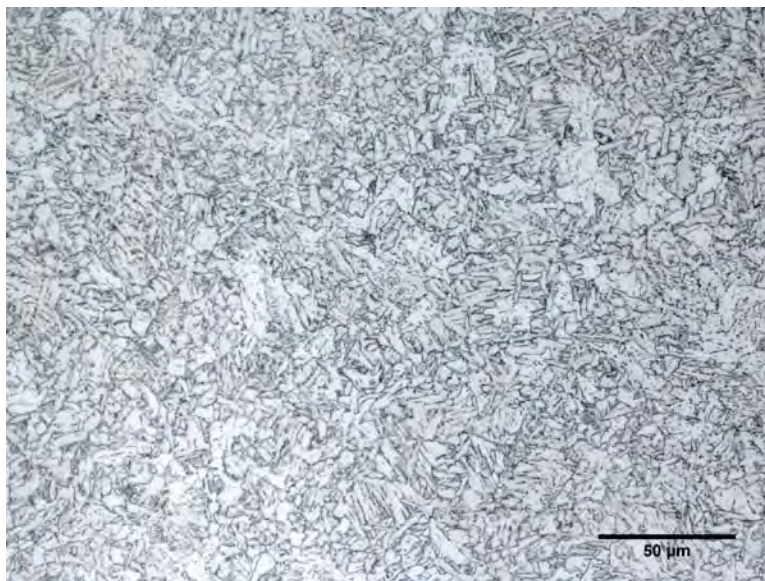


Figure 12. Micrograph image of API 5L X65 pipeline material used in this study. (Provided by Chevron Corporation.)⁴⁸

Sample Installation Procedures

For corrosion measurements, the H₂S system holds 7 weight loss probes in one test section for single phase and two test sections for bottom of the line multiphase testing. The X65 weight loss samples are 1.25" (31.75 mm) in diameter and 0.25" (6.35 mm) thick with a mounting hole in the middle of each. Weight loss samples are prepared so that only the top surface area that will be exposed to the test conditions will corrode by sealing all other surfaces with a Teflon coating[§]. The weight loss sample is secured on the end of a 36" (0.9 m) stainless steel probe with high pressure fittings by a nylon screw to minimize the possibility of galvanic corrosion.

[§] Xylan 1014 (blue) from Whitford Corporation (www.whitfordww.com).

The weight loss probes are installed and removed with the environmental conditions of each test maintained, meaning that the H₂S system is at the proper temperature, pCO₂, and pH₂S while the weight loss probes are in place. Two locations in the flow loop are used to install weight loss samples which will simulate a single phase flow (water) and a multiphase flow (two phase, water/gas) similar to what could be observed in a production pipeline. The samples are flush mounted with the internal pipe diameter to confer an environment akin to a continuous pipe surface. Safety procedures are adhered to when working with a “hot” system such as this. After sample insertion, the probe body is marked for orientation to flow. This marking is transferred to the weight loss sample after the probe is removed from the system.

Ending Each Experiment

Sample Handling Procedure

Samples removed from the research test equipment for analysis are carefully wetted with isopropyl alcohol from a lab wash bottle to remove water from the sample without creating physical damage to the corrosion product. All samples are stored in a vacuum dessicator prior to and throughout the analysis process. After drying, the sample weight is recorded and a digital photograph recorded.

The samples are first analyzed with the corrosion product intact; analytical equipment is described in the next part of this section. After review of data from the completed analyses, two samples are chosen for cross-sectioning to determine the depth

of the corrosion product. The remaining samples are put through a Clarke solution cleaning method as outlined in ASTM G1⁴⁹ to remove the corrosion product with minimal loss of the metal substrate. Samples chosen for cross-sectioning were fixed in a small container and a low viscosity epoxy was poured in to seal the corrosion product in place. Only half of the 1.25” (31.75 mm) diameter samples for cross-sectioning were fixed in epoxy and a diamond saw was used to separate the two halves. The half without epoxy was subjected to Clarke solution cleaning for approximately the same time as the other weight loss samples tested. This half was analyzed with the profilometer to determine the maximum penetration rate if indications of localized corrosion were present. The other half of this sample, which is fully contained in epoxy, was polished in steps down to a mirror finish using a 3 micron diamond suspension as the final step. This cross-section sample was then gold sputter coated for analysis.

Sample Analysis with Corrosion Product

Because of the importance of the corrosion product to this research, most of the effort in the analysis is spent on defining the topography and chemical make-up of the weight loss samples in order to provide a correlation with the corrosion process that is occurring to the metal substrate. An infinite focus microscope (IFM) was used to locate and document topographical surface features on each sample. The IFM was used to document a uniform surface area, a loss of material, a gain of material, or a crack in the corrosion product. Scanning electron microscopy (SEM) with accompanying

backscattered electron composition (BEC) and energy dispersive X-ray analysis (EDX) were used on each sample to document compositional uniformity, crystal morphology, and elemental compositions. Sample cross-sections provide documentation of corrosion product depth, composition, and possible indications of localized corrosion.

Sample Analysis without Corrosion Product

After analysis of the layer was complete, samples were cleaned using the Clarke solution cleaning method. The change in mass of each sample was reported as corrosion product layer weight. The half sample without epoxy from cross sectioning was subjected to Clarke solution for approximately the same time as the other weight loss samples tested. The profilometer was used again for documentation of topographical surface features of the metal substrate without the corrosion product for each of these samples. These measurements were used to calculate localized corrosion rate (penetration rate) and document the morphology of the localized corrosion, if present.

Analytical Equipment

SEM / BEC / EDX

A JEOL ** 6390 Scanning Electron Microscope (SEM) with Backscattered Electron Composition (BEC) capability and an Energy Dispersive X-Ray Analysis (EDX) attachment is used for initial surface analysis of the corrosion product layer

** Trade Name

developed on the weight loss samples. The combination SEM/BEC/EDX provides the ability to document surface features and crystalline morphologies observed at a high magnification along with chemical elements that are present. This allows the researcher to determine possible chemical compositions that are in the corrosion product layers and provide insight into their relationship to corrosion mechanisms.

Profilometer

An Alicona Infinite Focus Microscope^{††} (IFM) is used to characterize the topography of the corrosion product layer on each weight loss sample. The topography observed may include a local area of accelerated corrosion product growth, a circular hole or “pit” in the layer, a locally removed area of the layer, or loosely adherent corrosion product. The IFM is an optical microscope which characterizes the surface by recording only the pixels of digital images that are in focus for each X-Y plane through a series of steps in the Z direction to create a 3D image. This has advantages over similar techniques, such as a white light interferometer or a laser interferometer, since it can image dark and rough surfaces that would not provide the reflectance required of an interferometer. The IFM works well in tandem with the SEM since it can easily provide topographical distances (depth and height), and has no problem imaging loosely adherent and non-conductive layers which tend to “collect a charge” and become bright spots in SEM images. By analysis with the IFM, locations of high corrosion rate penetration can

^{††} Trade Name

be easily detected over the full surface of the coupon and analyzed. The IFM penetration rate is determined by measuring the deepest “hole” or penetration point of localized corrosion in relation to the average surface area of the sample after Clarke solution cleaning.

Definition of Localized Corrosion

General Corrosion Rate

The general corrosion rate is calculated by Equation (30):

$$General_Corrosion_Rate = \frac{mass_loss * conversion_factor}{density_of_iron * surface_area * time} \quad (30)$$

Where mass loss is measured in grams ± 0.001 g, the surface area of the samples is $7.4 \text{ cm}^2 \pm 0.26 \text{ cm}^2$, and the time is measured in days ± 0.01 . The density of iron is 7.85 g/cm^3 and a conversion factor of 3.65 produces a general corrosion rate value in mm/yr. The samples are weighed on a balance which has accuracy to 0.1 mg, but with a numerical uncertainty of ± 0.001 gram. The surface area calculation has a numerical uncertainty of $\pm 0.26 \text{ cm}^2$ from the measured values of diameter of the sample. And the time value is based on recorded date and time values during installation and removal procedures which should be documented ± 15 minutes from the true value which is 0.01 of a day.

Pitting Ratio

The definition for pitting ratio used in these experiments is shown in Equation (31) as the ratio of the deepest localized corrosion location found on the surface of the sample after layer removal to the general corrosion rate calculated by the weight loss method. But this equation is flawed by the fact that it doesn't take into account the surface area affected by localized corrosion.

$$\text{Pitting Ratio} = [\text{Penetration Rate (mm/yr)}] / [\text{General Corrosion Rate (mm/yr)}] \quad (31)$$

If the “localized corrosion” covers more than 50% of the sample surface and the pitting ratio $\cong 1$, then it can be assumed that the “localized” corrosion found is just the initiation points of the general corrosion rate on the metal surface. It is assumed that if the pitting ratio is between 3 and 5, is it possible that the amount of “localized” corrosion may still cover a significant percentage of the sample surface, but still could be just the initiation of general corrosion. But if the pitting ratio is greater than 5, the penetration rate exceeds the general corrosion rate by so much that it must be “localized” corrosion.

Localized Corrosion

The detailed description of localized corrosion used for this research is in the section entitled “Focus on Localized Corrosion.” The parameter used to define the observation of localized corrosion for this research is directly related to the pitting ratio

calculation of Equation (31) with the stipulation that pit depth must be greater than $10\ \mu\text{m}$ before it can be considered:

- If the pitting ratio is greater than 5 ($\text{PR} \geq 5$), then the sample is defined as having localized corrosion.
- If the pitting ratio is greater than 3, but less than 5 ($3 \leq \text{PR} < 5$), then the sample is defined as having an increased risk for localized attack.

CHAPTER 4: EXPERIMENTAL RESULTS

Introduction

To gain an understanding of the localized corrosion that would occur on mild steel in an H_2S/CO_2 environment, several sets of experiments were developed to provide documentation on how different components of the water chemistry in this environment would influence the corrosion product developed and what subsequent type of corrosion was observed. With such a broad goal in mind, several topics of interest were defined in an attempt to isolate the mechanisms related to corrosion. The research done for each experiment will be discussed with respect to the research topic which is not always sequential with respect to experiment number (chronological order). The seven topics chosen to review their effect “on localized corrosion in an H_2S/CO_2 environment” are:

1. Effect of Iron Carbonate and Iron Sulfide Saturation Values
2. Effect of a Higher Ionic Strength Solution at pH 6
3. Effect of a Decrease in Solution pH
4. Effect of a Lower Ionic Strength Solution and Lower pH_2S at pH 5
5. Effect of a Decrease in pCO_2
6. Effect of a Decrease in Temperature
7. Effect of the Presence of Acetic Acid

These topics, listed above, are arranged in order such that experimental observations from the previous topics may be used for discussion and comparison in the subsequent topic.

Effect of Iron Carbonate and Iron Sulfide Saturation Values

Introduction

The initial hypothesis for localized corrosion in an H₂S/CO₂ environment was the “gray zone”¹ theory related to the thermodynamic equilibrium of iron sulfide or iron carbonate precipitates in solution. The gray zone theory relates the bulk solution saturation value for species that will precipitate to the amount of precipitate that can be found on the metal surface. An over-saturated solution would develop excess precipitate which would fully cover the surface and dramatically lower the corrosion rate. An under-saturated solution would not provide any significant precipitation layer which could affect the general corrosion rate. But a solution which is slightly over-saturated with respect to iron sulfide or iron carbonate would develop a partially protective corrosion product layer on the metal surface, which would lead to the separation of anodic and cathodic reaction sites on the metal surface to initiate and develop localized corrosion.

The goal of this series of tests was to set environmental conditions so that the precipitation of iron carbonate and the precipitation of iron sulfide in the process mild steel corrosion could influence the likelihood of localized corrosion. The expectation is that, when the saturation value of a precipitating species is greater than one, but near thermodynamic equilibrium, the likelihood of localized corrosion increases dramatically. This series of tests were conducted by using the environmental parameters of [Fe⁺⁺] and/or pH₂S in the large scale H₂S system (documented in Chapter 3) to control or

maintain the iron carbonate and iron sulfide saturation values, as calculated using water chemistry Equations (22) through (25), in order to achieve conditions considered favorable to either iron carbonate precipitation or iron sulfide precipitation. The saturation values for iron sulfide and iron carbonate shown in Table 6 were calculated from Equation (22) and Equation (24), respectively, for each ferrous ion concentration measured during the experiments. The ratio of the saturation values, $S(\text{FeS})/S(\text{FeCO}_3)$, is also based on the same measurement.

Table 6. Experiments 1, 2, 3, & 4 – Change in Saturation Values

Parameter	Exp. 1	Exp. 2	Exp. 3	Exp. 4
Temperature	60°C			
Total Pressure	8 bar			
pCO ₂	7.7 bar			
Flow	V _{sl} = 1 m/s, V _{sg} = 3 m/s			
NaCl solution	1 wt%			
pH	6.0			
Measurements	WL, SEM			
Exposure Time	10, 20, 30 days	10, 20, 30 days	10, 15, 25 days	10, 16, 26 days
pH ₂ S (mBar)	0.15	0.1	1.2	10
S(FeCO ₃)	30.1 ± 11.5	15.2 ± 3.2	62.8 ± 10.5	13 ± 9
S(FeS)	7.4 ± 2.5	2.2 ± 1.2	90 ± 17	151 ± 111
S(FeS)/S(FeCO ₃)	0.26 ± 0.08	0.14 ± 0.06	1.4 ± 0.1	11.7 ± 0.5

Saturation values calculated from the recorded experimental data are shown in the following analysis as average and standard deviation using the “n-1” method:

$$\bar{x} \pm \sqrt{\frac{\sum(x-\bar{x})^2}{(n-1)}} \quad (32)$$

Where x represents each recorded value, \bar{x} is the average of the recorded values, and n is the number of recorded values.

Experimental Observations

Experiment 1: Iron Sulfide Saturation Value is 75% less than the Iron Carbonate Saturation Value.

Introduction

The average saturation value for iron sulfide was much lower than the average iron carbonate saturation value during this experiment; therefore, one would expect the surface layers to be dominated by an iron carbonate precipitation. This also makes the assumption that the reaction kinetics for the two precipitates are similar. The operating parameters for this experiment are shown in Table 7 including the averaged values for iron carbonate saturation, $S(\text{FeCO}_3)$, iron sulfide saturation, $S(\text{FeS})$, and the relationship between the two throughout the experiment, $S(\text{FeS})/S(\text{FeCO}_3)$. Measured values of pH_2S , pH , and $[\text{Fe}^{++}]$ are averaged over the duration of the experiment with standard deviation shown.

Table 7. Controlled Parameters for $S(\text{FeS}) \approx (25\%) [S(\text{FeCO}_3)]$.

Parameter	Description
Equipment	H ₂ S Flow Loop
Test duration	30 days
Temperature	60.1 ± 1.0 °C
pCO ₂	7.7 ± 0.1 bar
pH ₂ S	0.00015 ± 0.00007 bar
pH	6.0 ± 0.1
Solution	1 wt% NaCl
Ionic strength	0.27 ± 0.01
[Fe ⁺⁺] (ppm)	6.9 ± 2.8
S(FeCO ₃)	30.1 ± 11.5
S(FeS)	7.4 ± 2.5
S(FeS)/S(FeCO ₃)	0.26 ± 0.08

[#](avg ± std deviation)

Results and Discussion

The iron sulfide saturation value was approximately one-fourth of the iron carbonate saturation value for the duration of the experiment as confirmed by the average of the S(FeS)/S(FeCO₃) ratio of 0.26 ± 0.08. While the partial pressure of H₂S only varied slightly between 0.1 mbar and 0.2 mbar, the iron concentration diminished during this experiment from 10 ppm ± 2 ppm in the beginning to 4 ppm ± 0.2 ppm by the end of 30 days (Figure 13). The bulk saturation values shown in Figure 14 were calculated by Equations (25) through (22) from H₂S and Fe²⁺ measured concentrations. The decrease in iron concentration can be assumed to be caused by having precipitation kinetics that are faster than the corrosion kinetics under these test conditions.

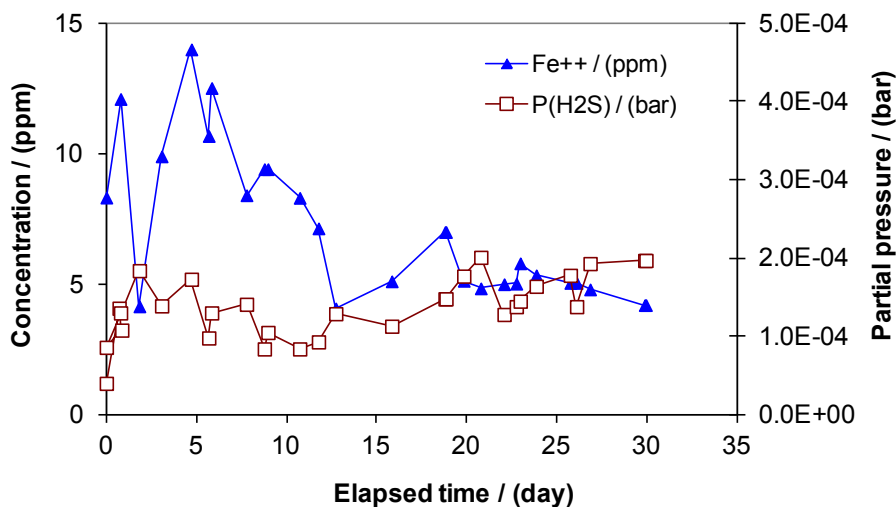


Figure 13. Variations of iron and hydrogen sulfide concentrations with time. (60°C, 0.77 MPa CO₂, pH 6, H₂S gas phase concentration = 20 ± 7 ppm)

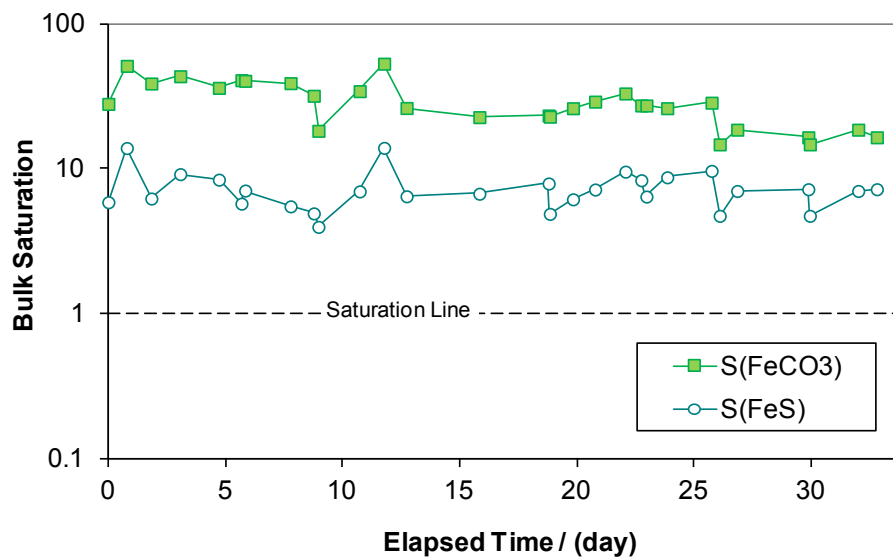


Figure 14. Calculated values of iron sulfide and iron carbonate saturation. (60°C, 0.77 MPa CO₂, pH 6, p_{H₂S} = 0.00015 bar ± 0.00005 bar)

Weight loss measurements did not agree well with the electrochemical measurements for this experiment which could be due to the corrosion product developed during the experiment. The measured values for polarization resistance of either probe in single phase or multiphase flow were at least a magnitude less than the weight loss corrosion rates as shown in Figure 15. There are a limited number of explanations which can answer this difference, assuming no mechanical or procedural errors:

1. A protective or thick corrosion product layer which negates the ability to use consistent Tafel slopes in the calculation of corrosion rate from LPR.
2. Conductive iron sulfide layers giving false electrochemical readings; or
3. Local loss of metal with a high ratio of localized corrosion to general corrosion;

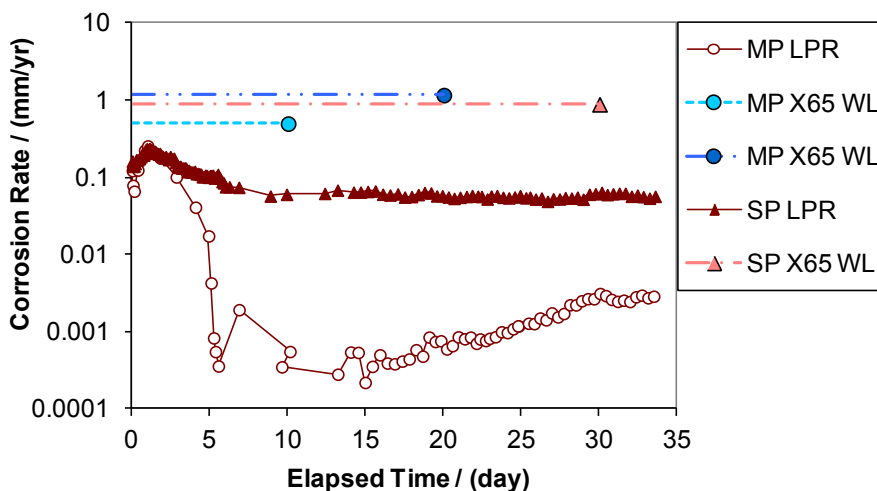


Figure 15. Corrosion rate measurements by LPR and X65 WL values. (60°C, 0.77 MPa CO₂, pH 6, V_{sg} = 3m/s, V_{sl} = 1m/s, pH₂S = 0.15 mbar ± 0.05 mbar)

From visual examination of the X-65 samples as removed from the experiment, it can be seen that all had significant coverage of iron sulfide on the surface. Figure 16 shows the samples after 10, 20, and 30 days exposure to the tested conditions; the full surface coverage by the corrosion product would support either of the first two assumptions. Indications that some of the corrosion product has been lost *in situ* also support the assumption that localized corrosion is highly probable. The mass of the corrosion product layers remaining intact after the experiment were measured at 0.3748 g and 0.1567 g, respectively, for the multiphase 10 day and 20 day samples and 0.0715 g for the single phase 30 day sample.

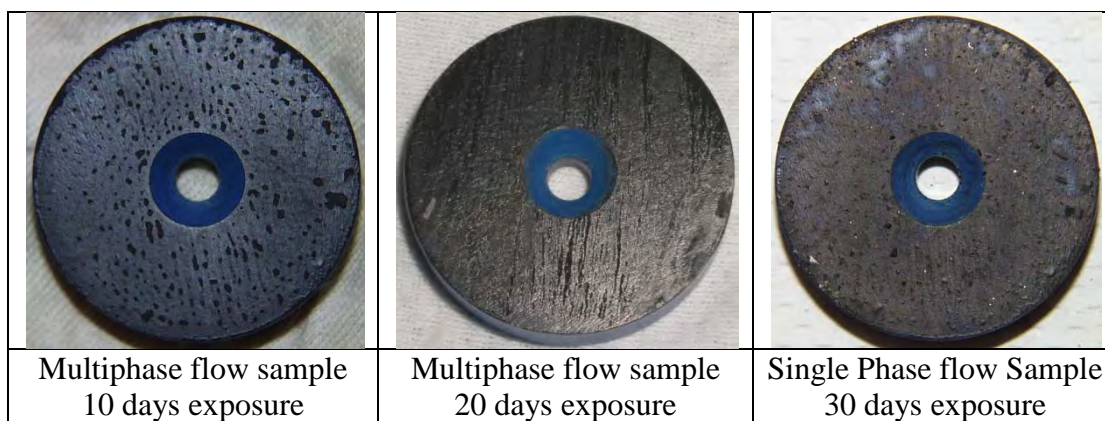


Figure 16. Visual examination of weight loss samples as removed from experiment. (60°C, 0.77 MPa CO₂, pH 6, V_{sg} = 3m/s, V_{sl} = 1m/s, pH₂S = 0.15 mbar ± 0.05 mbar)

Localized areas of corrosion were observed on every sample with the highest penetration rate occurring on the samples exposed for 30 days. The cross section of the WL sample from single phase flow after a 30 day exposure shows pit depths of 73 μm and 85 μm based upon the highest point of the remaining surface material. This WL

sample had undergone corrosion product layer removal prior to cross-sectioning procedures to determine a general corrosion rate of 0.89 mm/yr, so the 85 μm pit depth equates to a 3.3 mm/yr pit penetration rate or a ratio of pitting corrosion to general corrosion of 3.7. A top view metallurgical microscopic image of the localized loss of material for the X65 sample after a 20 day exposure in multiphase flow is shown in Figure 17. The loss of material on the 20 day sample is similar to the 30 day sample (Figure 18) as related to the diameter of the localized area, but a measured maximum pit depth of 27.5 μm for the 20 day sample is only one-third of the 85 μm pit depth measured for the 30 day sample.

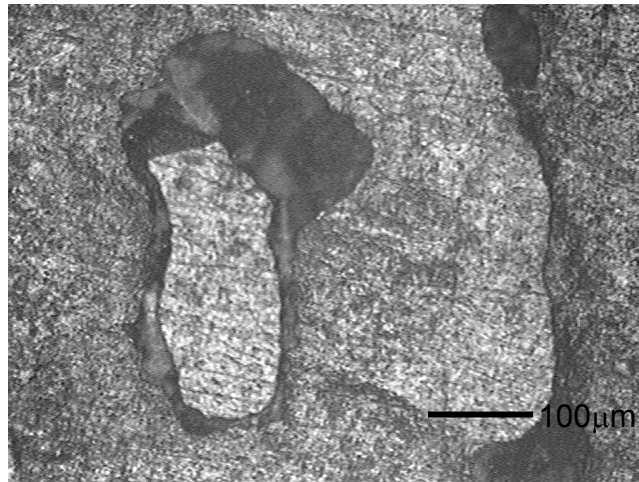


Figure 17. Top view, metallurgical microscope image, of multiphase weight loss sample after 20 day exposure to conditions; shown without corrosion product layer. (60°C, 0.77 MPa CO₂, pH 6, V_{sg} = 3m/s, V_{sl} = 1m/s, p_{H₂S} = 0.15 mbar ± 0.05 mbar)

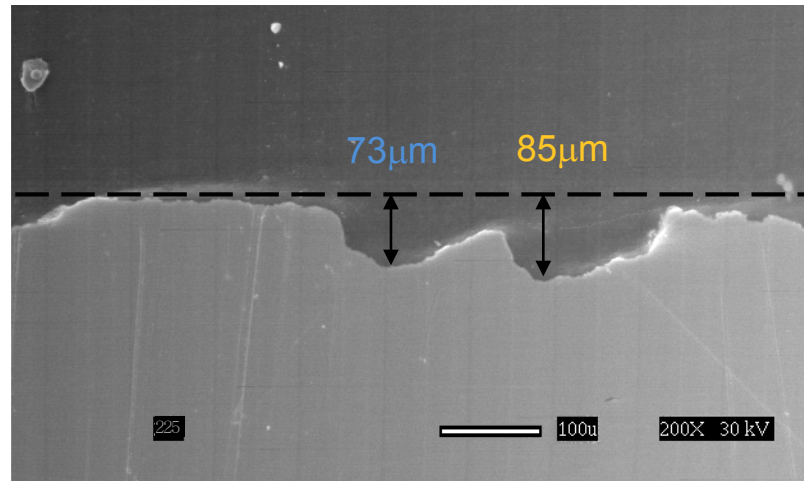


Figure 18. Single Phase, 30 Day Exposure, From SEM cross section: 73 μm and 85 μm pit depth, Localized Corrosion by max depth: 3.3 mm/yr, General Corrosion by wt loss: 0.89 mm/yr, Pitting Factor: 3.7

Corrosion rate values for the three WL samples in Figure 19 show both general corrosion weight loss and maximum pit depth for localized corrosion as pit penetration rate. The data indicates an increase in the localized corrosion rate based on time, independent of flow regime, which is substantiated by an additional cross sectioned sample taken after 30 days from the multiphase flow section of the same experiment. Figure 20 shows a 75 μm corrosion product layer developed in multiphase flow after 30 days with an additional 45 μm depth related to pitting under the corrosion product layer. Although direct WL corrosion rate is not available, since the overall pit depth is on the same order of magnitude as the single phase sample from a 30 day exposure, the ratio of localized corrosion to general corrosion rate would be expected to be similar.

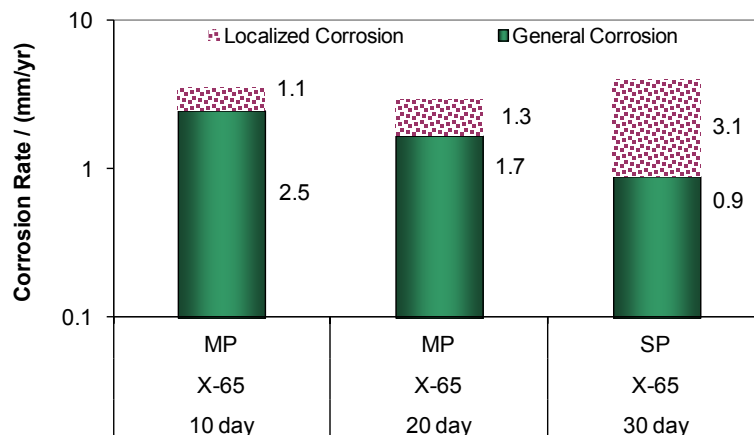


Figure 19. Sample weight loss comparison. (60°C , 0.77 MPa CO_2 , $\text{pH } 6$, $V_{\text{srg}} = 3\text{ m/s}$, $V_{\text{sl}} = 1\text{ m/s}$, $\text{pH}_2\text{S} = 0.15\text{ mbar} \pm 0.05\text{ mbar}$, 10, 20, & 30 days)

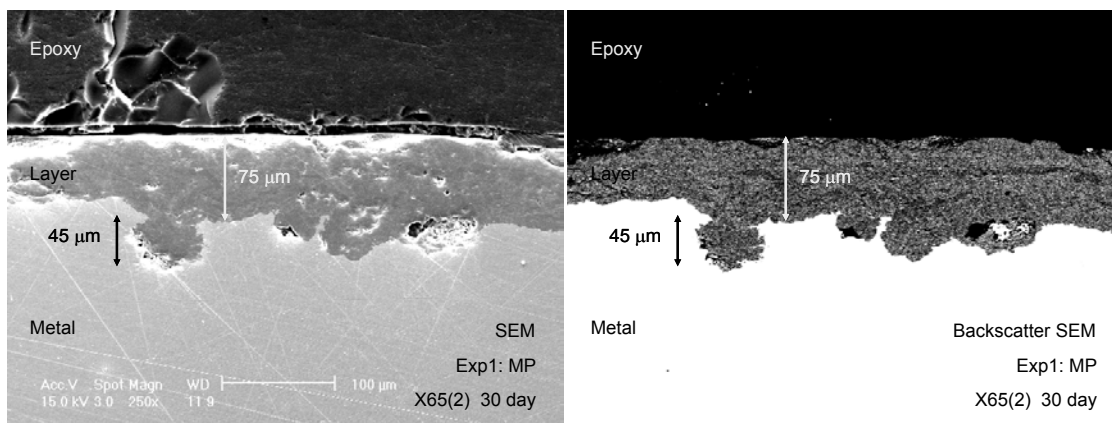


Figure 20. SEM and Backscatter cross-sectional analysis of X65 sample from 30 day exposure to multiphase flow conditions shows pit growth under the corrosion product layer. (60°C , 0.77 MPa CO_2 , $\text{pH } 6$, $V_{\text{srg}} = 3\text{ m/s}$, $V_{\text{sl}} = 1\text{ m/s}$, $\text{pH}_2\text{S} = 0.15\text{ mbar} \pm 0.05\text{ mbar}$) (227)

Some interesting features observed on the corrosion product layer of the multiphase sample exposed for 30 days were the existence of thin straight lines in various directions across the surface (Figure 21). These lines resemble the original polish marks on the bare steel surface prior to exposing them to the system conditions. This type of

corrosion product layer will be used in further discussions throughout this document for understanding the mechanisms related to the growth of the corrosion product layer in the presence of $\text{H}_2\text{S}_{(\text{aq})}$.

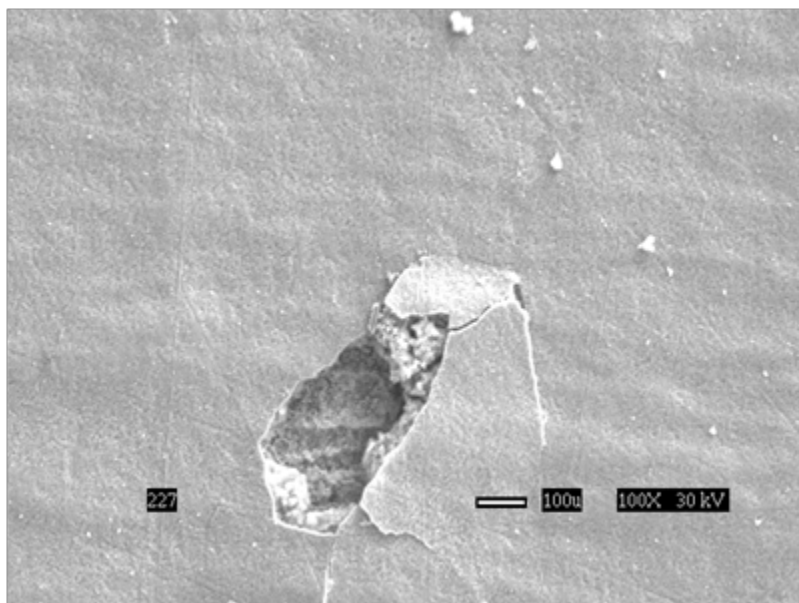


Figure 21. SEM image of corrosion product layer after 30 days in multiphase flow. Note the polish marks still visible across the surface. (60°C , 0.77 MPa CO_2 , $\text{pH } 6$, $V_{\text{sg}} = 3\text{m/s}$, $V_{\text{sl}} = 1\text{m/s}$, $\text{pH}_2\text{S} = 0.15\text{ mbar} \pm 0.05\text{ mbar}$)

Experiment 2: Iron Sulfide Saturation Value is 85% Less Than the Iron Carbonate Saturation Value.

Introduction

The average saturation value for iron sulfide was less than half of the average iron carbonate saturation value during this experiment; therefore, one would expect the surface layers to be slightly more influenced by iron carbonate precipitation than by iron sulfide precipitation. The operating parameters for this experiment are shown in Table 8

including the averaged values for iron carbonate saturation, $S(\text{FeCO}_3)$, iron sulfide saturation, $S(\text{FeS})$, and the relationship between the two throughout the experiment, $S(\text{FeS})/S(\text{FeCO}_3)$.

Table 8. Controlled Parameters for $S(\text{FeS}) \approx (15\%) [S(\text{FeCO}_3)]$.

Parameter	Description
Equipment	H ₂ S Flow Loop
Test duration	30 days
Temperature	60.2 ± 0.6 °C
pCO ₂	7.7 ± 0.1 bar
pH ₂ S	0.0001 ± 0.00005 bar
pH	6.0 ± 0.1
Solution	1 wt% NaCl
Ionic strength	0.254 ± 0.004
[Fe ⁺⁺] (ppm)	4.3 ± 0.6
S(FeCO ₃)	15.2 ± 3.2
S(FeS)	2.2 ± 1.2
S(FeS)/S(FeCO ₃)	0.14 ± 0.06

[#](avg ± std deviation)

Results and Discussion

The temperature, partial pressure of CO₂, and pH were stable for the entire experiment, but the partial pressure of H₂S did vary up to 50% due to the effects of corrosion and precipitation mechanisms on the small concentration. During this experiment, the iron concentration increased slightly from 3.5 ppm ± 0.2 ppm at start-up to 5.5 ppm ± 0.2 ppm by the end of 30 days and the partial pressure of H₂S was maintained by several small injections during the 30 day test (Figure 22). Calculations made with measured environmental conditions show the trends of the iron carbonate and iron sulfide supersaturation values during the experiment (Figure 23).

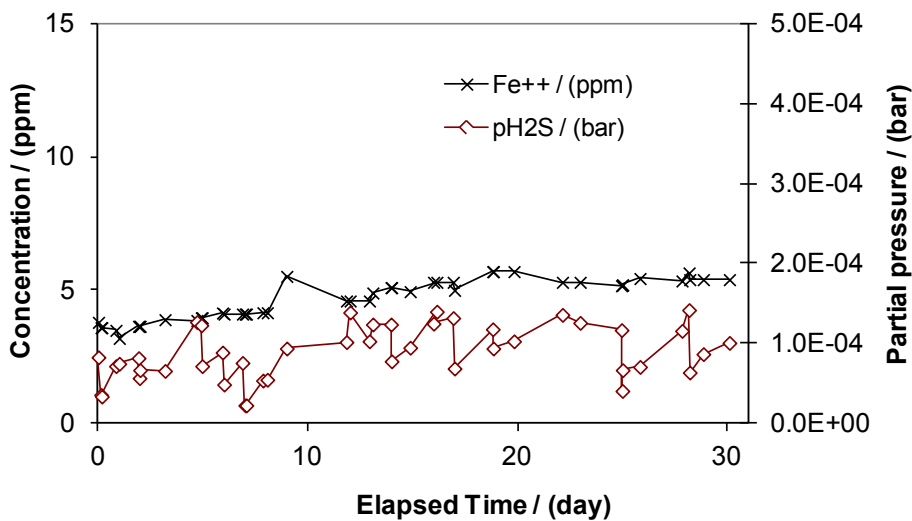


Figure 22. Variations of iron and hydrogen sulfide concentrations with time. (60°C , 7.7bar pCO_2 , $\text{pH } 6$, $0.00012\text{ bar} \pm 0.00004\text{ bar pH}_2\text{S}$)

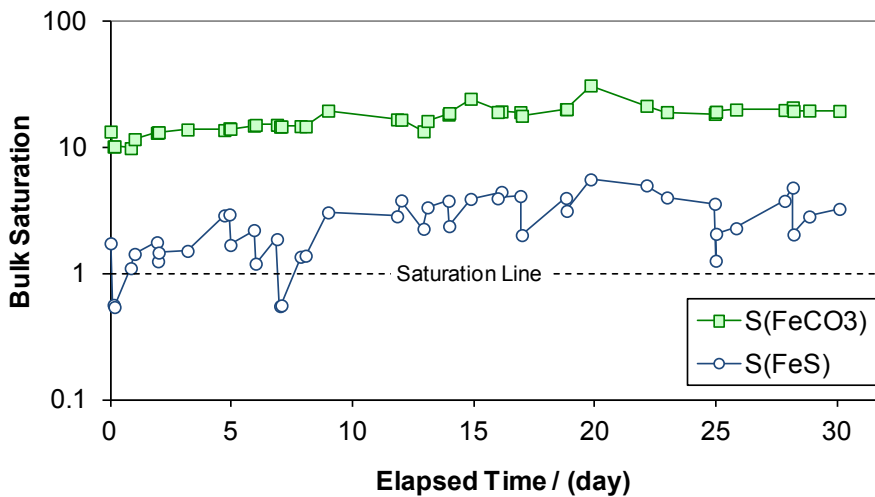


Figure 23. Calculated values of iron sulfide and iron carbonate saturation. (60°C , 7.7 bar pCO_2 , $\text{pH } 6$, $0.00012\text{ bar pH}_2\text{S}$).

The trend of the measured electrochemical corrosion rate (LPR) is similar to the measured weight loss measurements for both single phase and multiphase flow as shown in Figure 24. After removal from the system, visual inspection of the weight loss samples before surface analysis showed minimal corrosion product layer even after 30 days and no observable localized corrosion (Figure 25).

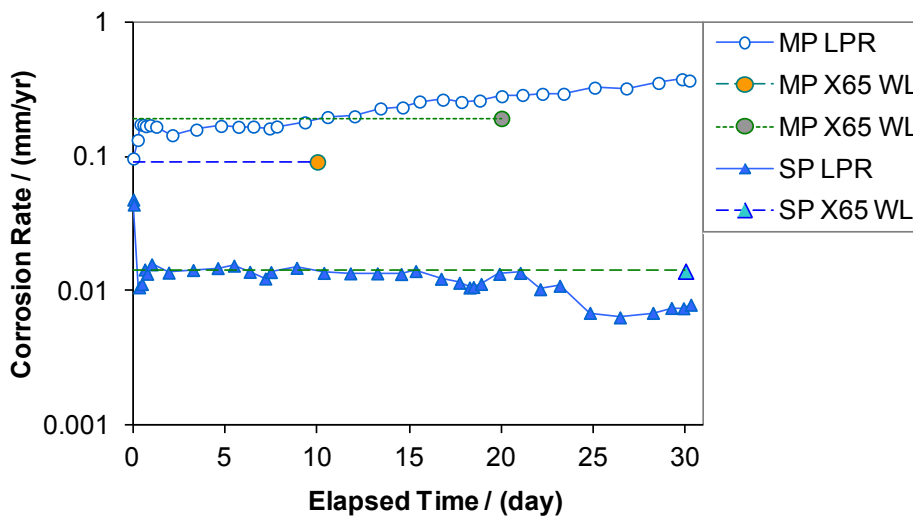


Figure 24. Corrosion rates in multiphase flow (MP) and single phase flow (SP) as measured by polarization resistance (LPR) and weight loss (WL). (60°C, 0.77 MPa CO₂, pH 6, p_{H₂S} = 0.00012 bar ± 0.00004 bar)

Observations of weight loss samples from three time exposures (10, 20, & 30 days) show that the corrosion product layer was thin with a more uniform coverage developed after the full 30 day exposure (Figure 25). The multiphase flow sample and single phase flow sample seem to have similar surface coverage of the corrosion product, although the measured corrosion rate for single phase was much less than for multiphase.

The mass of the corrosion product layers remaining intact after the experiment were measured at 0.0045 g and 0.0047 g, respectively, for the multiphase 10 day and 20 day samples and 0.0055 g for the single phase 30 day sample.

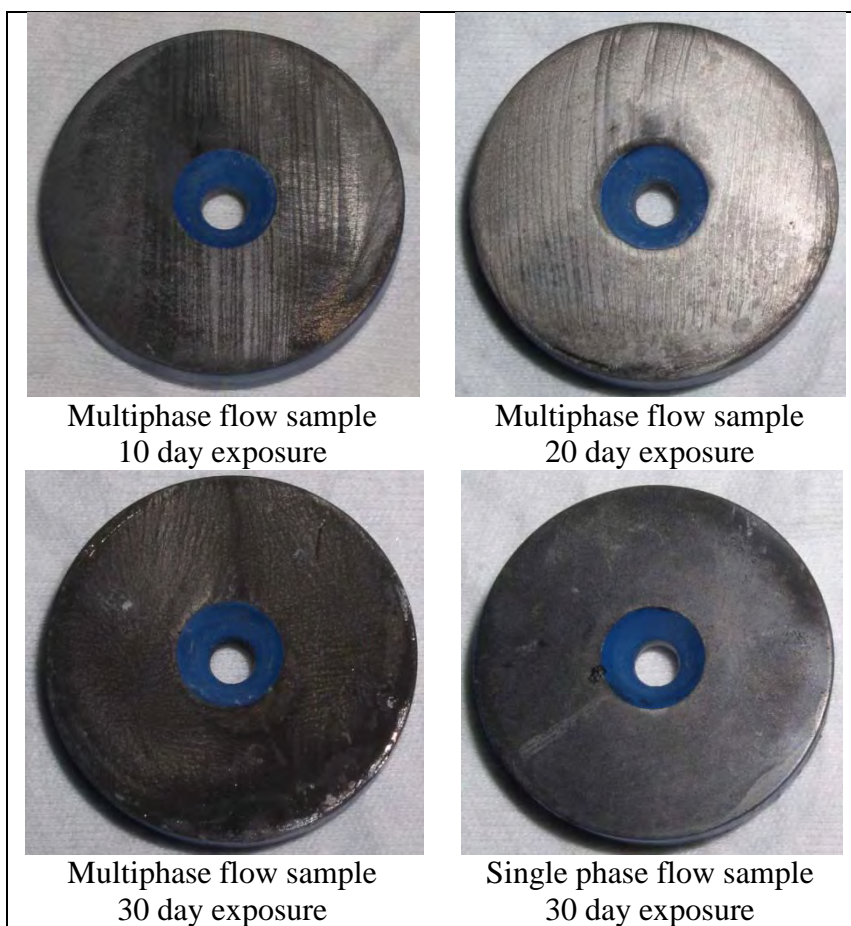


Figure 25. Visual examination of weight loss samples as removed from experiment. (60°C, 0.77 MPa CO₂, pH 6, p_{H₂S} = 0.00012 bar ± 0.00004 bar)

Scanning electron microscopy (SEM) of the surface of the corrosion product layer developed after 10 days shows indications of the original polishing marks on the metal surface, but does not show any features that could be interpreted as crystalline (Figure

26). Cross sectional analysis on the multiphase sample after 30 days shows a uniform corrosion product layer with a thickness of 28 to 30 μm (Figure 27).

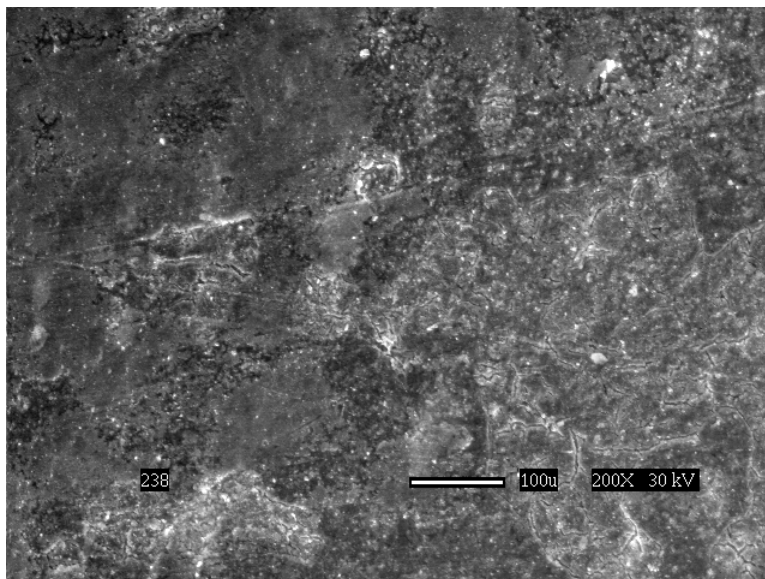


Figure 26. SEM surface analysis of multiphase flow sample of X65 after 10 days exposure (60°C , 0.77 MPa CO_2 , $\text{pH } 6$, $\text{pH}_2\text{S} = 0.00012\text{ bar} \pm 0.00004\text{ bar}$).

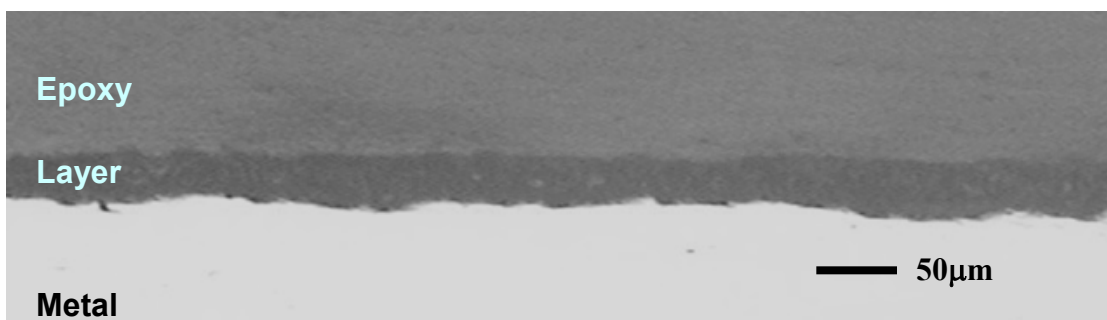


Figure 27. Cross sectional analysis of multiphase WL sample of X65 after 30 day exposure. Corrosion product is approximately 28 to 30 μm thick. (100X metallurgical microscope, 60°C , 0.77 MPa CO_2 , $\text{pH}_2\text{S} = 0.00012\text{ bar} \pm 0.00004\text{ bar}$).

Although the corrosion product layer developed under these conditions retards the corrosion as related to the same corrosive environment without the presence of H_2S , but

only required a few microns depth to retard corrosion. This very thin layer also seems to show that it may be influenced by flow as indicated by the lines and directional structure of the corrosion product in the images of the multiphase weight loss samples (Figure 25). This is an example of a corrosion product that has been thought to be amorphous in nature as no crystalline features are visible even at a high magnification. It is assumed that the lack of an iron carbonate component in the corrosion product layer for this experiment led to a general corrosion with a thin corrosion product layer and no observable localized corrosion.

Experiment 3: Iron Sulfide Saturation Value is 1.5 Times Greater Than the Iron Carbonate Saturation Value .

Introduction

In this experiment of the series, iron carbonate and iron sulfide were both supersaturated in solution, but iron sulfide was approximately 1.5 times greater throughout the test under the parameters shown in Table 9.

Table 9. Controlled Parameters for $S(\text{FeS}) \geq S(\text{FeCO}_3)$.

Parameter	Description
Equipment	H ₂ S Flow Loop
Test duration	25 days
Temperature	60.6 ± 0.8 °C
pCO ₂	7.8 ± 0.1 bar
pH ₂ S	0.0012 ± 0.0001 bar
pH	6.0 ± 0.1
Solution	1 wt% NaCl
Ionic strength	0.26 ± 0.007
[Fe ⁺⁺] (ppm)	17.3 ± 2.4
S(FeCO ₃)	62.8 ± 10.5
S(FeS)	90 ± 17
S(FeS)/S(FeCO ₃)	1.4 ± 0.1

#(avg ± std deviation)

Results and Discussion

System conditions were consistent during this experiment. The ferrous ion concentration remained relatively constant at 17.3 ± 2.4 along with the H₂S partial pressure at $1.2 \text{ mbar} \pm 0.1 \text{ mbar}$ (Figure 28). Therefore the saturation values for iron carbonate and iron sulfide were also stable at 1.1 ± 0.2 and 114 ± 19 , respectively (Figure 29).

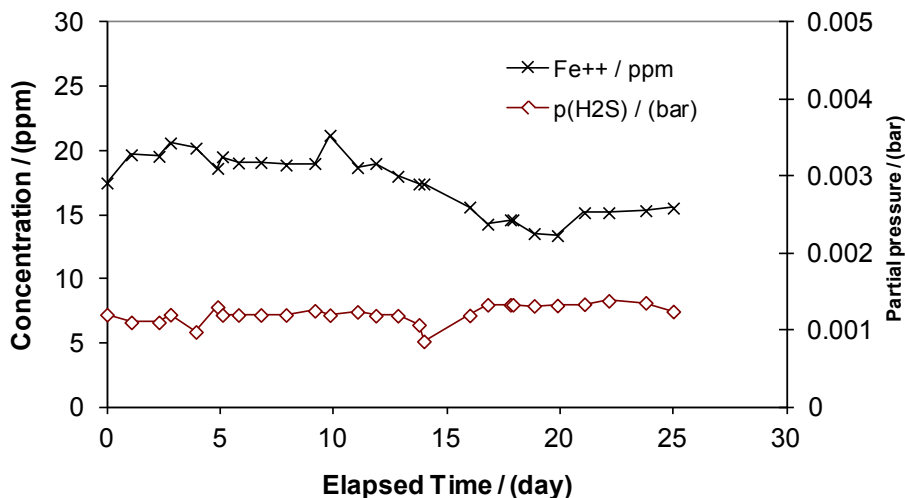


Figure 28. Iron concentration and H₂S partial pressure. (60°C, 0.77 MPa CO₂, pH 6, H₂S gas phase concentration = 120 ± 10 ppm)

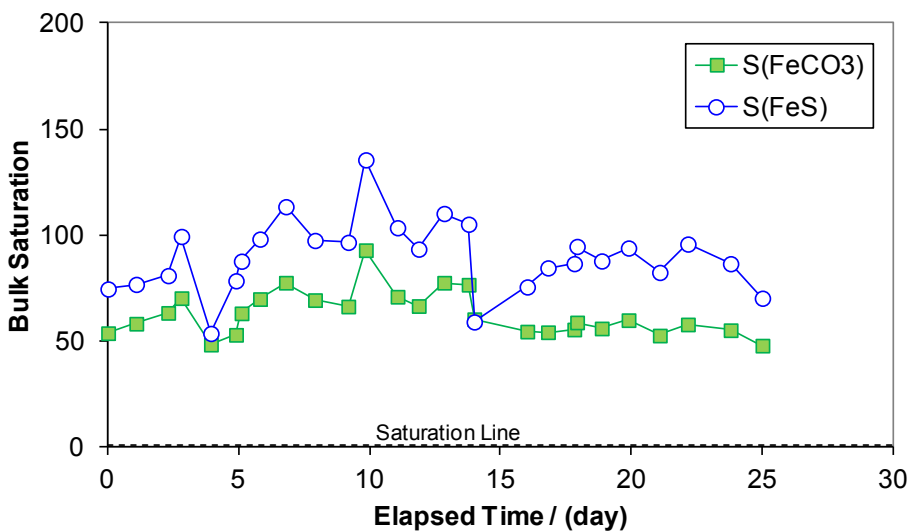


Figure 29. Saturation Values for Iron Carbonate and Iron Sulfide. (60°C, 0.77 MPa CO₂, pH 6, p_{H₂S} = 1.2 mbar ± 0.1 mbar)

Corrosion rates were low in single phase (SP) as compared to those in multiphase (MP) flow, although, electrochemical measurements in SP flow did not confirm this. As

seen in Figure 30 and Figure 31, corrosion rates measured by LPR for multiphase (MP) were less than 1 mm/yr as expected, but the single phase (SP) LPR measurements dramatically increased with the first few days of testing. During the experiment, this was assumed to be caused by conductive FeS layers and not actual measured corrosion rates.

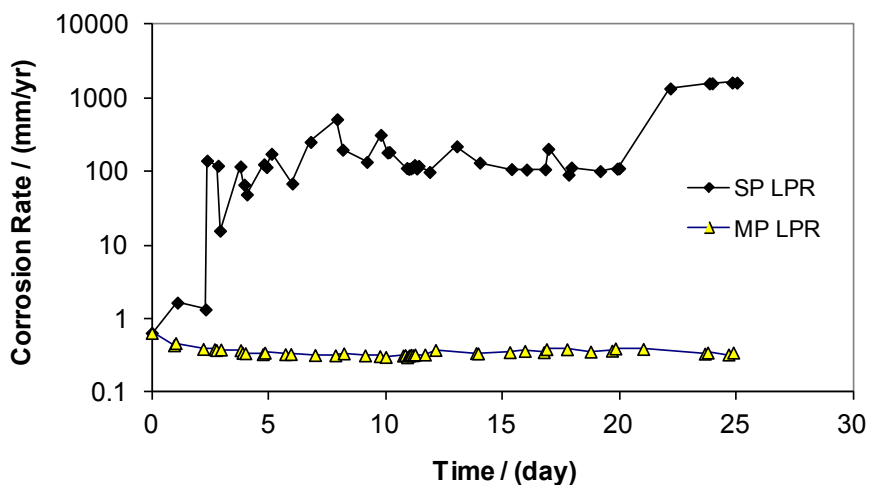


Figure 30. Polarization resistance measurements for single phase and multiphase flow showing a conductive layer was deposited on the SP probe giving false readings.

The probes were not disturbed in order to monitor the layer's resistance to consistent system flow conditions with time and the knowledge that the WL sample experiencing the same conditions would be removed after the first 10 days exposure for verification. None of the samples retrieved from the experiment had such a high corrosion rate and observation of the LPR probe surface after the experiment proved it was not metal loss that was causing the increase in measured corrosion rate, so this

provided proof of a conductive layer bridging the gap between the working and reference electrode which reduced the measured polarization resistance.

General corrosion rates of 6.7 mm/yr and 5.2 mm/yr were observed at 10 day and 15 day exposures, respectively, in multiphase flow and general corrosion rates of 1.1 mm/yr and 0.3 mm/yr were measured for the single phase flow at 10 day and 15 day exposures, respectively, but no localized corrosion was observed in this experiment (Figure 31).

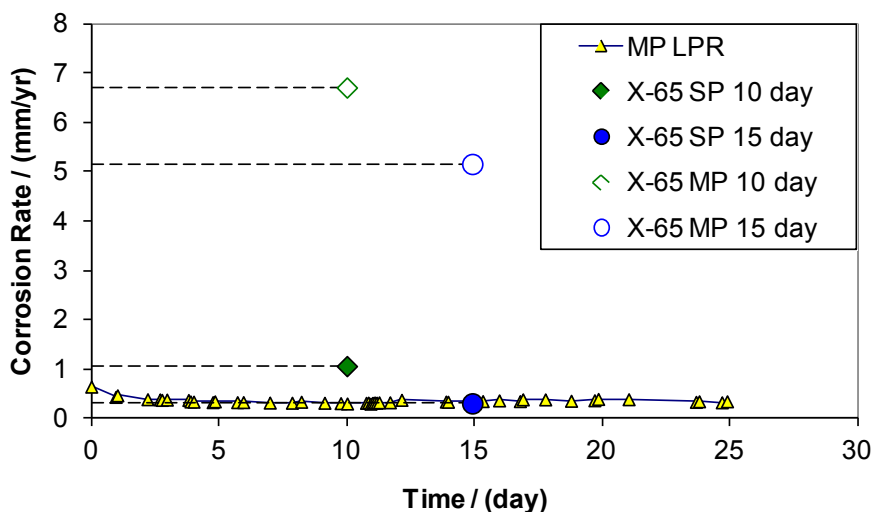


Figure 31. LPR and WL sample corrosion rate measurements. (60°C , 0.77 MPa CO_2 , $\text{pH } 6$, $\text{pH}_2\text{S} = 1.2\text{ mbar} \pm 0.1\text{ mbar}$).

Analysis of the corrosion product layers did show a slight increase in the mass of the corrosion product layer with time (Figure 32). The single phase samples had 0.0209 g corrosion product layer for the sample with 10 days exposure and 0.0255 g of corrosion

product for the sample with 15 days exposure. The multiphase samples had 0.0946 g corrosion product for the sample with 10 days exposure and 0.1112 g corrosion product for the sample with 15 days exposure to system conditions.

Further observations of the corrosion products that developed in single phase flow and multiphase flow were conducted with the SEM. Both surface layers shown in Figure 33 and Figure 34 show a drying and cracking of the surface after the samples were removed and dried with isopropyl alcohol. This suggests that the surface corrosion product layer contained water. Note the lifting and curling of the corrosion product layer from the multiphase flow sample surface. Due to this type of corrosion product layer, polish marks were not visible on any of the X65 samples taken from this experiment.

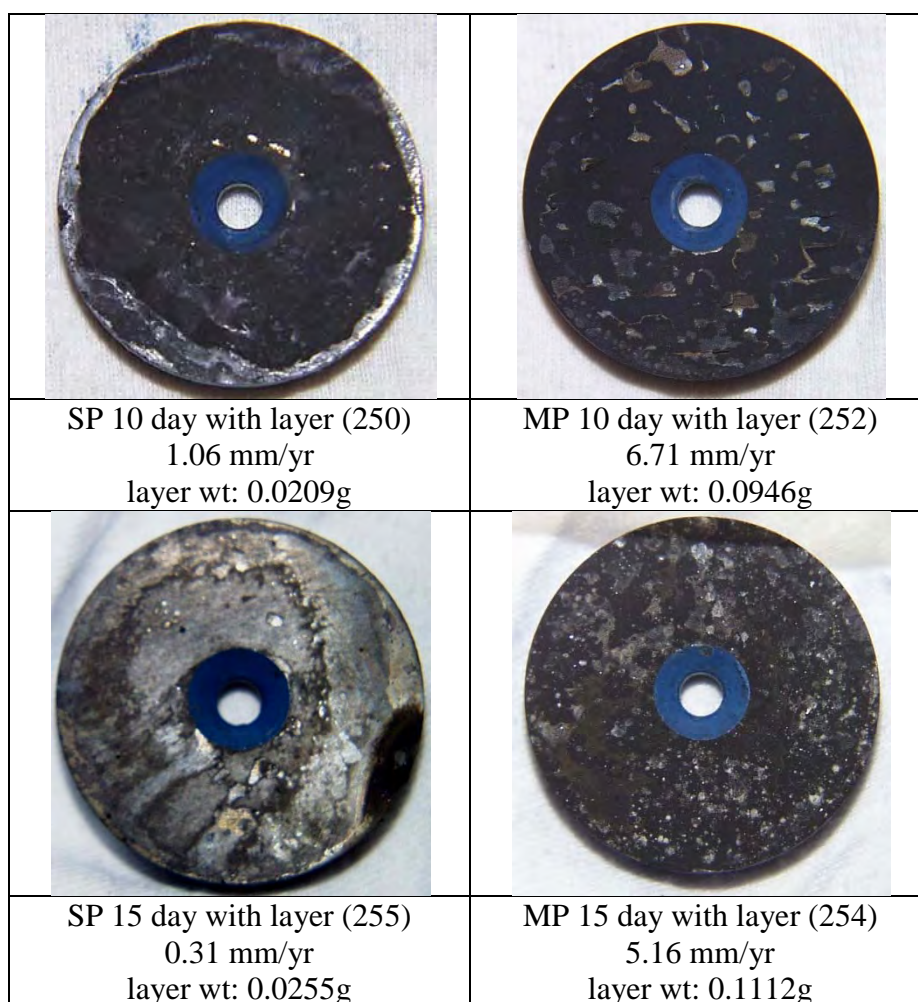


Figure 32. Visual examination of weight loss samples as removed from experiment for 10 day and 15 day exposure times. (60°C, 0.77 MPa CO₂, pH 6, p_{H₂S} = 1.2 mbar ± 0.1 mbar).

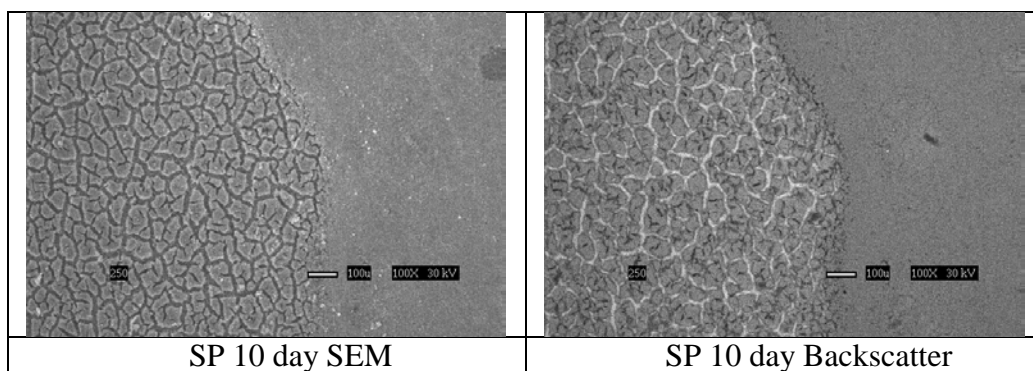


Figure 33. SEM and Backscatter images of surface layers developed in single phase flow (SP) after 10 day exposure to conditions. (60°C , 0.77 MPa CO_2 , $\text{pH } 6$, $\text{pH}_2\text{S} = 1.2\text{ mbar} \pm 0.1\text{ mbar}$).

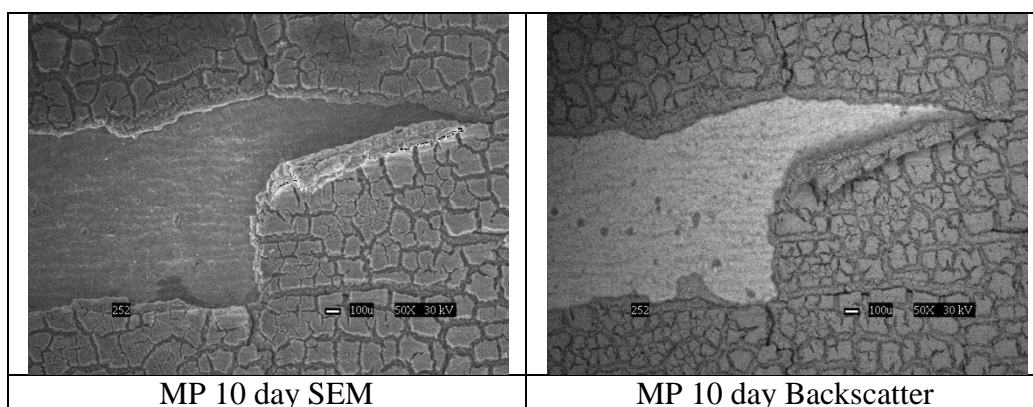


Figure 34. SEM and Backscatter images of surface layers developed in multiphase flow (MP) after 10 day exposure to conditions. (60°C , 0.77 MPa CO_2 , $\text{pH } 6$, $\text{pH}_2\text{S} = 1.2\text{ mbar} \pm 0.1\text{ mbar}$).

Only two representative images of the sample taken from multiphase after 25 days are available (Figure 35) and show a uniform surface coverage of corrosion product with no apparent localized corrosion. The cross section of this sample (Figure 36) provides an interesting observation of multiple layers of corrosion product developed in this experiment. The $120\text{ }\mu\text{m}$ to $150\text{ }\mu\text{m}$ thickness of the layer shown in Figure 36 is considered to be significant and the layering is an indication of the growth mechanisms.

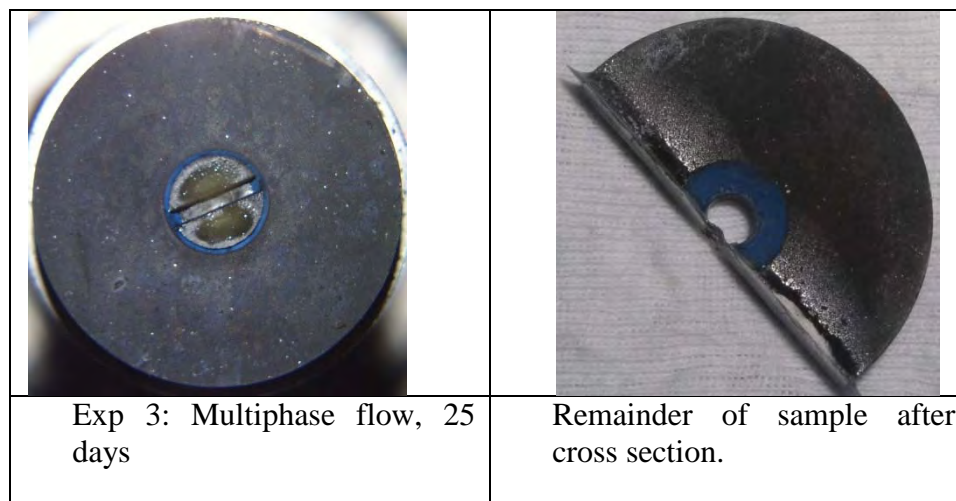


Figure 35. Visual examination of weight loss sample removed from multiphase flow after 25 days as used for cross sectional analysis. (60°C , 0.77 MPa CO_2 , $\text{pH } 6$, $\text{pH}_2\text{S} = 1.2\text{ mbar} \pm 0.1\text{ mbar}$).

In Figure 36, notice that the sulfide content decreases from 15% near the bulk solution side of the layer to 0.0% near the metal surface, indicating a possible iron carbonate corrosion product near the metal surface. This lack of sulfide content near the metal surface indicates that it did not have direct contact with the system solution containing aqueous H_2S , so the growth of this corrosion product had to occur by the diffusion of species through the bulk solution side of the layer to react with other species within the corrosion product layer. It also indicates that aqueous H_2S or $[\text{HS}^-]$ was not able to diffuse through the layer to the metal surface to form FeS . Yet, the increase in the mass of the corrosion product layer with time indicates a continuous growth process in both single phase and multiphase flow. To develop this type of corrosion product, carbon dioxide related species ($[\text{CO}_2]_{\text{aq}}$, $[\text{H}_2\text{CO}_3]$, $[\text{HCO}_3^-]$, $[\text{CO}_3^{2-}]$) would have to diffuse

through the corrosion product layer to react with ferrous ions near the metal surface, which provides evidence of an ion selective layer.²⁰

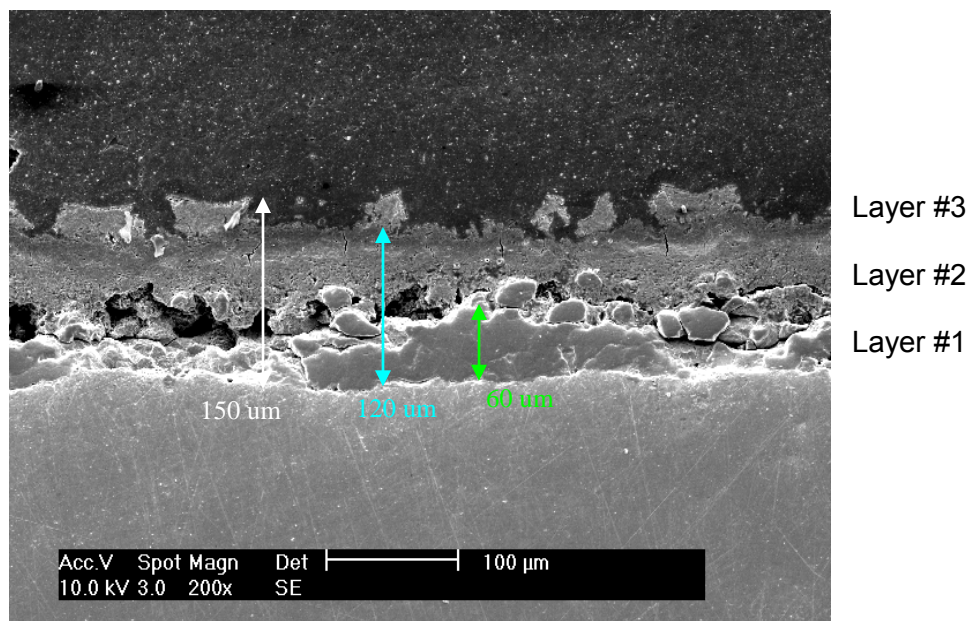


Figure 36. Experiment 3: Cross section of multiphase X65(2) coupon after 25 day exposure (60°C, 0.77 MPa CO₂, pH 6, p_{H₂S} = 1.2 mbar ± 0.1 mbar, 25 day exposure). (next to metal surface) layer #1: 60 μm, layer #2: 60 μm, and layer #3: 30 μm. Layer #1 EDS is [32.4% Fe, 0.0% S, 13.4% C, 26.5% O], the interface between layer #1 and layer #2 EDS is [35.4% Fe, 12.9% S, 14.0% C, 9.5% O], and the EDS of layer #2 is [31.2% Fe, 15.0% S, 20.8% C, 11.2% O].

The samples from multiphase flow had more corrosion product remaining on the metal surface after the test than the single phase flow samples. The weight loss samples after the corrosion product layer has been removed are seen in Figure 37. The samples in single phase flow had a much lower general corrosion rate than those from the multiphase flow test section, but none of the samples had an indication of localized corrosion.

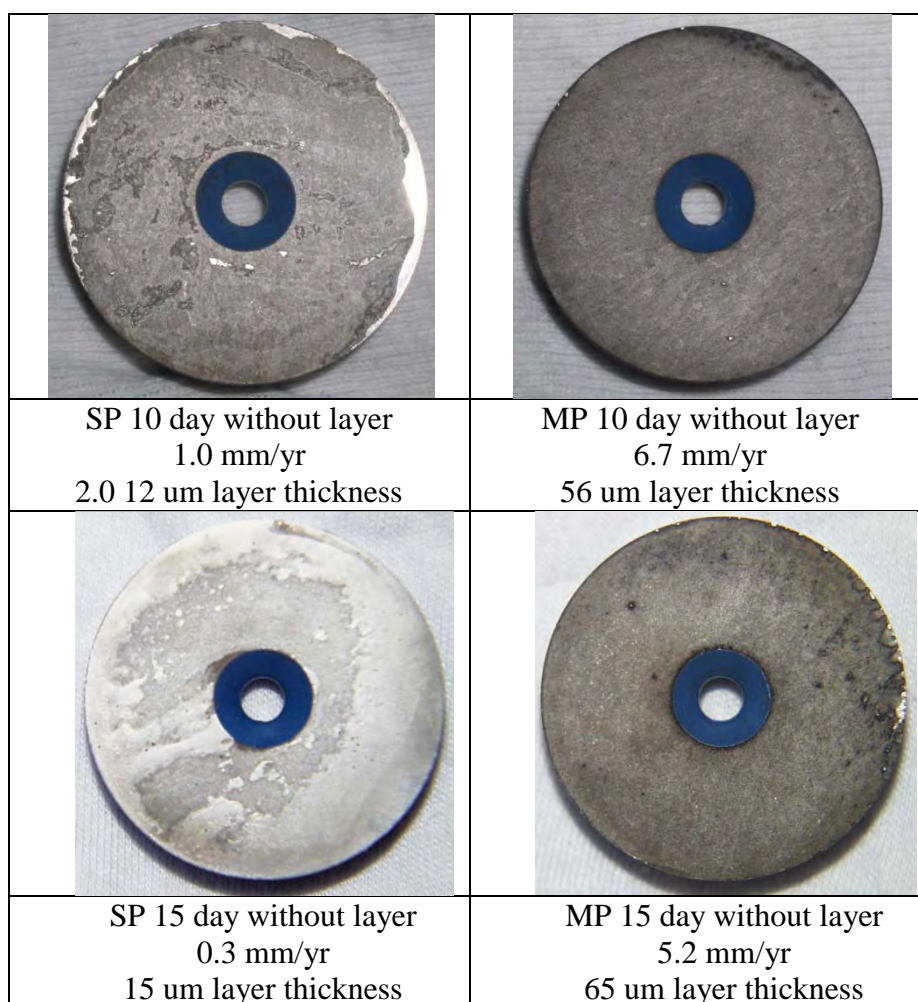


Figure 37. Visual examination of weight loss samples after Clarke solution procedures to remove the corrosion product layer; samples cut in half have undergone cross section analysis. (60°C, 0.77 MPa CO₂, pH 6, p_{H₂S} = 1.2 mbar ± 0.1 mbar).

Weight loss samples from single phase flow measured at 1.0 mm/yr after 10 days exposure which decreased to 0.3 mm/yr after 15 days. The samples from multiphase flow measured 6.7 mm/yr after 10 days exposure, but only decreased to 5.2 mm/yr for the sample exposed for 15 days. Because these samples only had general corrosion, a relationship between the corrosion rate and the amount of corrosion product layer

developed can be seen. The single phase flow samples experienced about 1/5th the corrosion rate calculated for the samples in multiphase flow and, as previously written, also had about 1/5th the mass of corrosion product layer.

This seems to confirm that a direct proportion of the iron lost in the corrosion reaction is trapped and maintained as part of the corrosion product independent of the flow regime. This behavior has been previously observed and well documented in previous research⁵ through the use of a scaling tendency (ST). None of the samples from this experiment show indications of localized corrosion.

Experiment 4: Iron Sulfide Saturation Value is 10 Times Greater Than the Iron Carbonate Saturation Value.

Introduction

In this experiment of the series, the average saturation value for iron sulfide was near 150 while the iron carbonate saturation value was just above 10; therefore, one would expect the corrosion product to be highly dominated by iron sulfide. The operating parameters for this experiment are shown in Table 10 including the averaged values for iron carbonate saturation, $S(\text{FeCO}_3)$, iron sulfide saturation, $S(\text{FeS})$, and the relationship between the two throughout the experiment, $S(\text{FeS})/S(\text{FeCO}_3)$.

Table 10. Controlled Parameters for $S(\text{FeS}) \approx 10[S(\text{FeCO}_3)]$

Parameter	Description
Equipment	H ₂ S Flow Loop
Test duration	25 days
Temperature	59.8 ± 0.8 °C
pCO ₂	7.7 ± 0.9 bar
pH ₂ S	0.010 ± 0.0016 bar
pH	6.0 ± 0.1
Solution	1 wt% NaCl
Ionic strength	0.28 ± 0.02
[Fe ⁺⁺] (ppm)	2.3 ± 1.2
S(FeCO ₃)	13 ± 9
S(FeS)	151 ± 111
S(FeS)/S(FeCO ₃)	11.7 ± 0.5

#(avg ± std deviation)

Results and Discussion

In order to dramatically increase the iron sulfide saturation value, the partial pressure of H₂S for this experiment is set a magnitude greater than previous testing while the partial pressure of CO₂, temperature, and water chemistry values were to remain constant. The low ferrous ion concentration (1 ppm < [Fe⁺⁺] < 5 ppm) kept the saturation value for iron carbonate below thermodynamic equilibrium while a higher partial pressure of H₂S, used to maintain the gas phase H₂S concentration near 1000 ppm, kept the average saturation value for iron sulfide near 200. The iron sulfide saturation value is near 800 times greater than the iron carbonate saturation value for the whole experiment as confirmed by the average of the S(FeS)/S(FeCO₃) ratio of 837 ± 68. The H₂S and Fe²⁺ measured concentrations from this experiment (Figure 38) were used to calculate the bulk saturation values shown in Figure 39 from Equations (25) through (22).

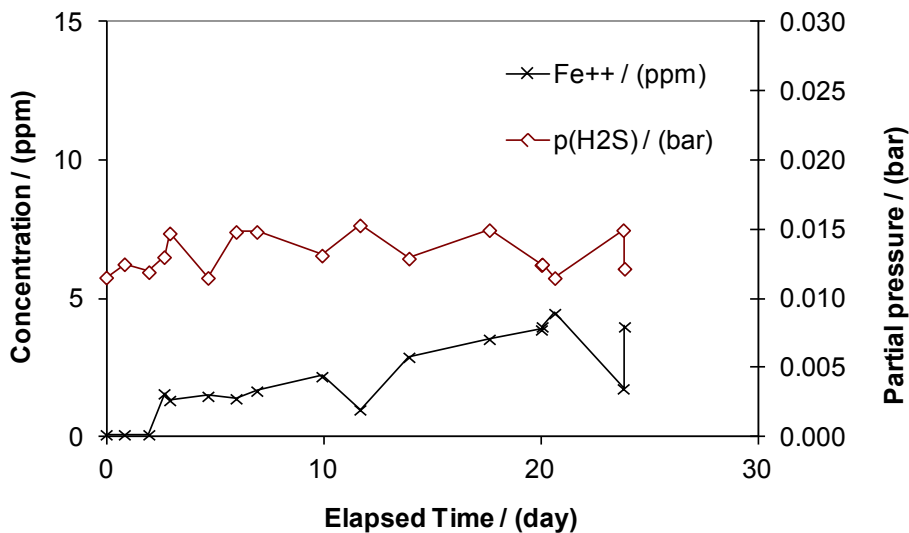


Figure 38. Variations of iron and hydrogen sulfide concentrations with time. (60°C , $P_{\text{total}} = 8 \text{ bar}$, $0.01 \text{ bar} \pm 0.001 \text{ bar } \text{pH}_2\text{S}$ [1000 ppm])

Both linear polarization resistance (LPR) and weight loss (WL) corrosion measurements were collected for comparison in this H_2S dominated environment. The weight loss coupons (WL) are used to provide the best representation of the general corrosion rate and also provide more information associated with the corrosion product layer and possibility of localized corrosion. Under these conditions, the electrochemical measurements were highly influenced by the corrosion product and did not give a valid interpretation of the corrosivity of the environment (Figure 40) as the true weight loss measurement ranged from 0.86 mm/yr to 3.3 mm/yr.

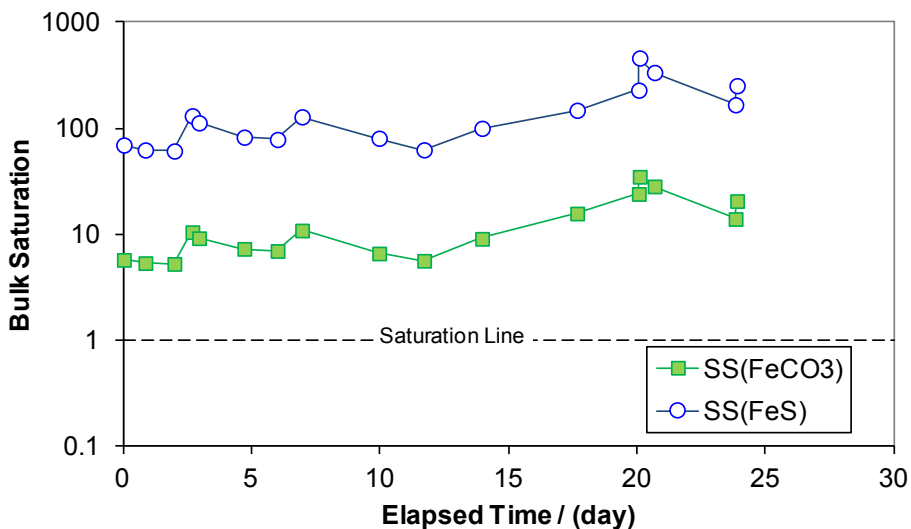


Figure 39. Comparison of Saturation values for iron carbonate (FeCO_3) and iron sulfide (FeS). (60°C , $P_{\text{total}} = 8 \text{ bar}$, $0.01 \text{ bar} \pm 0.001 \text{ bar}$ pH_2S [1000ppm], 1 wt% NaCl).

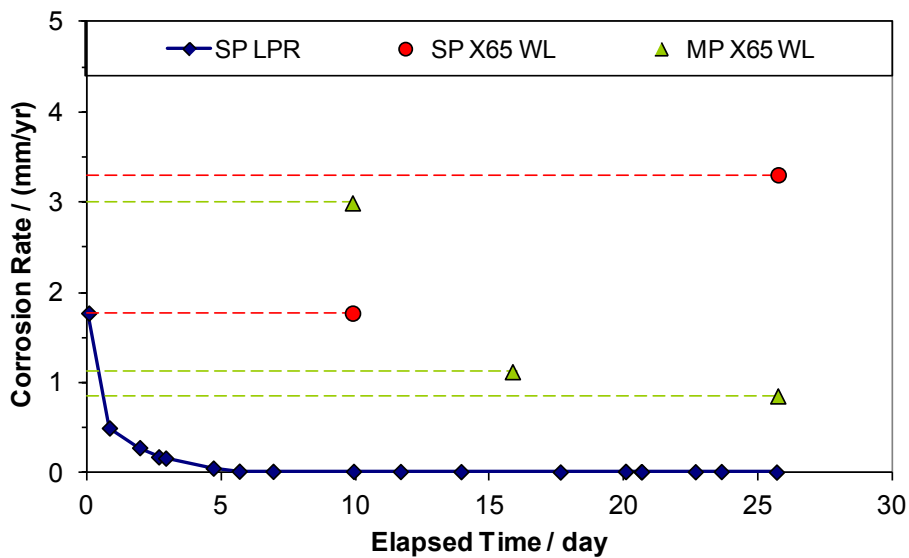


Figure 40. Comparison of Corrosion rates measured by linear polarization and weight loss coupons. SP – Single Phase, MP – Multiphase (60°C , $P_{\text{total}} = 8 \text{ bar}$, $0.01 \text{ bar} \pm 0.001 \text{ bar}$ pH_2S [1000ppm], 1 wt% NaCl)

All WL samples from this experiment show surface variations of 10 μm to 40 μm due to corrosion, but only the WL sample exposed for the first 10 days of the experiment in multiphase flow could be defined as having localized corrosion with a maximum pit depth measured from cross sectional analysis at 340 μm (Figure 41). Observations of weight loss samples from each time exposure to single phase and multiphase flow conditions are shown in Figure 42. As expected in an H_2S dominated environment, the corrosion product is black and fully covers the metal surface. Figure 43 shows the samples after corrosion product analysis was conducted and corrosion product layer removal procedures were completed. The mass of the corrosion product layer measured for each sample was inconclusive as it seemed to increase for samples in single phase flow and varied for the samples in multiphase flow. The single phase samples from the experiment had 0.3115 g corrosion product layer for the sample with 10 days exposure and 1.3472 g of corrosion product for the sample with 26 days exposure. The multiphase samples had 0.2205 g corrosion product for the sample with 10 days exposure, 0.9694 g corrosion product for the sample with 16 days exposure, and 0.1553 g corrosion product for the sample with a 26 day exposure to system conditions. Polish marks were visible only on the samples taken from 16 days exposure to the system conditions.

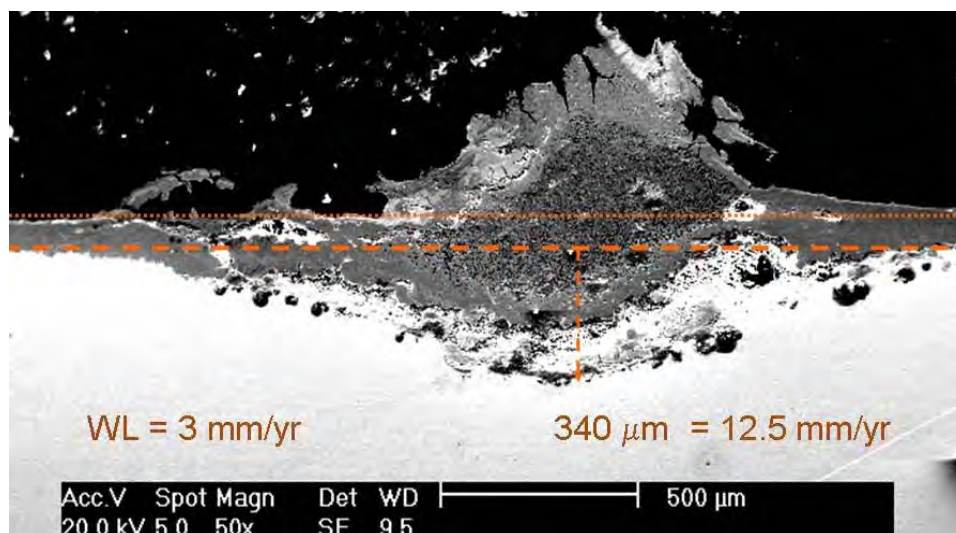


Figure 41. Cross section with calculation of general corrosion rate vs. localized corrosion rate for multiphase flow sample after 10 days exposure. (60°C , $P_{\text{total}} = 8 \text{ bar}$, $0.01 \text{ bar} \pm 0.001 \text{ bar pH}_2\text{S [1000ppm]}$, 1 wt\% NaCl)

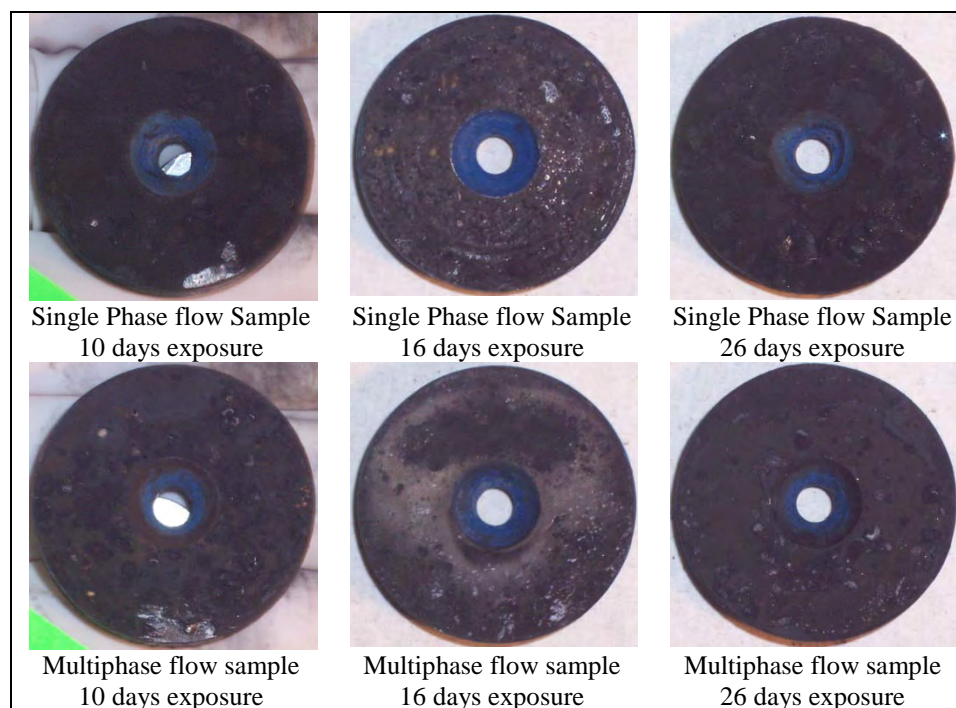


Figure 42. Visual examination of weight loss samples as removed from experiment. (60°C , $P_{\text{total}} = 8 \text{ bar}$, $0.01 \text{ bar} \pm 0.001 \text{ bar pH}_2\text{S [1000ppm]}$, 1 wt\% NaCl)

Surface views of the weight loss samples show circular features in multiple locations. SEM analysis of the WL sample exposed for 16 days in multiphase flow conducted before and after cross sectioning show a relationship between these circular surface features and the corrosion mechanisms that were occurring.

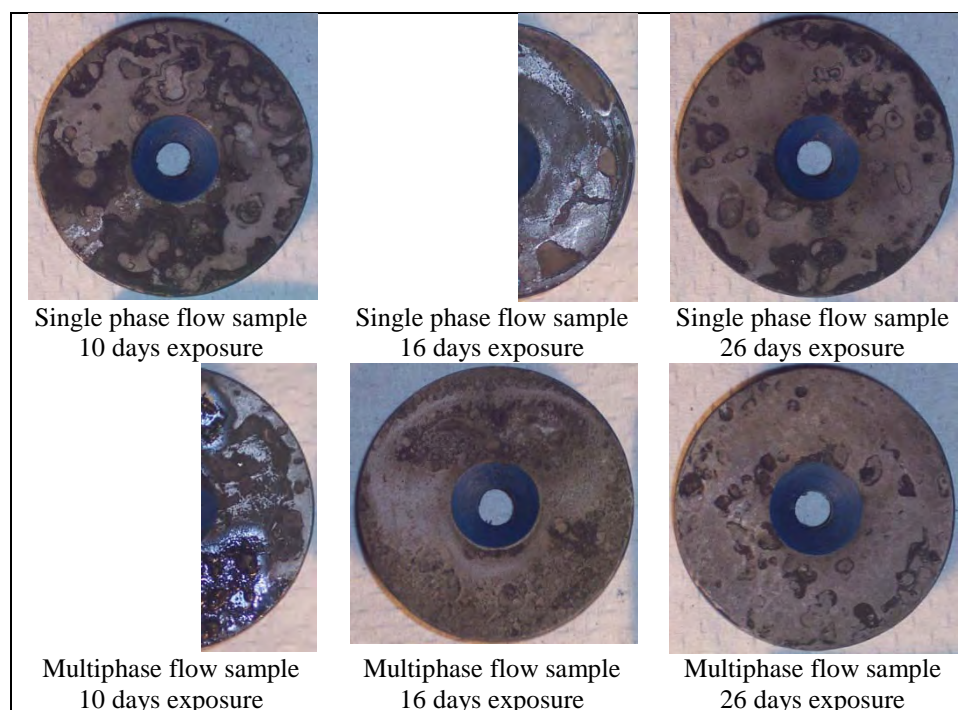


Figure 43. Visual examination of weight loss samples after Clarke solution procedures to remove the corrosion product layer; samples cut in half have undergone cross section analysis. (60°C , $P_{\text{total}} = 8 \text{ bar}$, $0.01 \text{ bar} \pm 0.001 \text{ bar } \text{pH}_2\text{S}$ [1000ppm], 1 wt% NaCl)

The circular pattern in the backscatter SEM image of Figure 44 measures approximately 1.4 mm in diameter. The cross sectional view of a similar area, Figure 45, measures 2.4 mm across the exposed pit. The white circular feature in the upper portion of the pit is caused by a bubble trapped inside the epoxy of the cross sectional mount.

This is of interest because it highlights the fact that the corrosion product layer in this area was damaged, but intact enough to hold a pocket of air.

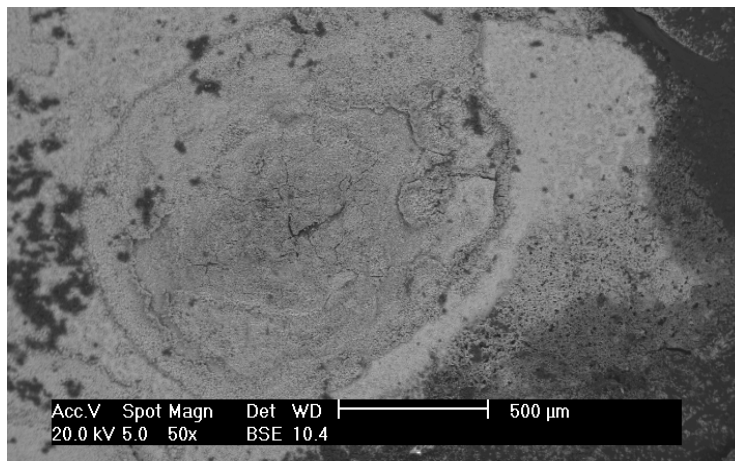


Figure 44. Backscatter SEM image of corrosion product layer showing circular pattern observed in many locations on multiphase flow sample after 10 days exposure. (60°C, $P_{\text{total}} = 8$ bar, 0.01 bar \pm 0.001 bar pH₂S [1000ppm], 1 wt% NaCl)

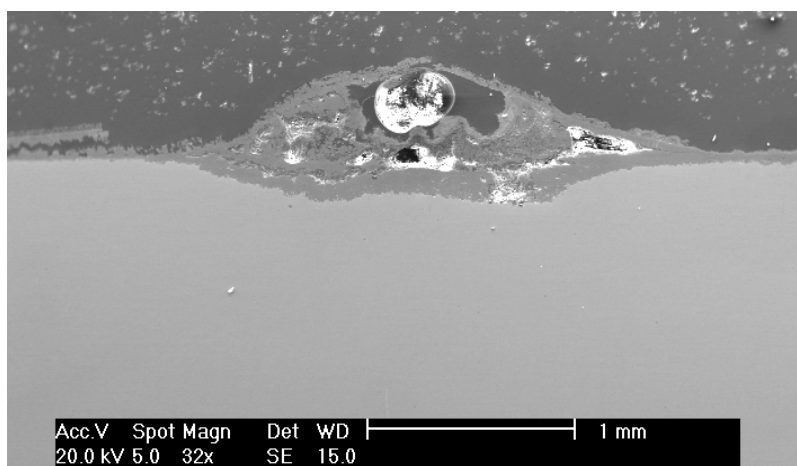


Figure 45. Visual example of layer breakdown and localized corrosion from SEM cross section analysis of multiphase flow sample after 10 days exposure. (60°C, $P_{\text{total}} = 8$ bar, 0.01 bar \pm 0.001 bar pH₂S [1000ppm], 1 wt% NaCl)

The example in Figure 45 provides proof of localized attack under these conditions. The general corrosion rate for a similarly exposed coupon measured 3 mm/yr and the penetration rate calculated from the maximum variation in the metal surface on the cross section is 9 mm/yr. With a penetration rate 3 times greater than the general corrosion rate, this can be considered localized corrosion and a greater penetration rate is possible since the cross sectional image is not guaranteed to show the deepest location of the pit.

There are three regions of corrosion product layer morphology represented in Figure 45. On the far right is the fully developed, intact corrosion product layer of approximately 69 μ m depth. In the center, break down of this layer occurred allowing the localized attack to occur. On the left is an area of exfoliation which could have occurred during experimentation or after removal from the corrosive environment in the drying process of analysis. EDS spot analysis of the corrosion product layer, Figure 46, shows a higher sulfide content in the overlying surface layer than in the corrosion product developed within the area of localized attack. This is thought to be caused only by the surface layer acting as a diffusion barrier.

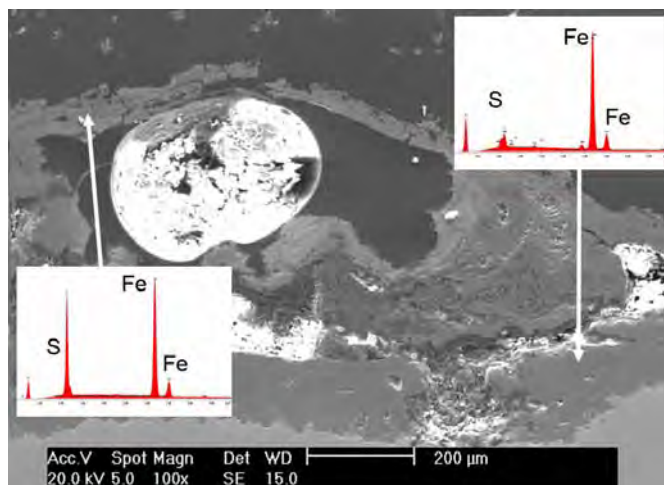


Figure 46. EDS composition of locations within the localized corrosion. (60°C , $P_{\text{total}} = 8$ bar, $0.01 \text{ bar} \pm 0.001 \text{ bar}$ pH_2S [1000ppm], 1 wt% NaCl, multiphase flow, 10 days) The bright circular region in the figure is due to an air bubble captured under the layer during epoxy coating of the sample for cross sectioning.

What is obvious from Figure 46 is the failure of the corrosion product layer through cracking and spalling. The initiation of localized corrosion is assumed to begin at locations where diffusion of H_2S through the layer finds a discontinuity in the corrosion product layer or an inclusion in the structure of the metal surface. Growth of the corrosion product underneath the existing layer will lift and damage the layer due to internal stresses. Iron sulfide species will be larger than the ferrous iron cations or bisulfide anions and have a lower state of energy as a precipitate. At this location a higher corrosion rate will occur because of the increased mass transfer of species through the damaged area, propagating the localized corrosion. Many locations similar to this were observed with pit penetration rates up to 12.5 mm/yr.

Figure 47 shows the corrosion product layer lifting from the surface, but is assumed to have occurred during the drying process because of the perfect match

between the upper and lower surfaces of the discontinuity. This provides insight into corrosion product layer morphology by deductive reasoning.

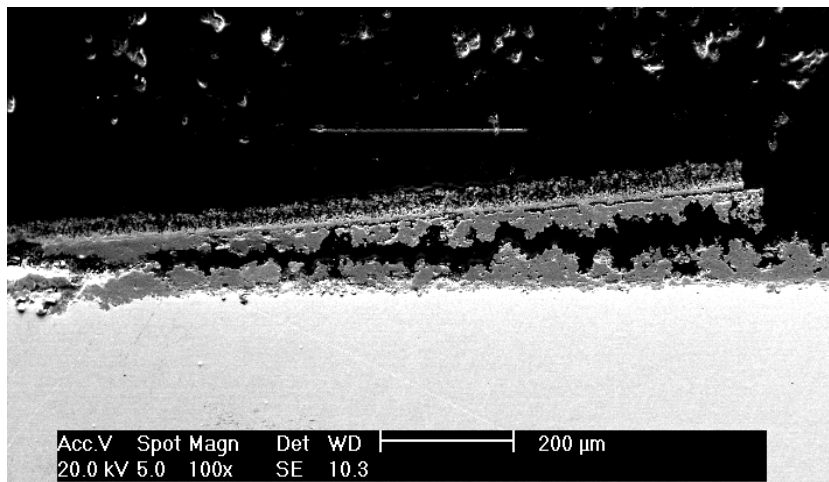


Figure 47. Region of layer exfoliation. (60°C , $P_{\text{total}} = 8 \text{ bar}$, $0.01 \text{ bar} \pm 0.001 \text{ bar pH}_2\text{S}$ [1000ppm], 1 wt% NaCl, multiphase flow, 10 days)

It is understood that a fast reaction occurs between hydrogen sulfide and a bare carbon steel surface to produce a mackinawite layer.⁵ The mackinawite corrosion product has structure and orientation since it was formed as a sheet across the metal surface, but it only acts as a diffusion boundary to retard the corrosion reaction. Although the corrosion reaction has been slowed by the added corrosion product layer, it has not been stopped.

Note the growth of the porous iron sulfide on top of the dense flat layer highlighted in Figure 48. This is thought to be caused by diffusion of ferrous ions through the existing mackinawite layer and subsequent fast reaction with aqueous hydrogen sulfide. Since the diffusion paths are limited by the initial mackinawite corrosion product

layer, the growth of this layer is more porous and open giving a visual impression from surface SEM analysis that has been labeled a “fluffy mackinawite.”⁵⁰

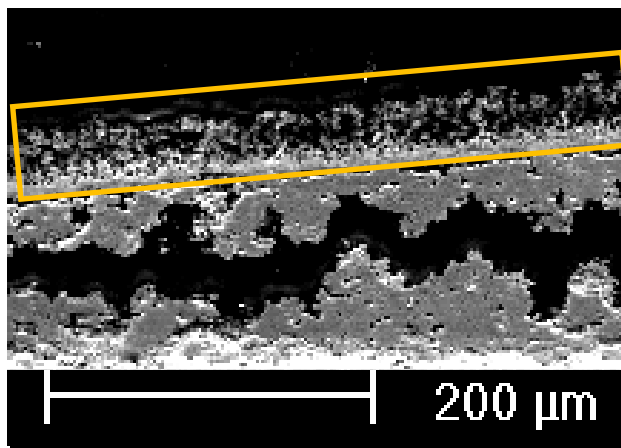


Figure 48. Upper layer of corrosion product – fluffy mackinawite. (60°C, $P_{\text{total}} = 8$ bar, 0.01 bar \pm 0.001 bar pH_2S [1000ppm], 1 wt% NaCl, multiphase flow, 10 days)

This corrosion product layer creates a subset of environmental conditions between it and the metal surface which are different, but related, to the conditions between the bulk solution and the corrosion product layer. These differences include more ferrous ion concentration and a resultant higher pH. The seclusion of this area would lead to a dissimilar composition of the corrosion product developed beneath the initial corrosion product layer as the fluid chemistry in this area may be equilibrated to a closed system in which reactions are based on a limited amount of reactants.

Initiation and propagation of localized corrosion can be explained in cases similar to this by understanding the characteristics of the corrosion product layers. The surface corrosion product layer can be considered to have lateral strength as it developed in a

sheet across the metal surface as very fast direct reaction, but is thin and can fail through brittle fracture more than likely caused by internal stresses. The underlying corrosion product could have weaknesses related to dissolution kinetics as it developed as a precipitate of the corrosion reaction in the area underneath the surface layer. This combination proves to initiate and propagate localized corrosion.

Increased propagation rates could occur if the surface layer (similar to that shown in Figure 46) were removed by flow. The underlying corrosion product layer would be exposed to bulk solution at a pH lower than during its development and would lead to dissolution of the corrosion product within the pit. If the assumption of a softer underlying layer with less structure also holds true, mass transfer through turbulent flow across the surface discontinuity would remove debris from the pit exposing the metal surface and increasing the rate of pit propagation.

An indication of these types of corrosion mechanisms occurring within the corrosion product layer are shown by analysis of the surface layer failures. An example from single phase flow after 16 days exposure to system conditions in Figure 49 shows an area which lost the upper crust of the corrosion product layer revealing a different surface morphology below. Cross sectioning of this sample was not able to capture a similar area with a surface failure, but indicated the overall thickness of the layer to be approximately 70 μm thick.

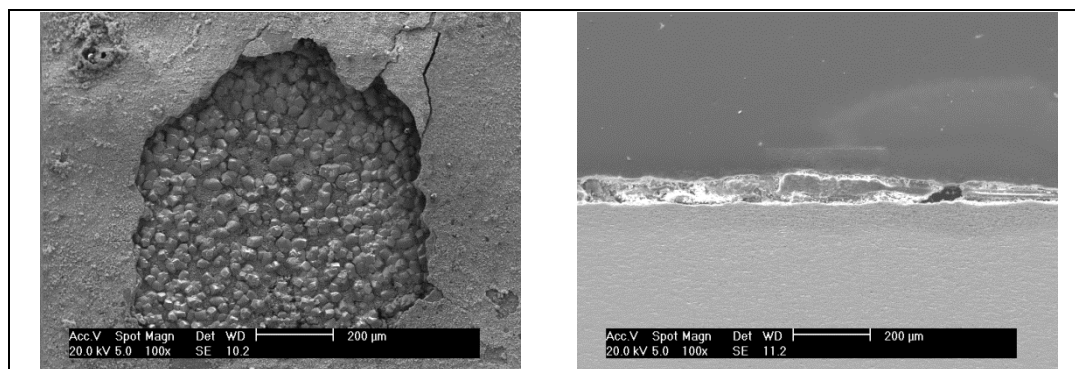


Figure 49. Surface layer failure and corrosion product layer thickness by cross section analysis for an X65 sample from single phase after 16 days exposure. (60°C , $P_{\text{total}} = 8$ bar, $0.01 \text{ bar} \pm 0.001 \text{ bar } \text{pH}_2\text{S}$ [1000ppm], 1 wt% NaCl)

EDS analysis was conducted on the surface areas outside and inside of the surface layer failure shown in Figure 49. The two contrasting areas are shown in Figure 50 and have a marked difference in composition. The area around the failure shows a composition high in iron sulfides, as the peaks in the EDS spectrum for sulfide (S) and iron (Fe) are equivalent, while a similar analysis to the area where the surface layer failure occurred shows a much lower sulfide to iron ratio with a larger oxygen (O) content indicated as well. The higher oxygen to iron ratio by EDS analysis is thought to indicate the presence of iron carbonate (FeCO_3) which seems reasonable due to the crystalline features observed.

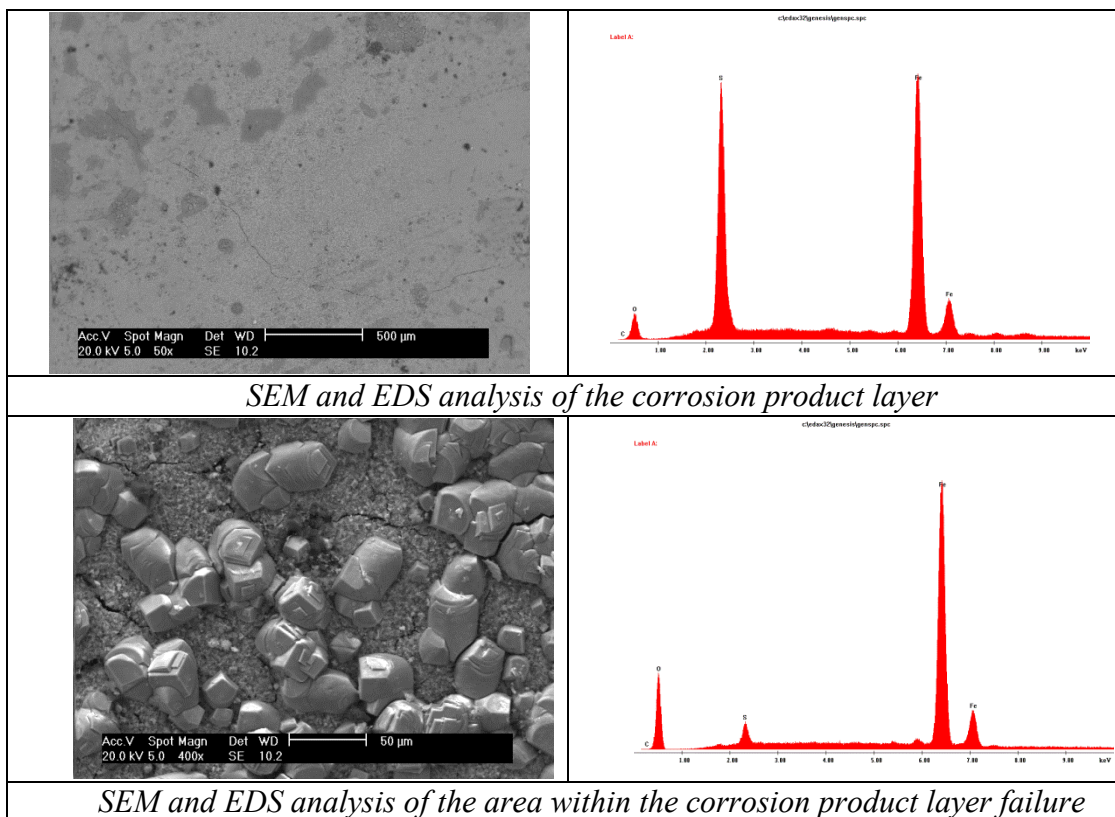


Figure 50. SEM and EDS analysis of the corrosion product layer outside and inside a surface layer failure from single phase flow after 16 days exposure. (60°C , $P_{\text{total}} = 8 \text{ bar}$, $0.01 \text{ bar} \pm 0.001 \text{ bar p}\text{H}_2\text{S}$ [1000ppm], 1 wt% NaCl)

Other areas representing the composition of the corrosion product layer by observations of surface layer failures and surface crystalline structure are shown in Figure 51, Figure 52, and Figure 53 for samples taken from multiphase flow after 26 days. The first images provide an indication that the composition of the area within the failure has a different and larger crystalline structure than outside the failure, Figure 51(a), and that the exposed area has components with a different molecular density, Figure 51(b), as indicated by the different intensities. The lighter color represents a higher reflected intensity of electrons to the detector indicating higher molecular density components.

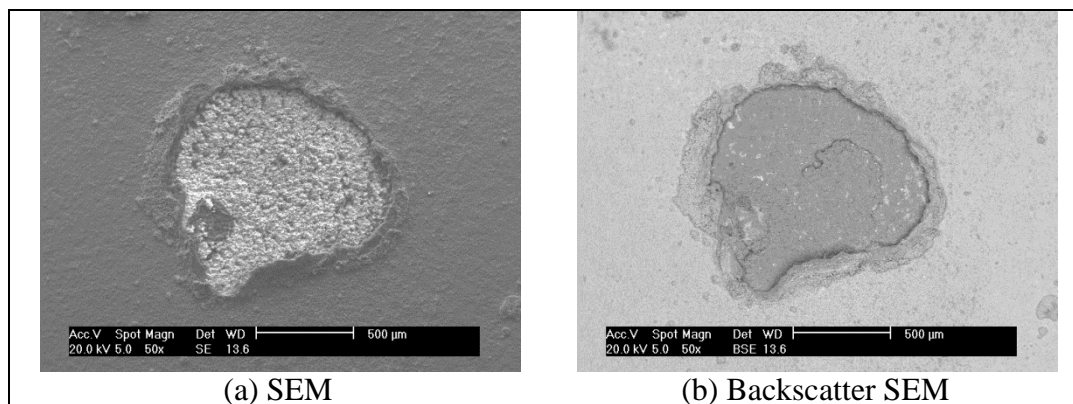


Figure 51. SEM and Backscatter images of surface layer failure for an X65 sample from multiphase after 26 days exposure. (60°C , $P_{\text{total}} = 8 \text{ bar}$, $0.01 \text{ bar} \pm 0.001 \text{ bar } \text{pH}_2\text{S}$ [1000ppm], 1 wt% NaCl)

The second image, Figure 52, shows similar results for the composition of the areas, but also indicates the areas of failure are on the order of $50 \mu\text{m}$ in depth for this sample and provides an indication of the thickness of the initial surface coverage layer (shown as a upward point arc from the surface) of approximately $10 \mu\text{m}$. And the third set of images at a higher magnification (Figure 53) shows the surface layer does have a crystalline structure with a composition high in iron sulfides, consistent with the description of a ‘fluffy’ mackinawite.

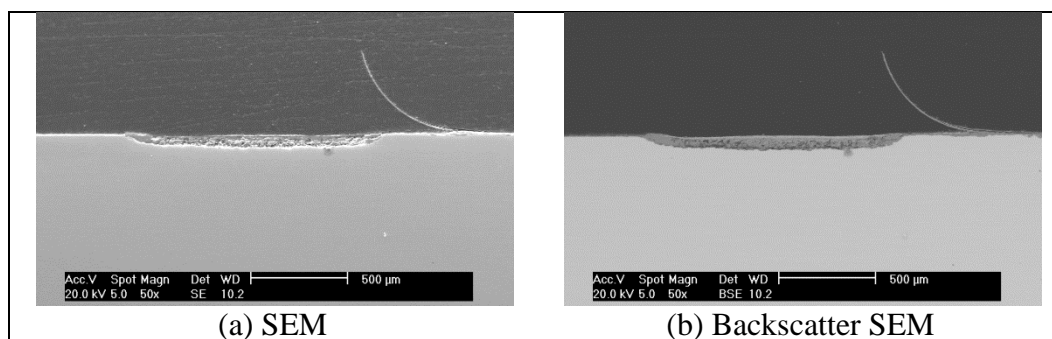


Figure 52. SEM and Backscatter images from cross sectional analysis of a surface layer failure for an X65 sample from multiphase after 26 days exposure. (60°C , $P_{\text{total}} = 8$ bar, $0.01 \text{ bar} \pm 0.001 \text{ bar pH}_2\text{S}$ [1000ppm], 1 wt% NaCl)

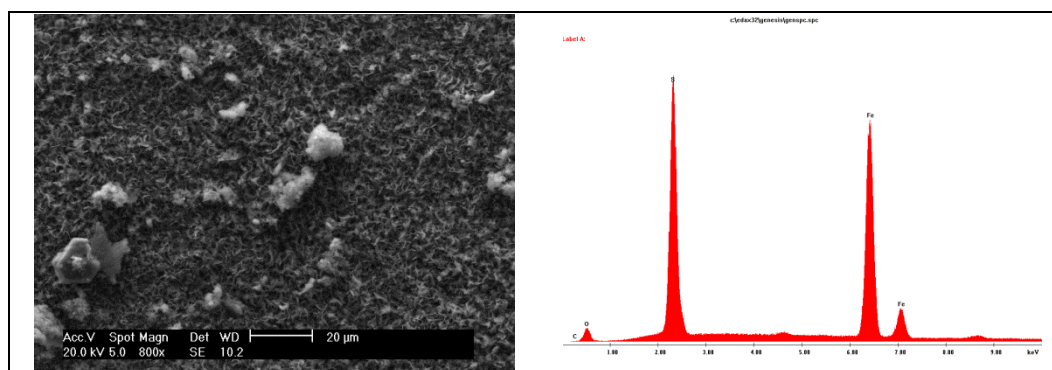


Figure 53. SEM and EDS analysis of a general surface area of corrosion product from an X65 sample in multiphase flow after 26 days exposure. (60°C , $P_{\text{total}} = 8$ bar, $0.01 \text{ bar} \pm 0.001 \text{ bar pH}_2\text{S}$ [1000ppm], 1 wt% NaCl)

The fact that iron carbonate could form as part of the corrosion product in a system where the bulk solution is under saturated with respect to iron carbonate, indicates that the surface layers of iron sulfide acted as a diffusion barrier. This diffusion barrier would dramatically slow down the transfer of species from the metal surface to the bulk solution and vice versa, which would allow any carbonate species that did diffuse through the iron sulfide layer to react with the increased ferrous ion concentration near the metal surface. The growth of iron carbonate crystals on the metal substrate shown in Figure 49,

Figure 50, and Figure 51 should not be possible if these areas shown were exposed to the bulk solution during the experiment; therefore it is assumed that the failure of the iron sulfide layer occurred during sample retrieval and analysis procedures. The failures of these local sites on the iron sulfide layer are also an indication that the iron sulfide corrosion product layer has weak points caused by internal stresses.⁵ Internal stresses are thought to arise from the fact that solid FeS is more voluminous than the iron it replaced. These internal stresses may be great enough to cause failure of the iron sulfide layer *in situ* which led to the observed localized corrosion (Figure 41) or *ex situ* which provided the images under review.

Conclusions Related to Saturation Values

The calculated values for saturation of iron carbonate and iron sulfide can be good indicators of when corrosion product layers are likely to occur, but are not directly related to the localized corrosion phenomenon since many factors are used in the calculation and each factor has its own direct relationship to the type of layer developed.

It is understood that a very fast reaction occurs between hydrogen sulfide and a bare carbon steel surface to produce a thin mackinawite layer as reflected in all electrochemical and weight loss measurements. It was also observed that a multilayer corrosion product was developed in this CO₂/H₂S environment as XRD analysis confirmed pyrrhotite and siderite on the metal surface, but these components did not correlate with an indication of localized corrosion. The likelihood of localized corrosion

was observed to increase with increased surface corrosion product as indicated by the mass of the corrosion product layer measured for each test. Without an observable corrosion product layer, the possibility of localized corrosion was minimized.

Effect of a Higher Ionic Strength Solution at pH 6

Introduction

Using the same experimental plan as the first four experiments, the amount of sodium chloride was increased to 10 wt% in solution, which increased the ionic strength of the solution from a previous range of 0.27 ± 0.01 mol/L to 1.88 ± 0.02 mol/L. By increasing the ionic strength of the solution through addition of such a large amount of NaCl, the saturation value for iron carbonate was reduced. This is caused by the fact that the solubility constants related to CO_2 [K_{sol} , in Equation (2), K_{ca} in Equation (8), and K_{bi} in Equation (10)] are all affected by an increase in the ionic strength of the solution which will cause a decrease in both the solubility of CO_2 in solution and a decrease in the iron carbonate saturation value. By comparison of calculations between a 1 wt% NaCl solution and a 10 wt% NaCl when all other conditions are constant, the increase in ionic strength would cause a decrease in $[\text{CO}_2]_{\text{aq}}$ by 23% and a subsequent decrease in $S(\text{FeCO}_3)$ by 71%.

The increase in both the ionic strength and chloride content are expected to have a dramatic effect on the corrosion mechanisms of mild steel. The addition of salt would increase the conductivity of the solution and reduce the solubility of iron carbonate which

should increase the general corrosion rate or increase the likelihood of localized corrosion. But previous research on mild steel samples in sweet conditions (CO₂ corrosion) with high sodium chloride concentrations⁵¹ in bulk solution conditions (where no iron carbonate corrosion product layer was expected) experienced a reduction in the general corrosion rate with no localized corrosion observed. In tests with H₂S, a report by Fang⁵² explains circumstances where a high chloride content in a sour (H₂S containing) solution acted as an initiator for localized corrosion. The next two experiments have a 10 wt% NaCl to continue the research with high ionic strength, Experiments 5 & 6 detailed in Table 11, with different partial pressures of H₂S at 0.001 bar and 0.010 bar for conditions set at 60°C, pH 6.0, and 8 bar total pressure.

Table 11. Experiments 5 & 6: higher ionic strength, two partial pressures of H₂S

Parameter	Exp. 5	Exp. 6
Temperature	60°C	60°C
Total Pressure	8 bar	8 bar
pCO ₂	7.7 bar	7.7 bar
Flow	Vsl = 1 m/s, Vsg = 3 m/s	Vsl = 1 m/s, Vsg = 3 m/s
NaCl solution	10 wt%	10 wt%
pH	6.0	6.0
pH₂S (mBar)	1	10
Measurements	WL, SEM	WL, SEM
Exposure Time	10, 20, 31 days	10, 20, 30 days

Experimental Observations

Experiment 5: 60°C, $p\text{CO}_2 = 7.7 \text{ bar}$, $p\text{H}_2\text{S} = 0.001 \text{ bar}$, $\text{pH} 6.0$, 10wt% NaCl

Introduction

For this experiment, the amount of sodium chloride is 10 wt% in solution and the average partial pressure of H_2S is 0.001 bar. All corrosion rate measurements in Experiment 5 are for single phase flow. With the increased ionic strength of the solution, the saturation value for iron carbonate was reduced. This is reflected in the reported values in Table 12 and Figure 54.

Table 12. Controlled Parameters for High Sodium Chloride Test at 1 mbar pH_2S .

Parameter	Description
Equipment	H_2S Flow Loop
Test duration	30 days
Temperature	$60.0 \pm 0.7 \text{ }^\circ\text{C}$
pCO_2	$7.7 \pm 0.5 \text{ bar}$
pH_2S	$0.0010 \pm 0.0004 \text{ bar}$
pH	6.1 ± 0.0
Solution	10 wt% NaCl
Ionic strength	1.86 ± 0.007
$[\text{Fe}^{++}]$ (ppm)	1.8 ± 0.5
S(FeCO_3)	3.1 ± 0.7
S(FeS)	13.2 ± 6.1
S(FeS)/S(FeCO_3)	4.2 ± 1.8

[#](avg \pm std deviation)

Results and Discussion

The water chemistry conditions of Experiment 5 are similar to those of Experiment 3 with the exception of the increased NaCl concentration which produced a dramatic increase in the ionic strength of the solution (from 0.26 to 1.8) with not much

affect on the corrosion rate. This increase in the ionic strength and the additional decrease in ferrous ion concentration, led to an iron carbonate saturation value near thermodynamic equilibrium ($S(\text{FeCO}_3) \approx 3$) as compared to the high saturation value for iron carbonate in Experiment 3 ($50 < S(\text{FeCO}_3) \leq 70$). The saturation values for iron carbonate, $S(\text{FeCO}_3)$, and iron sulfide, $S(\text{FeS})$, for this experiment are shown in Figure 54.

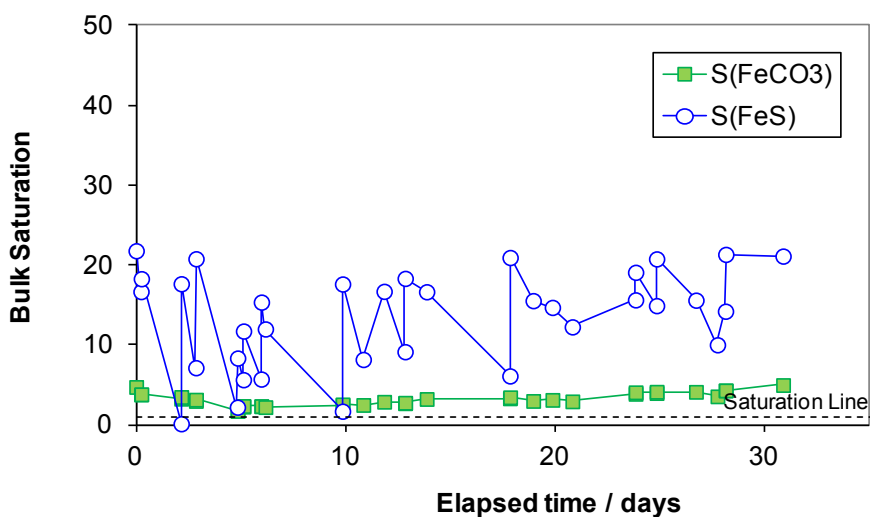


Figure 54. Experiment 5: Comparison of supersaturation values for iron carbonate (FeCO_3) and iron sulfide (FeS). (60°C , $P_{\text{total}} = 8 \text{ bar}$, $p_{\text{H}_2\text{S}} = 0.001 \text{ bar}$ [100ppm], 10wt% NaCl).

To maintain the low partial pressure of H_2S in this experiment, several additions of pure H_2S were added which can be inferred by the positive fluctuations in the value for $S(\text{FeS})$ in Figure 54. But the additional sodium chloride for Experiment 5 did not seem to have much effect on the general corrosion rate as compared to Experiment 3. LPR and

WL results, shown in Figure 55 for this experiment, are similar to LPR and WL results for single phase of Experiment 3, as shown in Figure 31.

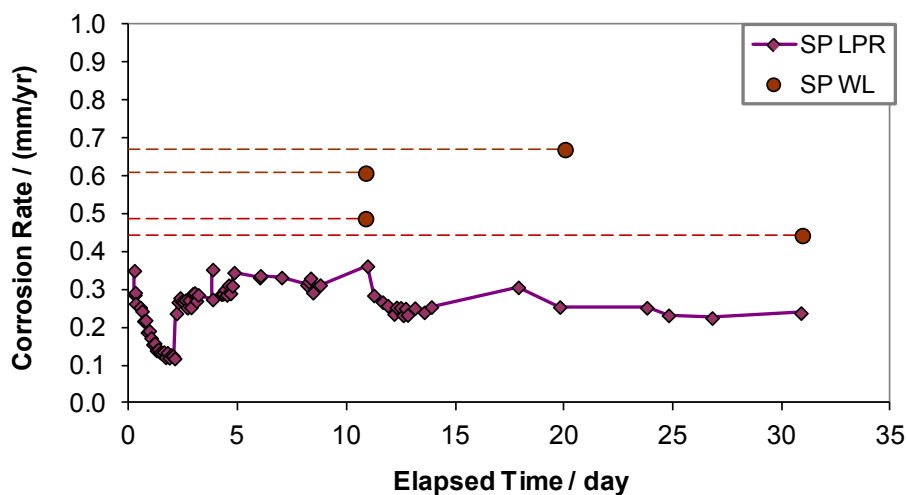


Figure 55. Experiment 5: Comparison of Corrosion rates measured by linear polarization (LPR) and weight loss (WL) coupons. SP – Single Phase (60°C, $P_{\text{total}} = 8$ bar, $p_{\text{H}_2\text{S}} = 0.001$ bar [100ppm], 10wt% NaCl).

The corrosion product layer for Experiment 5 also did not show any remarkable features during surface analysis. An SEM image of the surface layer developed under these conditions is shown in Figure 56. The large deposition of salt on the surface is thought to be from the sample removal process in which isopropyl alcohol is delicately flushed across the surface to remove water and the cracked surface layer is assumed to be from drying the sample in order to complete the surface analysis. The associated electron dispersion spectroscopy (EDS) indicates the surface layer is still dominated by iron sulfide even in the presence of a high chloride content solution.

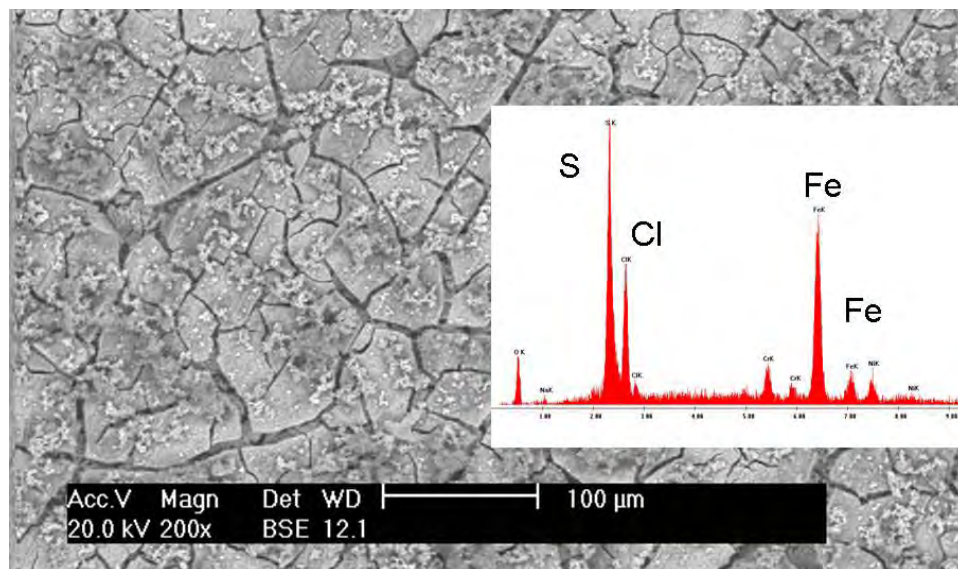


Figure 56. Experiment 5: Surface layer from influence of pH_2S and NaCl solution. (60°C , $P_{\text{total}} = 8$ bar, $\text{pH}_2\text{S} = 0.001$ bar [100ppm], 10wt% NaCl).

The difference observed between the corrosion that occurred in Experiment 3 and Experiment 5 can be seen in the cross sectional analysis, although most other corrosion product measurements were similar. Cross sectional analysis in Figure 57 shows a non-uniform type of corrosion on the surface of the coupon. These indications of corrosion initiation observed in cross sectional analysis are of the same magnitude as the general corrosion rate so, therefore, are not considered to be localized attack, but contain circular features not found in Experiment 3.

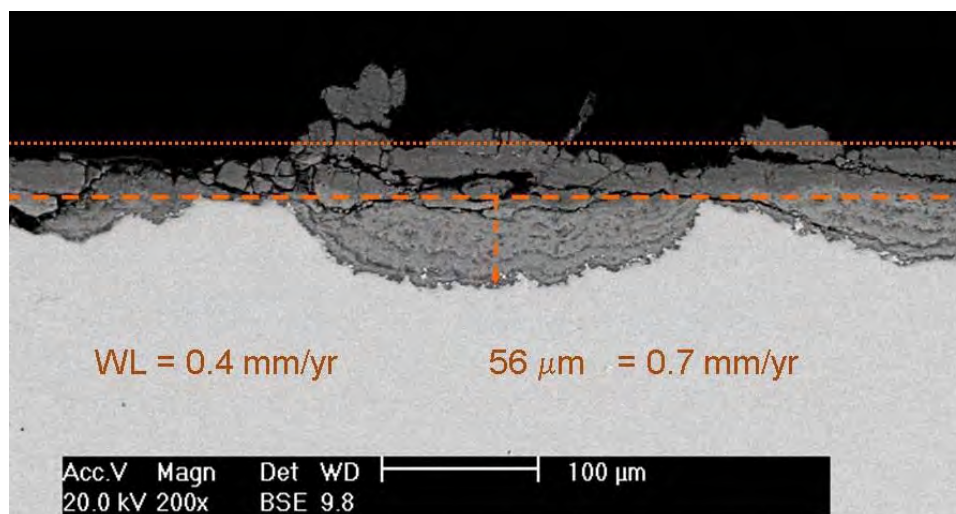


Figure 57. Experiment 5: Surface layer from influence of pH_2S and NaCl solution. (60°C , $P_{\text{total}} = 8$ bar, $\text{pH}_2\text{S} = 0.001$ bar [100ppm], 10wt% NaCl).

The SEM cross-sectional analysis in Figure 58 shows the type of corrosion is non-uniform across the sample surface with corrosion product developing in excess above the localized areas. The mass of the corrosion product on the surface of the samples was similar for 10 to 15 days of testing (0.0597g & 0.0560g)[Exp 5] vs. (0.0209g & 0.02556g)[Exp 3], but increased to 0.1649g after 20 days and 0.1977g after 30 days. A surface defect of the corrosion product layer, shown by SEM top surface image analysis in Figure 59, is an indication of where the non-uniform corrosion is beginning to occur. The defect, on a sample exposed to single phase flow for 31 days, has a cracked and uplifted surface layer with a location of failure in the corrosion product which may expose the surface below to the bulk solution conditions to locally increase the corrosion rate.

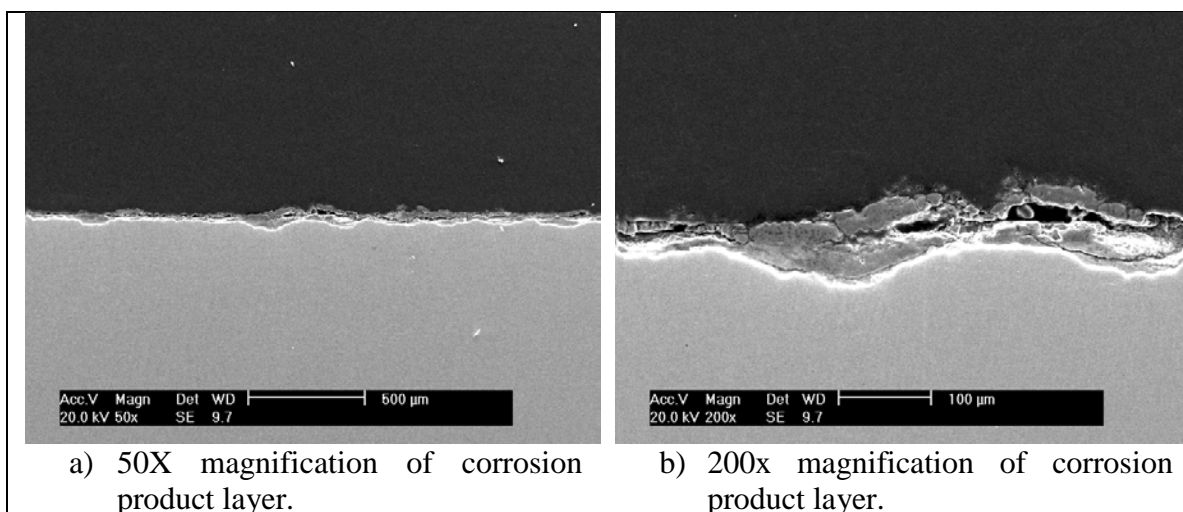


Figure 58. Surface features in cross sectional analysis of X65 sample from Single Phase flow after 31 day exposure to system conditions. (60°C , $P_{\text{total}} = 8$ bar, $\text{pH}_2\text{S} = 0.001$ bar [100ppm], 10wt% NaCl).

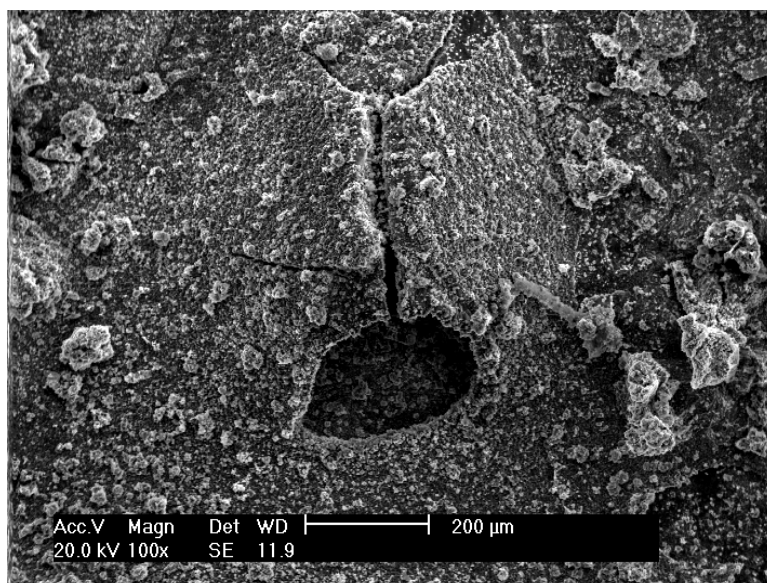


Figure 59. Surface features from SEM analysis of an X65 sample from Single Phase flow after 31 days exposure to system conditions. (60°C , $P_{\text{total}} = 8$ bar, $\text{pH}_2\text{S} = 0.001$ bar [100ppm], 10wt% NaCl).

A comparison of the corrosion rates observed in Experiment 3 (left side) and Experiment 5 (right side) is shown in Figure 60. The general corrosion rates for the two

experiments are considered to be similar, but a higher salt concentration in Experiment 5 shows an increased likelihood for localized corrosion. Weight loss samples from this experiment have measurable penetration rates and a maximum pitting ratio of 1.75, as defined by Equation (31), after 31 days is considered a “potential” location for localized corrosion.

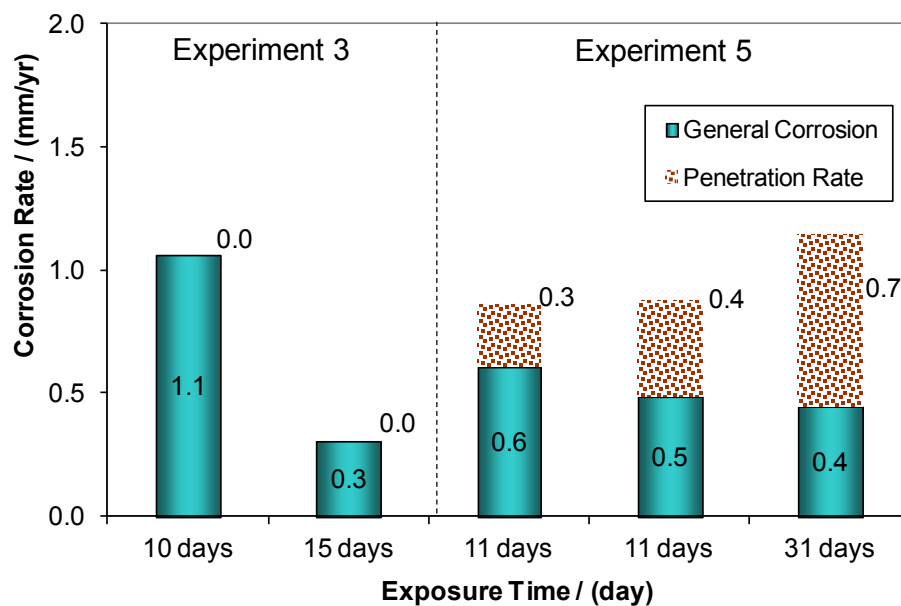


Figure 60. Bar chart comparison of WL general corrosion rate and IFM measured penetration rate for both sets of samples from Experiment 3 and Experiment 5. (60°C , $P_{\text{total}} = 8 \text{ bar}$, $p_{\text{H}_2\text{S}} = 0.001 \text{ bar}$ [100ppm], 10wt% NaCl).

Experiment 6: 60°C , $p_{\text{CO}_2} = 7.7 \text{ bar}$, $p_{\text{H}_2\text{S}} = 0.010 \text{ bar}$, $\text{pH } 6.0$, 10wt% NaCl

Introduction

For this experiment, the amount of sodium chloride is still 10 wt% in solution, but the average partial pressure of H_2S is increased to 0.010 bar (Table 13). The goal of this

experiment is to observe if an increase in the partial pressure of H₂S will increase the likelihood for localized corrosion in a system with 10 wt% NaCl.

Table 13. Controlled Parameters for High Sodium Chloride Test at 10 mbar pH₂S.

Parameter	Description
Equipment	H ₂ S Flow Loop
Test duration	30 days
Temperature	60.1 ± 1.0 °C
pCO ₂	7.7 ± 0.2 bar
pH ₂ S	0.010 ± 0.001 bar
pH	6.0 ± 0.2
Solution	10 wt% NaCl
Ionic strength	1.9 ± 0.07
[Fe ²⁺] (ppm)	2.5 ± 0.5
S(FeCO ₃)	7.7 ± 5.9
S(FeS)	32.8 ± 25.6
S(FeS)/S(FeCO ₃)	4.2 ± 0.1

[#](avg ± std deviation)

Results and Discussion

Environmental conditions were constant throughout the experiment with just a little increase in the ferrous ion concentration. The relationship of the partial pressures of CO₂ and H₂S are shown in Figure 61 and show less than a 10% change throughout the test period. Ferrous ion concentration and pH were fairly stable, Figure 62, with just a 3ppm increase in [Fe²⁺] and a 0.2 increase in pH. For this experiment, the calculated iron carbonate saturation value was between 1 and 3 while the iron sulfide saturation value was calculated to be between 3 and 5.

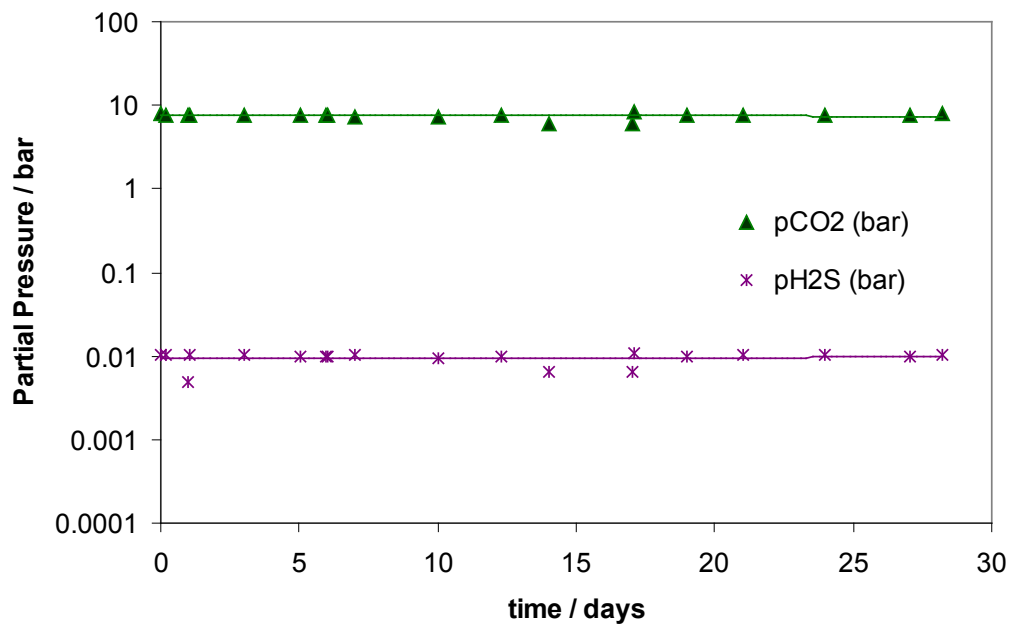


Figure 61. Experiment 6: partial pressures of CO₂ and H₂S vs. time.

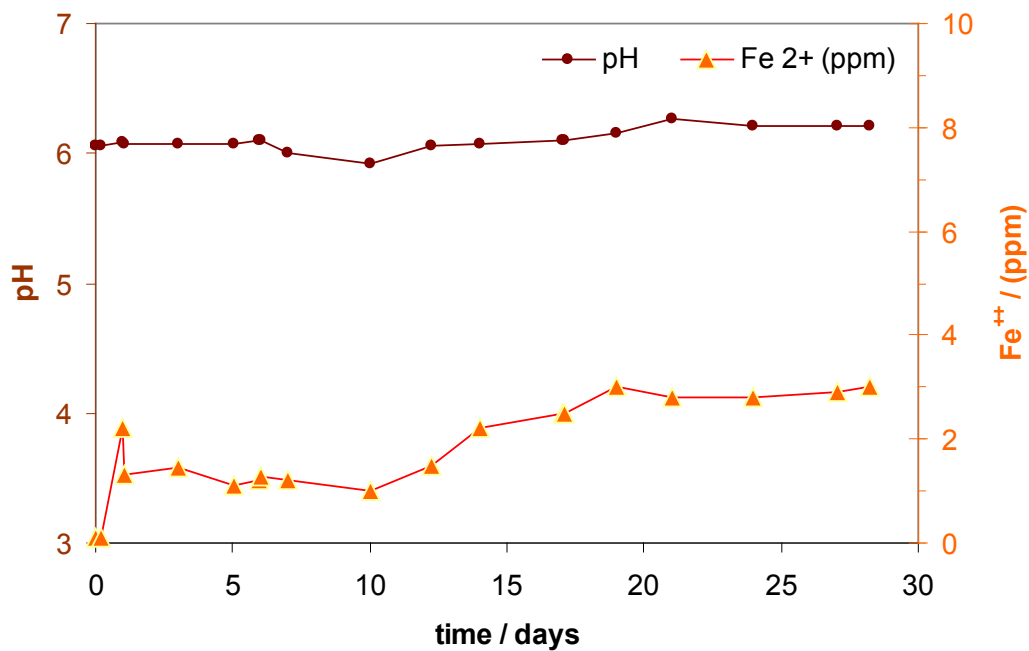


Figure 62. Experiment 6: pH and [Fe²⁺] vs. time

The effect of the increase in sodium chloride concentration is seen with the first WL sample removed. After 10 days exposure time in multiphase flow, the weight loss sample in Figure 63 shows localized corrosion through a comparison with and without the corrosion product layer as taken by profilometer measurements. With the corrosion product layer in place (top image), a location in the upper left quadrant of the coupon was selected for depth analysis. The variation of the layer surface is rather extreme as compared to all other coupons with a 1.7 mm peak of “debris” located on the coupon surface. With the corrosion product layer removed by Clarke solution⁴⁹ (bottom image), the upper left quadrant of the coupon again shows where the most surface corrosion activity occurred.

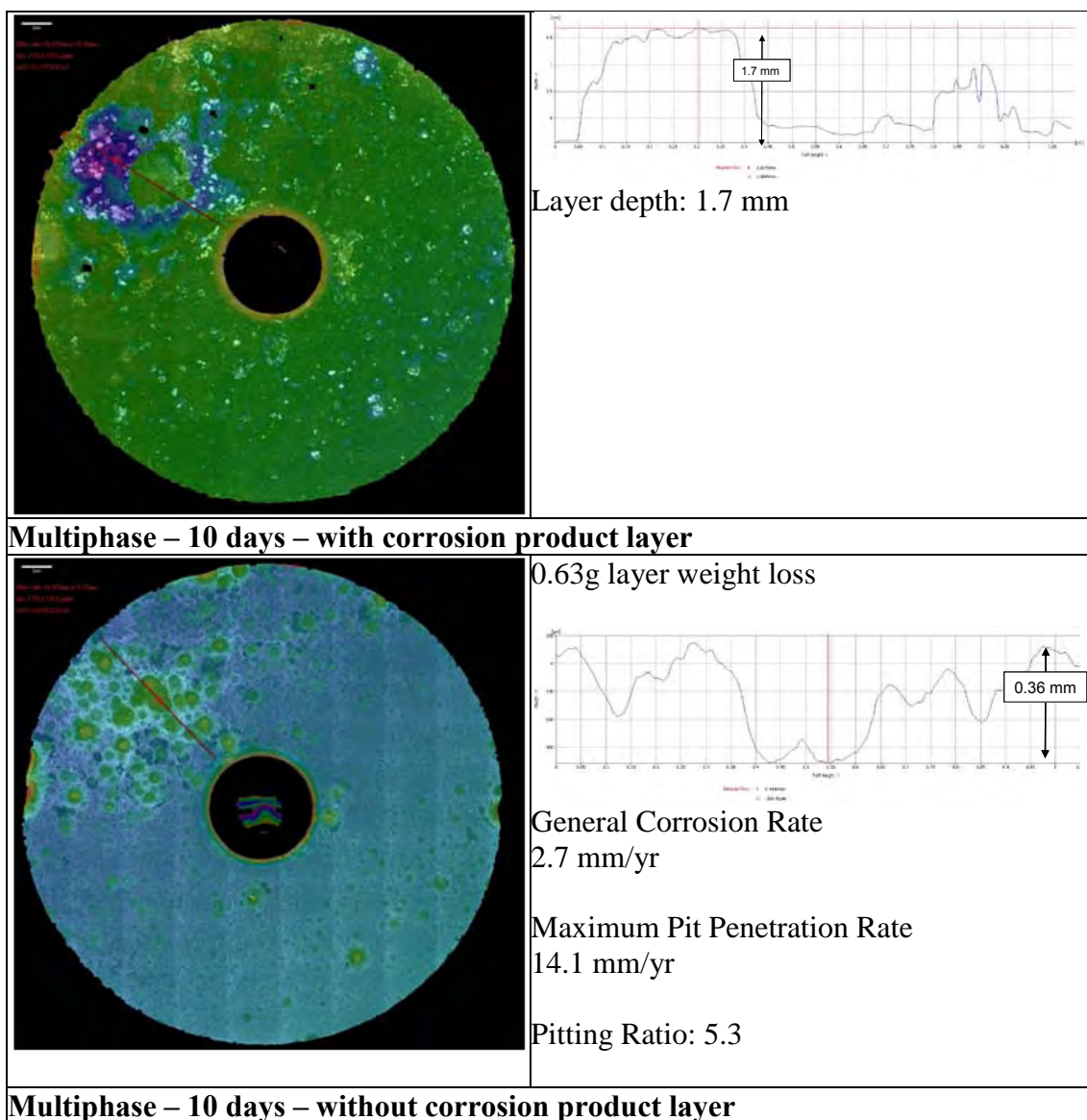


Figure 63. Experiment 6: Multiphase, 10 days, 60°C, pCO₂ = 7.7 bar, pH 6.0, 10 mbar H₂S, 10 wt% NaCl

After removal of the corrosion product layers, the general corrosion rate was calculated at 2.7 mm/yr and, through profilometer analysis, the maximum depth of attack was measured to be 0.36 mm or 14.1 mm/yr by calculation. This is considered to be

localized corrosion since the pitting ratio is greater than 5 (pitting ratio = 5.3) as defined by Equation (31).

After 30 days exposure, similar results to those seen after 10 days can be observed on a WL sample from single phase flow. Figure 64 and Figure 65 show the corrosion product topography and the resultant localized corrosion. Figure 64 provides 3 dimensional images of the corrosion product layer and the surface of the coupon after layer removal. By comparison of the morphology of the corrosion product layer to the morphology of the corroded surface, it is obvious that the areas of more metal loss occur under the peaks of corrosion product layer.

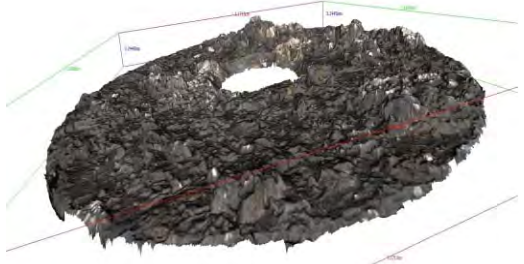
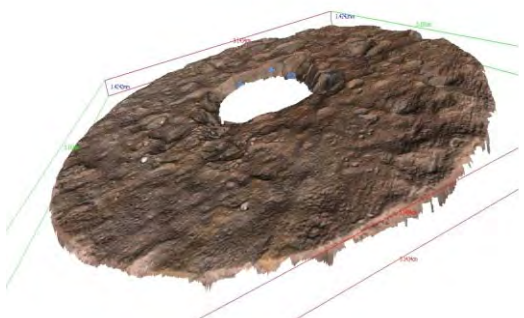
Relationship of Corrosion Product Layer to the Corroded Surface	
	<p>(a) Image of corrosion product layer developed during 30 day exposure in single phase flow.</p>
	<p>(b) Image of coupon surface after corrosion product layer removal by Clark solution.</p> <p>Notice areas of more metal loss occur UNDER peaks of corrosion product layer [Image (a)].</p>

Figure 64. Experiment 6: IFM surface imaging of X65 coupon exposed for 30 days in single phase flow for conditions: 60°C, $p\text{CO}_2 = 7.7$ bar, pH 6.0, 1.0 mbar H_2S , 10 wt% NaCl.

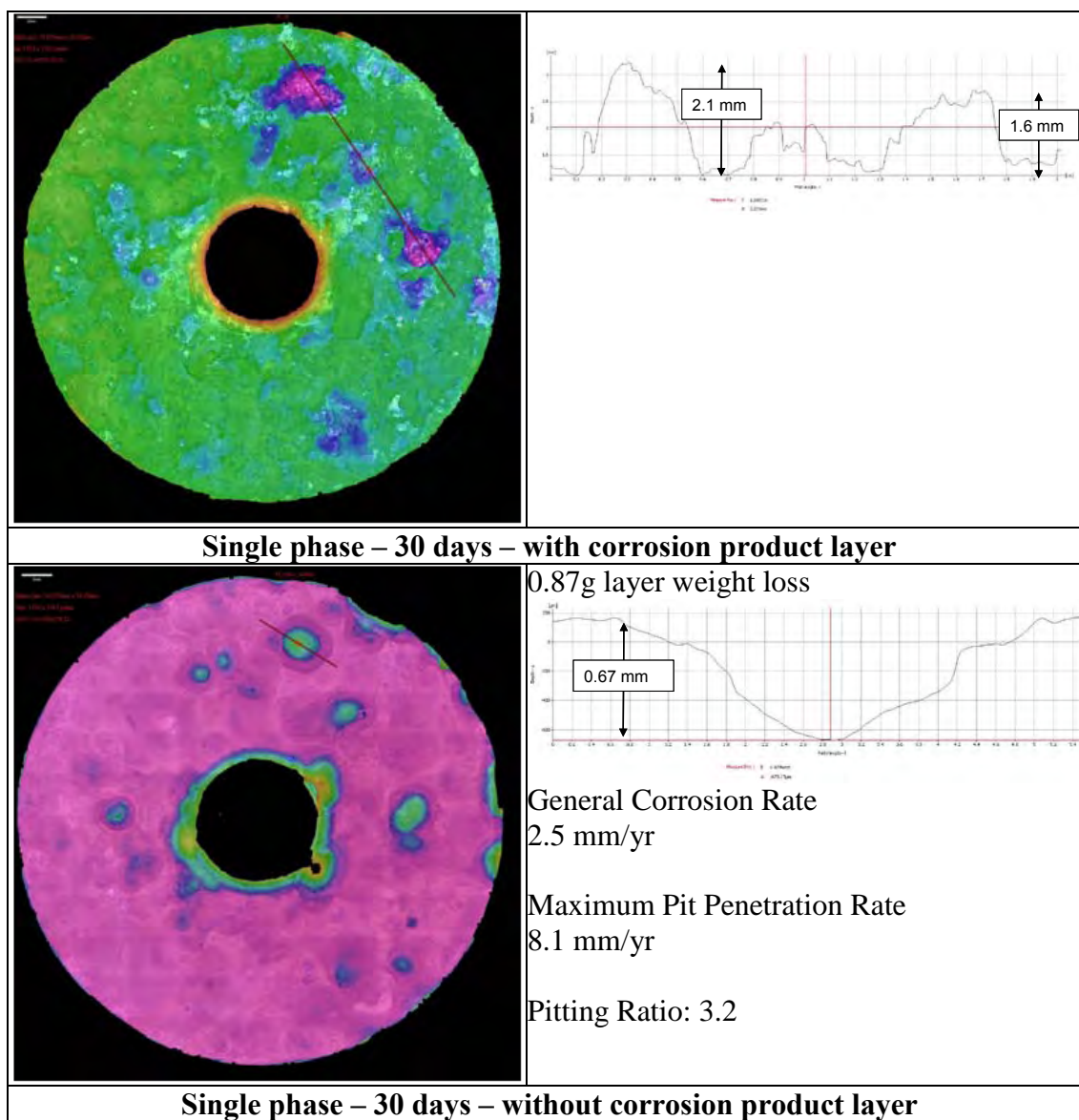


Figure 65. Experiment 6: IFM surface imaging of X65 coupon exposed for 30 days in single phase flow for conditions: 60°C, $p\text{CO}_2 = 7.7$ bar, pH 6.0, 1.0 mbar H_2S , 10 wt% NaCl

Figure 65 shows the view of the WL sample from a vertical perspective with orientation of the layer to the substrate maintained between the two images. Notice that the two large peaks of surface layer deposition are positioned over the locations where

pitting occurred, shown after layer removal. The corrosion product layer, with peaks up to 2.1 mm in height, was 0.87 grams in weight as removed by Clarke solution cleaning procedures. This is 1.5 times larger than the amount removed from the multiphase coupon. A location of 0.67 mm in depth and about 4 mm in diameter was found to have the maximum pit penetration rate of 8.1 mm/yr which equates to a pitting factor of 3.2 in this case since the general WL corrosion rate was calculated as 2.5 mm/yr.

Cross sectional analysis, Figure 66, of a similar sample from single phase flow after 20 day exposure to system conditions shows growth of the corrosion product to approximately 800 μm above the metal surface in relation to material losses of approximately 200 μm below the metal surface. This image provides confirmation of the growth to the corrosion product in relation to the areas of local metal loss. The penetration rate is approximately 4 mm/yr as calculated from this cross section analysis.

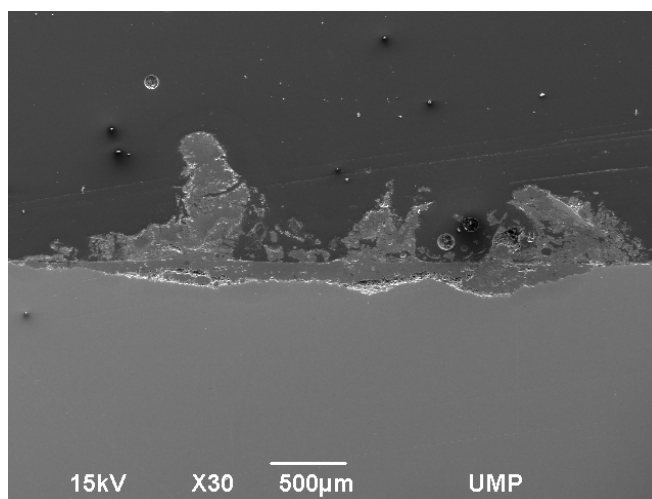


Figure 66. SEM cross sectional analysis of X65 coupon exposed for 20 days in single phase flow for conditions: 60°C, $p\text{CO}_2 = 7.7$ bar, pH 6.0, 1.0 mbar H_2S , 10 wt% NaCl

An overall view of the corrosion rates, both general and maximum localized, are presented in the bar graph of Figure 67. The instances of localized corrosion are shown as larger bars for the two coupons exposed for 10 days and two of the coupons exposed for 30 days as detailed in this section. All samples exposed during the 20 day exposure were inserted into the system after the 10 day samples were removed. Although these samples show a general corrosion rate with some indications of localized events, the depth of the pitting observed was not enough to categorize these as having “localized attack.”

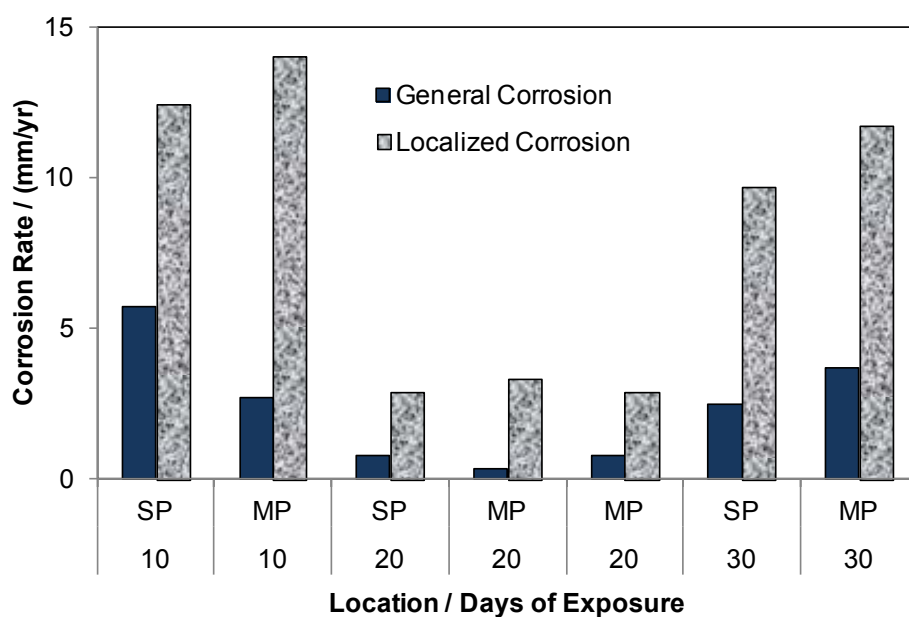


Figure 67. Corrosion rate vs location (SP – single phase, MP – multiphase), 60°C, pCO₂ = 7.7 bar, pH 6.0, 10.0 mbar H₂S, 10 wt% NaCl

Conclusions Related to Ionic Strength

The higher salt concentration in an H₂S/CO₂ corrosion experiment on mild steel was expected to have a direct effect on both the general and localized corrosion observed. This additional sodium chloride in Experiment 6 would be expected to increase the conductivity and ionic strength of the solution while it also reduced the saturation value for iron carbonate as compared to Experiment 5. These changes had a direct effect on the observation of localized corrosion and on the corrosion product layer developed.

Localized Corrosion

Comparison of Experiment 5 to Experiment 3 shows an increased likelihood for localized corrosion with a higher sodium chloride content (or higher ionic strength); the comparison of Experiment 6 to Experiment 5 shows that the likelihood for localized corrosion is increased with a ten-fold increase in the partial pressure of H₂S. It is assumed that the increased sodium chloride concentration acted to lower the general corrosion rate as previously seen in CO₂ corrosion, but the iron sulfide corrosion product layer has the propensity for local failures which become initiators for localized corrosion. A higher salt concentration led to localized corrosion in the presence of H₂S.

Corrosion Product Layer

Review of the corrosion product layers developed in the first 6 experiments show evidence that the mechanism related to localized corrosion under these conditions is

related to a failure of the corrosion product layer and not to the orientation or location of the weight loss samples in the pipeline. The multiphase flow coupons are flush mounted at the 6 o'clock position which is assumed to experience the most impact from slug flow turbulence and should minimize the corrosion product layer, but it did not seem to have that effect in these studies in a pH 6 solution. Maybe the 6 o'clock location could be the cause of the excess corrosion product layer by allowing solids that have precipitated in the section of pipe upstream of the corrosion coupon to travel along the bottom and find a resting place on the corroding surface of the coupon. If this were true, then the single phase weight loss samples should show much less corrosion product layer because the single phase samples are flush mounted at the 1 o'clock position in the pipeline and would not be favorable to deposition of precipitated solids migrating through the pipeline which may deposit through gravitational means. The single phase samples can be placed in the 1 o'clock position since the effect of flow in single phase is uniformly distributed 360 degrees around the pipeline ID. By comparison of the corrosion product layers shown in Figure 63, Figure 64, and Figure 65, this is proof that the excess corrosion product layer developed in both single phase and multiphase was caused by reaction of the species within the bulk fluid to the X65 material during the first 10 days of the experiment. It also shows that system bulk fluid conditions during the last 20 days of the experiment were stable and did not warrant removal of the already developed corrosion product layer.

This is evidence that the localized corrosion mechanism under these conditions is probably a failure of the corrosion product layer which allows corrosive species direct access to react with the metal surface. Localized corrosion in the presence of hydrogen sulfide is then shown by the increased amount of corrosion product layer on local areas of the sample surface in a pH 6 solution.

Effect of a Decrease in Solution pH

Introduction

The iron sulfide saturation value, $S(\text{FeS})$, calculated³⁵ at each test condition should give an indication of how the bulk conditions affect the developing iron sulfide corrosion product layer. By decreasing the pH of the solution, the saturation values of iron sulfide and iron carbonate will also decrease, directly affecting the corrosion product layer and providing the opportunity to observe different mechanisms of corrosion in an $\text{H}_2\text{S}/\text{CO}_2$ system. By decreasing the saturation values, it is assumed that the driving force for precipitation which could cause the formation of thick corrosion product layers will also be decreased. The next two experiments reviewed in this section are related to Experiment 6 by a decrease in pH as shown in the parameter comparison, Table 14.

Table 14. Experiments 9 & 12: change in pH

Parameter	Exp. 9	Exp. 12
Temperature	60°C	60°C
Total Pressure	8 bar	8 bar
pCO ₂	7.7 bar	7.7 bar
Flow	Vsl = 1 m/s, Vsg = 3 m/s	Vsl = 1 m/s, Vsg = 3 m/s
NaCl solution	10 wt%	10 wt%
pH	5.0	4.0
pH ₂ S (mBar)	10	10
Measurements	WL, SEM	WL, SEM
Exposure Time	7, 15, 21 days	7, 14, 21 days

Experimental Observations

Experiment 9: 60°C, pCO₂ = 7.7 bar, pH₂S = 0.010 bar, pH 5.0, 10wt% NaCl

Introduction

From the last experiment at pH 6 under similar conditions, the localized corrosion was found where an increased amount of corrosion product layer developed on local areas of the sample surface. The initiation of localized corrosion was thought to be caused by a failure of the corrosion product layer which allowed corrosive species direct access to the metal surface. With a decrease in experimental conditions from pH 6 to pH 5, the corrosion product should not be able to develop as quickly and more general corrosion should occur.

Results and Discussion

These test conditions caused the highest general corrosion rate measured and the largest pitting rate measured for the entire series of tests. The parameters of this test are shown as Experiment 9 in the current test matrix, Table 15. Note that iron carbonate was just above its saturation level while iron sulfide is considered to be well saturated in solution. The dominant corrosion product is expected to be iron sulfide since the $S(\text{FeS})/S(\text{FeCO}_3)$ ratio is much greater than 1.

Table 15. Controlled Parameters for Effect of Corrosion Product Layer test at 10 mbar pH_2S and 10 wt% NaCl.

Parameter	Description
Equipment	H_2S Flow Loop
Test duration	22 days
Temperature	60.1 ± 0.2 °C
pCO_2	7.7 ± 0.1 bar
pH_2S	0.0085 ± 0.0021 bar
pH	5.0 ± 0.0
Solution	10 wt% NaCl
Ionic strength	1.72 ± 0.00
$[\text{Fe}^{++}]$ (ppm)	127 ± 28
$S(\text{FeCO}_3)$	2 ± 0.5
$S(\text{FeS})$	25 ± 5
$S(\text{FeS})/S(\text{FeCO}_3)$	33 ± 8

[#](avg \pm std deviation)

The $\text{CO}_2/\text{H}_2\text{S}$ partial pressure ratio was in the range from 800 to 1000 during the 21 day exposure as inferred by Figure 68. Weight loss measurements are shown in Figure 69 for the samples removed from the single phase flow test section and Figure 70 for the samples removed from multiphase flow test sections. Both samples with 21 day exposure

in multiphase flow were subjected to cross sectional analysis and all other samples had the weight loss procedure and analysis referred to in Chapter 3. The calculated values for pitting ratio (Figure 71) show a higher general corrosion rate reduced the likelihood of localized corrosion in this case.

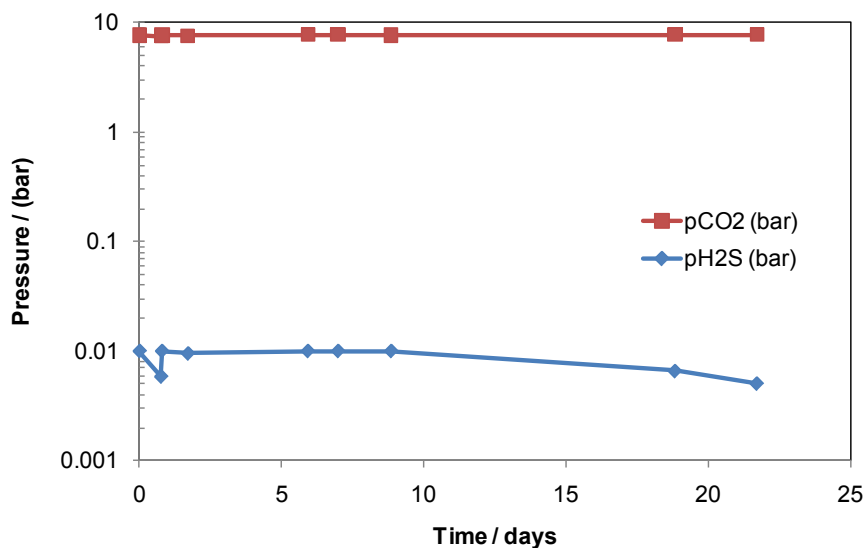


Figure 68. Partial pressure measurements of CO₂ and H₂S during the experiment of 60°C, pH 5, pCO₂ = 7.7 bar, pH₂S = 10 mbar, 10 wt% NaCl

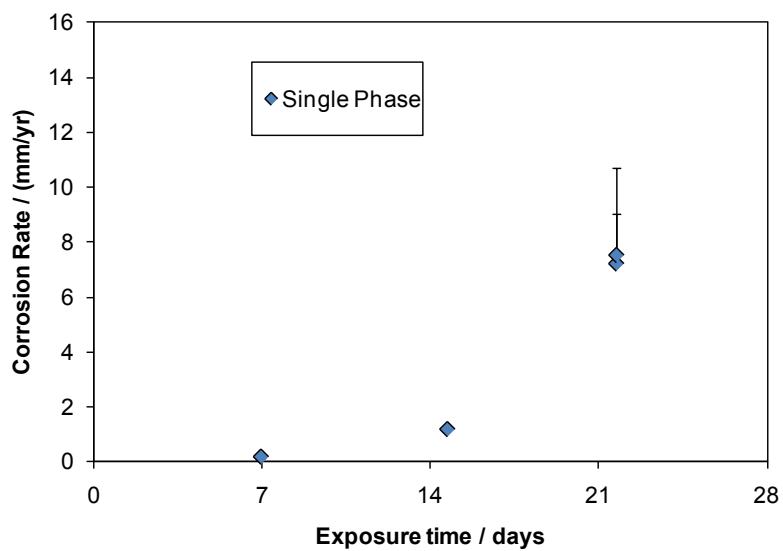


Figure 69. Single phase weight loss corrosion rate and penetration rate for samples in 60°C, pH 5, $p\text{CO}_2 = 7.7$ bar, $p\text{H}_2\text{S} = 10$ mbar, 10 wt% NaCl

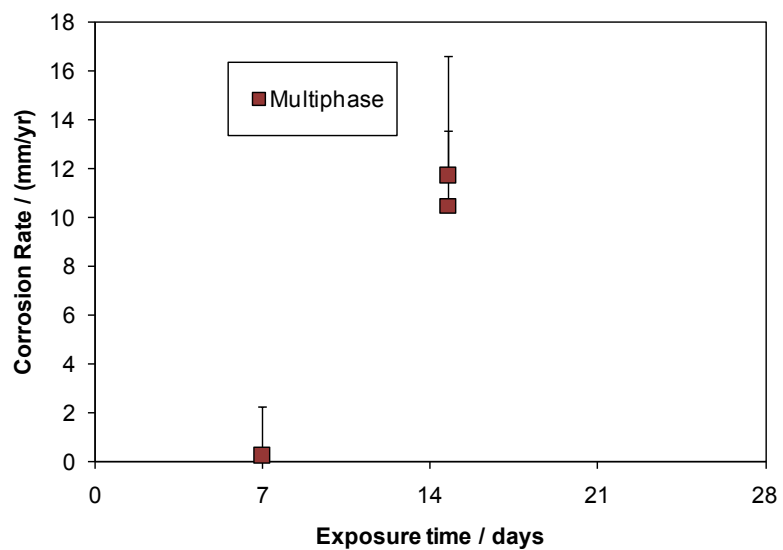


Figure 70. Multiphase weight loss corrosion rate and penetration rate for samples in 60°C, pH 5, $p\text{CO}_2 = 7.7$ bar, $p\text{H}_2\text{S} = 10$ mbar, 10 wt% NaCl

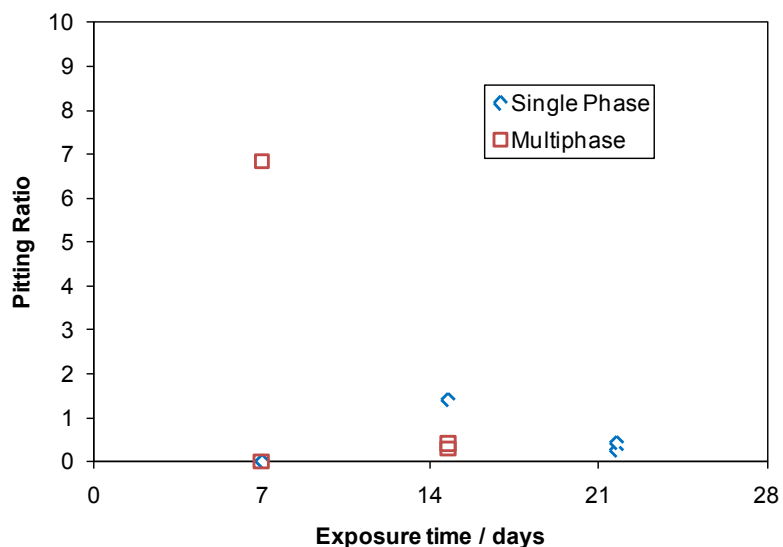
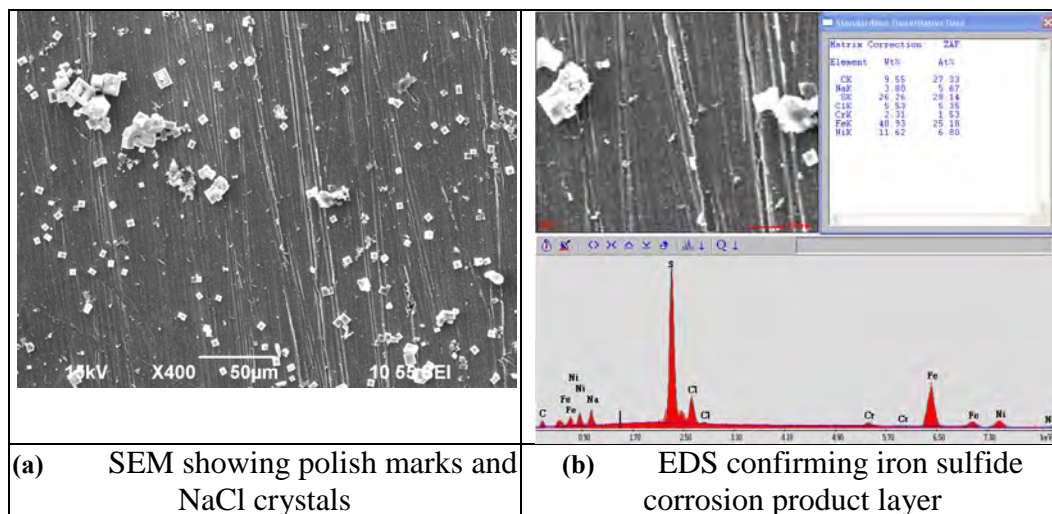


Figure 71. Exp 9. Pitting ratio for single phase and multiphase weight loss coupons in 60°C, pH 5, $p\text{CO}_2 = 7.7$ bar, $p\text{H}_2\text{S} = 10$ mbar, 10 wt% NaCl

Characterization of the Corrosion Product Layer

The higher general corrosion rate lowered the likelihood of a high ratio of penetration rate to general corrosion rate. The only sample that met the pitting ratio criteria for localized corrosion was in multiphase flow at 7 days (0.3 mm/yr general corrosion + 2.0 mm/yr penetration rate).

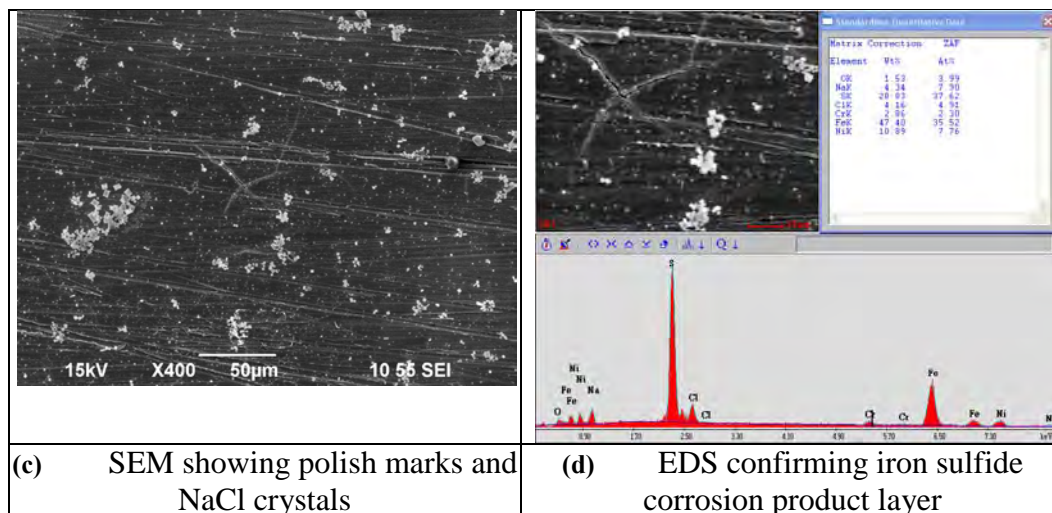
The general surface of the multiphase sample after the 7 day exposure shows the polish marks of the original surface features shown in both Figure 72 and Figure 73. This is thought to confirm the mechanism of the initial reaction of H_2S or HS^- with the metal surface, conferring complete surface coverage with FeS and rapidly decreasing the general corrosion rate. If a failure of this coverage layer occurs, localized corrosion is initiated and may continue. In this case, there was a singular event of this type found on the sample surface.



(a) SEM showing polish marks and NaCl crystals

(b) EDS confirming iron sulfide corrosion product layer

Figure 72. Exp 9. Multiphase weight loss sample taken from 60°C, pH 5, $p\text{CO}_2 = 7.7$ bar, $p\text{H}_2\text{S} = 10$ mbar, 10 wt% NaCl after 7 days' exposure.



(c) SEM showing polish marks and NaCl crystals

(d) EDS confirming iron sulfide corrosion product layer

Figure 73. Exp 9. Multiphase weight loss sample taken from 60°C, pH 5, $p\text{CO}_2 = 7.7$ bar, $p\text{H}_2\text{S} = 10$ mbar, 10 wt% NaCl after 7 days' exposure.

Some areas of corrosion initiation were observed on both single phase and multiphase WL samples after 21 days, but only the multiphase WL samples show corrosion initiation at 14 days exposure. Only one corrosion location found on a

multiphase WL sample exposed for 7 days shows a high pitting ratio because the overall general corrosion rate was high (10-12 mm/yr). The single pit location found on the WL sample after 7 days is shown by IFM measurement in Figure 74. The 38 μm depth calculates to be a 6.8 mm/yr penetration rate after 7 days.

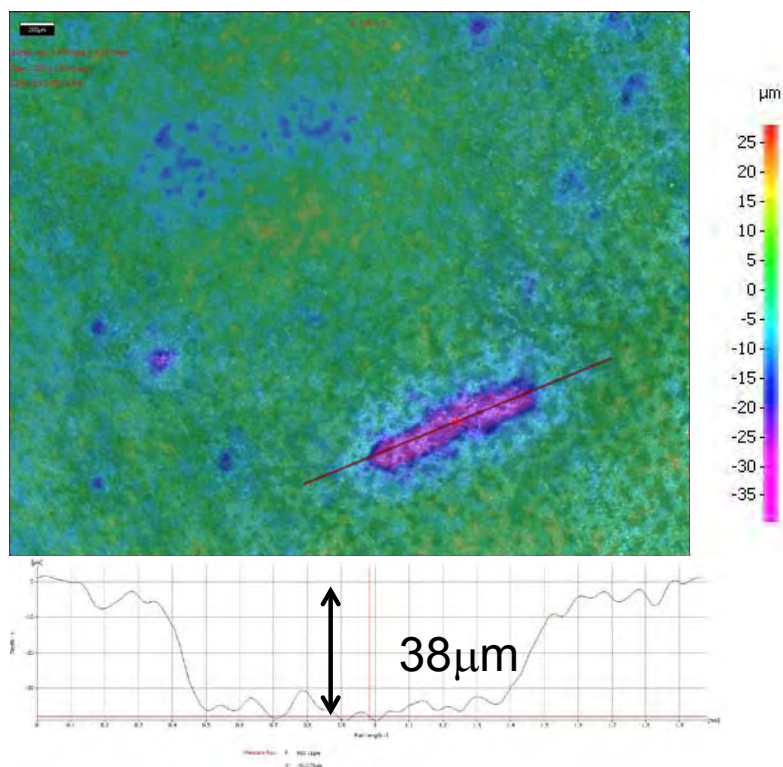


Figure 74. Exp 9. IFM analysis from multiphase flow sample showing the single localized corrosion location. Multiphase weight loss sample taken from 60°C, pH 5, $\text{pCO}_2 = 7.7$ bar, $\text{pH}_2\text{S} = 10$ mbar, 10 wt% NaCl after 7 days' exposure.

The corrosion product layer on the WL sample exposed for 15 days shows large cracks in the surface layer in Figure 75, which could be due to the removal and drying process in analyzing the sample, but has implications as to the characteristics of the

corrosion product, particularly with regard to adherence. The corrosion product weight for the two samples removed under these conditions was $0.20 \pm 0.02\text{g}$. With a general corrosion weight loss of $11.1 \pm 0.6 \text{ mm/yr}$, these samples have the highest general corrosion rate of the test series. IFM measurement (Figure 76) of a high penetration rate location shows a $121.5 \mu\text{m}$ depth which calculates to be a 3 mm/yr penetration rate.

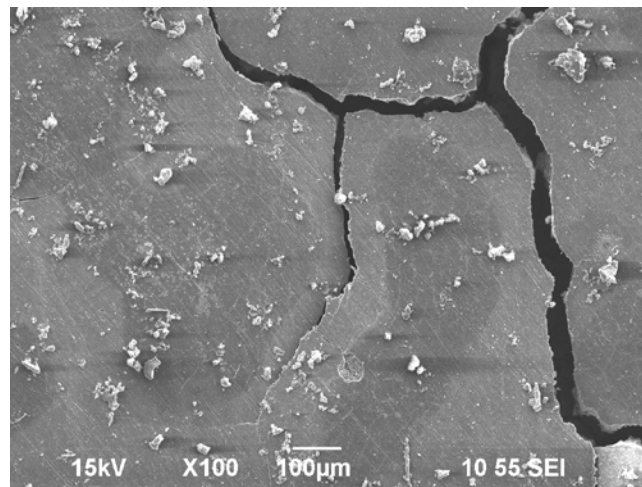


Figure 75. Exp 9. Multiphase WL sample, 15 days, with layer. Multiphase weight loss sample taken from 60°C , $\text{pH } 5$, $\text{pCO}_2 = 7.7 \text{ bar}$, $\text{pH}_2\text{S} = 10 \text{ mbar}$, 10 wt\% NaCl .

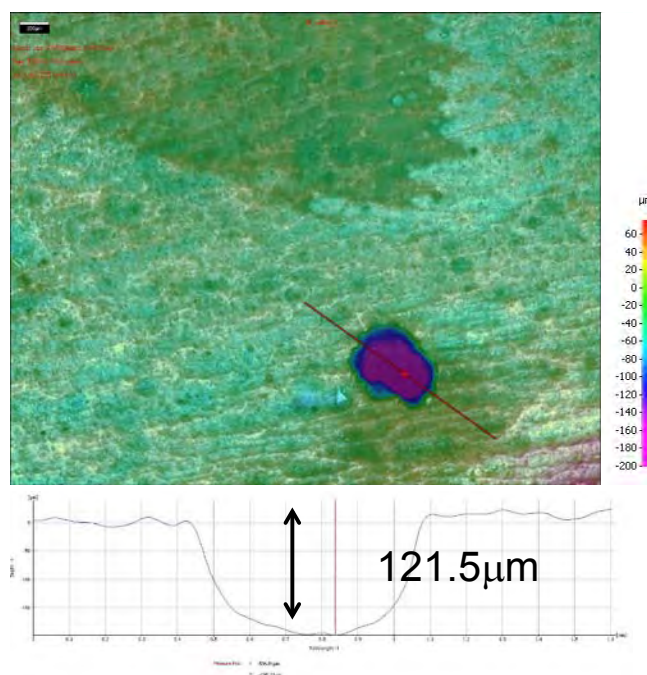


Figure 76. Exp 9. IFM of multiphase WL sample, 15 days, without layer. Multiphase weight loss sample taken from 60°C, pH 5, pCO₂ = 7.7 bar, pH₂S = 10 mbar, 10 wt% NaCl.

Failures of the Corrosion Product Layer

Two WL samples that were exposed to these conditions for the entire 22 day test were both analyzed by cross section and show high corrosion rates as well, but have remarkably different results. Figure 77, Figure 78, and Figure 79 refer to the first WL sample. The surface of this sample, Figure 77, still exhibits the original polish marks on the surface, yet it can be seen that corrosion product layer has depth, as indicated by the broken edge of the corrosion product layer shown in the SEM image that even seems to be detached from the lower layer. EDS analysis confirms a high sulfide content of the layer.

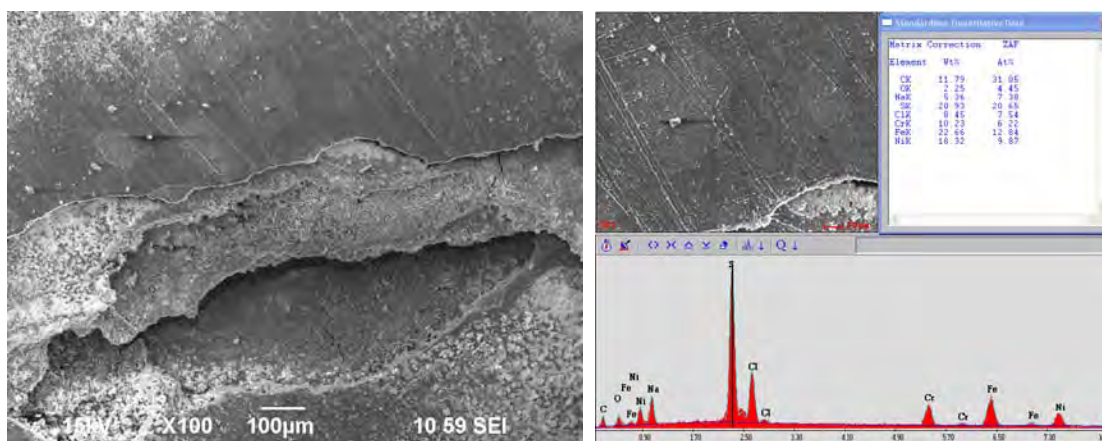


Figure 77. Exp 9. SEM and EDS of sample taken from multiphase flow after 22 days. Multiphase weight loss sample taken from 60°C, pH 5, $p\text{CO}_2 = 7.7$ bar, $p\text{H}_2\text{S} = 10$ mbar, 10 wt% NaCl.

This sample has a 0.5" (1.3 cm) area of localized corrosion that was too large to view in a single SEM image, so the image of the entire gold-coated cross sectional sample was captured by the IFM for Figure 78. Note the three localized areas of attack on the sample surface. The one to the farthest right still contains the corrosion product layer analyzed and has a measured depth of 1.8 mm for a 30 mm/yr penetration rate. This sample had a weight loss of 0.78 grams (including the corrosion product) for a general corrosion rate of 2.2 mm/yr. It can be assumed that the entire weight loss of this sample was related to localized corrosion. An attempt to image the main pit by SEM is shown as a collection of SEM images and two EDS analyses in Figure 79. From these SEM images, the corrosion product in the pit shows a porous structure with layers that do not seem to be well attached to the adjacent layer below. A lifted section of the corrosion product can be observed on the upper right of Figure 79 which can be an indication of the mechanism of layer removal that would have occurred in the turbulent multiphase flow.

Another interesting feature of the corrosion product layer that can be speculated to relate to the low general corrosion rate of the sample is the thin layer of corrosion product (iron sulfide) covering the flat portion of the upper left of the SEM in Figure 79, thought to represent the original metal surface, and covering the 4.5 mm wide pit in the left half of the image. This pit may have started at the same time as the one taking up the right half of the image, but through some mechanism lost its partial layer coverage and when subjected to the bulk conditions it developed the thin layer of corrosion product that provides some limitation to the corrosion reaction and the pit propagation stopped. This may be a case where one of two adjacent pits becomes dominant.

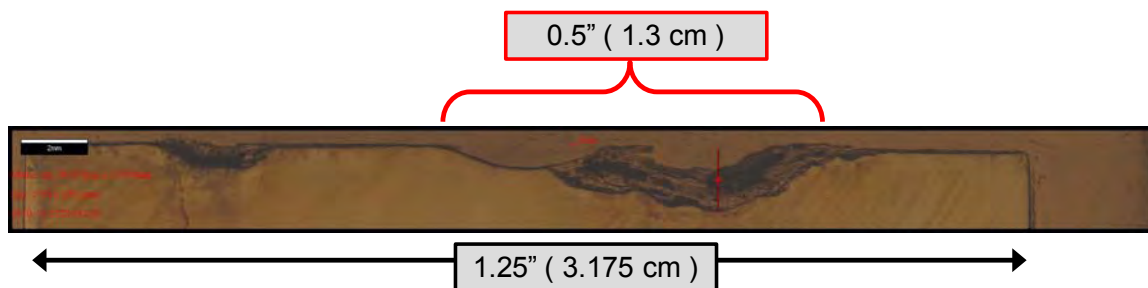


Figure 78. Exp 9. IFM image of the whole cross-section of the multiphase sample taken at 22 days. Multiphase weight loss sample taken from 60°C, pH 5, $p\text{CO}_2 = 7.7$ bar, $p\text{H}_2\text{S} = 10$ mbar, 10 wt% NaCl.

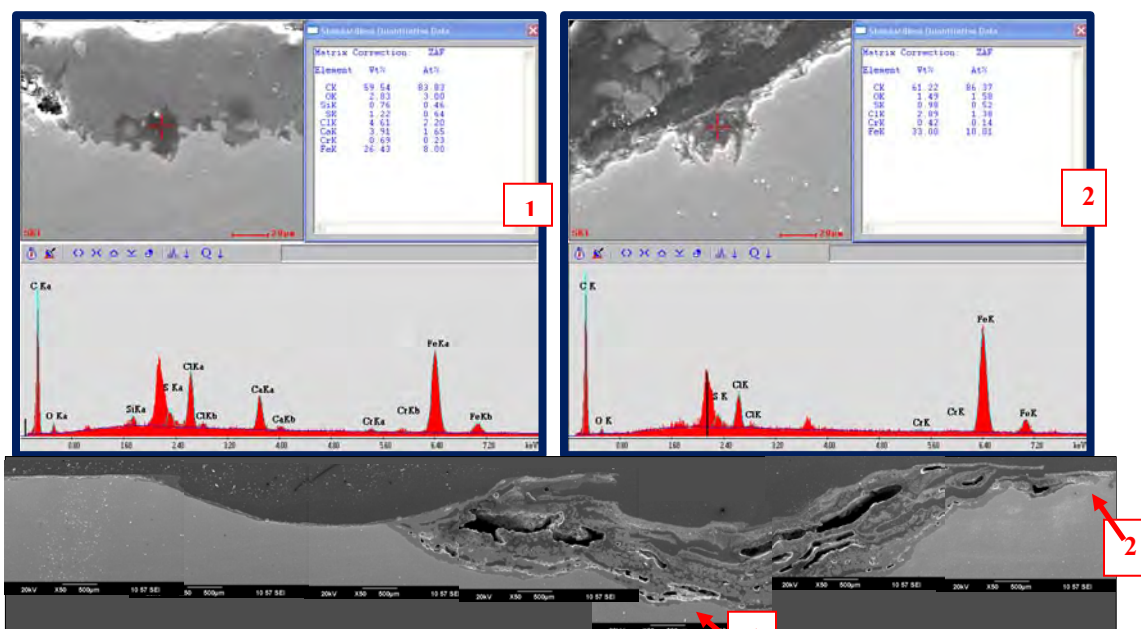


Figure 79. Exp 9. SEM composite image of Multiphase weight loss sample taken from 60°C, pH 5, $p\text{CO}_2 = 7.7$ bar, $p\text{H}_2\text{S} = 10$ mbar, 10 wt% NaCl. Arrow locations 1 & 2 were analyzed by EDS. Both locations show a higher chloride content than was observed elsewhere on the same sample.

The EDS spot analysis shown in Figure 79, taken at locations 1 & 2 in the overall image, shows two locations where chloride levels were measurable in the corrosion product at the metal surface. The EDS image on the right side was the first to be discovered as it is visually indicative of a location corroding more within the pit or a propagation point within the pit. The only difference in the EDS analysis at this location was the chloride peak which prompted further EDS spot checks along the bottom of the pit. Only these two locations show a peak for chlorides in the analysis, which leads to speculation on the species involved in the localized corrosion mechanism observed here. Chlorides are thought to be involved in the pit propagation process, but measured observations of this phenomenon in cross sectional analysis are usually discounted

because of possible contamination that could occur during the cross sectional sample preparation procedure. If contamination was a possibility in this current observation, it would presumably be more widespread than at just two locations, leading one to believe these two locations may be proof of the mechanism related to chloride initiated attack within the pit.

Figure 80 and Figure 81 refer to the second WL sample taken from multiphase flow after 22 days. Mass loss of this sample (3.27 g, including the corrosion product layer) equates to a 9.4 mm/yr general corrosion rate. Even with this amount of mass loss, the corrosion product layer shows the polish marks of the original surface (Figure 80). EDS confirms a high sulfide peak as expected. The cross section SEM image of this WL sample is shown in Figure 81. Note the open area between the corrosion product layer and the substrate (filled with epoxy). This was continuous across the surface of this sample and, assuming uniform loss of material, the depth of general corrosion would be 530 μm which is visually shown as being the same as the undermined material loss in Figure 81. Although this sample did not show localized corrosion, the weight loss that occurred could be equated to the amount of substrate material lost, so the hypothesis of an adherent layer that initially developed is still valid with continued loss of material under the layer (undermining) causing the massive weight loss.

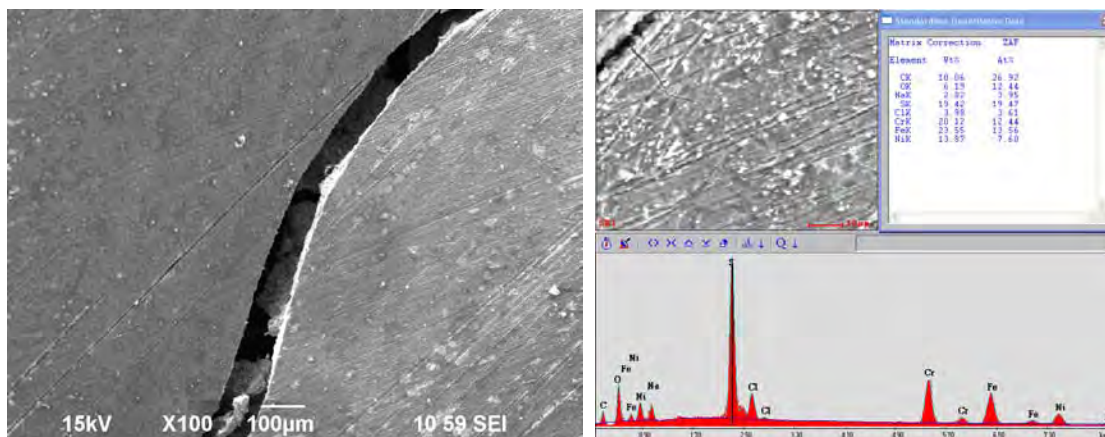


Figure 80. Exp 9. Sample surface after removal from H₂S system after 22 days exposure in multiphase flow. 60°C, pH 5, pCO₂ = 7.7 bar, pH₂S = 10 mbar, 10 wt% NaCl.

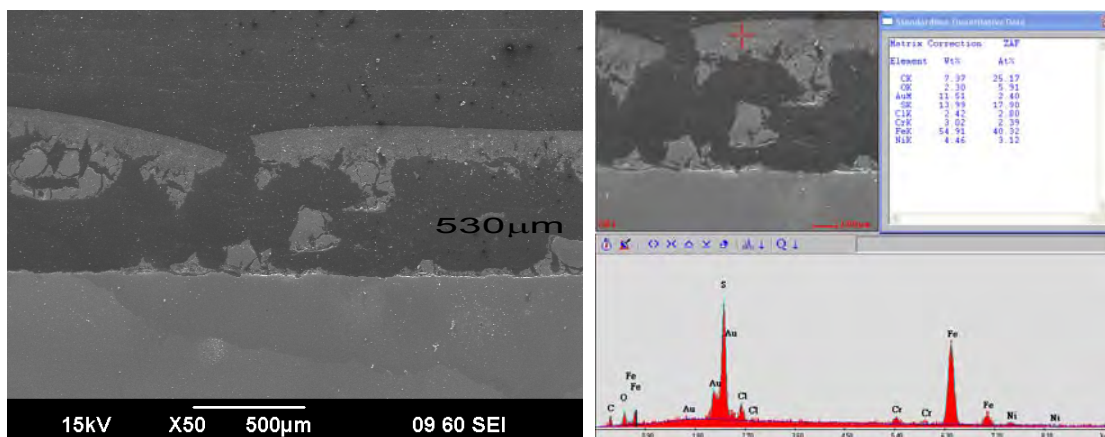


Figure 81. Exp 9. Cross section of multiphase sample taken after 22 days exposure. 60°C, pH 5, pCO₂ = 7.7 bar, pH₂S = 10 mbar, 10 wt% NaCl. (Sample mass loss = 3.27g, Corrosion rate calculation = 9.4 mm/yr. Uniform corrosion loss of substrate would be 530μm.)

Experiment 12: 60°C, pCO₂ = 7.7 bar, pH₂S = 0.010 bar, pH 4.0, 10wt% NaCl

Introduction

In order to finish the series of tests related to pH change in a 60°C, 7.7 bar pCO₂, 10 mbar pH₂S, 10 wt% NaCl solution, a test at pH 4.0 was necessary. The previous experiments at pH 6 (Experiment 6) and pH 5 (Experiment 9) have both shown localized

corrosion under these conditions. Localized corrosion in Experiment 6, at pH 6.0, was observed where an increased growth of iron sulfide corrosion product was found in local areas which reflected the increased pitting corrosion below the corrosion product.

Experiment 9, at pH 5.0, had locations where the original polish marks could still be observed on the surface, but where that corrosion product layer collapsed, the pit penetration rate was excessive (over 20 mm/yr in a cross section observation). Both of these previous experiments indicate that the metal surface was initially covered with an iron sulfide layer which retards the general corrosion rate. So with a decrease in solution pH, from pH 5.0 to pH 4.0, while keeping the other test parameters the same, there are two hypotheses:

1. At pH 4.0, areas protected by an iron sulfide layer could exist, but at less percentage area than was observed at pH 5.0. The availability of more hydrogen ions would create a higher penetration rate and, thus, a much higher pitting ratio and more likelihood of localized corrosion.
2. At pH 4.0, there may be no areas protected by an iron sulfide layer, which would lead to a higher general corrosion rate with a lower pitting ratio and a lowered likelihood of localized corrosion.

Results and Discussion

The conditions tested were 60°C, $p\text{CO}_2 = 7.7$ bar, $p\text{H}_2\text{S} = 10$ mbar, 10 wt.% NaCl, pH 4.5 for 7, 14 and 21 days exposure for weight loss samples (Table 16). Only

one sample of the 7 weight loss samples exposed during the experiment had localized corrosion. The probe arrangement, installation procedure, and timing of sample removal were previously described in Chapter 3.

Table 16. Exp 12. Controlled Parameters for Effect of pH test at 10 mbar pH₂S and 10 wt% NaCl.

Parameter	Description
Equipment	H ₂ S Flow Loop
Test duration	21 days
Temperature	60.2 ± 0.4 °C
pCO ₂	7.4 ± 0.6 bar
pH ₂ S	0.010 ± 0.002 bar
pH	4.5 ± 0.2
Solution	10 wt% NaCl
Ionic strength	1.72 ± 0.001
[Fe ⁺⁺] (ppm)	189 ± 20
S(FeCO ₃)	0.3 ± 0.2
S(FeS)	12 ± 7.4
S(FeS)/S(FeCO ₃)	42.3 ± 5.5

[#](avg ± std deviation)

The partial pressures of CO₂ and H₂S were consistent during the 21 day experiment (Figure 82) with minimal changes observed for pCO₂ and repeatable variations in pH₂S due to reactions within the system. H₂S was added to the system at day 3, 10 and 17 to keep the partial pressure of H₂S between 8 and 12 mbar.

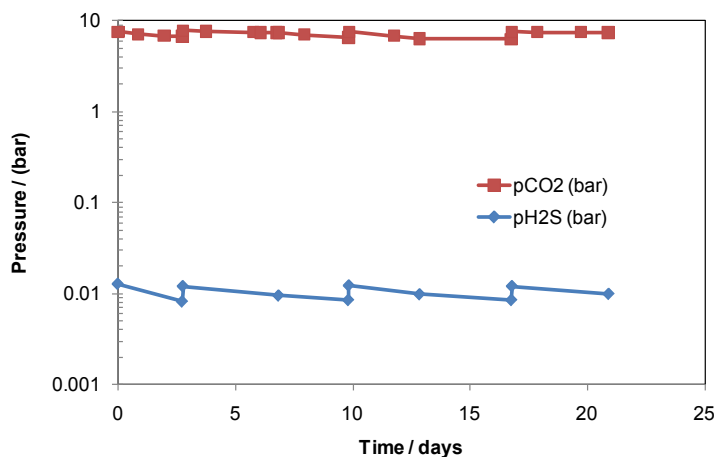


Figure 82. Exp 12. Partial pressures of CO₂ and H₂S for pH 4.0 experiment.

The general weight loss of all the samples is shown in Figure 83 and the general weight loss with additional pit penetration rates (shown by the single sided error bar on top of the data point) are shown for single phase flow in Figure 84 and for multiphase flow in Figure 85. Both show relatively high corrosion rates with most values above 5 mm/yr. Due to these high general corrosion rates, the penetration rates measured by Infinite Focus Microscope (IFM) after the corrosion product layer was removed were similar to the general corrosion rate and therefore not considered to be true localized corrosion.

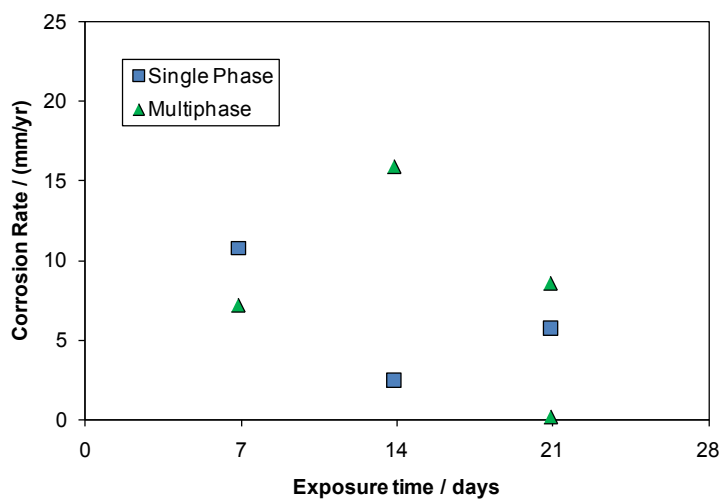


Figure 83. Exp 12. General corrosion rates for 60°C, $p\text{CO}_2 = 7.7$ bar, $p\text{H}_2\text{S} = 10$ mbar, 10 wt.% NaCl. pH 4.5.

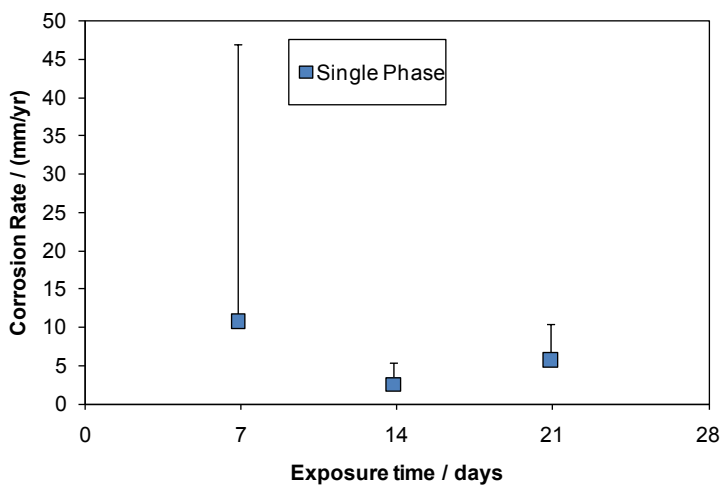


Figure 84. Exp 12. General corrosion (squares), as well as “localized” corrosion from IFM (single sided error bars), from weight loss of samples exposed to single phase flow in 60°C, $p\text{CO}_2 = 7.7$ bar, $p\text{H}_2\text{S} = 10$ mbar, 10 wt.% NaCl. pH 4.5.

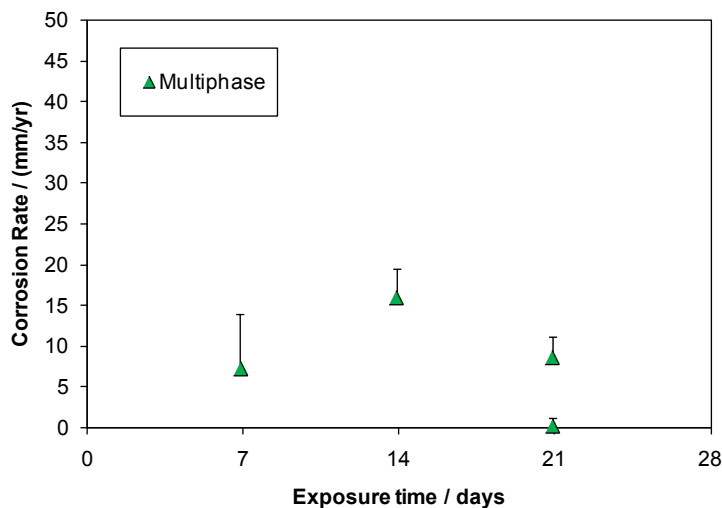


Figure 85. Exp 12. General corrosion (triangles), as well as “localized” corrosion from IFM (single sided error bars), rates from weight loss samples exposed to multiphase flow in 60°C, $p\text{CO}_2 = 7.7$ bar, $p\text{H}_2\text{S} = 10$ mbar, 10 wt.% NaCl. pH 4.5.

Figure 86 confirms the pitting ratio for five of the seven weight loss samples was less than 3 and, therefore, those were not considered to have localized corrosion.

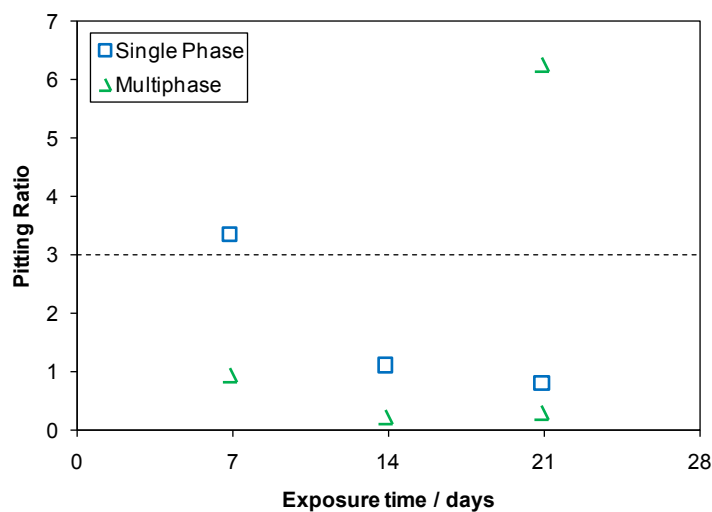


Figure 86. Exp 12. Pitting ratio for weight loss samples exposed in 60°C, $p\text{CO}_2 = 7.7$ bar, $p\text{H}_2\text{S} = 10$ mbar, 10 wt.% NaCl. pH 4.5.

Specific examples from the WL samples showing the corrosion product layer and subsequent corrosion of the substrate will be used to highlight key aspects of this experiment. WL samples from both single phase flow and multiphase flow after 7 days exposure are shown in full analysis as examples of the initiation of corrosion under these conditions. Two WL samples from multiphase flow after 7 days and 14 days exposure are highlighted to show the development of the corrosion product layer in relation to time. And two WL samples from multiphase flow after 21 days exposure are contrasted to show the inconsistencies found under the same experimental procedures.

- At pH 4.5, the general corrosion rate was higher in most cases as 6 of the 7 weight loss samples had corrosion rates greater than 5 mm/yr which led to a higher general corrosion rate with a lower pitting ratio and a lowered likelihood of localized corrosion.
- The iron sulfide corrosion product layer developed from corrosion of the substrate material with little or no precipitation from the bulk solution at this lower pH.
- Although not prominent, indications of the original surface features (polish marks) were still visible for every time exposure tested (7, 14 & 21 days).
- Two samples met the criteria for localized corrosion:
 - Multiphase flow at 7 days: 10.8 mm/yr + 36.3 mm/yr
 - Multiphase flow at 21 days: 0.16 mm/yr + 1.0 mm/yr

- Localized corrosion initiation during the short time exposure was negated by the high general corrosion rates with only one case having low general corrosion (< 5 mm/yr) after 21 days.

Characterization of the Corrosion Product Layer

Only the weight loss samples exposed for 7 days provide good examples of the development and failure of the corrosion product layer. These types of failures are similar to the observations experienced in tests at pH 5.0 where the corrosion product layer still has the original polish marks on the surface and failures were observed as a loss or collapse of this original corrosion product layer. The WL sample without localized corrosion is shown in Figure 87 and the WL sample with localized corrosion is shown in Figure 88. These WL samples, which are also represented by the two data points on the left hand side of Figure 86, show examples of how the corrosion product layer failures initiate under the current conditions.

Figure 87 is the analysis of the X65 weight loss sample exposed in multiphase flow for 7 days. The image of the sample as removed from the system shows multiple failures of the corrosion product layer across the surface; IFM measurement of a representative failure location shows an 83 μm depth, which is indicative of the thickness of the layer if the failure is considered to have reached the substrate.

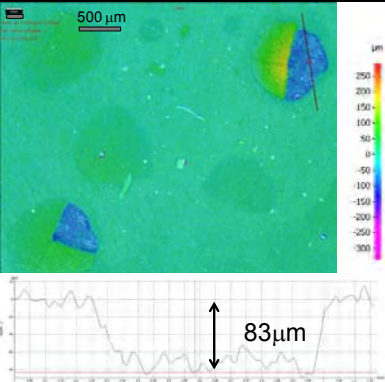
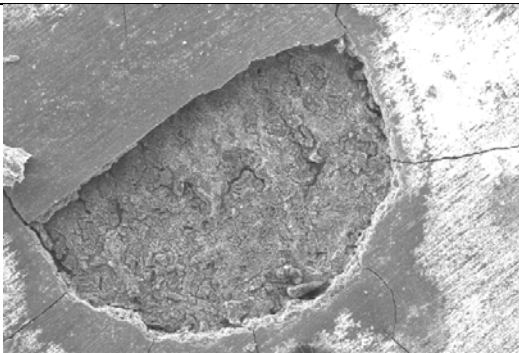
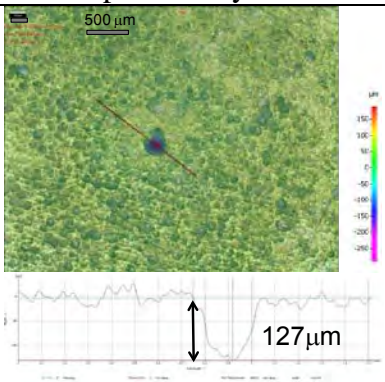
#56		
	Multiphase, 7 days, with layer	IFM of layer failure depth. (83 μm)
		
	SEM image of failure location in corrosion product layer.	Polish marks visible on corrosion product layer.
		
	Multiphase, 7 days, without layer	IFM of penetration depth. (127 μm)
	General Corrosion rate = 7.2 mm/yr Pit penetration rate = 6.8 mm/yr Ratio = 0.9	0.07 g layer weight

Figure 87. Exp 12. Analysis of WL sample exposed in 60°C, $p\text{CO}_2 = 7.7$ bar, $p\text{H}_2\text{S} = 10$ mbar, 10 wt% NaCl, multiphase flow, 7 days.

The IFM image and the higher magnification SEM image of a failure location seem to show a weakly adherent corrosion product layer that spalls off or is removed by flow. Since this WL sample was exposed to the repeated fluctuations of high turbulence with a slug frequency from 20 to 30 slugs per minute, failure and removal of the corrosion product are likely to be related to the flow regime. Note that even under these conditions, the original polish marks of the metal surface are visible on the top of the corrosion product layer; a characteristic which is consistent with previous experimental results at pH 5.0. Removal of the corrosion product layer shows a direct correlation between the multiple locations of failures seen in the corrosion product layer, when comparing the images of the WL sample with and without layer in Figure 87. An IFM analysis of a representative “pit”, or location of corrosion initiation, measured at a depth of 127 μm . However, this calculates as 6.8 mm/yr which is almost equivalent to the general corrosion rate of 7.2 mm/yr. Therefore, this would not be considered localized corrosion.

Figure 88 is the analysis of the X65 weight loss sample exposed in single phase flow for 7 days. The image of the sample as removed from the system shows a roughened surface that shows more oxidation of the surface after removal from the H_2S system than the multiphase WL sample, even though both were treated by the same procedures. IFM measurement of a representative failure location shows a 238 μm depth, which is considered to be indicative of localized corrosion. The IFM image and the higher magnification SEM image of failure locations show a corrosion product layer that has

collapsed, similar to what was observed in tests at pH 5.0. The original surface morphology has also been preserved, as shown by the polish marks seen at 400x magnification. When the corrosion product was removed, this sample did show multiple locations of 'pits' with an average depth of 150 μ m, which calculates to an 8 mm/yr penetration rate. This is consistent with the multiple locations where a collapsed surface layer was observed, but this penetration rate is similar to the general corrosion rate of 10.8 mm/yr. Only one location, shown at the bottom left of Figure 88, was found with a depth great enough to be defined as localized corrosion. This is a 681 μ m pit near the edge of the sample, which calculates to a 36.3 mm/yr penetration rate. Consequently, this is considered localized corrosion.

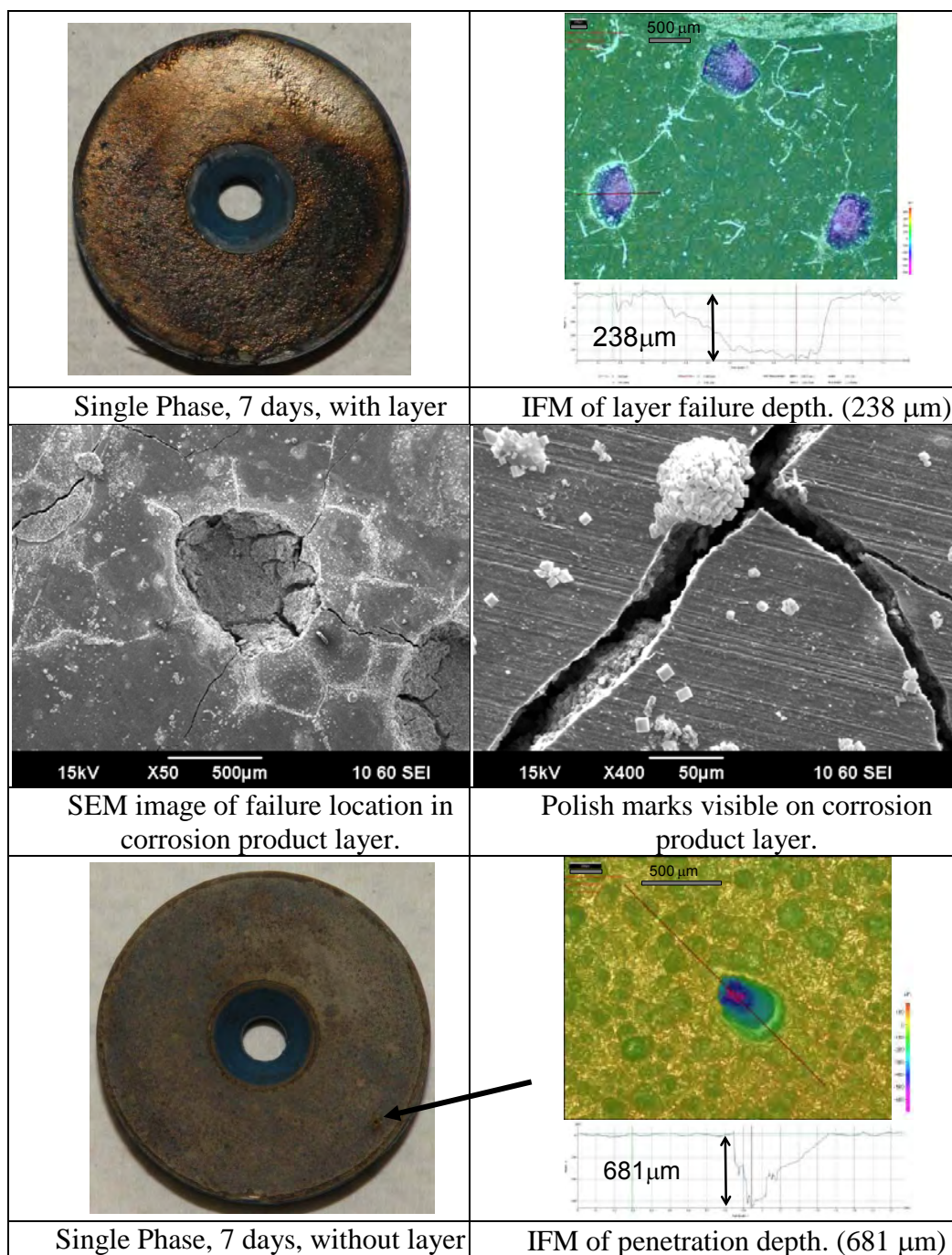


Figure 88. Exp 12. Sample #51. Analysis of WL sample exposed in 60°C, $p\text{CO}_2 = 7.7$ bar, $p\text{H}_2\text{S} = 10$ mbar, 10 wt% NaCl, single phase flow, for 7 days. pH 4.5. General Corrosion rate = 10.8 mm/yr; pit penetration rate = 36.3 mm/yr; Ratio = 3.4; Layer weight = 0.9 grams; multiple smaller pits of ~ 150 μm (8 mm/yr) were observed.

Failures of the Corrosion Product Layer

A set of experiments was conducted at 60°C, 7.7 bar pCO₂ and 10 mbar pH₂S for purged solutions at pH 4.5, pH 5.0 and pH 6.0. Experiments conducted for both the pH 5.0 and pH 6.0 experiments were highly saturated while the pH 4.5 experiment was calculated to be near the saturation point for iron sulfide (Table 17).

Table 17. The range of S(FeS) calculated for experiments at 60°C, 7.7 bar pCO₂, 10 mbar pH₂S.

Experiment	S(FeS)³⁵
pH 4.5	1 – 10
pH 5.0	50 – 100
pH 6.0	100 – 300

Cross-sectional analysis on two WL samples taken from the multiphase test section at 7 days and 14 days shows that extreme changes in the corrosion product layer occurred during the time exposure difference. Figure 89 shows the surface morphology of the two corrosion product layers on the upper left side of the figure. Some polish marks are still visible in both sample surfaces shown by the SEM images at 400x magnification. The cubic crystals correspond to recrystallized NaCl.

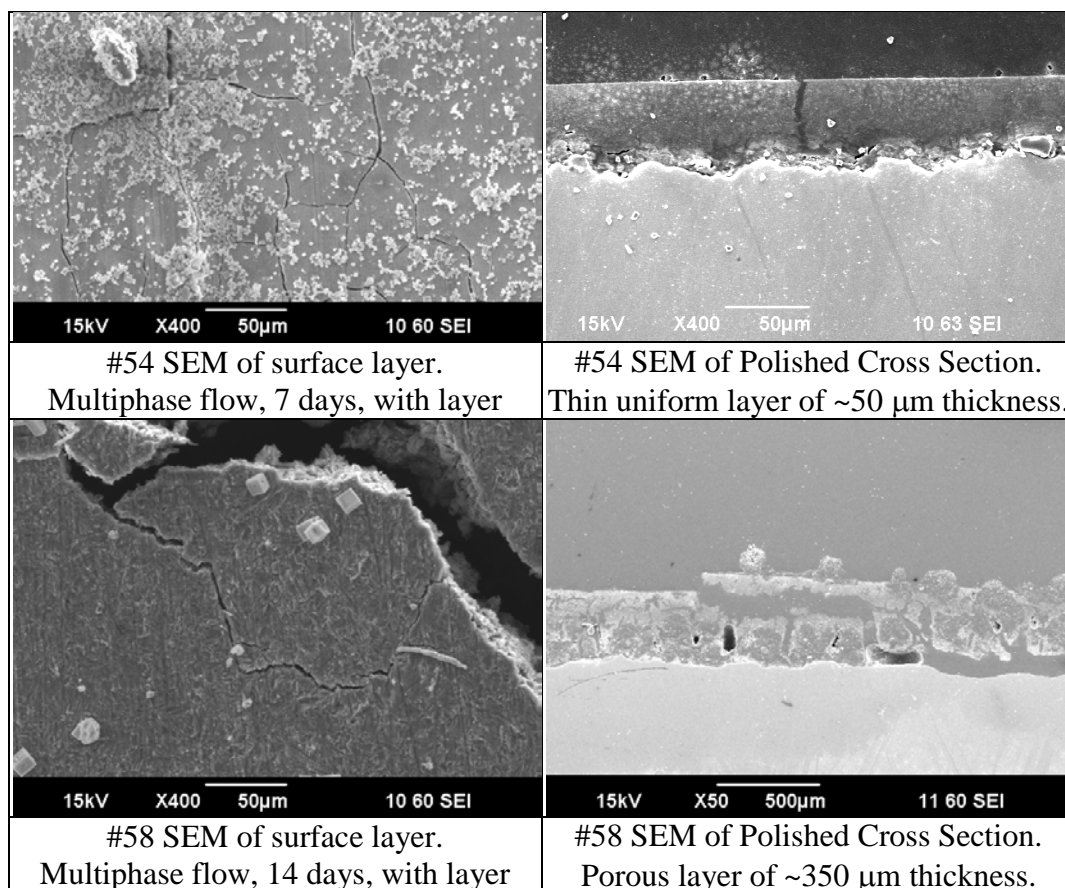


Figure 89. Exp 12. Analysis of corrosion product layer thickness for two WL samples exposed in 60°C, $p\text{CO}_2 = 7.7$ bar, $p\text{H}_2\text{S} = 10$ mbar, 10 wt.% NaCl, multiphase phase flow, for 7 and 14 days.

An immediate difference is noticed in the size of the cracks in the surface layer. Cross-sections of the corrosion product layers are shown to the right, where a 50µm layer formed at 7 days has a uniform density with a flat upper surface. It is difficult to determine whether the cracks seen in this layer occurred *in situ* or not. The corrosion product layer of the WL sample after 14 days exposure, in the middle right of Figure 89, shows a porous, weakened corrosion product layer that is becoming detached from the surface. The gray color in the upper portion of the image is the epoxy the sample is

mounted in and the light color at the bottom of the image is the metal substrate. The corrosion product layer, between these two materials, has a variation in color as observed by SEM; EDS analysis confirms this color change from light to dark as containing much higher carbon content similar to the same measurement done directly on the mounting epoxy. This observation leads one to believe the corrosion product layer observed is porous, along with being non-protective and poorly adherent. The images in Figure 90 provide a direct comparison of the corrosion product layer thickness difference between the two exposure times. The sample with a 7 day exposure, on the left, has ~50 μm thick corrosion product, while the sample with the 14 day exposure, on the right, has ~350 μm thick corrosion product.

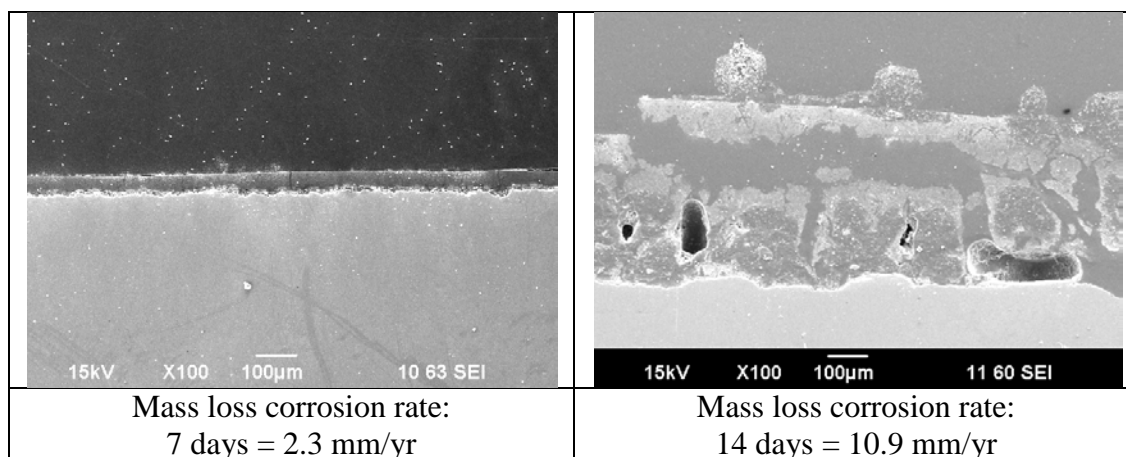


Figure 90. Exp 12. Direct comparison of corrosion product layer thickness for two WL samples exposed in 60°C, $p\text{CO}_2 = 7.7$ bar, $p\text{H}_2\text{S} = 10$ mbar, 10 wt.% NaCl, multiphase phase flow, for 7 and 14 days.

Note the similarity between the upper 100 μm of the failed corrosion product layer and the tight adherent 50 μm corrosion product on the right: a flat upper surface and an uneven bottom surface which is assumed to show the initial coverage of FeS (flat top) and the continued corrosion through this porous layer (uneven bottom surface). It can be assumed that corrosion occurred below the corrosion product layer that formed initially on the surface, causing undermining of the original layer until failure occurred. Interestingly, a vertical fracture can be observed in each of the images between this flat top layer and the uneven bottom surface which indicates failures of this initial layer could be assumed to occur by brittle fracture of an over-stressed surface layer.

Since the corrosion product layer was not removed in this case, an approximate weight loss was calculated with the corrosion product layer intact for each of these samples. After 7 days, the 0.25 grams lost from the original weight is equivalent to 2.3 mm/yr corrosion rate while the 2.28 grams lost from the original WL sample weight after 14 days is equivalent to 10.9 mm/yr. Calculations using the measured general corrosion rate values to determine the approximate depth of the substrate that would be lost (assuming 7.87 g/cm^3 density of iron) is visually the same as the depths of the corrosion product layers (44 μm vs. 50 μm and 418 μm vs. 350 μm , respectively). With the corrosion product still in place for these measurements, it means that the density of the corrosion product layer is almost negligible due to porosity and other associated factors.

Inconsistencies in CO₂ / H₂S corrosion

Two WL samples that have been exposed to the same environment and have slightly different results can be considered experimental error, but this case was an exception. The two samples were both inserted into the hydrogen sulfide system at 60°C, pCO₂ = 7.7 bar, pH₂S = 10 mbar, 10 wt.% NaCl, pH 4.5, at the 6 o'clock position in a multiphase slug flow regime for 21 days exposure, but in two different test sections.

The SEM images at 400x magnification (top of Figure 91) show that the polish marks of the original surface are still visible after 21 days, but the overall view of the samples without the corrosion product layer shows the difference unequivocally. The sample on the left (#55) shows a uniform corrosion that was calculated by weight loss to be 8.6 mm/yr. Pit penetration depths of up to 149 μm were measured by IFM on sample #55 and are equivalent to a 2.6 mm/yr penetration rate. Notice that the 21 day weight loss sample on the right (#57) had an uneven corrosion occurring across the surface. This WL sample also had a negligible general corrosion rate of 0.16 mm/yr with a single pit of 58.5 μm depth found for a penetration rate of 1 mm/yr, making sample #57 have the highest pitting ratio with the lowest pit penetration rate found in this series.

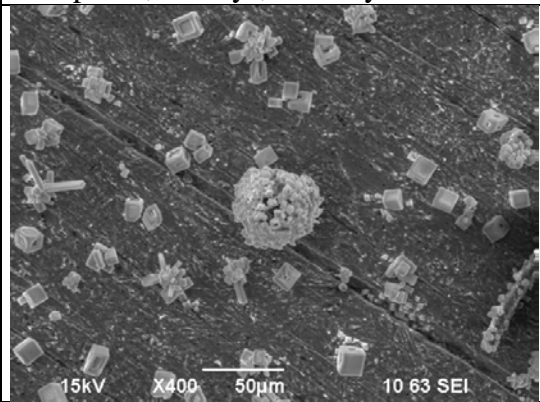
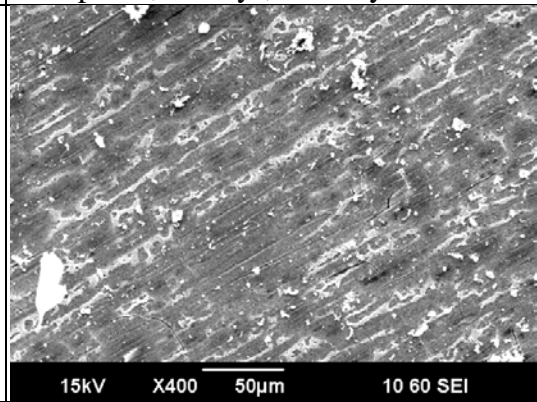
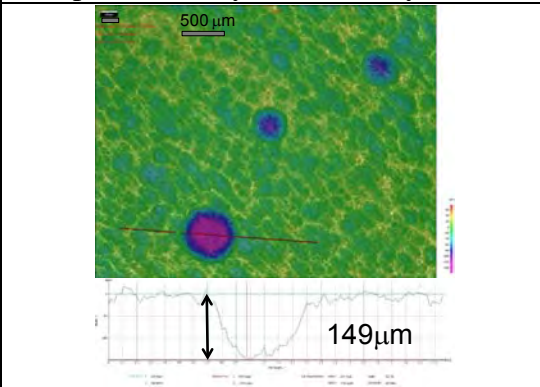
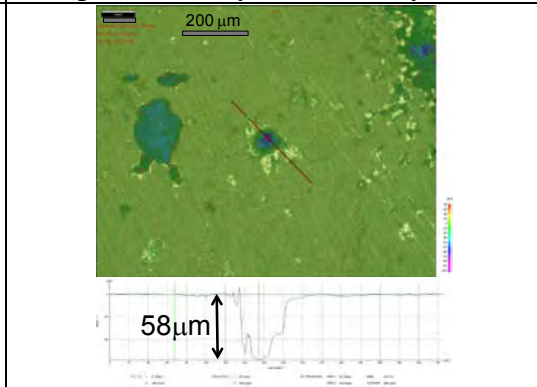
Sample #55	Sample #57
Multiphase, 21 days, with layer	Multiphase, 21 days, with layer
	
Polish marks visible on corrosion product layer.	Polish marks visible on corrosion product layer.
	
Multiphase, 21 days, without layer	Multiphase, 21 days, without layer
	
IFM of penetration depth. (149 µm)	IFM of penetration depth. (58 µm)

Figure 91. Exp 12. Comparison of weight loss samples: 21 days, 60°C, $p\text{CO}_2 = 7.7$ bar, $p\text{H}_2\text{S} = 10$ mbar, 10 wt.% NaCl, multiphase flow.

A review of these statistics in Table 18 shows that a high percentage of the ferrous ions lost to corrosion were maintained as part of the corrosion product layer.

Table 18. Statistics for comparison of two weight loss samples: 21 days , 60°C, pCO₂ = 7.7 bar, pH₂S = 10 mbar, 10 wt.% NaCl, multiphase flow.

Sample #55 – Multiphase, 21 days	Sample #57 – Multiphase, 21 days
General Corrosion rate = 8.6 mm/yr	General Corrosion rate = 0.16 mm/yr
0.36 g layer weight	0.004 g layer weight
Pit depth = 149 μm	Pit depth = 58 μm
Pit penetration rate = 2.6 mm/yr	Pit penetration rate = 1.0 mm/yr
Ratio = 0.3	Ratio = 6.3

Comparison of experiments at pH 4.5, pH 5.0 & pH 6.0

The overall comparison of the general corrosion rates, collected from weight loss samples from each experiment at pH 4.5, pH 5.0 and pH 6.0, are shown in Figure 92. The basic trend is a decrease in general corrosion rate as related to the increase in pH. However, the localized corrosion rates have the opposite trend in relation to the general corrosion rates. The overall comparison of localized corrosion rates, as measured by IFM, is shown in Figure 93. This change from general corrosion to localized corrosion is due to the buildup of the iron sulfide corrosion product layer which limits the general corrosion, but increases the likelihood of localized corrosion.

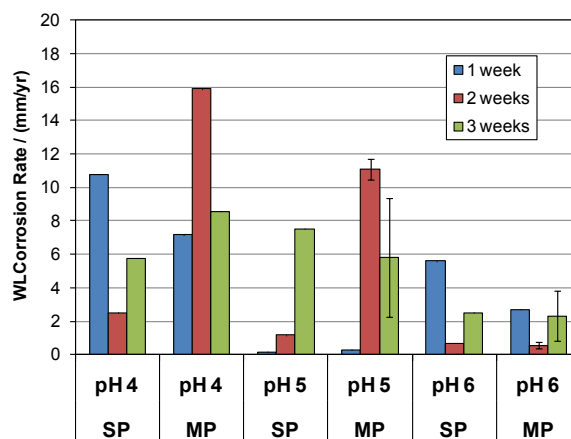


Figure 92. Comparison of weight loss general corrosion rates for pH 4.5, pH 5.0 and pH 6.0 (60°C, pCO₂ = 7.7 bar, pH₂S = 10 mbar, 10 wt.% NaCl).

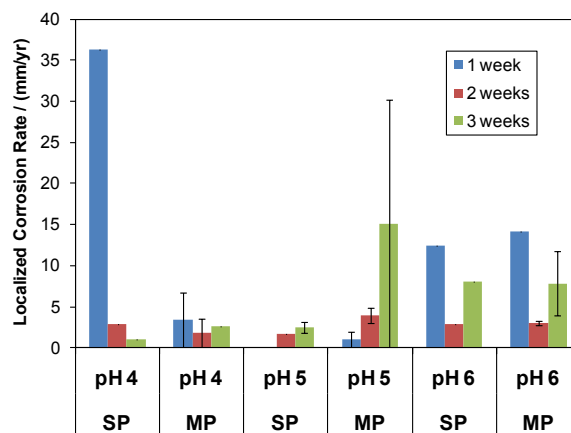


Figure 93. Localized corrosion rates measured by IFM. Shown for testing conducted at pH 4.5, pH 5.0 & pH 6.0 in the multi-week experiment under the same test conditions (60°C, pCO₂ = 7.7 bar, pH₂S = 10 mbar, 10 wt.% NaCl).

By breaking down the large data set of experiments into exposure by time, flow regime and bulk pH, some characteristics of the iron sulfide layer with respect to general and localized corrosion are revealed. Figure 94, Figure 95 and Figure 96 provide the comparison of data at 1 week, 2 weeks and 3 weeks exposure time, respectively, with

each figure providing a separation of corrosion rates for the a) single phase flow and b) multiphase flow regimes.

After 1 week exposure time, the iron sulfide corrosion product layer has already covered the surface of the mild steel. From Figure 94, it can be seen that the corrosion rate for pH 5.0 is almost negligible, indicating that the initial corrosion product layer formed for this experiment is still protective while localized corrosion has already initiated at pH 4.5 and pH 6.0.

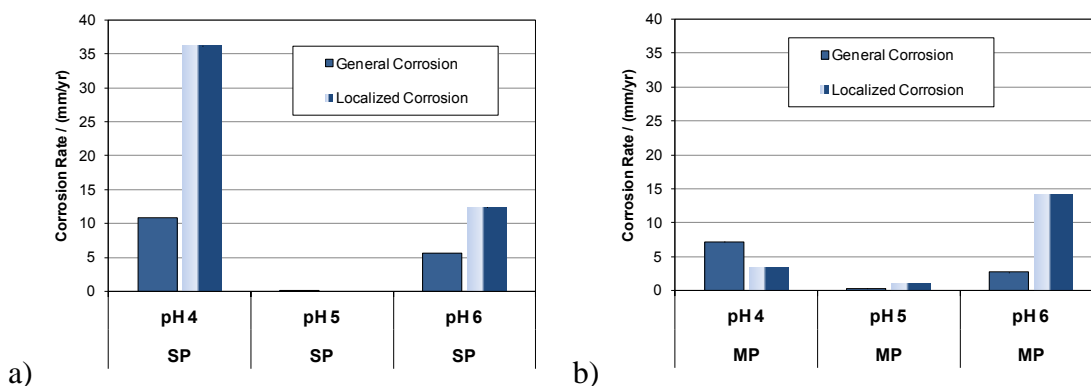


Figure 94. Comparison of general and localized corrosion for single phase flow and multiphase flow at pH 4.5, pH 5.0, & pH 6.0 for a 1 week exposure under the same test conditions (60°C , $p\text{CO}_2 = 7.7$ bar, $p\text{H}_2\text{S} = 10$ mbar, 10 wt.% NaCl).

For the samples exposed for 2 weeks, the flow regime has a much greater effect on the general corrosion rate observed at pH 4.5 and pH 5.0. By comparison of Figure 95a) to Figure 95b), the corrosion product formed at pH 4.5 and pH 5.0 was not a good mass transfer barrier and may have promoted an increased corrosion rate since there is such a large difference observed. Neither the general or localized corrosion rates at pH 6.0 were influenced by the flow regime.

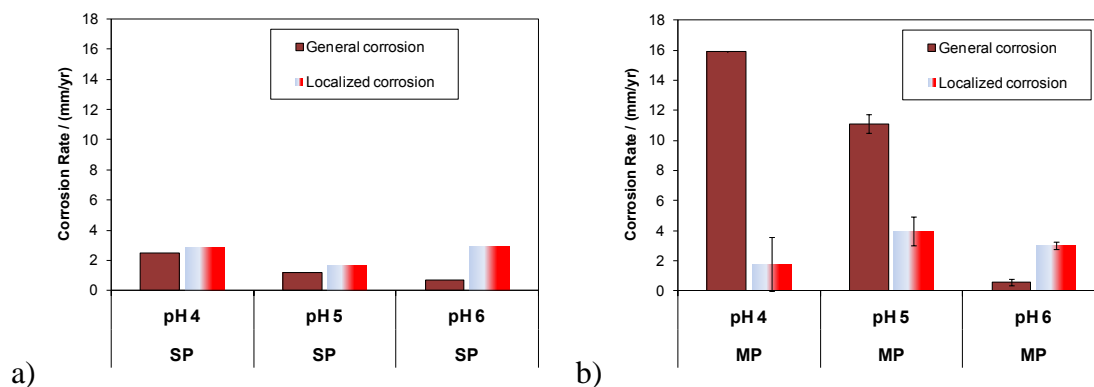


Figure 95. Comparison of general and localized corrosion for single phase flow and multiphase flow at pH 4.5, pH 5.0 & pH 6.0 for a 2 week exposure under the same test conditions (60°C , $p\text{CO}_2 = 7.7$ bar, $p\text{H}_2\text{S} = 10$ mbar, 10 wt.% NaCl).

After exposure for 3 weeks, corrosion rate comparison in Figure 96 shows high general corrosion rates at pH 4.5 and pH 5.0 which appear to limit the likelihood of localized corrosion. When localized corrosion occurred at pH 5.0, it was the highest recorded localized loss of material for this entire test series. Localized corrosion at pH 6.0 was consistent and similar between the different flow regimes.

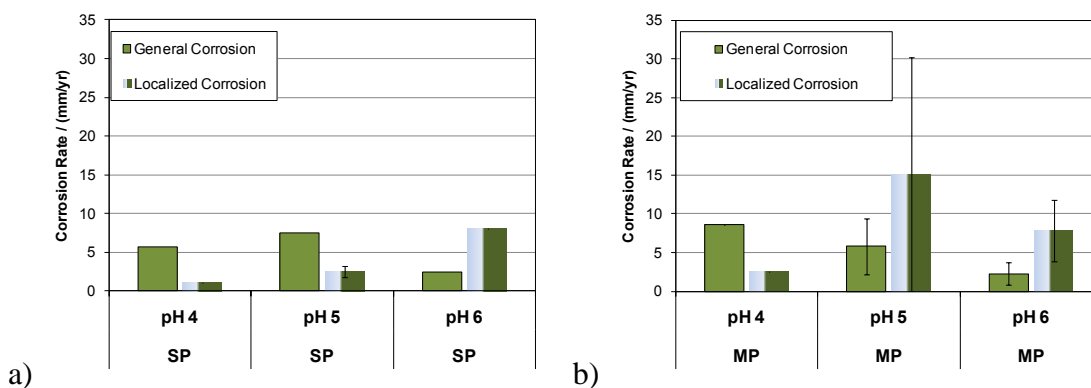


Figure 96. Comparison of general and localized corrosion for single phase flow and multiphase flow at pH 4.5, pH 5.0 & pH 6.0 for a 3 week exposure under the same test conditions (60°C , $p\text{CO}_2 = 7.7$ bar, $p\text{H}_2\text{S} = 10$ mbar, 10 wt.% NaCl).

Conclusions Related to Solution pH

The saturation values (iron sulfide, iron carbonate) are not thought to provide a direct indication of a tendency toward localized corrosion, although the parameters involved in the calculation of these saturation values are important. With a change in pH, the failure mechanism of corrosion product layer changed. For pH 6, localized corrosion was observed where corrosion product layer growth had exceeded that of the surrounding area. For pH 5, localized corrosion was observed where the corrosion product layer had failed, allowing the bulk solution to reach the substrate. Early stages of corrosion product layer formation seem to be similar between pH 4.5 and pH 5.0 bulk solution environments, but the more acidic solution was closer to the solubility limit of mackinawite or iron sulfide and increased the overall corrosion rate. The corrosion product and failure by collapse of the surface layer are similar between pH 4.5 and pH 5.0, although dissolution and subsequent failure of this layer occurs under pH 4.5 conditions at a much faster rate.

The iron sulfide saturation value in the bulk solution and near the surface of the corroding steel directly influences the corrosion product and, therefore, the corrosion rate. The corrosion product is related to the ferrous ions released from the surface of the steel which react very quickly with any aqueous hydrogen sulfide ($[H_2S]_{aq}$) or bisulfide (HS^-) to form a layer of iron sulfide on the metal surface. This thin reactant layer, which occurs when bare metal is exposed to a solution with aqueous hydrogen sulfide, has shown excellent surface coverage which retards the general corrosion rate dramatically. The bulk conditions then influence the thin precipitate layer in relation to the solubility of the iron sulfide precipitate formed while the flow regime provides the transport of species to and away from the surface with the additional turbulence of multiphase flow removing weakly or loosely adherent corrosion products. General corrosion occurs below/through the initial iron sulfide reactant layer while localized corrosion occurs when a defect in this layer initiates a galvanic cell.

Ferrous ions released from the iron sulfide corrosion product at pH 4.5 or pH 5.0 bulk conditions did not precipitate on top of the initial iron sulfide precipitate layer formed so localized corrosion was related to a loss of material, but ferrous ions released from the iron sulfide corrosion product at pH 6.0 bulk conditions did precipitate on top of the initial iron sulfide layer and formed a thicker layer which seemed to promote localized corrosion under the areas of excess corrosion product.

Effect of a Lower Ionic Strength Solution and Lower pH_2S at pH 5

Introduction

Previous discussion has shown that the iron carbonate and iron sulfide saturation values are not good indicators for the likelihood of localized corrosion, but the relationship of the environmental factors which influence precipitation and formation of the corrosion product to the likelihood of localized corrosion is beginning to emerge.

Under conditions with 10 wt% NaCl, 60°C, 7.7 bar pCO_2 :

- An increase from 1 mbar to 10 mbar pH_2S at pH 6 increased the likelihood of localized corrosion. (Experiment 5: 1 mbar, Experiment 6: 10 mbar)
- An increase in the $[\text{H}^+]$ from pH 6 to pH 5 dramatically increased the localized corrosion rate. (Experiment 6: pH 6, Experiment 9: pH 5)
- But a further increase in the $[\text{H}^+]$ from pH 5 to pH 4 decreased the likelihood of localized corrosion by increasing the general corrosion rate. (Experiment 9: pH 5, Experiment 12: pH 4.5)

Since a maximum point was observed at pH 5, 10 wt% NaCl, 60°C, 7.7 bar pCO_2 , the influence of a change in the sodium chloride concentration and pH_2S under these conditions is necessary for comparison. The next two experiments reviewed in this section are related to Experiment 9 by a decrease in ionic strength for Experiment 8 and a decrease in both ionic strength and pH_2S in Experiment 7 as shown in the parameter comparison, Table 19.

Table 19. Experiments 7 & 8: decreased ionic strength, lower pH₂S

Parameter	Exp. 8	Exp. 7
Temperature	60°C	60°C
Total Pressure	8 bar	8 bar
pCO ₂	7.7 bar	7.7 bar
Flow	V _{sl} = 1 m/s, V _{sg} = 3 m/s	V _{sl} = 1 m/s, V _{sg} = 3 m/s
NaCl solution	1 wt%	1 wt%
pH	5.0	5.0
pH ₂ S (mBar)	10	1
Measurements	WL, SEM	WL, SEM
Exposure Time	7, 14, 21 days	7, 14, 21 days

Experimental Observations

Experiment 8: 60°C, pCO₂ = 7.7 bar, pH₂S = 0.010 bar, pH 5.0, 1wt% NaCl

Introduction

As seen previously at pH 6, the likelihood of localized corrosion was increased by increasing the partial pressure of H₂S. For this experiment (Table 20), pH₂S is 10 millibar while maintaining a pH 5 solution as compared to the previous experiment in order to determine if the likelihood of localized corrosion will also increase with pH₂S.

Table 20. Controlled Parameters for Effect of pH test at 10 mbar p_{H2S} and 1 wt% NaCl.

Parameter	Description
Equipment	H ₂ S Flow Loop
Test duration	21 days
Temperature	59.9 ± 0.2 °C
pCO ₂	7.7 ± 0.1 bar
pH ₂ S	0.0100 ± 0.0004 bar
pH	4.9 ± 0.1
Solution	1 wt% NaCl
Ionic strength	0.179 ± 0.01
[Fe ⁺⁺] (ppm)	113.4 ± 12.4
S(FeCO ₃)	2.7 ± 1.2
S(FeS)	26.3 ± 11.0
S(FeS)/S(FeCO ₃)	9.6 ± 0.4

[#](avg ± std deviation)

Results and Discussion

All of the parameters shown in Table 20 were documented during the experiment. The concentration of hydrogen sulfide, concentration of ferrous ions, and pH during this 21 day experiment are shown in Figure 97. Sample mass loss and IFM depth measurements are combined in Figure 98 to provide the corrosion rates of single phase and multiphase samples, respectively.

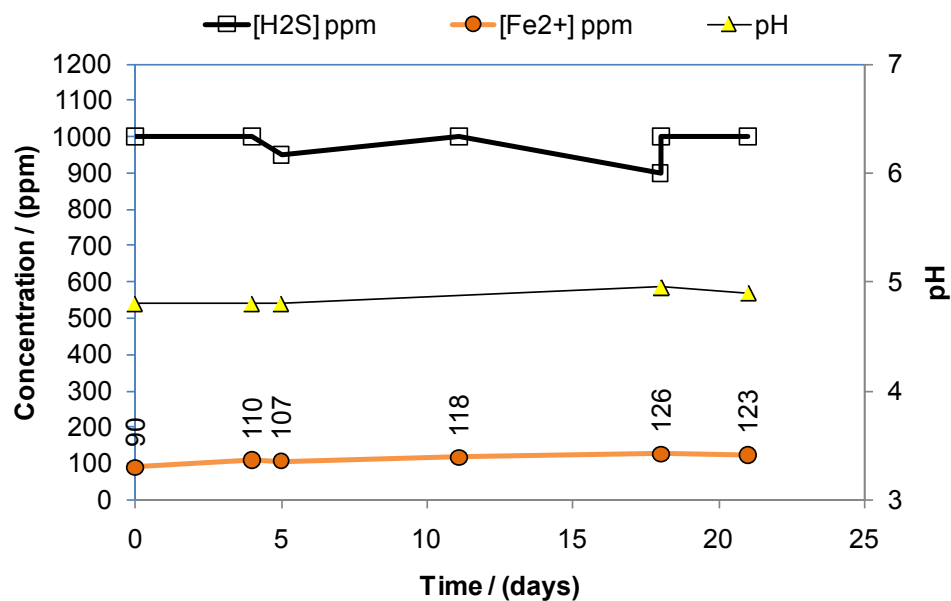


Figure 97. Exp 8: As measured concentrations of hydrogen sulfide and iron ions with pH. Information necessary to calculate saturation values of iron sulfide and iron carbonate. (60°C, 7.7 bar pCO₂, 10 mbar pH₂S, 1wt% NaCl, pH 5)

A curious phenomenon occurred with the multiphase flow WL samples as the corrosion rate was high (5.2 mm/yr) for the 7 day sample, but was low (0.8 mm/yr) for both 14 day and 21 day exposures Figure 98.

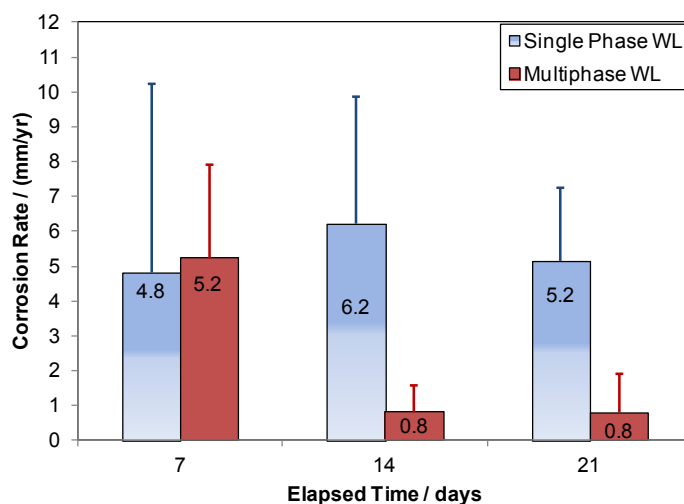


Figure 98. Exp 8: Single phase and Multiphase weight loss corrosion rate (bar) and penetration rate measurement (vertical error bar). (60°C, 7.7 bar pCO₂, 10 mbar pH₂S, 1wt% NaCl, pH 5)

Corrosion product mass loss is shown in Figure 99. There seems to be a direct relationship of the increase in corrosion product mass to exposure time for the samples exposed in the single phase test section, which is considered to be reflected in the consistent corrosion rate (5.4 ± 0.7 mm/yr) over the full experiment. With a somewhat constant corrosion rate, the corrosion product layer builds almost linearly with time meaning that a consistent rate of ferrous ions which were released in the corrosion process were retained as part of the iron sulfide corrosion product. The samples exposed in multiphase flow (during the same experiment) had a corrosion rate less than 1 mm/yr, no localized corrosion, and relatively no corrosion product build up on the sample surface. The penetration rate for every sample in multiphase flow had a negligible effect on the overall corrosion rate.

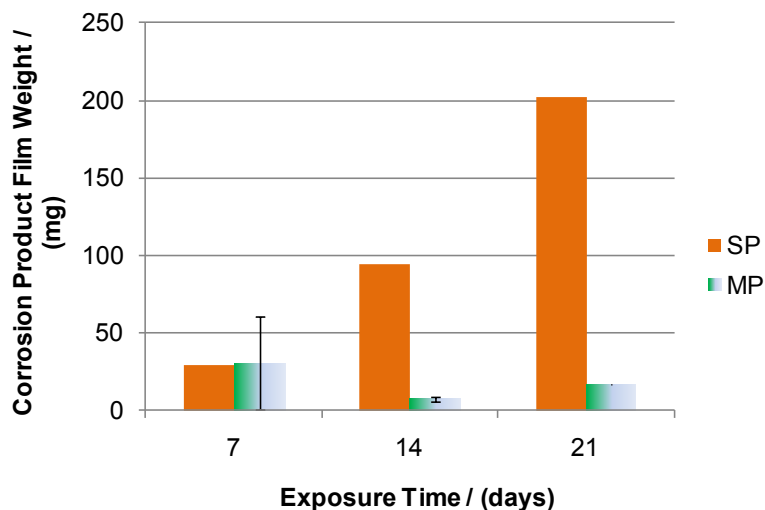


Figure 99. Exp 8: Corrosion product layer mass loss after Clarke solution cleaning of single phase (SP) and multiphase (MP) samples. (60°C, 7.7 bar pCO₂, 10 mbar pH₂S, 1wt% NaCl, pH 5)

Characterization of the Corrosion Product Layer

SEM Backscatter (BSE) images are similar to those collected for the 1mbar pH₂S test: a uniform composition of the top surface of the corrosion product was observed on every sample removed from both single phase and multiphase with some intermittent dark spots. Figure 100 shows two examples of the characteristic features of the corrosion product layer. Cracking of the corrosion product layer has been seen elsewhere and is expected to be related to the amount of water that the mackinawite corrosion product can hold. Note that the surface polish marks are still visible in both samples after 14 and 21 days respectively in the corrosive environment. The multiphase flow sample in Figure 99a had 0.81 mm/yr general corrosion rate with no localized corrosion, while a single phase sample equivalent to that shown in Figure 99d had a general corrosion rate of 6.2

mm/yr; profilometer measurements showed penetration rates equal to or less than the general corrosion rate in both cases.

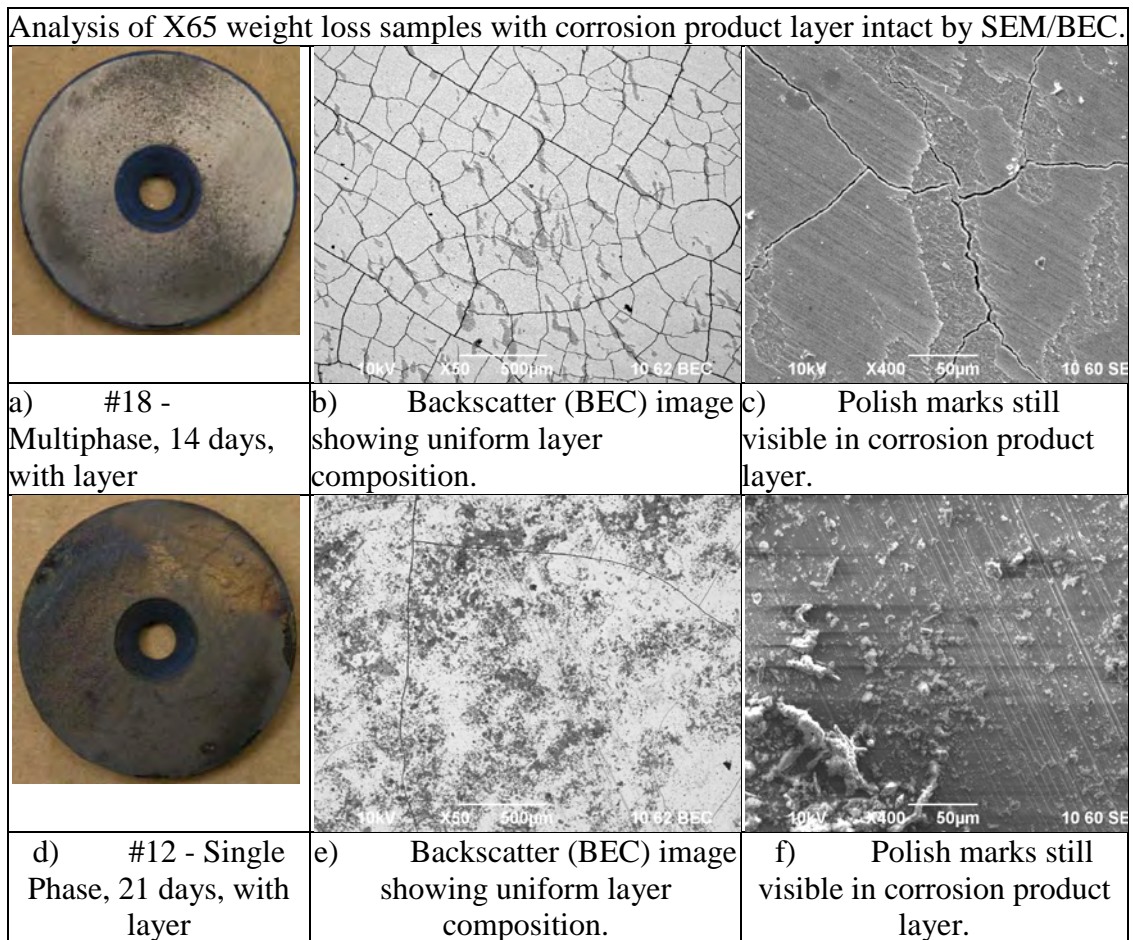


Figure 100. Examples of corrosion product layers formed at in multiphase flow after 14 days and in single phase flow after 21 days at 60°C, 7.7 bar pCO₂, 10 mbar pH₂S, 1wt% NaCl, pH 5. (BEC images at 50X magnification and SEM images at 400X magnification.)

The results seen on the surface of the weight loss samples are similar to the observations of the previous test at a lower partial pressure of H₂S. The original polish marks are also visible on the corrosion product surface of samples #12, #15, #16, #17,

#18, and #19. Examples are shown in Figure 101 and Figure 102 for samples #12 and #15, respectively.

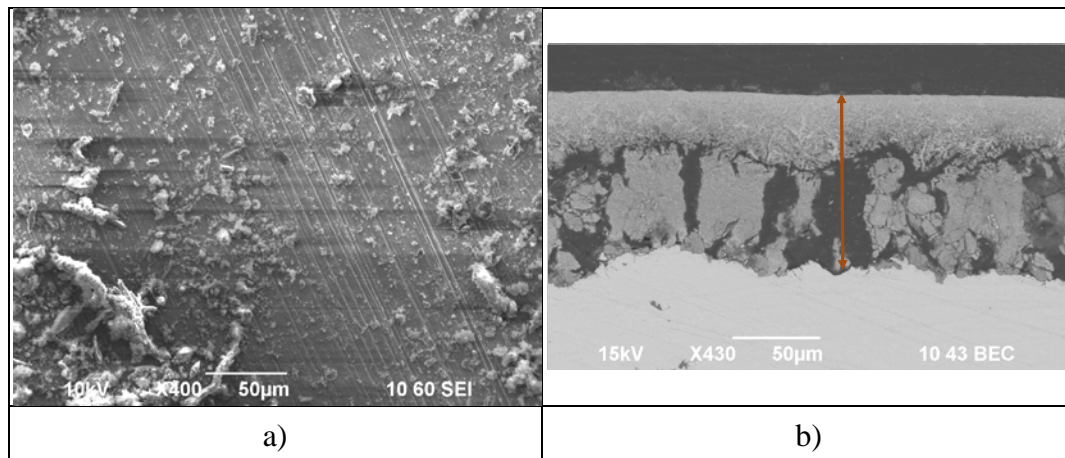


Figure 101. SEM images of surface (a) and cross-section (b) for X65 sample #12 after 21 day exposure to single phase H_2S system conditions of $60^\circ C$, 7.7 bar pCO_2 , 10 mbar pH_2S , 1 m/s V_{sl} .

In these images, sample #12 shows two different corrosion product morphologies which are assumed to be two different types of iron sulfide on top of the metal substrate. In the cross section image, it can also be seen that the corrosion product next to the metal substrate is ‘open’ as there are cracks or gaps between the underlying corrosion product that have been filled with epoxy during the corrosion product layer preservation process.

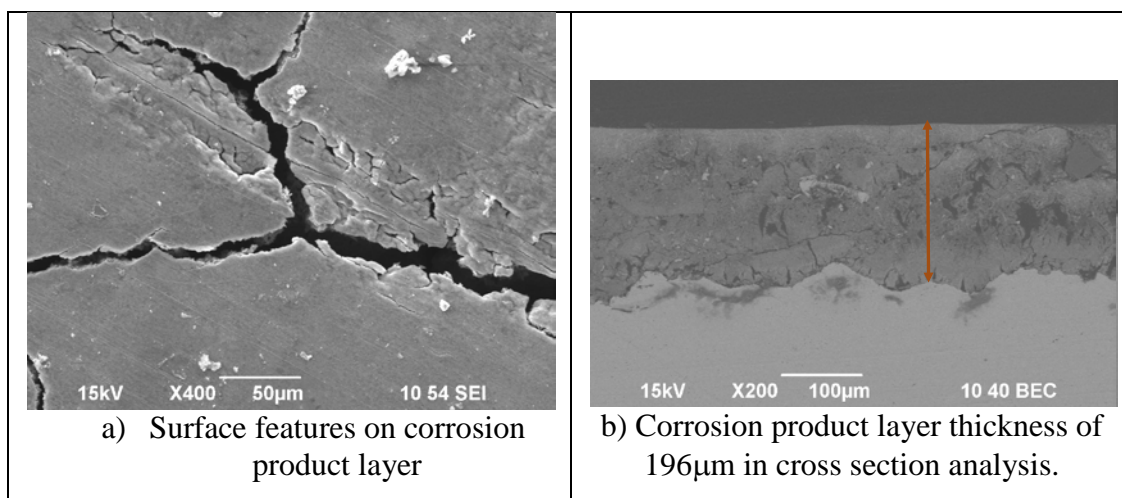


Figure 102. SEM images of surface (a) and cross-section (b) for X65 sample #15 after 21 day exposure to multiphase H_2S system conditions of $60^\circ C$, 7.7 bar pCO_2 , 10 mbar pH_2S , 1 m/s V_{sl} . (196 μm in 21 days = 3.4 mm/yr)

Failures of the Corrosion Product Layer

Failure of the upper corrosion product layer was not as widely observed as in the previous test at lower pH_2S . The sample exposed in single phase flow for 21 days shows important characteristics of the corrosion product layer developed in the conditions of $60^\circ C$, 7.7 bar pCO_2 , 10 mbar pH_2S , pH 5, and 1 m/s V_{sl} . Images in Figure 103 show the sample before corrosion product layer removal (a – d) and after corrosion product layer removal (e & f). Figure 103a is the sample after removal from system and drying with isopropyl alcohol. (Note the flow direction for all full size samples shown is from the bottom of the image to the top of the image.) Circular failures were noted in the corrosion product layer and were imaged by SEM (b) and IFM (c & d). The SEM image in Figure 103b shows the same circular failure in the upper corrosion product layer as seen at the lower partial pressure test, and shows a clear example of a different structure of the

bottom corrosion product layer. Indications of the failure mechanism are provided in the IFM images, as it can be seen that another circular location is raised to the left of the layer failure location; these can be observed as multiple locations within the dotted line area of Figure 103a. It is assumed that these failures occurred as the sample was being removed from the experimental conditions; CO₂ trapped in the void spaces beneath the iron sulfide layer expanded with dissolution upon depressurization when the sample was removed from the test conditions.

When the corrosion product layer was removed using a Clarke solution procedure, this area of the sample had a different type of corrosion product layer under the upper layer which was more difficult to remove (1 o'clock position on the sample in Figure 103e). Enough of this secondary corrosion product layer was removed in order to confirm the absence of localized corrosion, but some was left for documentation. There were no indications of localized corrosion near the secondary corrosion product layer, but the area in the 7 o'clock to 8 o'clock portion of the sample had circular pit initiation locations of 198 μm (~3.5 mm/yr) as measured in Figure 103f. With a 202 mg corrosion product layer, this sample had the most corrosion product developed for both experiments with a similarly high corrosion rate of 5.2 mm/yr.

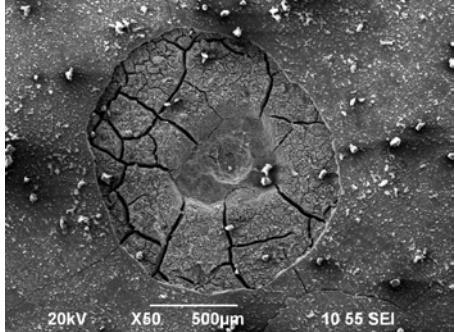
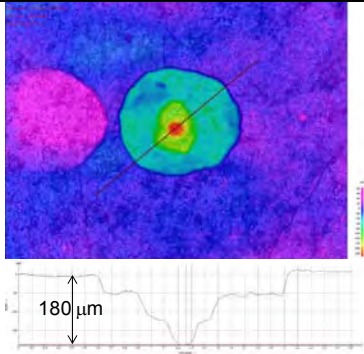
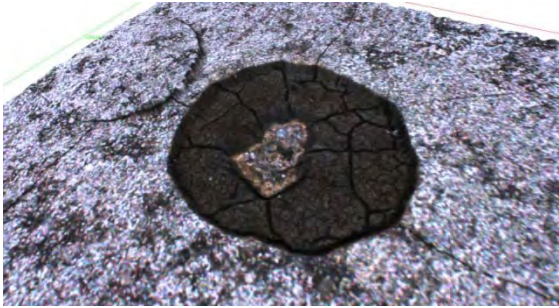
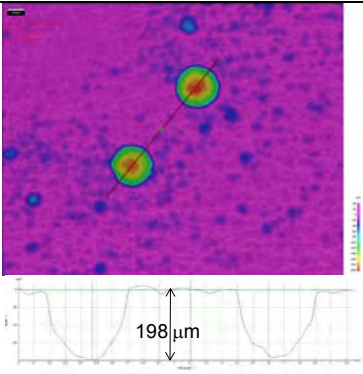
#11 - Single Phase, 21 days, with corrosion product layer	
	
a) Sample with layer, as removed & dried.	b) SEM of surface layer failure
	
c) IFM measurement of surface layer failure	d) IFM 3D image of surface layer failure
	
e) Sample after layer removal	f) IFM measurement of the pits in the substrate after layer removal

Figure 103. Aspects of analysis for X65 weight loss sample after 21 day exposure in H₂S flow loop. (Single phase, 60°C, 7.7 bar pCO₂, 10 mbar pH₂S, pH 5, 1 m/s V_{sl}).

Contents of the local corrosion product layer failure

Further analysis of the surface features within the corrosion product layer failure for sample 11 (Figure 103) show a circular indentation in the center which has some interesting features. The rounded shape gives the impression of CO₂ pitting corrosion and the location shows that it would have been below the other layers of corrosion product. IFM measurements before corrosion product layer removal (180 μm depth) and after corrosion product layer removal (198 μm) are fairly consistent which indicate the rounded indentation is a pit in the substrate material. A single iron carbonate crystal prism was observed to be located in the center circular depression and is shown in better detail in Figure 104.

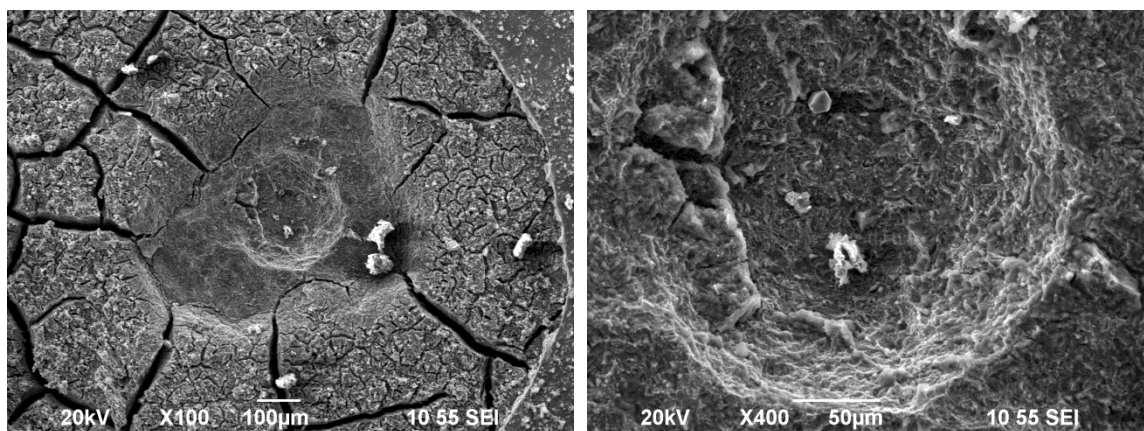


Figure 104. SEM images at increased magnification of local corrosion product failure from Figure 103b. (Sample 11, 21 days, with corrosion product layer, single phase, 60°C, 7.7 bar pCO₂, 10 mbar pH₂S, pH 5, 1 m/s V_{sl}).

Although this seems to be an anomaly, the crystal in all images of Figure 105 indicates that ferrous ions and carbonate ions were supersaturated in solution at the base

of this layer failure which allowed the precipitation reaction to occur. And the failure is assumed to have occurred ex situ, since the surface of the pit does not show a high sulfide peak (Figure 105c).

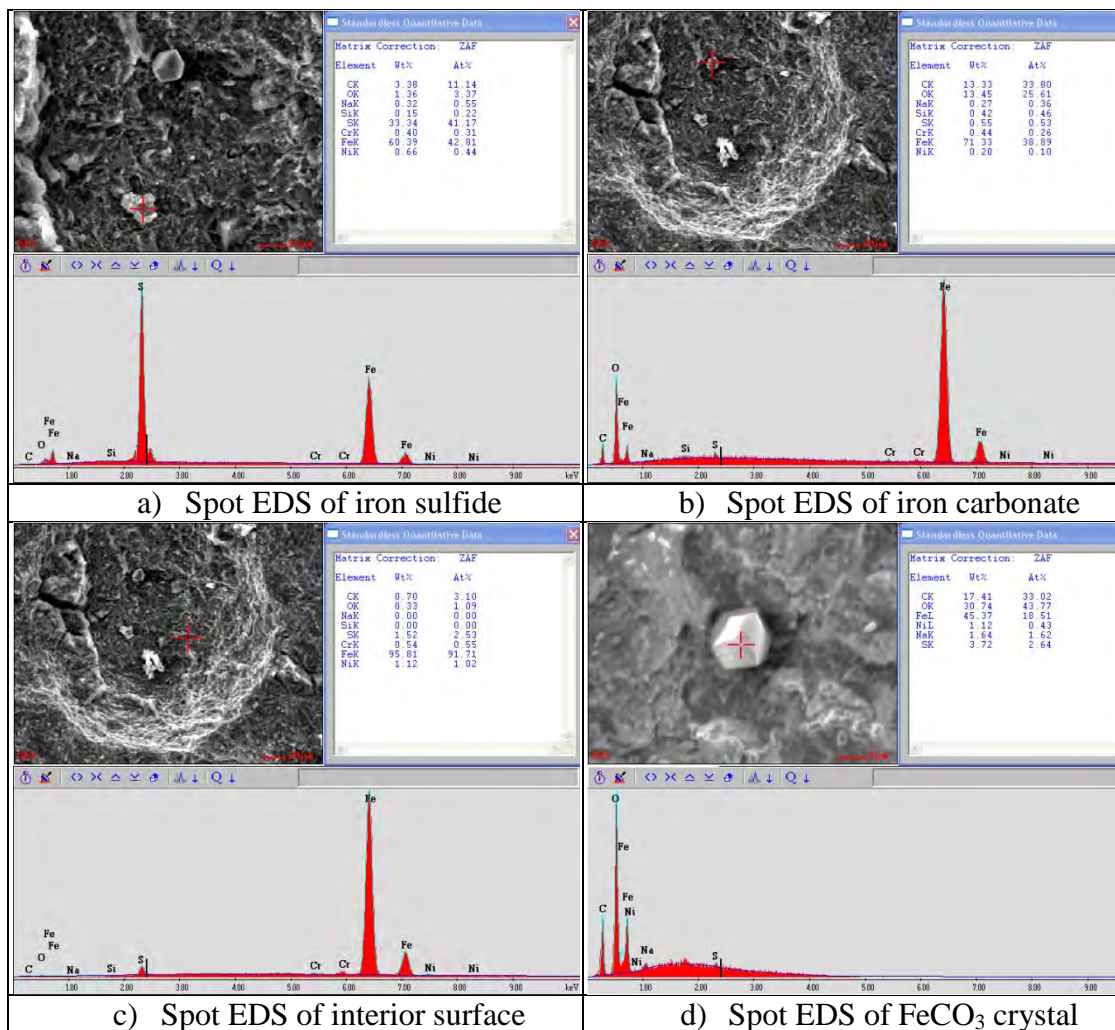


Figure 105. Spot EDS of materials observed in center of local corrosion product failure from Figure 103b. (Sample 11, 21 days, with corrosion product layer, single phase, 60°C, 7.7 bar pCO₂, 10 mbar pH₂S, pH 5, 1 m/s V_{sl}).

Experiment 7: 60°C, $p\text{CO}_2 = 7.7 \text{ bar}$, $p\text{H}_2\text{S} = 0.001 \text{ bar}$, $\text{pH} 5.0$, 1wt% NaCl

Introduction

The effect of a system at pH 5 and 1 wt% sodium chloride concentration should have less of a corrosion product layer developed than for the same system at pH 6. Under these conditions (Table 21), a lower likelihood of localized corrosion is also expected.

Table 21. Controlled Parameters for Effect of pH test at 1 mbar pH_2S and 1 wt% NaCl.

Parameter	Description
Equipment	H ₂ S Flow Loop
Test duration	21 days
Temperature	60.2 ± 0.4 °C
pCO ₂	7.7 ± 0.2 bar
pH ₂ S	0.0010 ± 0.0004 bar
pH	5.2 ± 0.1
Solution	1 wt% NaCl
Ionic strength	1.73 ± 0.01
[Fe ⁺⁺] (ppm)	65 ± 18
S(FeCO ₃)	2.3 ± 1.7
S(FeS)	11 ± 12
S(FeS)/S(FeCO ₃)	4.1 ± 1.6

[#](avg ± std deviation)

Results and Discussion

All of the parameters shown in Table 21 were documented during the experiment and the corrosion rates were determined from X65 sample analysis. The concentration of hydrogen sulfide, concentration of ferrous ions, and pH during this 21 day experiment are shown in Figure 106. Sample mass loss and profilometer depth measurements are combined in Figure 107 for single phase and multiphase WL samples. While all WL samples show some penetration rate measured, only the multiphase WL sample at 14

days had the potential to be localized corrosion (general corrosion rate = 0.7 mm/yr + penetration rate = 3.2 mm/yr) with a 4.5 pitting ratio (see Definition of Localized Corrosion, page 88).

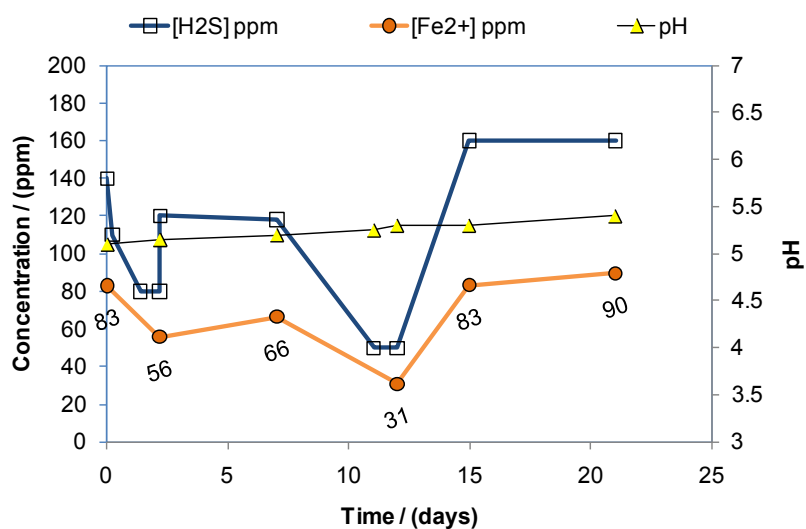


Figure 106. Exp 7: As measured concentrations of hydrogen sulfide and iron ions with pH. Information necessary to calculate saturation values of iron sulfide and iron carbonate. (60°C, 7.7 bar pCO₂, 1 mbar pH₂S, 1wt% NaCl, pH 5)

A much higher corrosion rate was observed on single phase samples from every time exposure in Experiment 8, Figure 98, as compared to Experiment 7, Figure 107, with the increase in pH₂S from 1 mbar to 10 mbar.

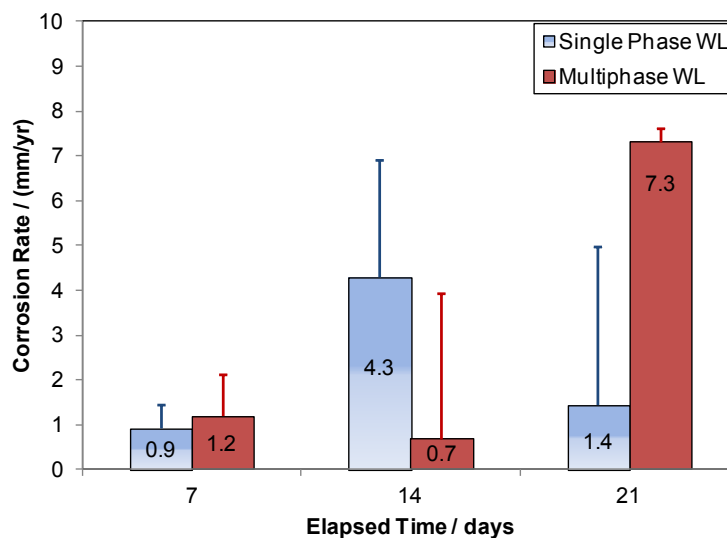


Figure 107. Exp 7: Single phase and Multiphase weight loss corrosion rate (bar) and penetration rate measurement (vertical error bar). (60°C, 7.7 bar pCO₂, 1 mbar pH₂S, 1wt% NaCl, pH 5)

Determination of the mass of the corrosion product layer can be used in a simple mass balance between the metal lost from the substrate, ferrous ions in solution, and iron atoms captured in the corrosion product layer on the metal surface. The corrosion product mass measurement from Experiment 7 WL samples, collected from the Clarke solution cleaning procedure, is shown in Figure 108. The trend of this data does not show any direct correlation of corrosion product development with time, but does seem to be directly related to the corrosion rate measured if the penetration rate is also taken into account.

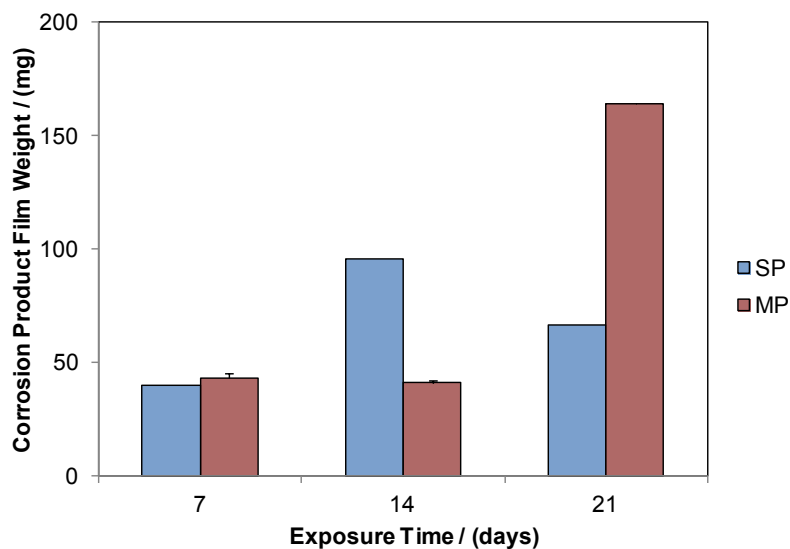


Figure 108. Exp 7: Corrosion product layer mass loss after Clarke solution cleaning of single phase (SP) and multiphase (MP) samples. (60°C, 7.7 bar pCO₂, 1 mbar pH₂S, 1wt% NaCl, pH 5)

Characterization of the Corrosion Product Layer

SEM Backscatter (BSE) images in Figure 109 show a uniform composition of the top surface of the corrosion product on every sample removed from both single phase and multiphase. BSE image intensity is related to molecular weight of the element detected. All of these samples show a flat gray surface color with some intermittent small dark spots. Dark areas in cracks and crevices are artifacts of the technique and are not considered to be different elements in the material under analysis.

With a uniform composition, the corrosion product had relatively the same surface topography in every case. The surface of the corrosion product was flat with cracks that are assumed to have been developed as the corrosion product was dried

outside of the experiment. One important observation was that the original polish marks on the metal were visible on the surface of the corrosion product for all but one sample.

The importance of the original polish marks still being visible on the corrosion product layer can be directly related to the corrosion mechanisms. When mild steel is exposed to an environment with H_2S , a very fast reaction occurs between the iron substrate and hydrogen sulfide to form iron sulfide (mackinawite). The mackinawite begins as surface tarnish which increases in coverage of the surface over time related to H_2S concentration and temperature.^{3,4,6} This coverage effect of iron sulfide on the mild steel surface will slow the overall corrosion process as measured by weight loss or by electrochemical methods. This initial corrosion mechanism creates a corrosion product so densely packed across the metal substrate that it mimics the polish marks of the original surface. This also infers that the reaction taking place is on the nanometer scale since polishing with a 600 grit abrasive paper should approximately make a 110 nm surface roughness on steel.⁵³

Although the densely packed corrosion product mimics the initial surface topography of the metal substrate, the corrosion reaction does not stop. Subsequent corrosion still occurs through this layer to the substrate underneath. Confirmation of this is shown by SEM analysis of a WL sample (Figure 109) exposed to multiphase flow for 21 days. The SEM image of the corrosion product layer topography shows polish marks still visible while the cross sectional analysis of the same sample shows an irregular metal substrate surface with a 40 to 50 μm corrosion product layer.

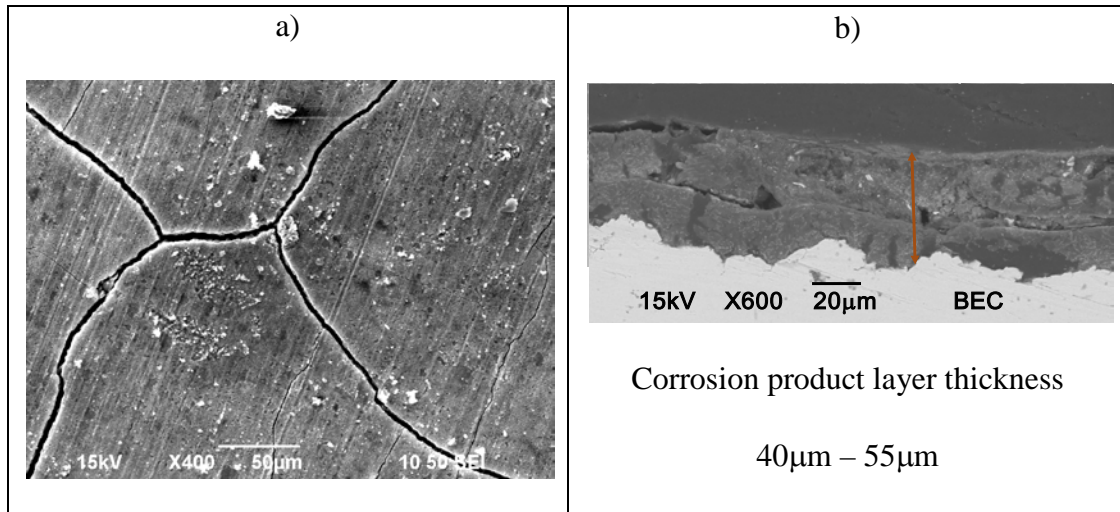


Figure 109. SEM images of surface (a) and cross-section (b) for X65 sample #04 after 21 day exposure to multiphase H_2S system conditions of $60^\circ C$, 7.7 bar pCO_2 , 0.1 mbar pH_2S , 1 m/s V_{sl} , 3 m/s V_{sg} .

All samples removed from this experiment show the same trait. Initial inspection of the SEM image of the corrosion product layer topography of the WL sample (Figure 110) exposed to single phase flow for 21 days did not seem to show polish marks and this was initially assumed to have been related to the amount of corrosion product developed ($300\mu m$ for sample #02 vs. $50\mu m$ for sample #04). Further inspection of the SEM image confirmed that the polish marks were overlooked in documentation of aspects of layer failure.

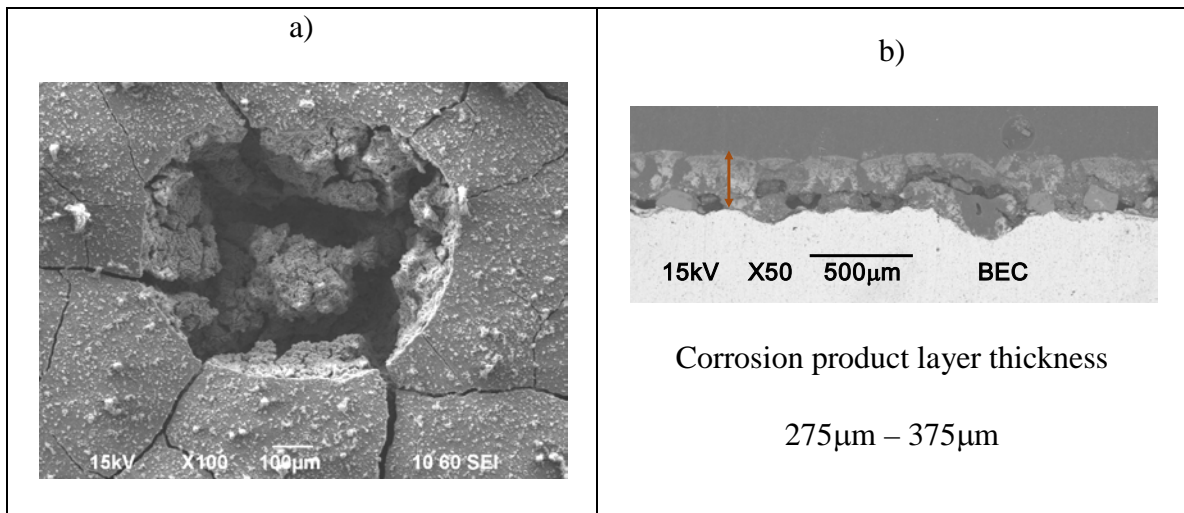


Figure 110. SEM images of surface (a) and cross-section (b) for X65 sample #02 after 21 day exposure to single phase H_2S system conditions of 60°C , 7.7 bar pCO_2 , 0.1 mbar pH_2S , 1 m/s V_{sl} .

A portion of the SEM image in Figure 110(a) was magnified so that the physical size reference matches the SEM image in Figure 109(a); this new image is shown as Figure 111. Although the surface topography is quite different between these two samples, as may be expected since they were taken from single phase flow and multiphase flow respectively, the initial polish marks are still present on the top of the corrosion product surface.

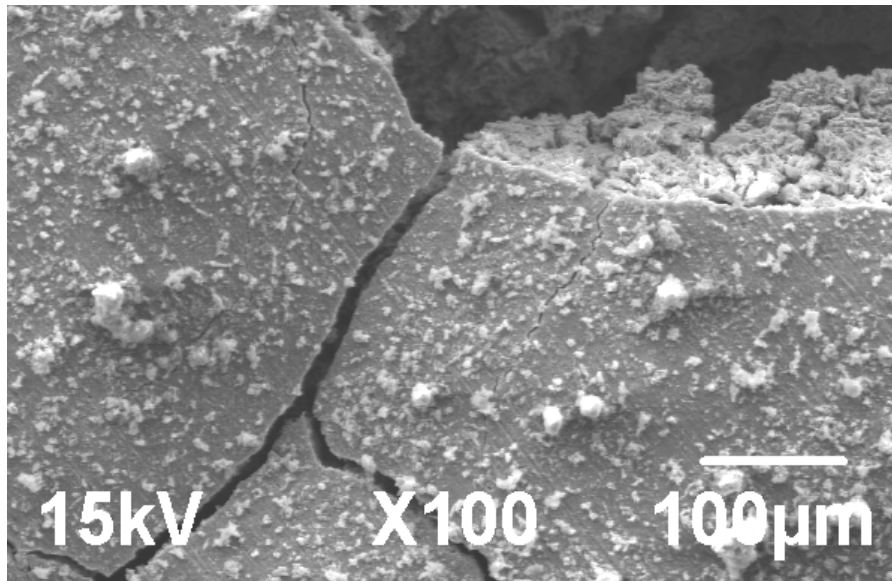


Figure 111. Polish marks visible in SEM image of the corrosion product layer for X65 sample #02 as lines from the upper left to the lower right. A portion of Figure 110(a) is magnified to match the physical measurement shown in Figure 109(a).

Failures of the Corrosion Product Layer

Failures in the upper layer of the corrosion product layer were observed for all four samples that were exposed for 21 days, but only one was classified as having localized corrosion. Images of the types of failures observed are in Figure 113. Sample #02 in single phase flow for 21 days had visible surface corrosion product layer failures that measured 380 μm in depth. The image shown in Figure 110(a) and Figure 113(a) is of a circular layer failure that was observed in random locations over the sample surface. SEM results show circular failures of about 500 μm in diameter. Cross section of this sample (Figure 110b) shows a layer depth between 275 μm and 375 μm , so the conclusion would be that the corrosion product failure was all the way to the metal substrate. This was confirmed by profilometer analysis of sample #02 after corrosion

product layer removal showing a pit depth of 333 μm or a penetration rate of 5.8 mm/yr. Compared to the WL corrosion rate of 1.4 mm/yr, this is localized corrosion with a pitting ratio of 4 (see definition of Pitting Ratio).

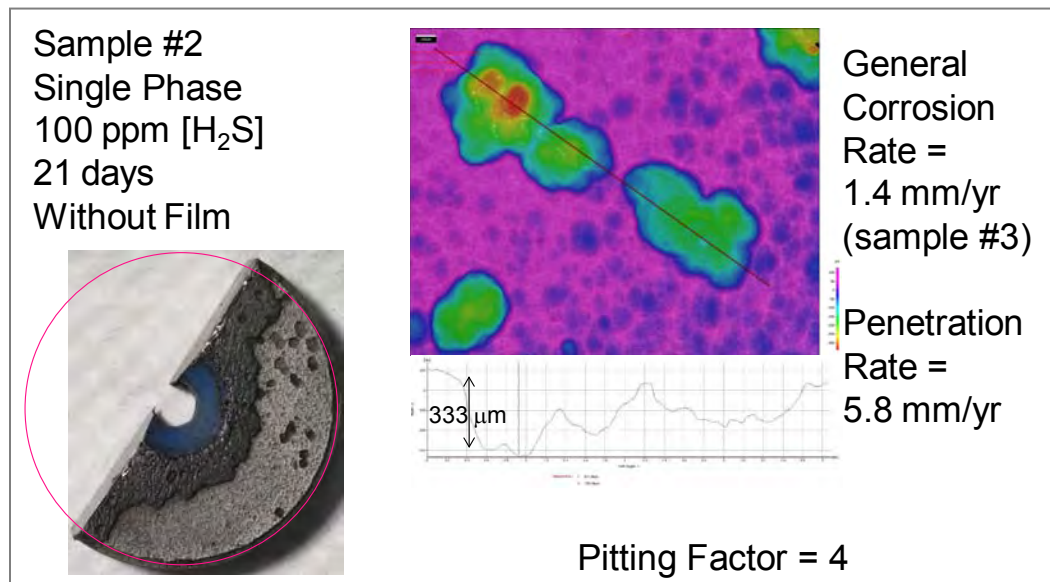


Figure 112. Exp 7: Picture of weight loss sample plus IFM surface imaging of X65 coupon exposed for 21 days in single phase flow for conditions: 60°C, pH 5.0, pCO₂ = 7.7 bar, 1.0 mbar H₂S, 1 wt% NaCl. (General corrosion rate was calculated from Sample #3.)

Three more samples that had observable corrosion product layer failures were also from exposures of 21 days, but two of these did not show failure of the underlying layer. Sample #03, Figure 113(b), was in single phase flow for 21 days and had a few circular failures of the upper layer of corrosion product, but the 43 μm depth of the failures measured by IFM was much less than the 380 μm depth measured for sample #02. Sample #04, Figure 113(c), was in multiphase flow for 21 days and exhibited a peeling and curling effect of the layer as it dried. These defects are not expected to have

been in this form *in situ* as the turbulence of the flow would have removed this fragile layer. The failure in the third sample (#06), Figure 113(d), obviously occurred *in situ* with measured values of 10.6 mm/yr penetration rate of the substrate with a 7.3 mm/yr general corrosion rate after the corrosion product layer was removed.

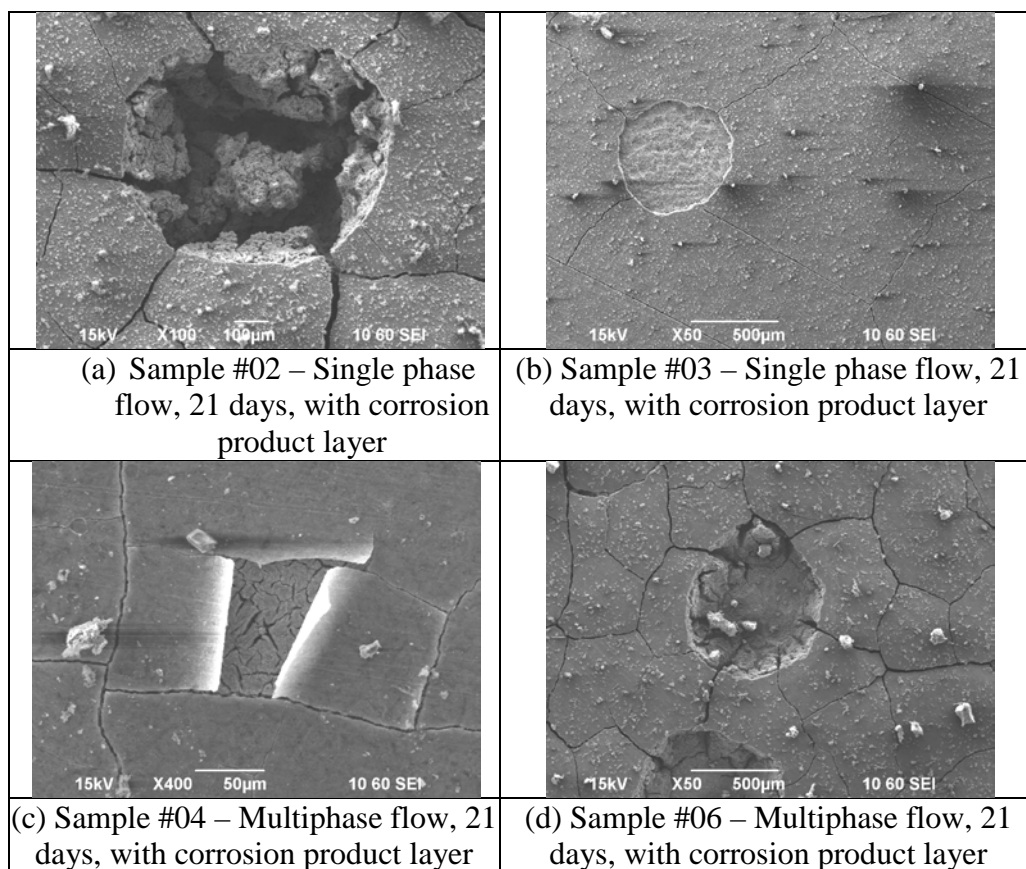


Figure 113. SEM image evidence of an upper corrosion product layer different from the underlying corrosion product layer after 21 days on four samples exposed to H₂S system conditions of 60°C, 7.7 bar pCO₂, 0.1 mbar pH₂S, 1 m/s V_{sl}, 3 m/s V_{sg}.

An interesting failure mechanism was captured by IFM analysis of sample #06 that was not seen on other samples. Figure 114 shows two different locations on the

sample where the corrosion product failed. In Figure 114(a), the upper layer failure had occurred *in situ* allowing dissolution and corrosion of the underlying corrosion product and substrate, respectively. The image in Figure 114(b) shows a “dome-like” raised corrosion product layer with a “pie-shaped” missing piece.

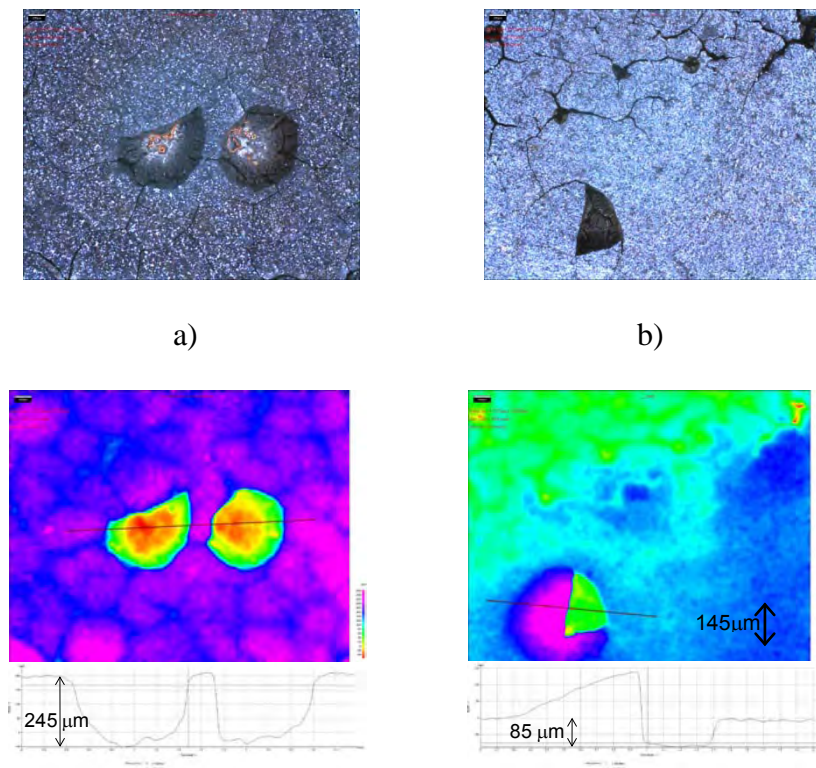


Figure 114. IFM images and analysis of the corrosion product layer on sample #06 showing (a) open pit failures up to 245 μm in depth [1.2 & 1.0 mm diameter, L to R] and (b) a partial layer failure with a raised corrosion product layer [1.3 mm diameter].

IFM analysis can only reproduce visual images related to vertical measurements, so horizontal openings in a pit or a dome (ie. a horizontal loss of material like a cave) are represented by a vertical line. It is not apparent that this failure occurred *in situ* because

the surface inside the “dome” is somewhat flat as compared to the profile inside of the open pits of Figure 114(a). The IFM photos of these failure locations also show the visual difference between the top layer and the underlying layer of corrosion product. These images lead to the conclusion that the upper corrosion product layer failed due to a mechanism which would ‘lift up’ the upper layer as a bubble. And the initial assumption would be that this bubble was an accumulation of hydrogen gas, but the failure may have occurred during the sample removal process which indicates that dissolved CO₂ coming out of solution during de-pressurization would have damaging effects on the corrosion product layer.

What is most interesting about all four of these different corrosion product failures is that the underlying corrosion product has a much different visual structure than the first layer of corrosion product layer described above. And for each of these samples from the tested conditions (60°C, pH 5.0, pCO₂ = 7.7 bar, 1.0 mbar H₂S, 1 wt% NaCl), more material loss was observed associated with the areas where corrosion product layer failure occurred. These conditions are assumed to have a high likelihood of localized corrosion since half of the samples had measureable penetration rates, although penetration rates were equivalent to general corrosion rates in most cases from 3 to 6 mm/yr, except for Sample #2 in Figure 112.

Conclusions Related to Experiments at pH 5

The observation that the original topography of every sample was maintained with varying amounts of subsequent corrosion of the metal substrate underneath provides conclusive evidence of at least two corrosion mechanisms related by time (or the kinetics of the reactions involved).

1. The initial reaction(s) on the metal surface are kinetically fast, cover the surface thoroughly, and do not develop large crystalline features similar to iron carbonate. The initial surface corrosion that occurs when the sample comes in contact with the corrosive environment creates a corrosion product layer across the metal substrate that is only nanometers in thickness. With a surface roughness of approximately 100 nm, this nano-crystalline layer mimics the original surface features. In order to capture this level of surface detail, the reaction must be fast and target sites on the metal substrate with available ferrous iron.
2. Further corrosion, after the initial corrosion product layer is formed, must occur through the initial corrosion product layer without disrupting its topographical continuity. This infers that further corrosion reactions release ferrous ions from the metal substrate below the initial corrosion product layer without producing a precipitate on top of the initial corrosion product layer.

Effect of a Decrease in $p\text{CO}_2$

Introduction

Operating parameters were varied in the H_2S system in order to gain an understanding of the type of corrosion product and corrosion product morphology that are associated with localized corrosion in $\text{H}_2\text{S} / \text{CO}_2$ environments. The following experiments were conducted at a lower partial pressure of CO_2 in order to develop iron sulfide layers and observe, through surface analysis methods, the corrosion products developed and the type of corrosion attack experienced (Table 22). In comparison to previous testing in the H_2S system, this first experiment (Experiment 10) has only a decrease in the partial pressure of CO_2 from approximately 8 bar to approximately 3 bar while maintaining the operating environment similar to Experiment 4. The next experiment, Experiment 11, maintains the lower $p\text{CO}_2$ content at approximately 3 bar, but decreases the other operating parameters of temperature, pH, and pH_2S . As previously shown in Experiment 4, the initiation of localized corrosion was indicated by excessive growth of the corrosion product layer (Figure 43 & Figure 45) with some locations showing a possible iron carbonate layer beneath the iron sulfide corrosion product (Figure 47). The decrease in the $p\text{CO}_2$ for Experiment 10 will reduce the carbonic acid and bicarbonate concentrations to limit the likelihood of developing an iron carbonate, while the combination of lowering temperature, pH, and pH_2S will reduce the reaction kinetics of precipitation for both FeCO_3 and FeS to increase the likelihood of failure of the corrosion product layer.

Table 22. Test Matrix for Experiment 10 & 11 with changes in $p\text{CO}_2$, Temperature, Flow, [NaCl], & $p\text{H}_2\text{S}$.

Parameter	Exp. 10	Exp. 11
Temperature	60°C	40°C
Total Pressure	3 bar	3 bar
$p\text{CO}_2$	2.7 bar	2.9 bar
Flow	$V_{sl} = 1 \text{ m/s}$, $V_{sg} = 3 \text{ m/s}$	$V_{sl} = 0.1 \text{ m/s}$, $V_{sg} = 1 \text{ m/s}$
NaCl	1 wt%	1 wt%
pH	6	5
$p\text{H}_2\text{S}$ (mBar)	14	4
Measurements	WL, SEM	WL, SEM
Exposure Time	7, 14, 21 days	7, 14, 21 days

Experimental Observations

Experiment 10: 60°C, $p\text{CO}_2 = 2.7 \text{ bar}$, $p\text{H}_2\text{S} = 0.010 \text{ bar}$, pH 6.0, 1wt% NaCl

Introduction

The parameters of this test (Table 23) are related to the parameters of Experiment 4 by a change in partial pressure of carbon dioxide from 7.7 bar to 2.8 bar.

Table 23. Controlled Parameters for Effect of Corrosion Product Layer test at 14 mbar pH_2S and 1 wt% NaCl.

Parameter	Description
Equipment	H_2S Flow Loop
Test duration	21 days
Temperature	60.8 ± 0.1 °C
pCO_2	2.9 ± 0.1 bar
pH_2S	0.014 ± 0.003 bar
pH	6.0 ± 0.0
Solution	1 wt% NaCl
Ionic strength	0.20 ± 0.002
$[\text{Fe}^{++}]$ (ppm)	5.7 ± 1.6
S(FeCO_3)	9.3 ± 2.8
S(FeS)	360 ± 118
S(FeS)/S(FeCO_3)	39.5 ± 8.0

#(avg \pm std deviation)

Results and Discussion

The $\text{CO}_2/\text{H}_2\text{S}$ partial pressure ratio was in the range from 180 to 200 during the 21 day exposure. The comparison of pCO_2 to pH_2S is shown in shown in Figure 115.

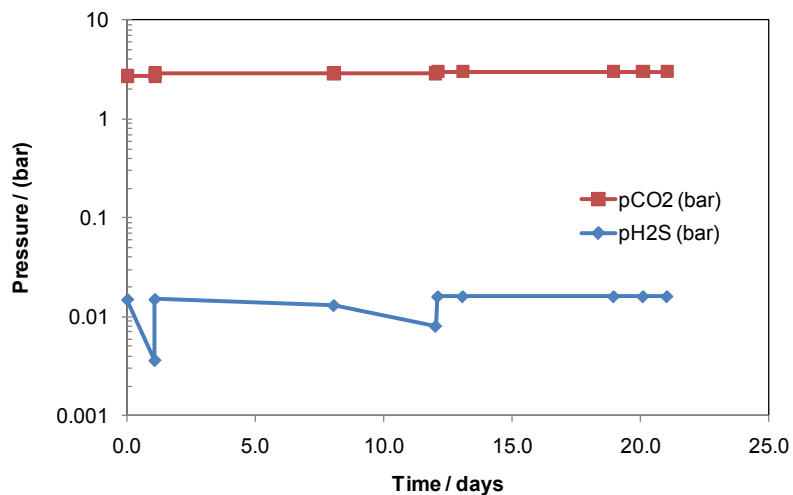


Figure 115. Partial pressure measurements for 60°C, pH 6, $\text{pCO}_2 = 2.8$ bar, $\text{pH}_2\text{S} = 10$ mbar, 1 wt% NaCl experiment

Weight loss measurements are shown in Figure 116 for the samples removed from the single phase flow test section and Figure 117 for the samples removed from multiphase flow test sections. Corrosion rates in single phase flow decreased with time and were all less than 1 mm/yr at 0.8, 0.6, and 0.2 mm/yr for 7, 14, and 21 days, respectively. Local corrosion penetration rates are indicated by the vertical error bar on each of the weight loss sample measurements and localized corrosion measured on the same coupons ranged from 1.3 to 2.9 mm/yr, with a pitting ratio of 3.3, 2.1, 7.1 for 7, 14, and 21 days, respectively.

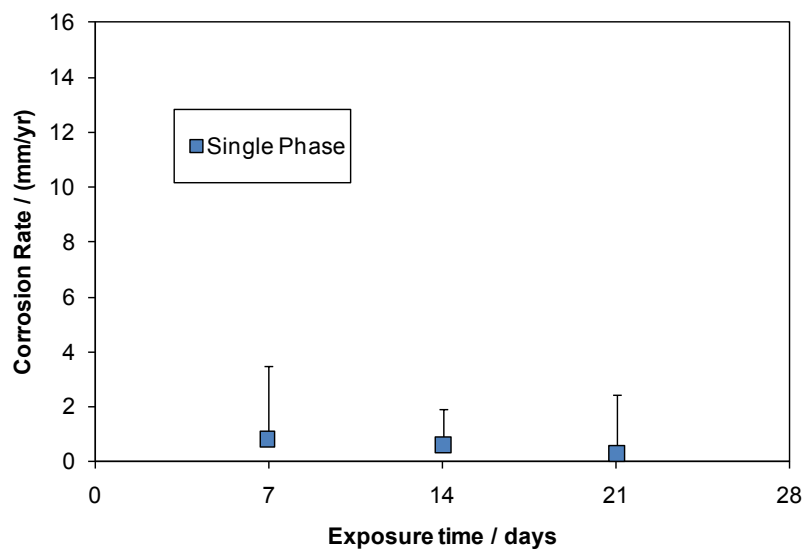


Figure 116. Single phase corrosion rate measurements. Weight loss + IFM for penetration rates. X65 steel, 60°C, pH 6, pCO₂ = 2.8 bar, pH₂S = 10 mbar, 1 wt% NaCl

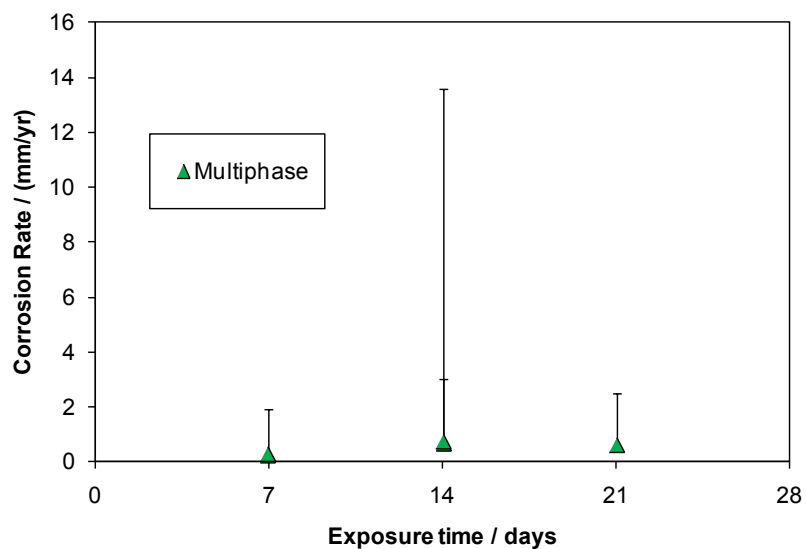


Figure 117. Multiphase corrosion rate measurements. Weight loss + IFM for penetration rates. X65 steel, 60°C, pH 6, pCO₂ = 2.8 bar, pH₂S = 10 mbar, 1 wt% NaCl

Multiphase samples had a similarly low general corrosion rate, averaging 0.5 mm/yr, but a localized corrosion location at 14 days of 0.49 mm is equal to a 12.8 mm/yr penetration rate and a pitting ratio of 17. Figure 118 shows that most of the samples experienced localized corrosion as 6 of 7 WL samples had pitting ratios greater than 3.

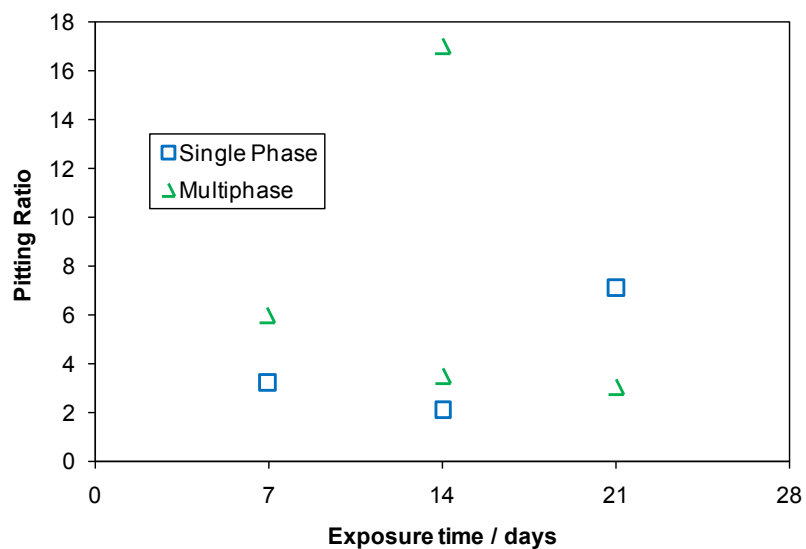


Figure 118. Pitting ratio for single phase and multiphase X65 steel weight loss coupons in 60°C, pH 6, $p\text{CO}_2 = 2.8$ bar, $p\text{H}_2\text{S} = 10$ mbar, 1 wt% NaCl

The SEM/EDS analyses of the corrosion product layer after 14 days are shown in Figure 119 and Figure 120 for single phase and Figure 121 for multiphase. An interesting feature found in both of these samples is where a part of the iron sulfide corrosion product layer has spalled off to reveal an iron carbonate layer underneath. EDS analysis of this layer beneath the iron sulfide shown in Figure 120 confirms the presence of the constituent elements of iron carbonate, the visual image is consistent with this analysis.

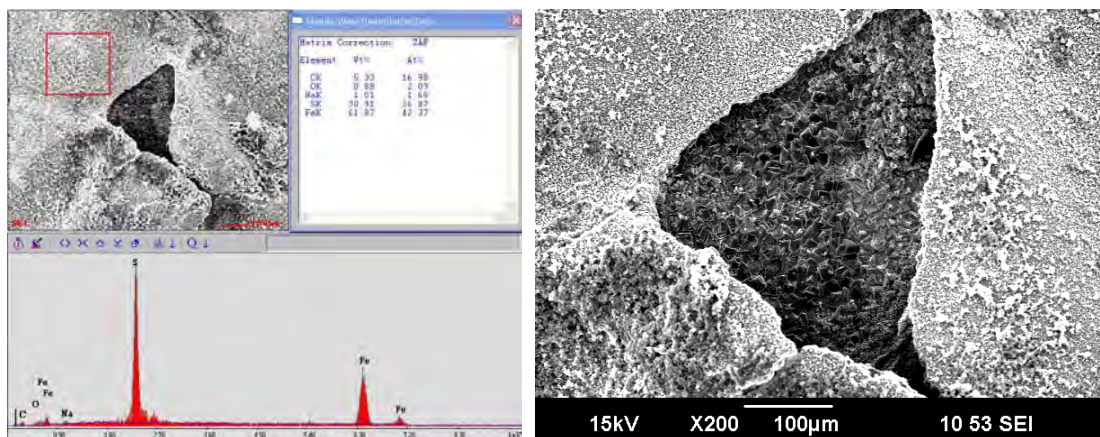


Figure 119. Exp 10. SEM / EDS analysis 14 day WL sample, iron sulfide corrosion product layer cover, 60°C, pH 6, $p\text{CO}_2 = 2.8$ bar, $p\text{H}_2\text{S} = 10$ mbar, 1 wt% NaCl

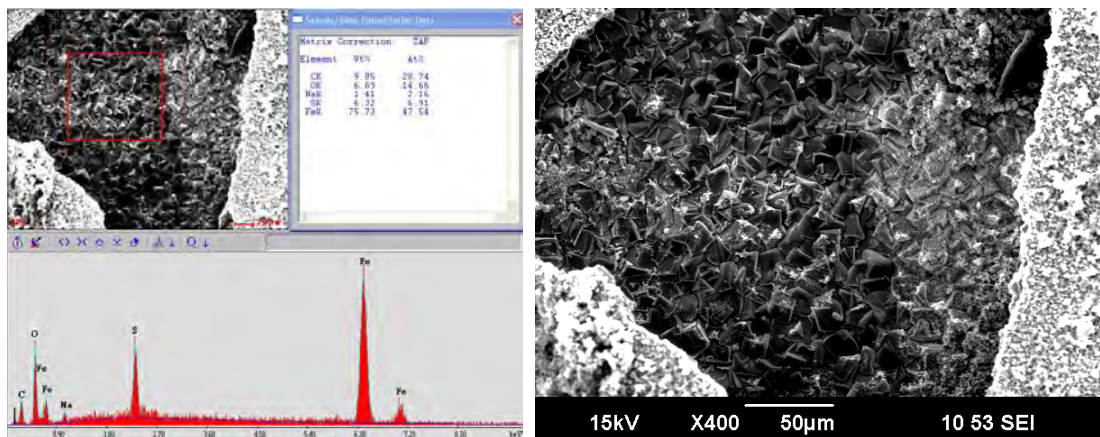


Figure 120. Exp 10. SEM / EDS analysis 14 day WL sample, iron carbonate dominated corrosion product "under" iron sulfide, 60°C, pH 6, $p\text{CO}_2 = 2.8$ bar, $p\text{H}_2\text{S} = 10$ mbar, 1 wt% NaCl

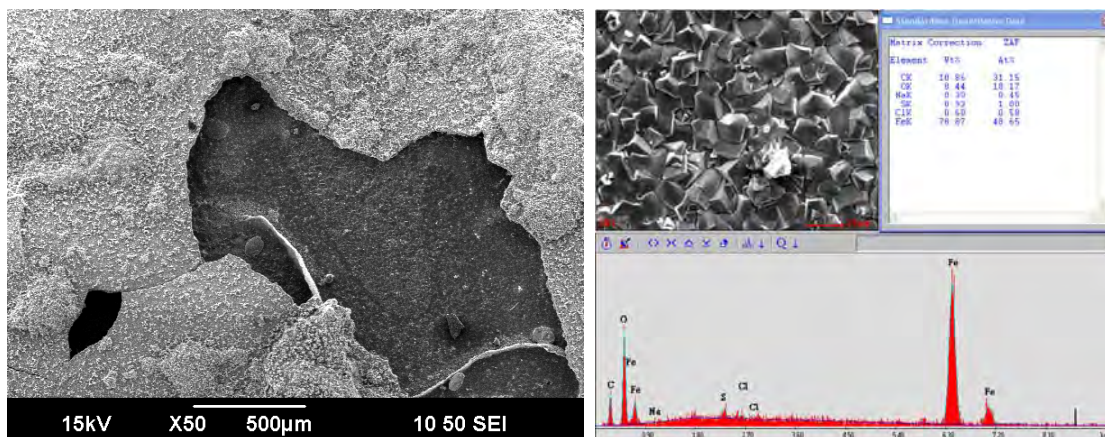


Figure 121. Exp 10. SEM / EDS analysis, Multiphase flow WL sample 14 days, iron sulfide exterior, iron carbonate interior, 60°C, pH 6, $p\text{CO}_2 = 2.8$ bar, $p\text{H}_2\text{S} = 10$ mbar, 1 wt% NaCl

The sulfide peak may be an indication that layer failure occurred *in situ*. After the corrosion product was removed, the topography of the metal substrate had areas with more metal loss as shown in Figure 122 and no distinct pit locations.

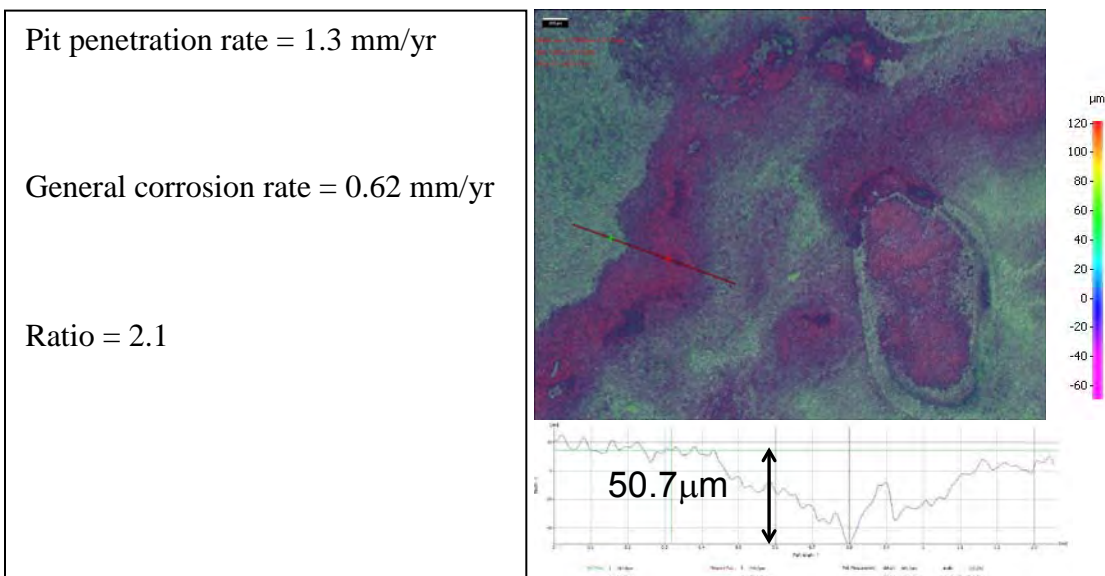


Figure 122. Exp 10. IFM analysis with corrosion product removed, 14 day sample, single phase flow, 60°C, pH 6, $p\text{CO}_2 = 2.8$ bar, $p\text{H}_2\text{S} = 10$ mbar, 1 wt% NaCl

The localized corrosion rate was calculated to be 1.3 mm/yr when the WL corrosion rate was only 0.6 mm/yr, giving a pitting ratio of 2.1. The multiphase sample surface in Figure 121 shows the same loss of iron sulfide corrosion product to reveal iron carbonate crystals, but only shows a trace of sulfide in the EDS analysis. Upon closer examination of Figure 123, the large iron carbonate crystals are dominant over the moss-like iron sulfide features seen mainly in the lower right corner near the one possible void space in the iron carbonate layer leading to the substrate.

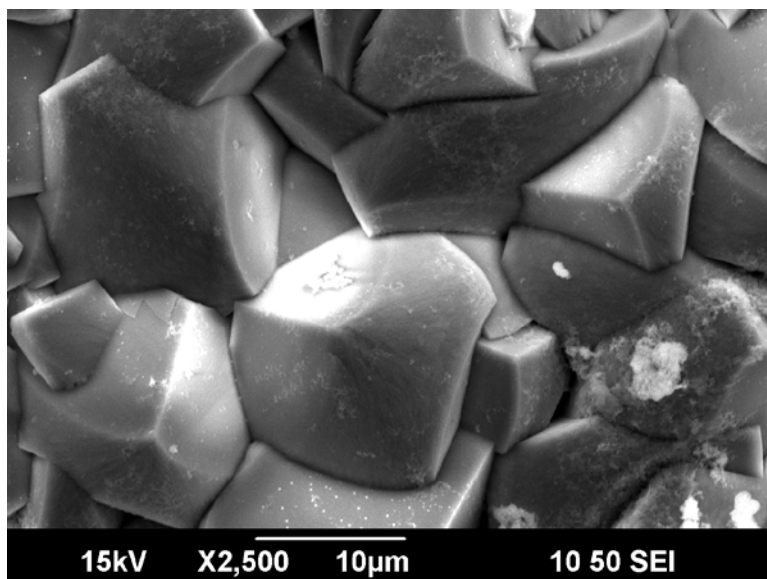


Figure 123. Exp 10. SEM of iron carbonate crystals, Multiphase flow WL sample 14 days, iron sulfide exterior, iron carbonate interior, 60°C, pH 6, $p\text{CO}_2 = 2.8$ bar, $p\text{H}_2\text{S} = 10$ mbar, 1 wt% NaCl

When the test solution is at pH 6, previous tests have seen an excess corrosion product layer growth at a point of localized corrosion and this test was no exception. The

IFM analysis of the WL sample with the corrosion product layer in Figure 124, shows a raised area of material with a local failure. The measurement from the top of the raised area to the bottom of the failure is approximately 670 μm . When the corrosion product is removed, the same area in Figure 125 shows a severe type of localized corrosion. With a general corrosion rate of only 0.75 mm/yr, the pit corrosion depth of over 490 μm was calculated to be 12.8 mm/yr and has a pitting ratio of 17.

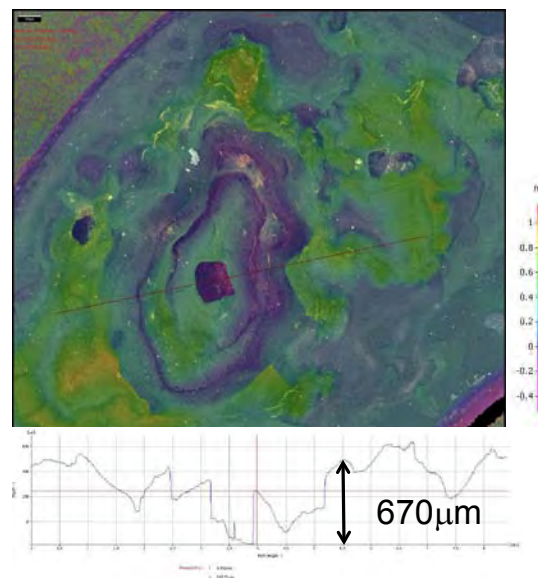


Figure 124. Exp 10. IFM of sample WITH corrosion product layer showing growth and failure leading to localized corrosion, Multiphase flow WL sample 14 days, 60°C, pH 6, $p\text{CO}_2 = 2.8$ bar, $p\text{H}_2\text{S} = 10$ mbar, 1 wt% NaCl

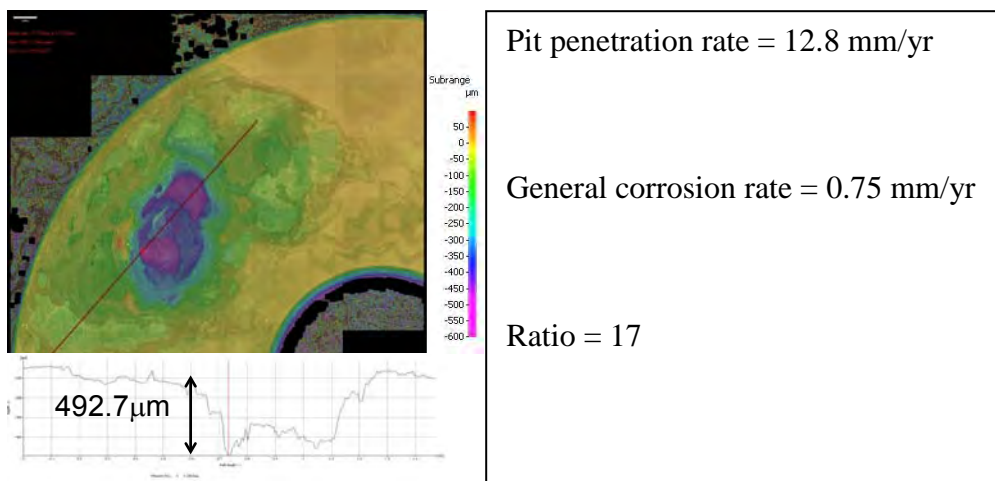


Figure 125. Exp 10. IFM of sample WITHOUT corrosion product layer showing growth and failure leading to localized corrosion, Multiphase flow WL sample 14 days, 60°C, pH 6, pCO₂ = 2.8 bar, pH₂S = 10 mbar, 1 wt% NaCl

WL samples exposed for the whole 21 day experiment time did not show excessive general corrosion or pitting corrosion, but were still conformed as having excess corrosion product where the localized corrosion occurred. An interesting type of iron sulfide was observed from the single phase test where small ‘nodes’ of iron sulfide about 50 to 100 μm in diameter grew randomly across the surface (Figure 126). Closer visual analysis of these ‘nodes’ (Figure 127) show small crystalline structures similar to the rest of the iron sulfide layer. After removal of the corrosion product by Clarke solution (Figure 128), localized pitting was observed in relative proportion to the nodes that were on the surface. With a general corrosion rate of 0.3 mm/yr, the pit depth measurement of 122.7 μm is equivalent to a 2.1 mm/yr pit penetration rate for a pitting ratio of 7.

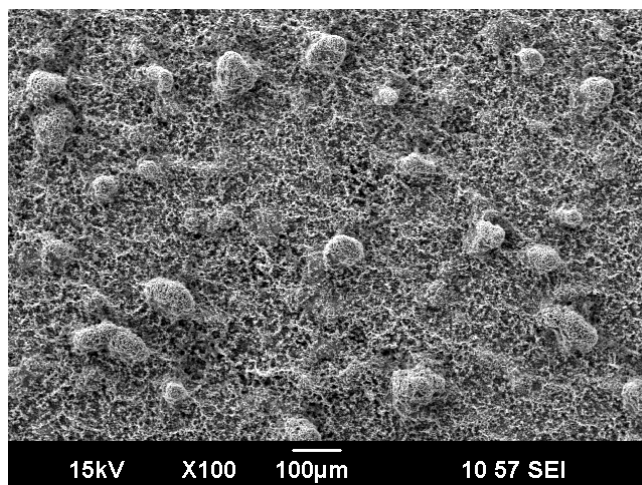


Figure 126. Exp 10. SEM of iron sulfide layer growth, Single phase flow, 21 days, 60°C, pH 6, $p\text{CO}_2 = 2.8$ bar, $p\text{H}_2\text{S} = 10$ mbar, 1 wt% NaCl

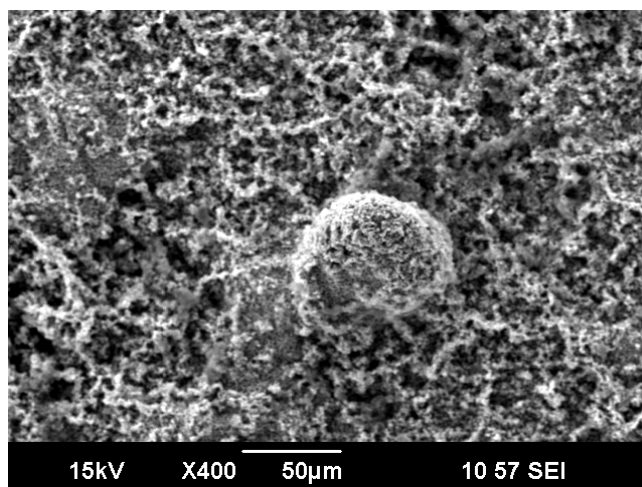


Figure 127. Exp 10. Close up image for SEM of iron sulfide layer growth, Single phase flow, 21 days, 60°C, pH 6, $p\text{CO}_2 = 2.8$ bar, $p\text{H}_2\text{S} = 10$ mbar, 1 wt% NaCl

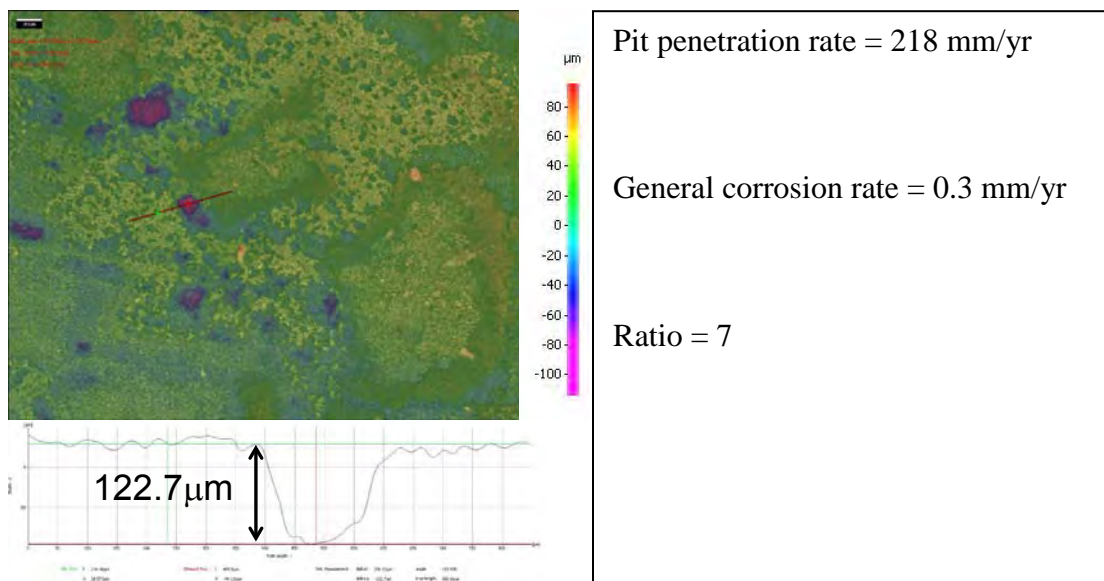


Figure 128. Exp 10. IFM analysis of sample WITHOUT corrosion product layer, Single phase flow, 21 days, 60°C, pH 6, pCO₂ = 2.8 bar, pH₂S = 10 mbar, 1 wt% NaCl

Another interesting feature of the corrosion product layer was observed in the cross section of a second WL sample taken from the single phase flow after 21 days. Most of the surface was still covered with a thin, adherent layer of approximately 5 to 10 μm which would have limited the general corrosion across the surface. This thin layer can be observed in Figure 129 on the extreme right and left of the image. The localized corrosion location shows the growth of corrosion product layer and upon closer examination in Figure 130, the continued growth of iron sulfide is observed as a light color change in the epoxy above the corrosion product. Smith *et al.*⁵⁰ have described this type of corrosion product as a “fluffy mackinawite.”

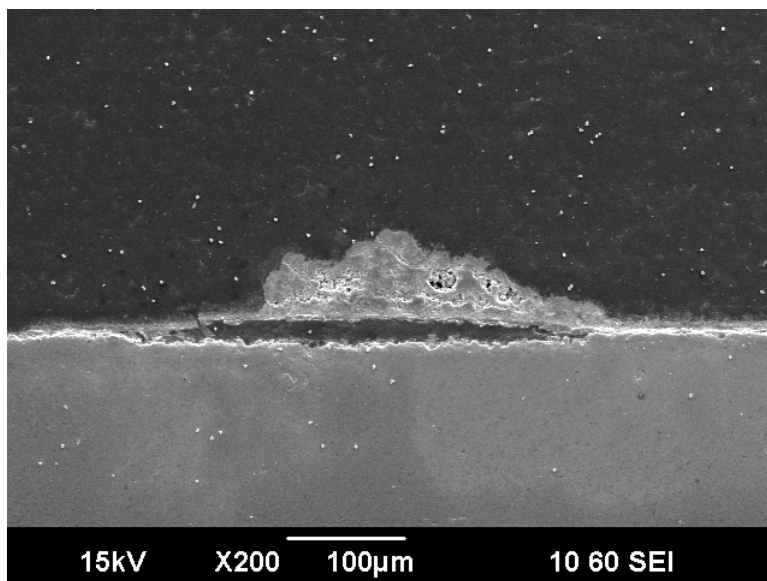


Figure 129. SEM cross-section analysis view of localized corrosion, Single phase flow, 21 days, 60°C, pH 6, $p\text{CO}_2 = 2.8$ bar, $p\text{H}_2\text{S} = 10$ mbar, 1 wt% NaCl, Thin adherent layer, (10 mm) with 'fluffy mackinawite' on top, failed as seen by the loss of material under the layer.

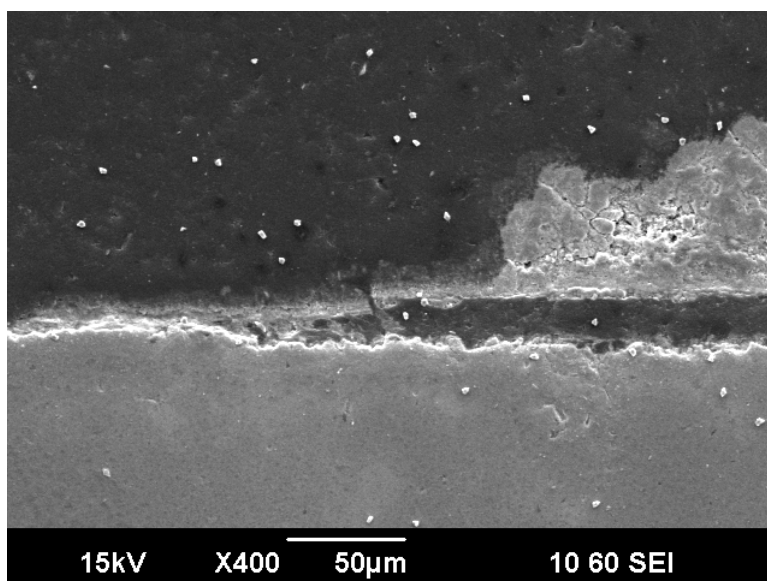


Figure 130. Exp 10. Close up view of SEM cross-section analysis view of localized corrosion, Single phase flow, 21 days, 60°C, pH 6, $p\text{CO}_2 = 2.8$ bar, $p\text{H}_2\text{S} = 10$ mbar, 1 wt% NaCl, Fluffy mackinawite seen on top of corrosion product buildup, possible fracture in layer.

What was not seen in any of the corrosion product analysis for these test conditions was the presence of the original polish marks on the top surface. This is of great interest because the changes in bulk chemistry parameters of this test have caused a change in the layer growth mechanisms.

Experiment 11: 40°C, $p\text{CO}_2 = 2.9$ bar, $p\text{H}_2\text{S} = 0.004$ bar, pH 5.0, 1wt% NaCl

Introduction

The parameters of this test represent (Table 24) a decrease in temperature, flow velocities, and partial pressure of H_2S as compared to Experiment 10.

Table 24. Controlled Parameters for Effect of Corrosion Product Layer test at 4 mbar pH_2S and 1 wt% NaCl.

Parameter	Description
Equipment	H_2S Flow Loop
Test duration	21 days
Temperature	40.7 ± 0.9 °C
$p\text{CO}_2$	2.8 ± 0.2 bar
$p\text{H}_2\text{S}$	0.004 ± 0.0005 bar
pH	5.0 ± 0.0
Solution	1 wt% NaCl
Ionic strength	0.177 ± 0.0004
$[\text{Fe}^{++}]$ (ppm)	101 ± 7.4
S(FeCO_3)	1.1 ± 0.2
S(FeS)	5.3 ± 1.2
S(FeS)/S(FeCO_3)	5.0 ± 0.9

[#](avg \pm std deviation)

Results and Discussion

The comparison of $p\text{CO}_2$ to $p\text{H}_2\text{S}$ is shown in Figure 131. The $\text{CO}_2/\text{H}_2\text{S}$ partial pressure ratio was in the range from 700 to 1000 during the 21 day exposure, but averaged 770. Weight loss measurements are shown in Figure 132 for the samples removed from the single phase flow test section and Figure 133 for the samples removed from multiphase flow test sections.

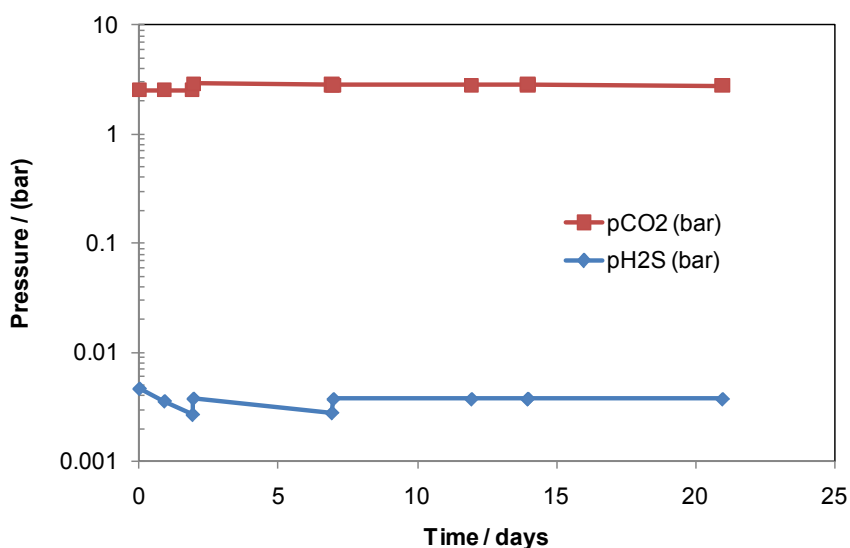


Figure 131. Partial pressure measurements for 21 day experiment with lower partial $p\text{CO}_2$, lower partial $p\text{H}_2\text{S}$, lower temperature, lower pH, lower flow rate, 40°C pH 5, 2.9 bar $p\text{CO}_2$, 4 mbar $p\text{H}_2\text{S}$

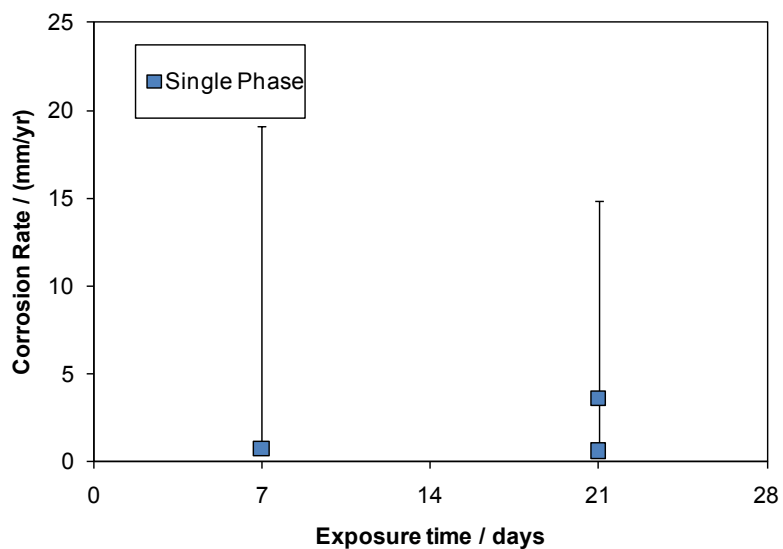


Figure 132. Single phase corrosion rate measurements. Weight loss + IFM for penetration rates. X65 steel, 40°C, pH 5, pCO₂ = 2.8 bar, pH₂S = 4 mbar, 1 wt% NaCl

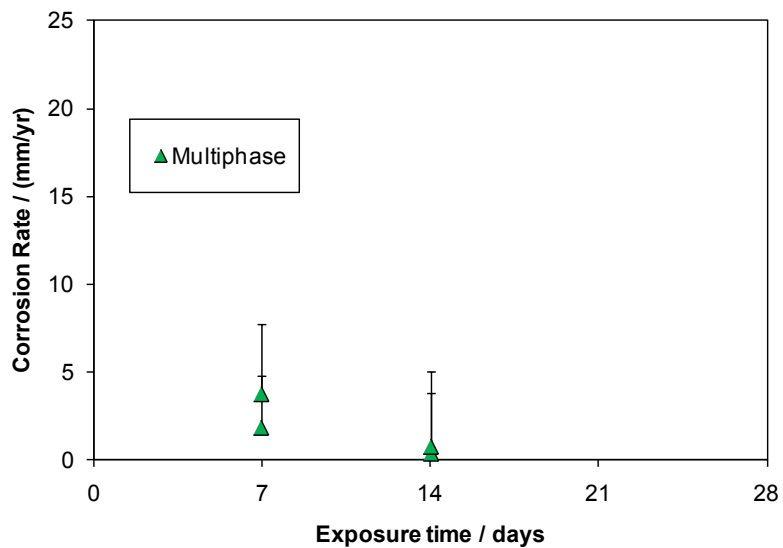


Figure 133. Stratified flow corrosion rate measurements. Weight loss + IFM for penetration rates. X65 steel, 40°C, pH 5, pCO₂ = 2.8 bar, pH₂S = 4 mbar, 1 wt% NaCl

General corrosion rates for all samples range from 0.35 mm/yr to 3.7 mm/yr with no direct relationship to exposure time or location. The WL samples from single phase

flow show the highest pitting penetration rates of 18.4 mm/yr at 7 days and 11.3 mm/yr at 21 days. The comparison of pitting ratios for this experiment (Figure 134) show that 2/3 of the WL samples had significant localized corrosion, but the larger pitting ratios occurred at 7 and 14 days.

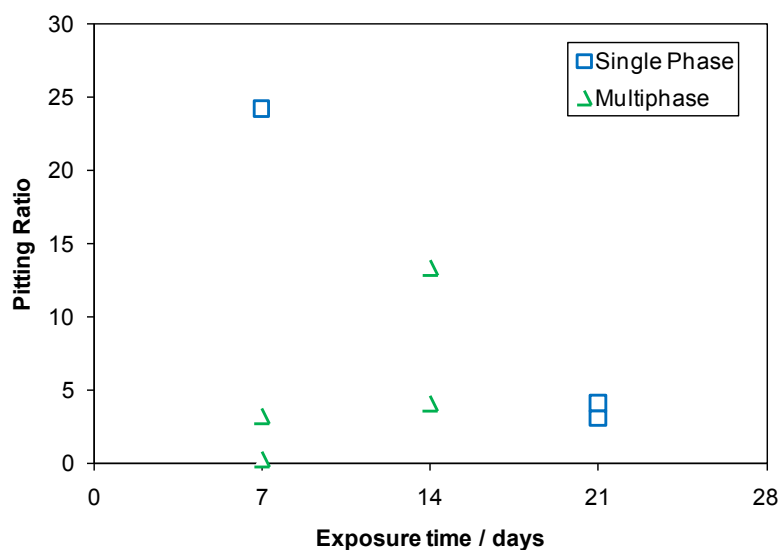


Figure 134. Pitting ratio for single phase and stratified flow X65 steel weight loss coupons in 40°C, pH 5, pCO₂ = 2.8 bar, pH₂S = 4 mbar, 1 wt% NaCl

Similar types of corrosion product layer and failures were observed for samples from 7 days and 21 days exposure. After 7 days, circular failure locations were observed as shown in Figure 135 and Figure 136 that were 100 to 150 μm in diameter, but only affected a small portion of the surface layer. The rest of the iron sulfide layer around the failure locations still has the original polish marks as seen in Figure 137.

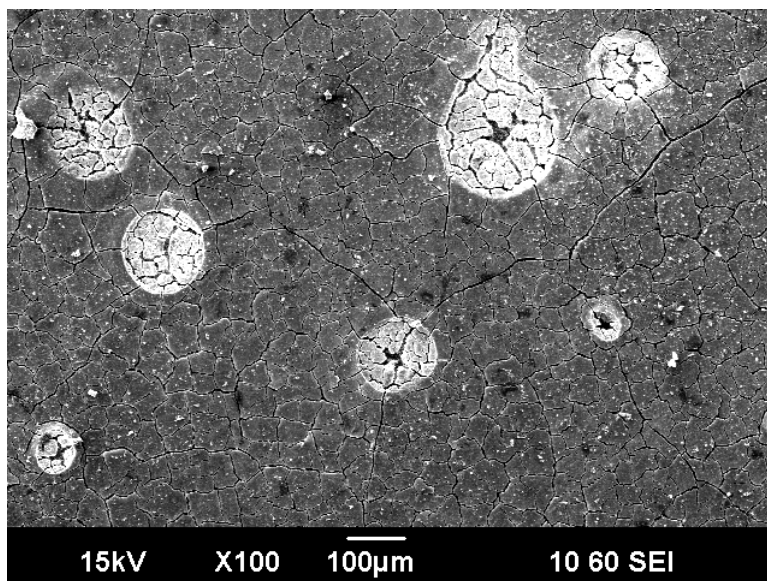


Figure 135. Exp 11. Local layer failures found after 7 day exposure, Single phase flow, 40°C, pH 5, $p\text{CO}_2 = 2.8$ bar, $p\text{H}_2\text{S} = 4$ mbar, 1 wt% NaCl

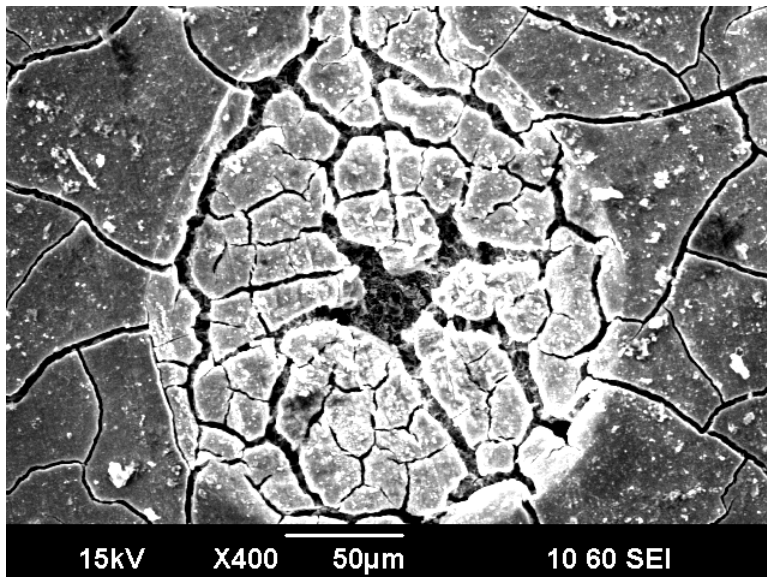


Figure 136. Exp 11. Close up of local corrosion product layer failure found after 7 day exposure, Single phase flow, 40°C, pH 5, $p\text{CO}_2 = 2.8$ bar, $p\text{H}_2\text{S} = 4$ mbar, 1 wt% NaCl

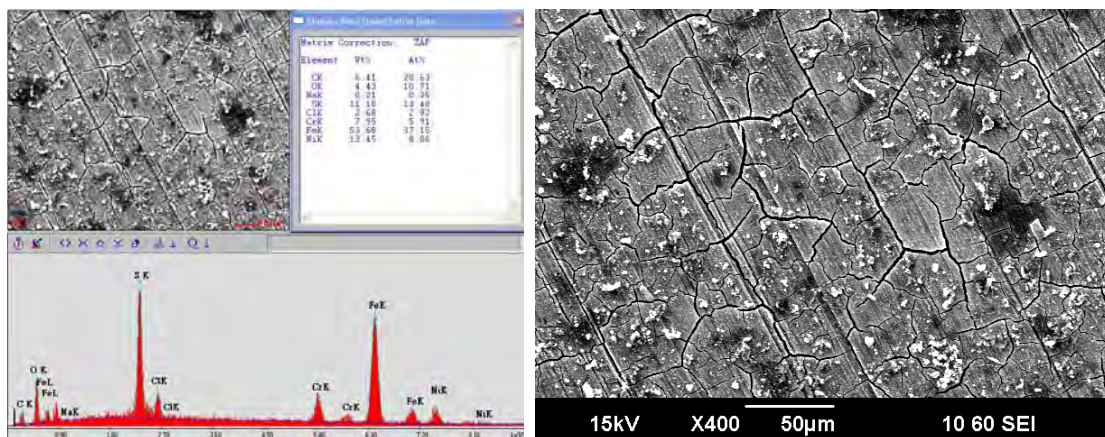


Figure 137. Exp 11. SEM / EDS of WL sample, corrosion product layer showing polish marks of original corrosion product, 7 days, 40°C, pH 5, $p\text{CO}_2 = 2.8$ bar, $p\text{H}_2\text{S} = 4$ mbar, 1 wt% NaCl

With the corrosion product removed, IFM analysis in Figure 138 of one large pit location was found with a 600 µm diameter and 350 µm depth. This equated to an 18.4 mm/yr penetration rate and the pitting ratio of 24. Notice the 3 to 6 smaller circular pits surrounding the large pit. These smaller pits have a diameter of 50 to 150 µm, similar to the size of the failure locations shown in Figure 135 and Figure 136.

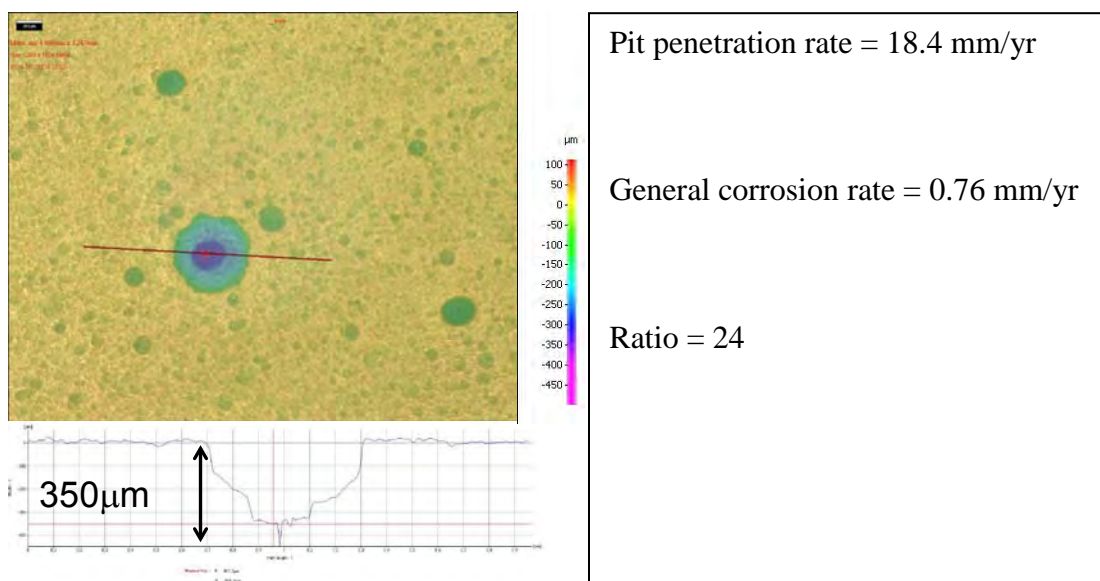


Figure 138. Exp 11. IFM of WL sample WITHOUT corrosion product layer. stratified flow, 40°C, pH 5, pCO₂ = 2.8 bar, pH₂S = 4 mbar, 1 wt% NaCl, 7 days.

This same type of corrosion mechanism is seen to occur in the later WL samples at 21 days. Two separate examples of corrosion product layer failure from the sample in stratified flow can be seen in Figure 139. These measure at approximately 850 µm in diameter and were in multiple locations on the surface of the WL sample. Comparison to the substrate localized corrosion is shown by the IFM analysis in Figure 140. The pit measures 1.15 mm diameter by 745 µm in depth. This is equivalent to a pit penetration rate of 12.5 mm/yr.

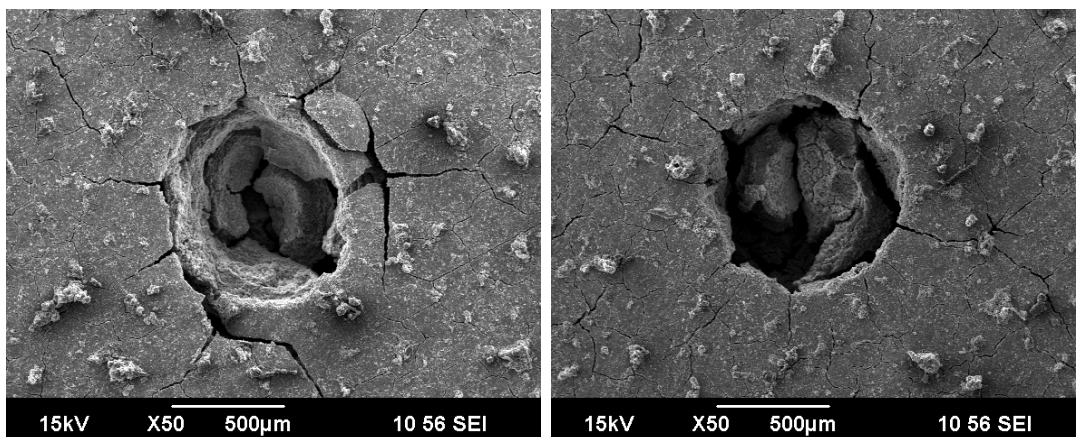


Figure 139. Exp 11. Two separate examples of corrosion product layer failure from stratified flow, 21 days, 40°C, pH 5, $p\text{CO}_2 = 2.8$ bar, $p\text{H}_2\text{S} = 4$ mbar, 1 wt% NaCl

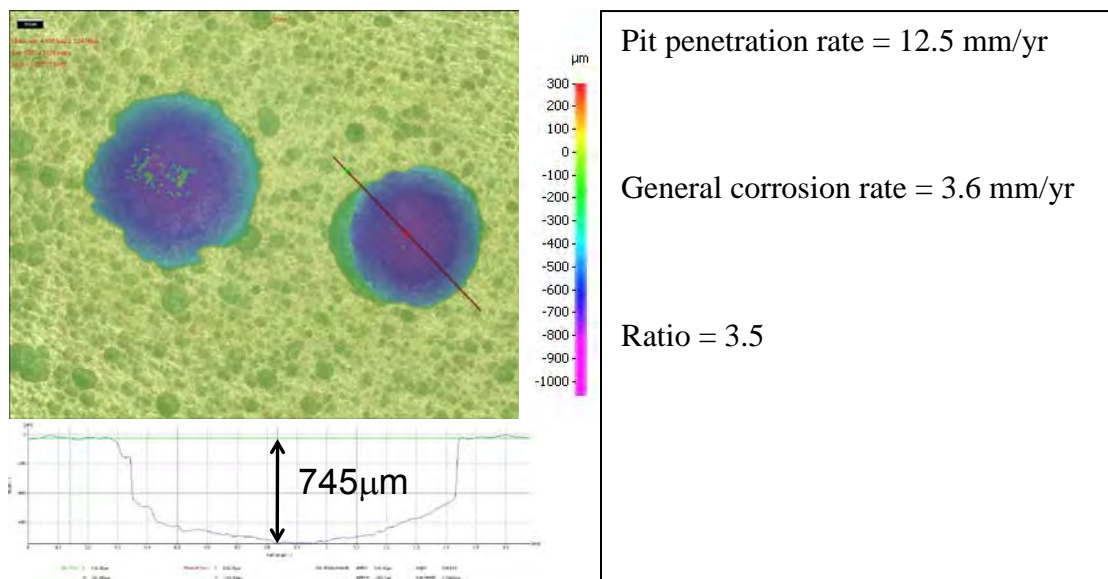


Figure 140. Exp 11. IFM of WL sample WITHOUT corrosion product layer, 21 days, stratified flow, 40°C, pH 5, $p\text{CO}_2 = 2.8$ bar, $p\text{H}_2\text{S} = 4$ mbar, 1 wt% NaCl

With a general WL corrosion rate of 3.6 mm/yr, the pitting ratio is 3.5. In this case, the marginal pitting ratio is due to the high general corrosion rate and may be misleading. This case may be one to consider adding the high general corrosion rate to the pit penetration rate for a maximum localized corrosion since both values are high and

the localized corrosion was not widespread enough to affect the general corrosion WL measurement.

The sample from the 21 day exposure to single phase flow has developed a morphologically different iron sulfide corrosion product, but with the same overall result.

Figure 141 shows a view of the iron sulfide corrosion product covering the surface.

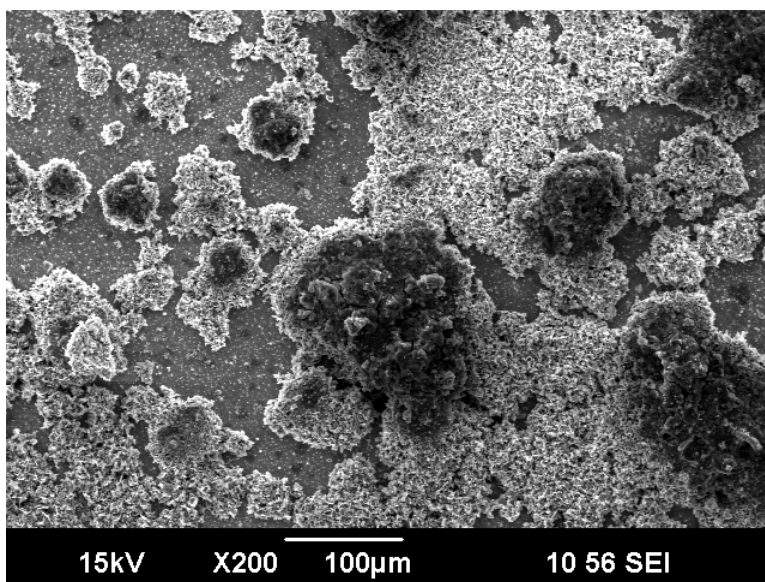


Figure 141. Exp 11. Corrosion product layer, 21 days, single phase flow, 40°C, pH 5, $p\text{CO}_2 = 2.8$ bar, $p\text{H}_2\text{S} = 4$ mbar, 1 wt% NaCl

Everything in the SEM image has a high content of sulfides, but the light colored areas of crystal growth have an EDS of specifically Fe and S. Higher magnification images of Figure 142 and Figure 143 show this as a crystal structure observed for mackinawite (Smith *et al.*⁵⁰) referred to as “lettuce leaf” because of its shape.

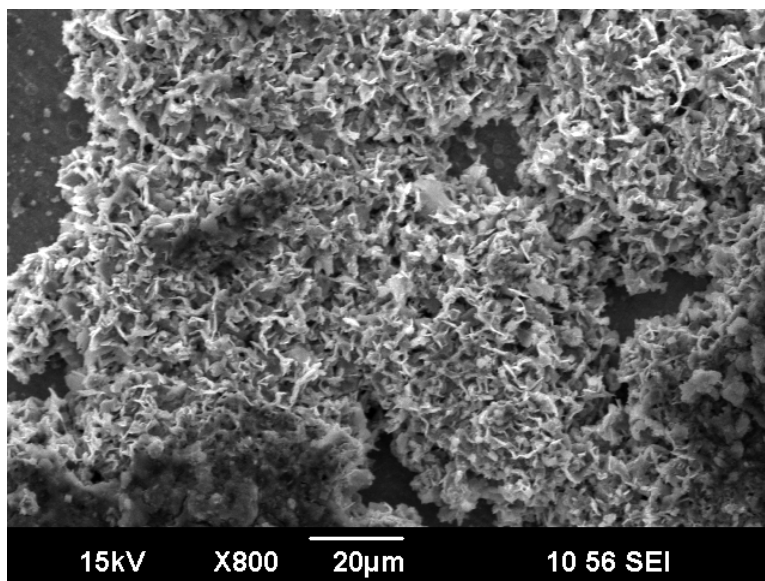


Figure 142. Exp 11. Iron sulfide corrosion product layer, 21 days, single phase flow, 40°C, pH 5, $p\text{CO}_2 = 2.8$ bar, $p\text{H}_2\text{S} = 4$ mbar, 1 wt% NaCl

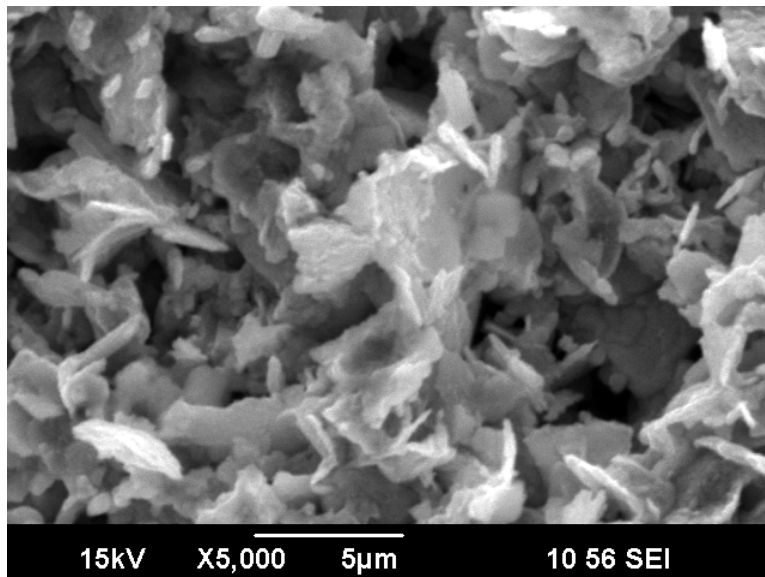


Figure 143. Exp 11. "Lettuce Leaf Mackinawite," Corrosion product layer, 21 days, single phase flow, 40°C, pH 5, $p\text{CO}_2 = 2.8$ bar, $p\text{H}_2\text{S} = 4$ mbar, 1 wt% NaCl

On the flat areas of the same WL sample, the original polish marks can still be observed in Figure 144. With the corrosion product removed (Figure 145), areas under

the crystal structures of mackinawite show 2.7 mm/yr penetration rates giving a pitting ratio of 4.1 for this sample.

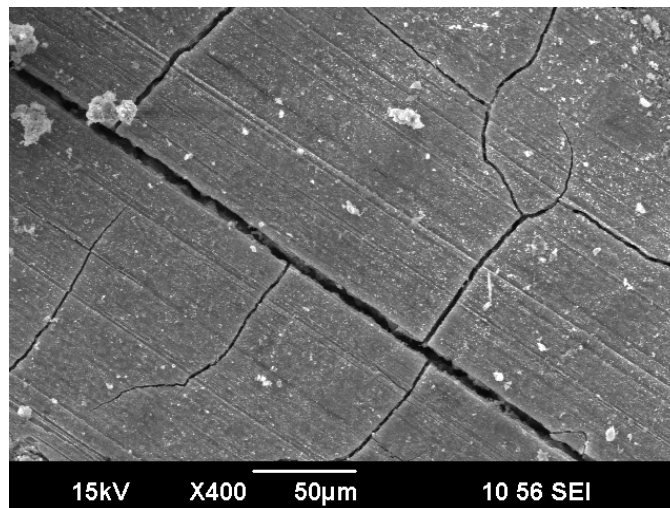


Figure 144. Exp 11. Iron sulfide corrosion product layer, same sample, different location, 21 days, single phase flow, 40°C, pH 5, $p\text{CO}_2 = 2.8$ bar, $p\text{H}_2\text{S} = 4$ mbar, 1 wt% NaCl

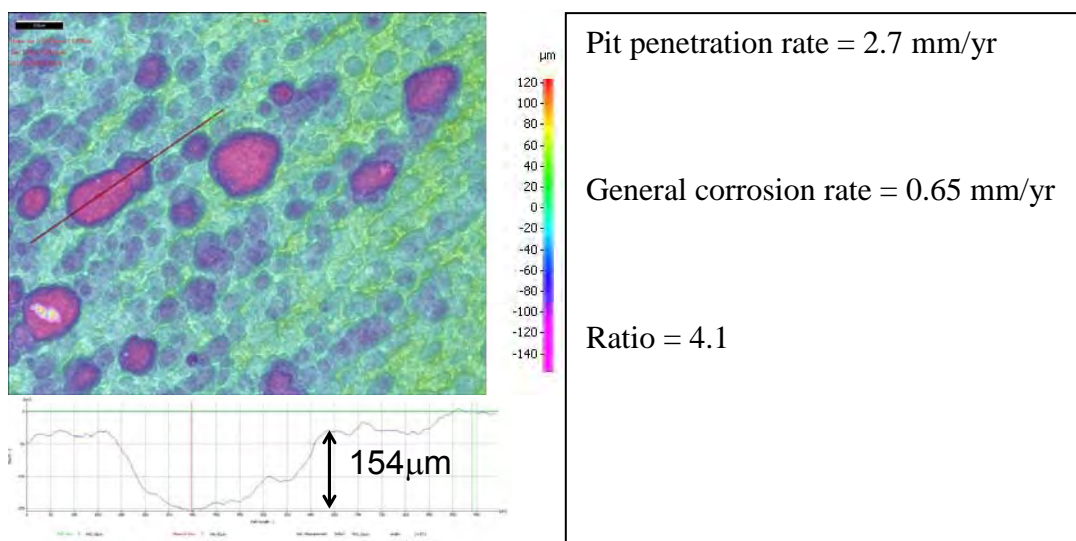


Figure 145. Exp 11. IFM analysis without corrosion product layer, 21 days, single phase flow, 40°C, pH 5, $p\text{CO}_2 = 2.8$ bar, $p\text{H}_2\text{S} = 4$ mbar, 1 wt% NaCl

Conclusions Related to $p\text{CO}_2$

A dramatic decrease in the partial pressure of CO_2 was expected to limit the likelihood of developing iron carbonate as a recognizable species in the corrosion product layer, but it did just the opposite. Experiment 10, which tested a decrease in $p\text{CO}_2$ as compared to Experiment 4, has shown almost identical results to Experiment 4. In both cases:

- Polish marks were not an obvious feature in the corrosion product layer,
- An iron carbonate corrosion product layer was observed underneath the iron sulfide corrosion product layer on multiple samples, and
- Localized corrosion was observed where corrosion product layer growth had exceeded that of the surrounding area.

And a combination of lowering the temperature, pH, and $p\text{H}_2\text{S}$ was expected to reduce precipitation of both FeCO_3 and FeS to increase the likelihood of localized corrosion. In this case, Experiment 11 was similar to Experiment 7 which was conducted at pH 5, where:

- Observations of original surface features (polish marks) in micron thick corrosion product layers indicate that a thin corrosion product initially formed, but allowed corrosion to continue underneath, and
- Localized corrosion was observed where failures in the corrosion product layer could be related to locations of metal loss underneath.

These two experiments strengthen the conclusion that solution pH has more influence on the corrosion product layer than the partial pressures of CO₂ and H₂S under the range of conditions tested.

Effect of a Decrease in Temperature

Introduction

Review of the parameter combinations used in the series of experiments up to this point had shown a need for testing at lower temperatures in order to fill in gaps in the experimental design. The current research (Table 25) was conducted to fill in the gaps of knowledge at pH 5.0 by using lower temperatures, lower flow rates, and increased partial pressure of H₂S.

Table 25. Test Matrix – Effect of a Decrease in Temperature

Parameter	Exp. 13	Exp. 14
Temperature	25°C	40°C
Total Pressure	3 bar	3 bar
pCO ₂	2 bar	2 bar
Flow	Vsl = 0.1 m/s, Vsg = 3.0 m/s	Vsl = 0.1 m/s, Vsg = 3.0 m/s
NaCl solution	1 wt%	1 wt%
pH	5.0	5.0
pH ₂ S (mBar)	100	100
Measurements	WL, SEM	WL, SEM
Exposure Time	7, 14, 21 days	7, 14, 21 days

The lower temperatures are expected to slow the reaction kinetics while the increase in pH₂S along with the decrease in pCO₂ will provide an H₂S dominated environment with the intention to increase the likelihood of localized corrosion. The lower flow rate was also assumed to influence more growth of the corrosion product layer, but little difference was observed by this parameter. The probe arrangement, installation procedure, and the timing of sample removal are previously described in Chapter 3.

Experimental Observations

Experiment 13: 25°C, pCO₂ = 2.8 bar, pH₂S = 0.10 bar, pH 5.0, 1wt% NaCl

Introduction

The temperature in this experiment was controlled at 25°C using heat exchangers available in the H₂S flow loop to show the effect of a lower temperature on the corrosion reactions occurring in a CO₂/H₂S environment (Table 26). With a decrease in temperature, the kinetics of the reactions are slowed, but the change in the rate or area of the initial coverage of FeS on the metal surface is expected to be negligible.⁵ The increase in [CO₂]_{aq} and [H₂S]_{aq} by the decrease in temperature and increase in pH₂S, respectively, are expected to challenge the initial coverage layer of FeS to cause breakdown and increase the possibility of localized corrosion.

Table 26. Exp 13. Controlled Parameters for the Effect of Temperature at 2.8 bar pCO₂, and 100 mbar pH₂S.

Parameter	Description
Equipment	H ₂ S Flow Loop
Test duration	21 days
Temperature	25.1 ± 0.1 °C
pCO ₂	2.8 ± 0.0 bar
pH ₂ S	0.10 ± 0.03 bar
pH	5.0 ± 0.0
Solution	1 wt% NaCl
Ionic strength	0.178 ± 0.001
[Fe ⁺⁺] (ppm)	10 ± 3
S(FeCO ₃)	0.14 ± 0.03
S(FeS)	11.5 ± 5.1
S(FeS)/S(FeCO ₃)	81 ± 28

[#](avg ± std deviation)

Results and Discussion

The conditions tested were 25°C, $p\text{CO}_2 = 2.8$ bar, $p\text{H}_2\text{S} = 100$ mbar, 1 wt.% NaCl, pH 5.0 for 7, 14 and 21 days exposure for weight loss samples. The general weight loss and IFM measured penetration rate of all the samples are shown for single phase flow in Figure 146 and for multiphase flow in Figure 147. Both data sets show general corrosion rates between 1 and 2 mm/yr with equivalent IFM penetration rates. Since the penetration rates are approximately equivalent to the weight loss corrosion rates, no localized corrosion was observed in this experiment.

Figure 148 confirms the pitting ratios for all weight loss samples was less than 3 and, therefore, are not considered to have localized corrosion.

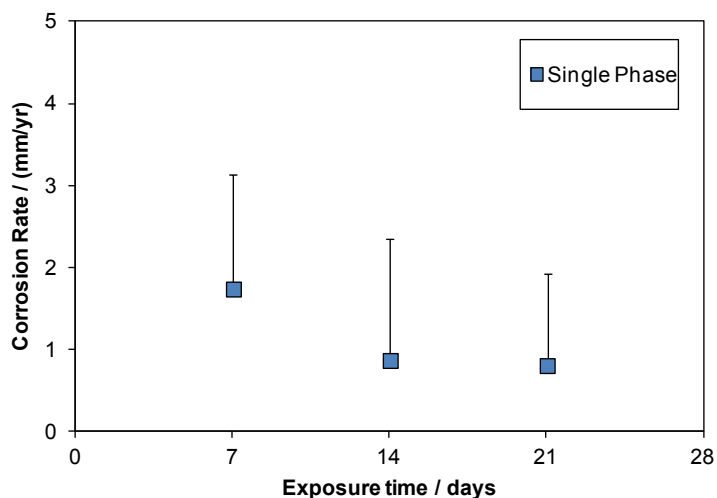


Figure 146. General corrosion (squares), as well as “localized” corrosion from IFM (single sided error bars), from weight loss of samples exposed to single phase flow in 25°C, $p\text{CO}_2 = 2.8$ bar, $p\text{H}_2\text{S} = 100$ mbar, 1 wt.% NaCl.

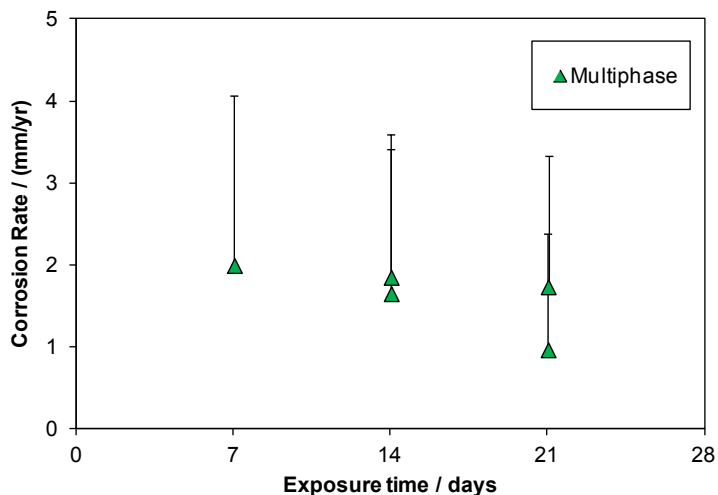


Figure 147. General corrosion (triangles), as well as “localized” corrosion from IFM (single sided error bars), rates from weight loss samples exposed to multiphase flow in 25°C, $p\text{CO}_2 = 2.8$ bar, $p\text{H}_2\text{S} = 100$ mbar, 1 wt.% NaCl.

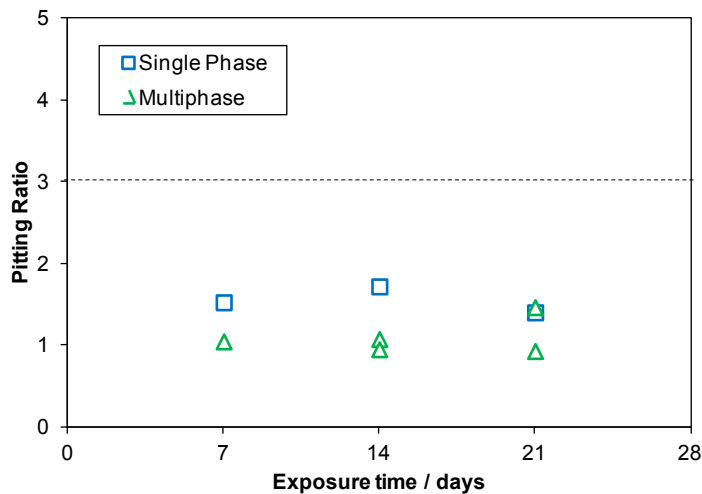


Figure 148. Pitting ratio for weight loss samples exposed in 25°C, $p\text{CO}_2 = 2.8$ bar, $p\text{H}_2\text{S} = 100$ mbar, 1 wt.% NaCl.

Scaling Tendency

Since corrosion product layer growth is considered an important characteristic, the mass of the corrosion product remaining on the weight loss samples was converted to a layer thickness assuming the density is 4.84 g/cm^3 and the available surface area of the sample is 7.6 cm^2 . The importance of Figure 149 is to show that the corrosion product layer is still developing over the entire 21 day experiment.

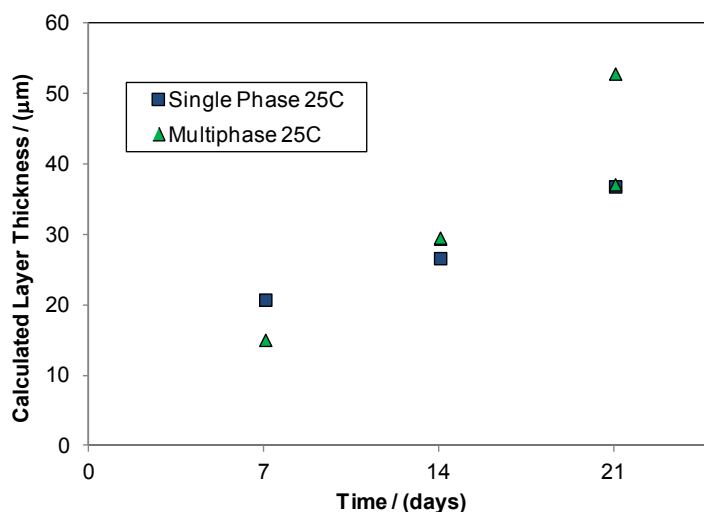


Figure 149. Corrosion product layer growth vs. time. 25°C , $p\text{CO}_2 = 2.8 \text{ bar}$, $p\text{H}_2\text{S} = 100 \text{ mbar}$, $1 \text{ wt.}\% \text{ NaCl}$.

Scaling tendency (ST%) is a comparison of corrosion rate (CR) and scale retention rate (SRR) in the same molar units and is a reflection of how much of the iron lost from corrosion is retained in the corrosion product scale. The value is calculated according to Equation (33). Sun⁵ hypothesized that approximately half of the sulfide

layer that forms due to corrosion in an H_2S/N_2 system is lost from the steel surface due to spalling or mechanical means so that ST% is assumed to be 50%.

$$ST\% = \frac{\text{Scale_Retention_Rate_}(mol/hr/m^2)}{\text{General_Corrosion_Rate_}(mol/hr/m^2)} \times 100 \quad (33)$$

Although not exactly 50%, Figure 150 shows agreement with the hypothesis for samples taken from 14 and 21 days in single phase flow.

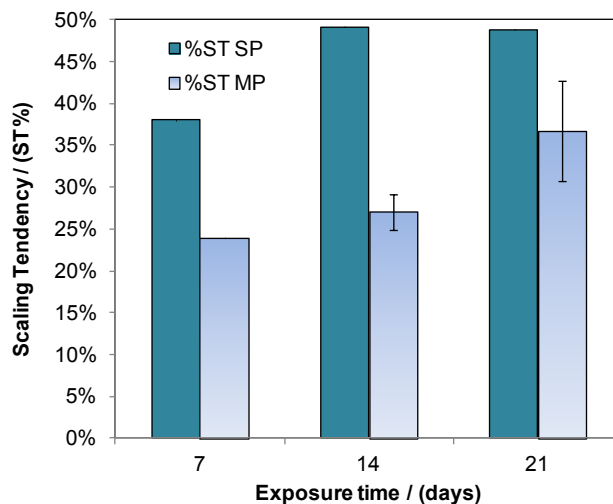
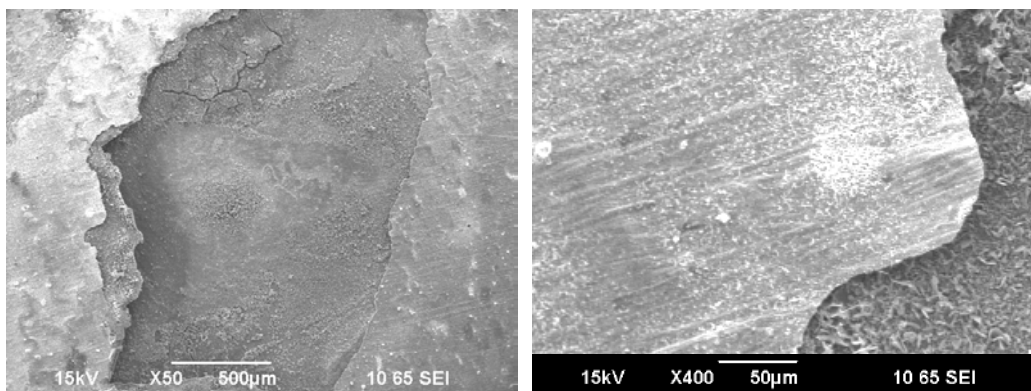


Figure 150. Scaling Tendency for $25^\circ C$, $pCO_2 = 2.8$ bar, $pH_2S = 100$ mbar, 1 wt.% NaCl.

Specific examples from the WL samples showing the corrosion product layer and subsequent corrosion of the substrate will be used to highlight key aspects of this experiment.

Corrosion product layer at 7 days (Single Phase Flow).

Figure 151 through Figure 154 show examples of the corrosion product surface features found on the weight loss sample taken after 7 days of exposure to the single phase flow test conditions at 25°C. The first characteristic noticed is that there are *multiple layers of corrosion product* underneath the original corrosion product surface. The original corrosion product surface is defined by the fact that the *original sample surface polish marks* are still visible on corrosion product layer. This layer is representative of the first initial reaction between H₂S and the metal surface to form a mass transfer limiting layer which is so thin it mimics the exact surface features of the metal. This iron sulfide layer, which is considered to be mackinawite under these conditions, continues to grow based on the environmental conditions. Figure 151 shows a fractured edge of the corrosion product on the left side of the 50X SEM image, an area where some corrosion product was lost in the center, and then the top layer again on the left side of the image. It is difficult to determine if the loss of the corrosion product layer in the center occurred in situ or in the removal and analysis procedures, but it does show a multi-layer corrosion product with crystalline growth beneath the original top surface corrosion product. This indicates the original corrosion product layer is non-protective as corrosion continues beneath the layer.

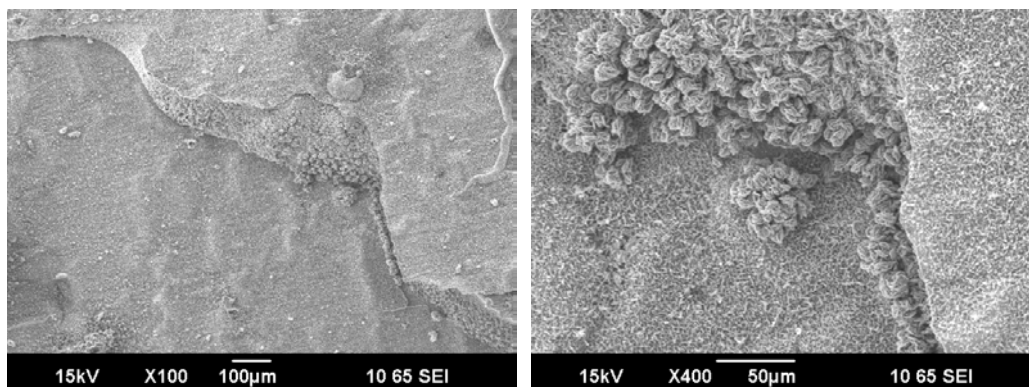


a) SEM at 50X magnification.

b) SEM at 400X magnification.

Figure 151. SEM images of corrosion product on sample from single phase after 7 days exposure to conditions, 25°C, pH 5, $p\text{CO}_2 = 2$ bar, $p\text{H}_2\text{S} = 100$ mbar, 1 wt% NaCl solution. Images show corrosion product has multiple layers (a) and the upper layer shows original polish marks (b).

On the other hand, Figure 152 represents a similar original top surface corrosion product that failed in situ. A similar broken edge of the original top surface corrosion product, as indicated by the directional polish marks, is shown with an iron sulfide corrosion product filling in the gap created by the failure.



a) SEM at 100X magnification.

b) SEM at 400X magnification.

Figure 152. SEM images of corrosion product on sample from single phase after 7 days exposure to conditions, 25°C, pH 5, $p\text{CO}_2 = 2$ bar, $p\text{H}_2\text{S} = 100$ mbar, 1 wt% NaCl solution. Images show a location where the corrosion product layer failed in situ (a) and corrosion product growth filled the area (b).

Further analysis of this corrosion product by EDS did not provide any further information. EDS is a quantitative measurement based on the penetration and scattering of the electrons from the electron beam used. Figure 153 shows a comparison of the elemental wt% of Fe, S, C, O, and Cl found in the three areas of this failure. The “bottom” represents the original corrosion product without lifting or failure, the “top” represents the corrosion product that filled in the gap created by the in situ layer failure, and “right” represents the corrosion product layer that failed and was apparently lifted by corrosion and precipitation that occurred beneath the layer. In this case, the author believes the analysis only reflects the thickness of the corrosion product layer analyzed with all three locations being dominated by an iron sulfide like mackinawite.

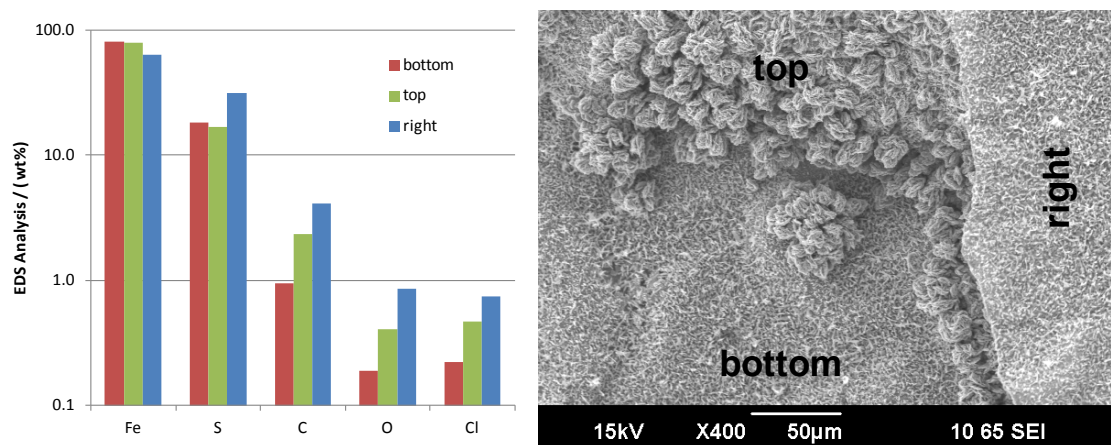


Figure 153. EDS analysis of corrosion product layer surface features. 25°C, pH 5.0, $p\text{CO}_2 = 2.8$ bar, $p\text{H}_2\text{S} = 100$ mbar, 1 wt.% NaCl, 7 days.

By assuming the corrosion product observed is a layered structure, the “bottom” area in the image would be the thinnest and therefore EDS would reflect more electrons from the underlying metal substrate than either the “top” or the “right” sections. By the same logic, the “right” side is the thickest layer and would reflect the least amount of electrons from the underlying metal substrate.

A photograph of the entire weight loss sample after exposure to the test conditions for 7 days is shown on the left side of Figure 154. A dark corrosion product is observed with some indications of non-uniformity across the surface. IFM analysis of the sample with the corrosion product layer intact shows that there was corrosion product growth above the original surface, shown as a 150 μm peak in Figure 154. This characteristic was commonly observed in previous experiments where the bulk pH was pH 6.0 or greater. After the corrosion product was removed, the sample was again subjected to IFM analysis, and a representative image is shown on the right side of Figure 154. In IFM analysis of the metal substrate after corrosion product layer removal, the population of possible localized corrosion locations is noted along with the depth of each, but only the maximum depth is reported as the worst case scenario. The maximum local corrosion depth measured by IFM for this sample was 27 μm , which equivalent to a 1.4 mm/yr penetration rate. With a weight loss corrosion rate of 1.7 mm/yr, the pitting ratio is 0.8 and these local areas of corrosion are considered to be part of the general corrosion rate, so no localized corrosion was found for this sample.

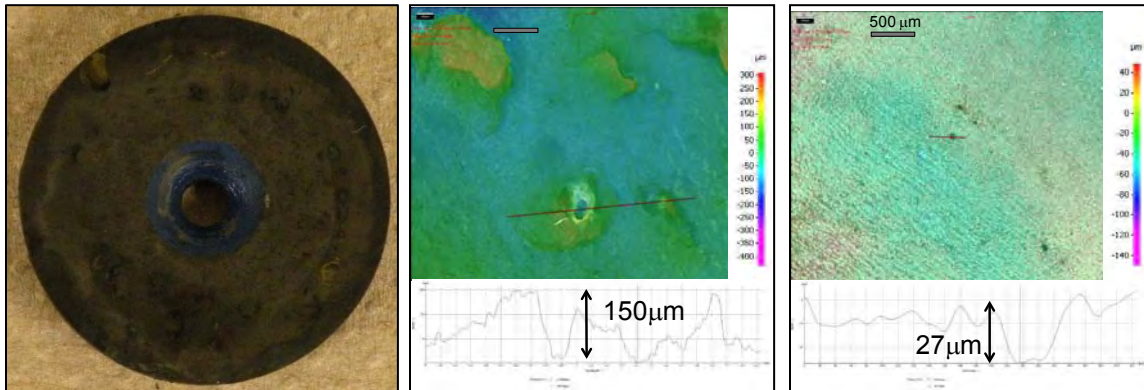


Figure 154. Single phase, 7 days exposure to (25°C); Sample “as removed” on left, IFM image of surface both with the corrosion product layer (middle) and without the corrosion product layer (right).

Corrosion product layer at 21 days (Single Phase Flow).

Figure 155 through Figure 156 show examples of the corrosion product surface features found on the weight loss sample taken after 21 days of exposure to the single phase flow test conditions at 25°C. More iron sulfide growth or precipitation is observed on the surface than was seen at 7 days, but the original polish marks are still visible. Both of these characteristics can be observed in Figure 155.

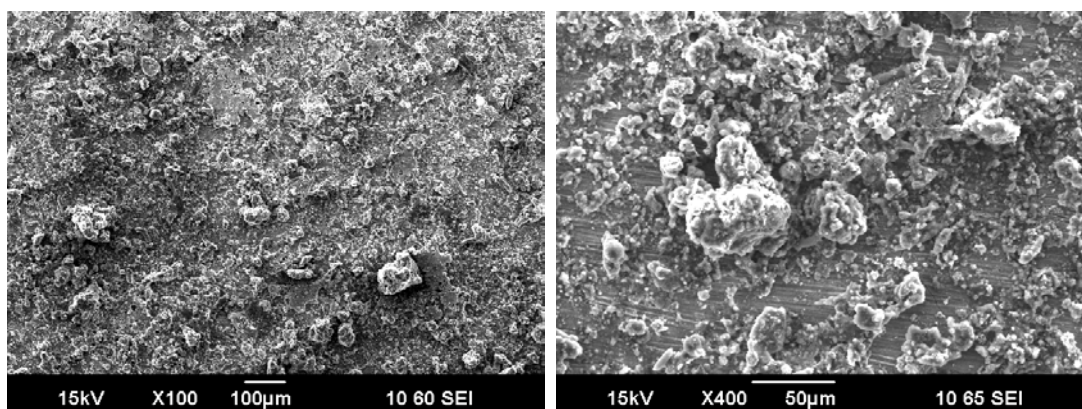


Figure 155. Single phase flow, 21 days, corrosion product layer. SEM image on the left at 100x magnification shows the surface topography covered with iron sulfide. On the right side, increasing the magnification of the SEM image to 400x shows the ‘polish marks’ visible in the substrate below the precipitation.

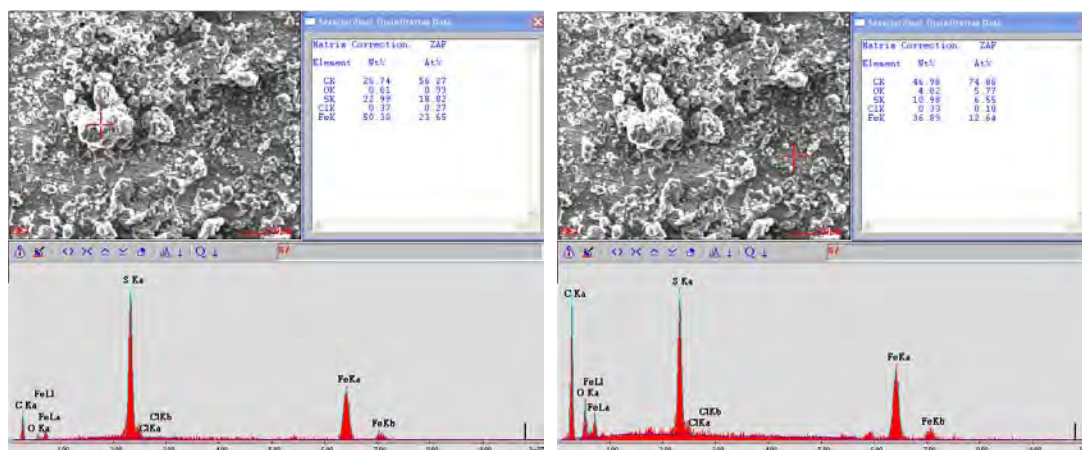


Figure 156. EDS analysis of surface precipitate (left) and substrate material (right) after 21 day exposure to conditions, 25°C, pH 5, $p\text{CO}_2 = 2$ bar, $p\text{H}_2\text{S} = 100$ mbar, 1 wt% NaCl solution.

In some cases, qualitative analysis by EDS can show a difference in the precipitated surface corrosion product versus the original corrosion product layer (indicated by the polish marks). With an environment containing a $\text{CO}_2/\text{H}_2\text{S}$ gas mixture, a determination must be made about whether a mixed iron carbonate - iron sulfide

corrosion product exists and under what conditions. In this case, the oxygen content measured in the surface layer is thought to be attributed to iron carbonate. EDS analysis shows less Fe, less S, more C, and more O in the substrate corrosion product than in the precipitate that is on top. These can be seen obviously by comparison of values in the graph of Figure 157a. By changing the y-axis to a log scale in Figure 157b, the comparison of the oxygen content, O, is shown as a magnitude of difference between the substrate corrosion product and the precipitate on top. Although some oxygen content seemed to be measured in the precipitate on top, this is thought to be a negligible (maybe nil) amount due to the qualitative measurement of the EDS and the close proximity of the precipitate to the substrate. EDS is considered a qualitative measurement because it is a measure of the electrons “reflected” back from the surface, where the elemental analysis can be influenced by the depth of penetration of the electron beam and the spot size used; is it also not a “perfect” direct beam, so some of the “reflected” electrons may come from the area adjacent to the analysis location, especially in a point EDS analysis. This means that part of the EDS analysis wt% of each element could be from a deeper depth or from the nearby area surrounding the analysis point. But this actually strengthens the argument that there is a marked compositional difference between the substrate corrosion product and the precipitate on top of the sample as will be seen in the following analysis.

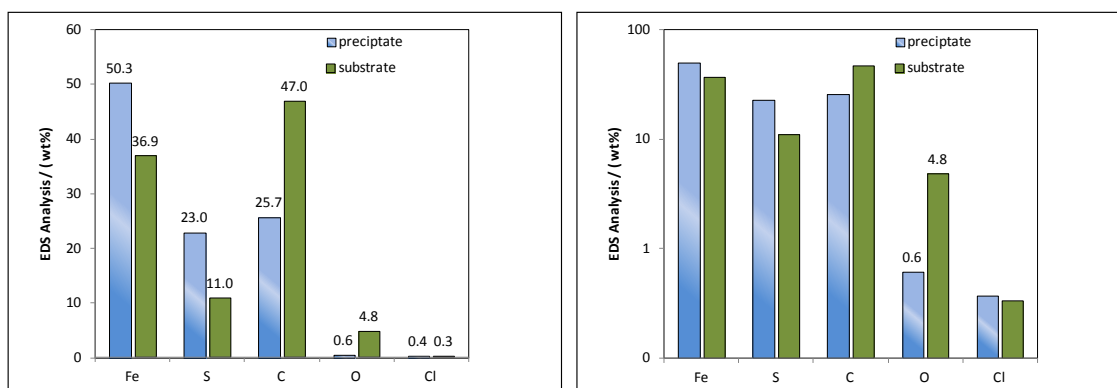


Figure 157. EDS analysis comparison of the precipitate to the substrate in (left) linear scale and (right) log scale on the y-axis after 21 day exposure to conditions, 25°C, pH 5, $p\text{CO}_2 = 2$ bar, $p\text{H}_2\text{S} = 100$ mbar, 1 wt% NaCl solution.

Analysis of the sample removed from single phase flow after 21 days, shows the surface to be fully covered with dark corrosion product as seen in Figure 158 (left image). IFM analysis shows a growth or precipitate on top of a flat substrate, both are dominated by iron sulfide. This growth amount is shown to have about 100 μm peak height above the surface and a 3.5 mm width. When the corrosion product layer was removed (Figure 158, far right), a pattern of corrosion initiation points can be observed that are similar in surface coverage density to the surface precipitate growth (Figure 158, middle). The maximum depth of corrosion penetration measured by the IFM is 64.8 μm , which over 21 days is equivalent to 1.1 mm/yr. With an overall weight loss corrosion rate measured at 0.8 mm/yr, these are almost equivalent with a pitting ratio of only 1.4, so this is considered to be part of the general corrosion.

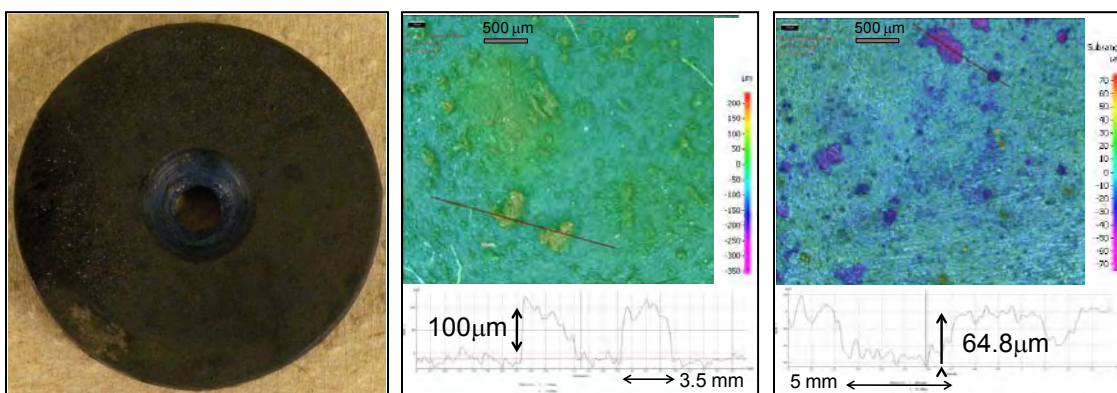
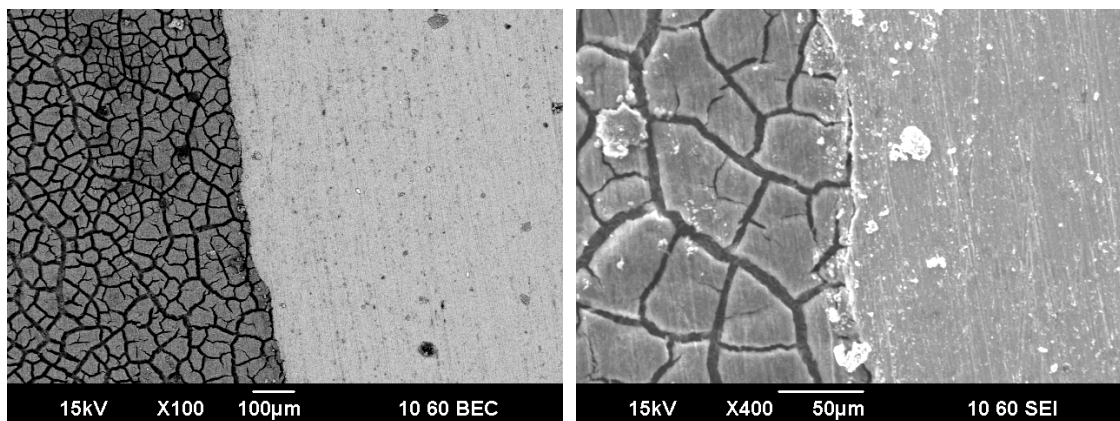


Figure 158. Single phase, 21 days exposure to 25°C; Sample “as removed” on left, IFM image of surface both with the corrosion product layer (middle) and without the corrosion product layer (right).

Corrosion product layer at 7 days (Multiphase Flow).

Figure 159 through Figure 161 show examples of the corrosion product surface features found on the weight loss sample taken after 7 days of exposure to the multiphase flow test conditions at 25°C. Multiple layers of corrosion product occurred on this sample as shown by either image in Figure 159. The 400X SEM image shows the top layer on the right side since there are polish marks still visible in this surface. Note that precipitation on top of this surface is minimal and is thought to be a result of the flow regime. Underneath the original surface layer is a corrosion product that has the appearance of a dried mud with an excessive amount of cracking. Notice that the backscatter image (Figure 159a) shows a compositional difference between the original surface layer and the underlying corrosion product. The underlying corrosion product is assumed to have a higher content of the alloying elements used in the X65 pipeline material with iron depletion caused by the corrosion process. This assumption is confirmed by the EDS analysis of the two areas (Figure 160) showing mainly iron sulfide

composition for the top surface (left) and a much higher ratio of carbon and chromium to iron that is seen in the original material.



a) Backscatter SEM at 100X magnification. b) SEM at 400X magnification. Figure 159. SEM images of corrosion product on sample from multiphase flow after 7 days exposure to conditions, 25°C, pH 5, $p\text{CO}_2 = 2$ bar, $p\text{H}_2\text{S} = 100$ mbar, 1 wt% NaCl solution. Images show corrosion product has multiple layers of slightly different composition in backscatter analysis (a) and upper layer shows original polish marks (b).

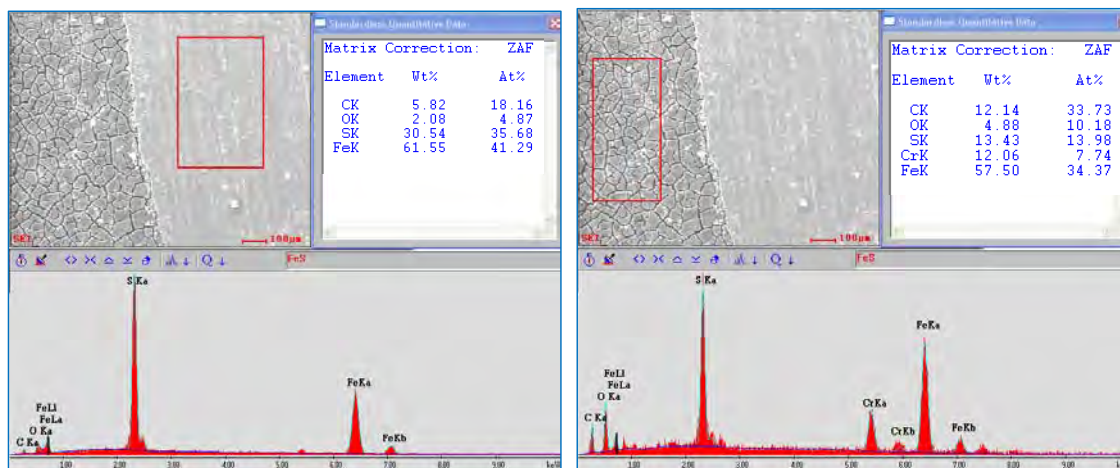


Figure 160. Corrosion product layer has two components. The top layer shows the polish marks (left side image), while the bottom layer could be described as the remaining carbide layer or an iron depleted substrate. Multiphase flow, 7 days' exposure to conditions, 25°C, pH 5, $p\text{CO}_2 = 2$ bar, $p\text{H}_2\text{S} = 100$ mbar, 1 wt% NaCl solution.

Analysis of the sample removed from multiphase flow after 7 days, shows the surface to be fully covered with dark corrosion product as seen in Figure 161 (left image). IFM analysis of the surface layer shows a uniform surface coverage. When the corrosion product layer was removed (Figure 161, far right), uniform corrosion was observed with maximum penetration depths less than $20\mu\text{m}$ (Figure 161, middle). With an overall weight loss corrosion rate measured at 2.0 mm/yr , the maximum penetration rate measured makes the pitting ratio = 1; therefore, not localized corrosion.

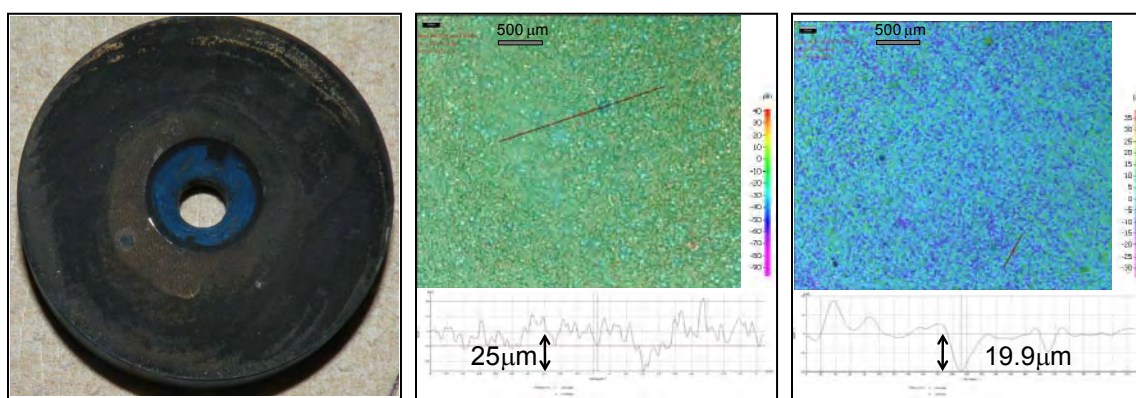


Figure 161. Multiphase, 7 days exposure to 25°C ; Sample “as removed” on left, IFM image of surface both with the corrosion product layer (middle) and without the corrosion product layer (right).

Corrosion product layer at 21 days (Multiphase Flow).

Figure 162 and Figure 163 show examples of the corrosion product surface features found on the weight loss sample taken after 21 days of exposure to the multiphase flow test conditions at 25°C .

SEM analysis (Figure 162, left image) at 50X magnification shows a fully covered surface with some precipitate and some cracking failures in the top corrosion

product layer. Closer analysis of a cracked and failed area (by both SEM and backscatter, respectively, in the split image of Figure 162, right side) shows the compositional difference between the substrate and surface layer as observed and analyzed for the sample exposed for 7 days. Note the polish marks are still visible on the initial corrosion product layer which has a lighter color (higher atomic mass) in the backscatter image.

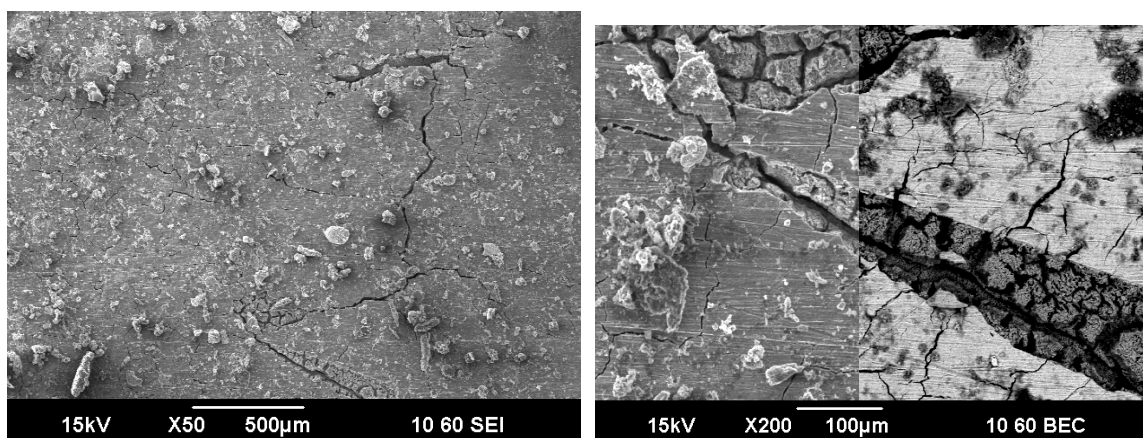


Figure 162. Thin layer, top layer failure. Multiphase 21 days, thin layer, top layer failure. Polish marks are still visible. Multiphase flow after 21 days exposure to conditions, 25°C, pH 5, $p\text{CO}_2 = 2$ bar, $p\text{H}_2\text{S} = 100$ mbar, 1 wt% NaCl solution.

Analysis of the sample removed from multiphase flow after 21 days, shows only a partially covered surface as seen in Figure 163 (left image). IFM analysis of the surface layer shows a uniform surface coverage with variation of 25µm. When the corrosion product layer was removed (Figure 163, far right), a somewhat uniform corrosion was observed and the maximum penetration depth was measured at 92.1µm. With an overall weight loss corrosion rate measured at 1.7 mm/yr, the maximum penetration rate measured makes the pitting ratio = 1; therefore, not localized corrosion.

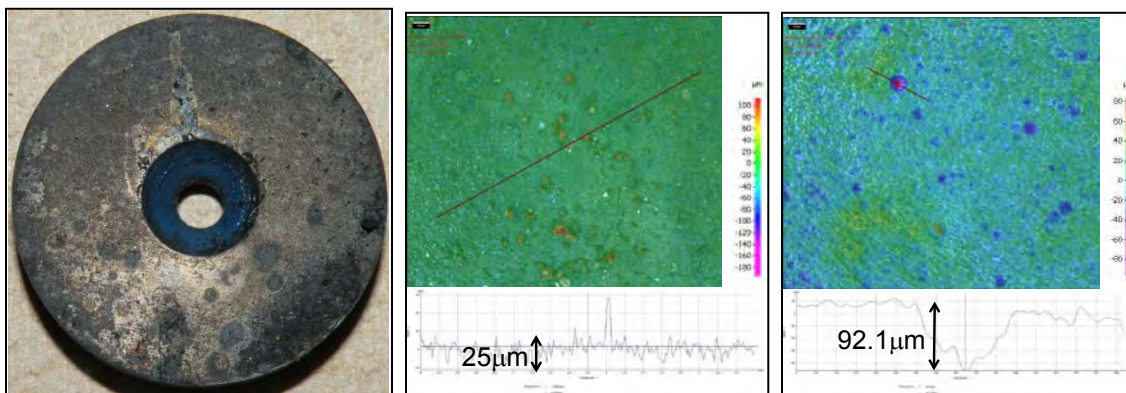


Figure 163. Multiphase, 21 days exposure to 25°C; Sample “as removed” on left, IFM image of surface both with the corrosion product layer (middle) and without the corrosion product layer (right).

Experiment 14: 40°C, $pCO_2 = 2.8$ bar, $pH_2S = 0.13$ bar, pH 5.0, 1wt% NaCl

Introduction

The temperature in this experiment was controlled at 40°C using the heating elements available in the H₂S flow loop as the added heat from the pumps was not enough to exceed 35°C (Table 27). The slight increase in temperature from 25°C slightly increased the corrosion rate and may have slightly increased the likelihood of localized corrosion, but was not enough of a change to sustain localized corrosion.

Table 27. Exp 14. Controlled Parameters for Effect of Higher pH₂S at 40°C

Parameter	Description
Equipment	H ₂ S Flow Loop
Test duration	21 days
Temperature	40.0 ± 0.1 °C
pCO ₂	2.8 ± 0.1 bar
pH ₂ S	0.13 ± 0.02 bar
pH	5.0 ± 0.3
Solution	1 wt% NaCl
Ionic strength	0.176 ± 0.01
[Fe ⁺⁺] (ppm)	20 ± 5
S(FeCO ₃)	0.28 ± 0.2
S(FeS)	50 ± 1
S(FeS)/S(FeCO ₃)	178 ± 5

[#](avg ± std deviation)

Results and Discussion

The conditions tested were 40°C, pCO₂ = 2.8 bar, pH₂S = 100 mbar, 1 wt.% NaCl, pH 5.0 for 7, 14 and 21 days exposure for weight loss samples. The general weight loss and IFM measured penetration rate of all the samples are shown for single phase flow in Figure 164 and for multiphase flow in Figure 165. Both data sets show general corrosion rates between 1 and 3 mm/yr with IFM penetration rates up to 5 mm/yr. For most cases, the penetration rates are approximately equivalent to the weight loss corrosion rates. Localized corrosion was observed in this experiment as the two samples in multiphase flow for 7 days.

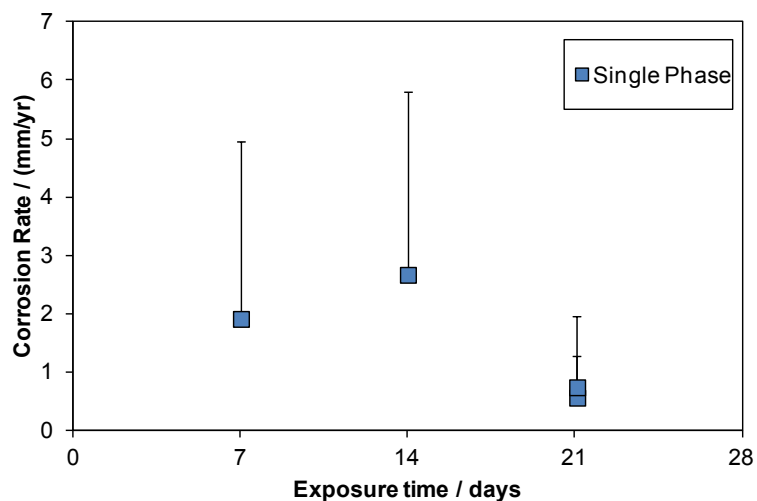


Figure 164. General corrosion (squares), as well as “localized” corrosion from IFM (single sided error bars), from weight loss of samples exposed to single phase flow in 40°C, $p\text{CO}_2 = 2.8$ bar, $p\text{H}_2\text{S} = 100$ mbar, 1 wt.% NaCl, pH 5.0 for 7, 14 and 21 days exposure.

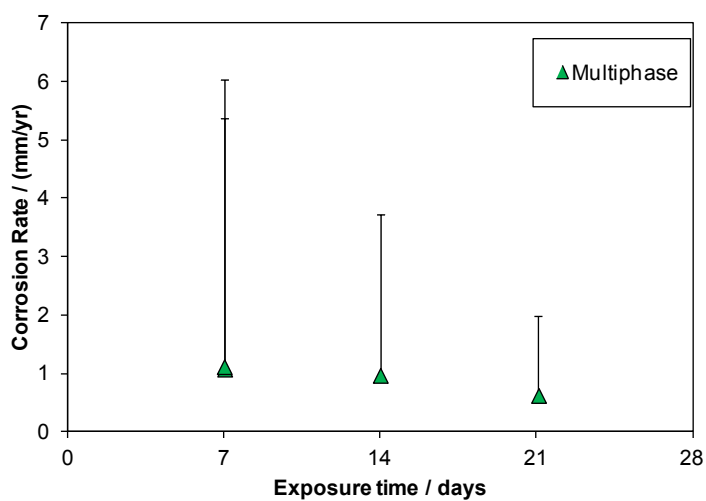


Figure 165. General corrosion (squares), as well as “localized” corrosion from IFM (single sided error bars), from weight loss of samples exposed to multiphase flow in 40°C, $p\text{CO}_2 = 2.8$ bar, $p\text{H}_2\text{S} = 100$ mbar, 1 wt.% NaCl, pH 5.0 for 7, 14 and 21 days exposure.

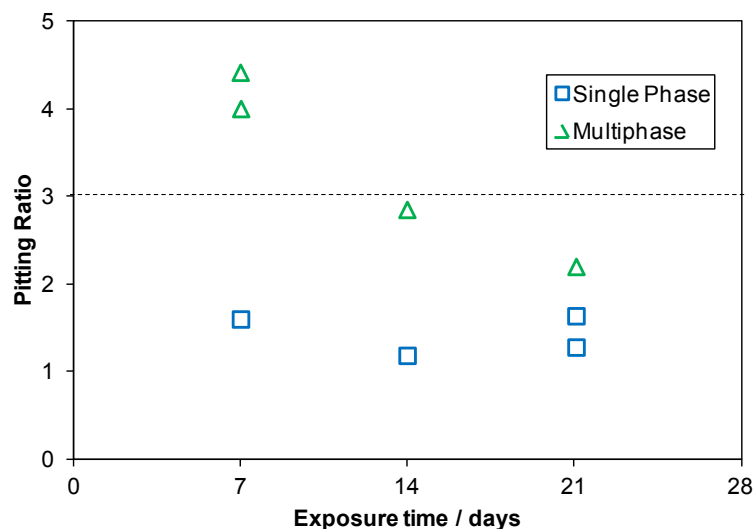


Figure 166. Pitting ratio for weight loss samples exposed in 40°C, $p\text{CO}_2 = 2.8$ bar, $p\text{H}_2\text{S} = 100$ mbar, 1 wt.% NaCl.

With corrosion product layer growth considered an important characteristic, the mass of the corrosion product remaining on the weight loss samples was converted to a layer thickness by assuming an iron sulfide density of 4.84 g/cm^3 over the entire available surface area of 7.6 cm^2 . The importance of Figure 167 is to show that the corrosion product layer is still developing over the entire 21 day experiment. The growth of the corrosion product layer is supported by the calculation of scaling tendency (Figure 168) which remained between 30 to 45% during this experiment.

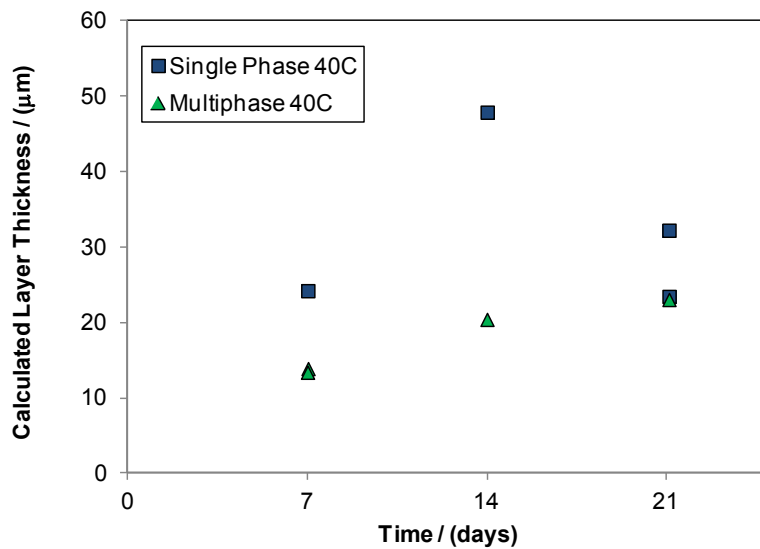


Figure 167. Corrosion product layer growth vs. time. 40°C, $p\text{CO}_2 = 2.8$ bar, $p\text{H}_2\text{S} = 100$ mbar, 1 wt.% NaCl.

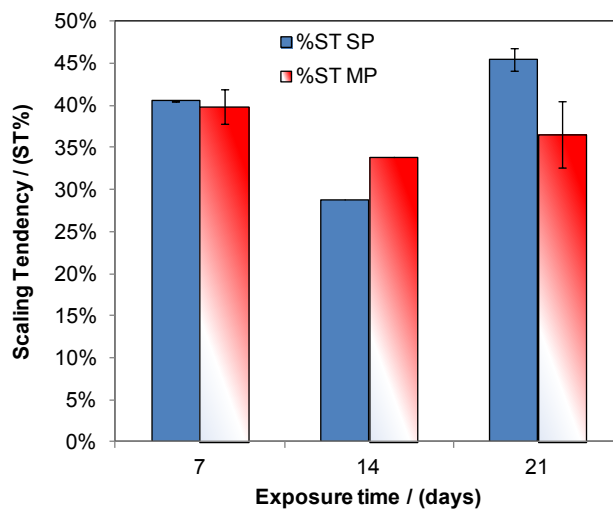


Figure 168. Scaling Tendency for 40°C, $p\text{CO}_2 = 2.8$ bar, $p\text{H}_2\text{S} = 100$ mbar, 1 wt.% NaCl.

Corrosion product layer at 7 days (Single Phase Flow).

Figure 169 through Figure 171 show examples of the corrosion product surface features found on the weight loss sample taken after 7 days of exposure to the single

phase flow test conditions at 40°C. For this case, none of the original polish marks are visible which means there is more of a precipitate covering the surface. Some areas showing damage to the precipitate coverage were inspected by SEM and EDS to look for indications of the original surface features and to determine differences in composition.

Figure 169 shows an area of failure in the corrosion product layer with a closer inspection of the same area on the right side image. EDS analysis of these areas (Figure 170) show a similar phenomena as seen previously, that analysis of the underlying metal substrate shows more alloying materials than in the surface layer which is considered an indication of the loss of ferrous ions from the metal, as expected in the corrosion process.

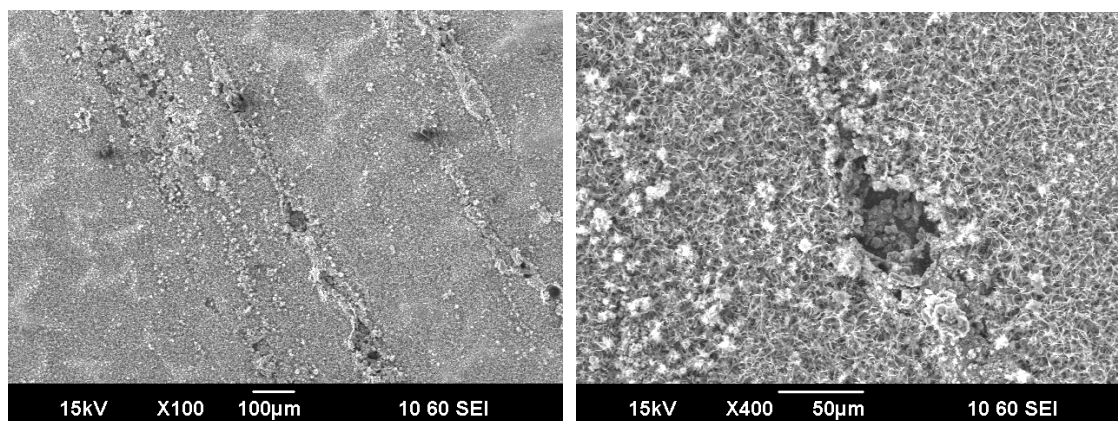


Figure 169. SEM images of corrosion product on sample from single phase after 7 days exposure to conditions, 40°C, pH 5, $p\text{CO}_2 = 2.8$ bar, $p\text{H}_2\text{S} = 100$ mbar, 1 wt% NaCl solution. Images show a failure area in the corrosion product layer (left), but no polish marks can be seen on the surface next to a failure location (right).

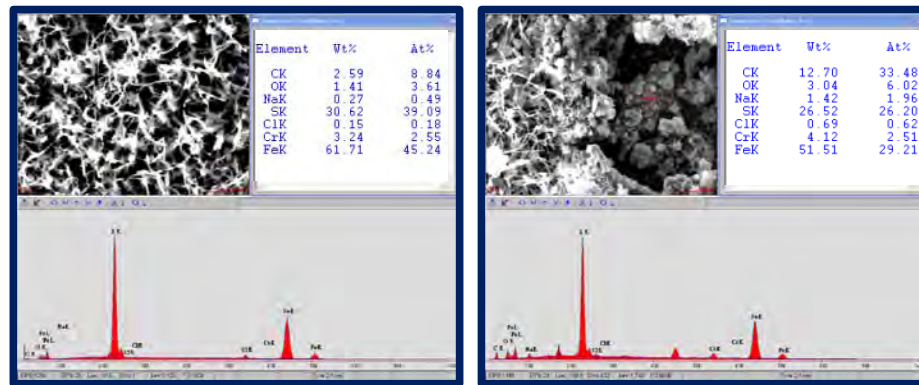


Figure 170. EDS analysis of the corrosion product found on the surface (left) and in the failure location (right) shown in Figure 169.

Analysis of the sample removed from single phase flow after 7 days, shows a fully covered surface with a layer that has dried and is thick enough to start to curl up at the edges (Figure 171, left image). IFM analysis of the surface layer shows an area where the corrosion product layer failed showing the layer thickness measured at $127.8\mu\text{m}$. When the corrosion product layer was removed (Figure 171, far right), it can be seen that uniform corrosion was observed and the maximum penetration depth was measured at $58.6\mu\text{m}$ (3.0 mm/yr). With an overall weight loss corrosion rate measured at 1.9 mm/yr , the maximum penetration rate measured makes the pitting ratio = 1.6; therefore, this is not localized corrosion.

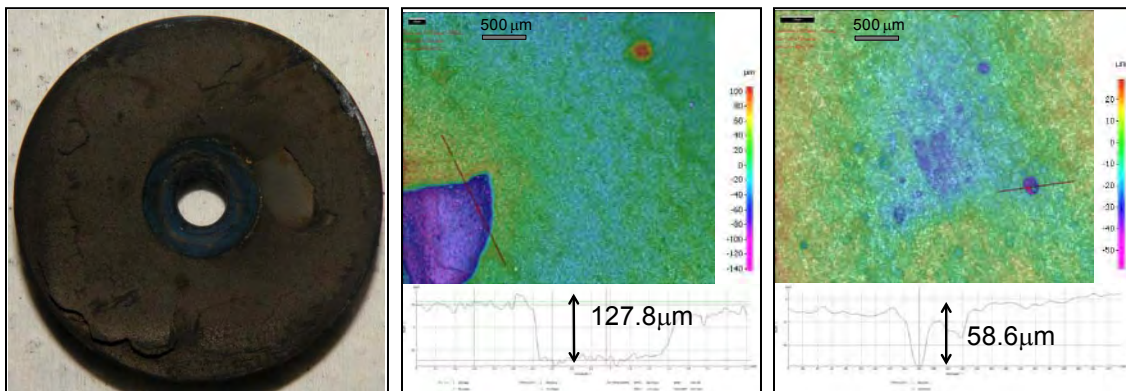


Figure 171. Single phase, 7 days exposure to 40°C; Sample “as removed” on left, IFM image of surface both with the corrosion product layer (middle) and without the corrosion product layer (right).

Corrosion product layer at 21 days (Single Phase Flow).

Figure 172 through Figure 175 show examples of the corrosion product surface features found on the weight loss sample taken after 21 days of exposure to the single phase flow test conditions at 40°C. Figure 172 shows an example of an in situ corrosion product layer failure determined by the fact that all of the surfaces are covered by iron sulfide, as confirmed by EDS, Figure 173.

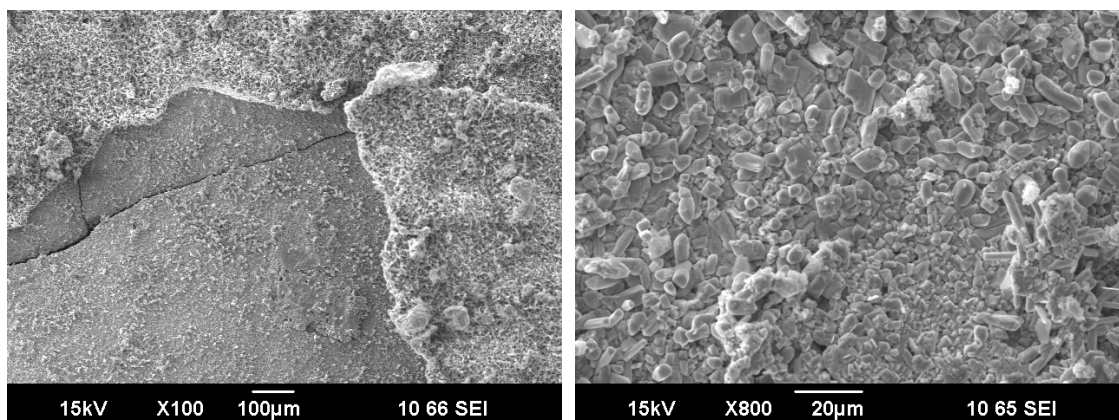


Figure 172. Corrosion product shown in two different magnifications for emphasis that failure of the layer occurred in situ (left) and a closer view of the crystalline surface features.

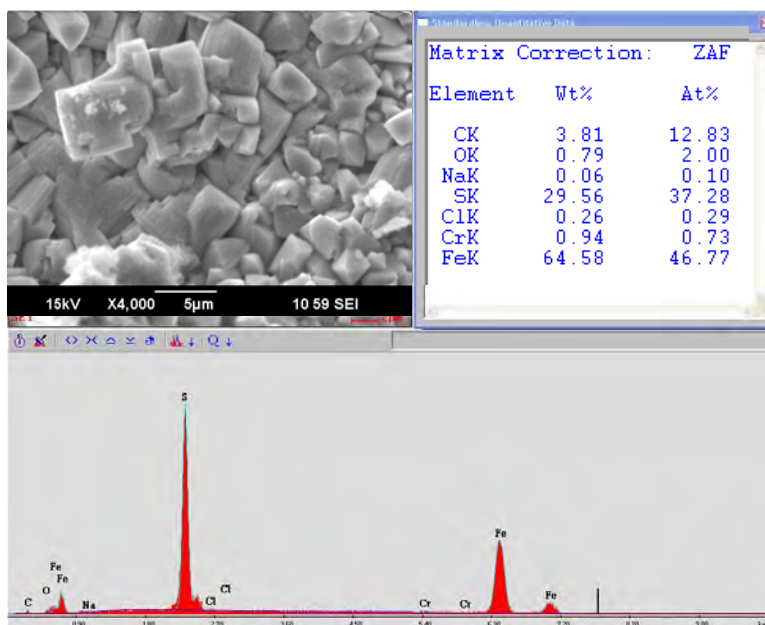


Figure 173. Higher magnification and EDS analysis of crystal structures found on the corrosion product surface. 21 days exposure to conditions, 40°C, pH 5, $p\text{CO}_2 = 2.8$ bar, $p\text{H}_2\text{S} = 100$ mbar, 1 wt% NaCl solution, single phase flow.

It should be noted that the weight loss samples exposed for 21 days to the same environmental conditions as the samples that were exposed for 7 and 14 days seem to

have a much lower general corrosion rate (Figure 164). In review of this perceived discrepancy, the mass loss of the two 21 day samples ($0.219 \pm 0.030\text{g}$) is almost identical to the mass loss of the 7 day sample (0.215g), indicating that corrosion dramatically ‘stopped’ at or before the 7 day sample was removed for these three samples in single phase flow. Although this quick analysis seems to show continuity within the experiment, it was also noted that the corrosion product was different between the two samples removed at 21 days. As shown above in Figure 172, the original surface polish marks were not visible in the corrosion product layer after 21 days with similarity to the sample surface observed after 7 days in Figure 169. But the second sample removed from the experiment at 21 days has the lowest mass lost (0.189g) and has the original polish marks visible over much of the surface (Figure 174).

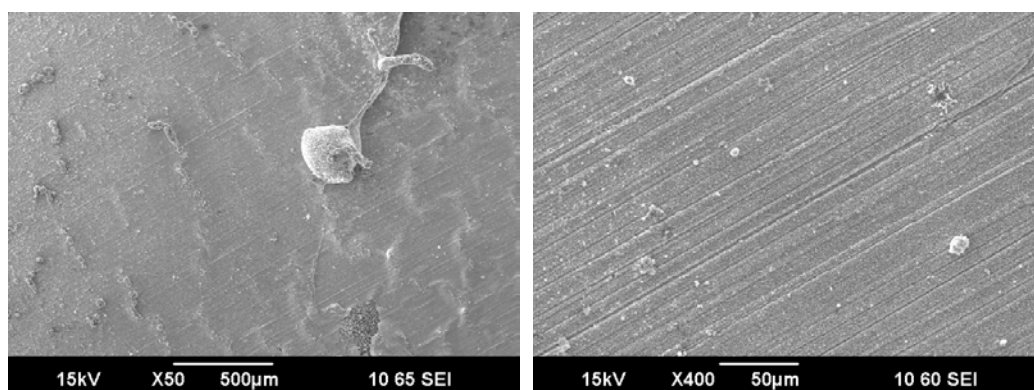


Figure 174. Corrosion product and polish marks observed after 21 days exposure to conditions in single phase flow, 40°C, pH 5, $p\text{CO}_2 = 2.8$ bar, $p\text{H}_2\text{S} = 100$ mbar, 1 wt% NaCl solution.

This second sample taken at 21 days from single phase flow also has an interesting feature not prominently observed in previous surface layer analysis. Wave-

like features that can be seen to dominate the surface in Figure 174 are analyzed by IFM in Figure 175 to show they represent an uplifted surface. This deformation of corrosion product layer is thought to indicate the internal stresses developed during the growth of the iron sulfide corrosion product layer. The current theory behind the Multicorp H₂S corrosion model takes into account the stresses developed within the corrosion product layer as one of the mechanisms related to scale retention rate (SRR).⁵

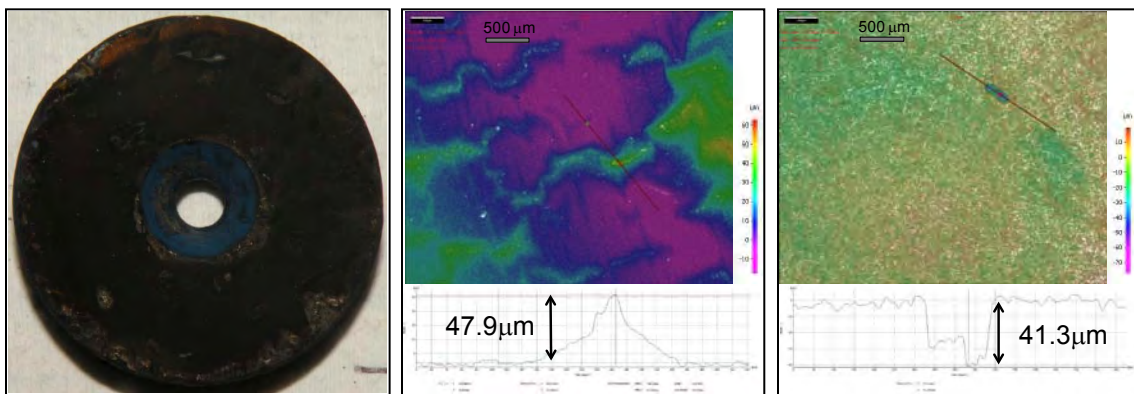


Figure 175. Single phase, 21 days exposure to 40°C; Sample “as removed” on left, IFM image of surface both with the corrosion product layer (middle) and without the corrosion product layer (right).

After removal of the corrosion product layer, the sample surface did not have many indications of corrosion. One indication, shown on the right side of Figure 175, of 41.3 μm calculates to be a 0.7 mm/yr penetration rate. When compared to the general corrosion rate of 0.56 mm/yr, this is a pitting ratio of 1.3 which is not considered to indicate localized corrosion.

Corrosion product layer at 7 days (Multiphase Flow).

Figure 176 through Figure 178 show examples of the corrosion product surface features found on the weight loss sample taken after 7 days of exposure to the multiphase flow test conditions at 40°C. Figure 176 provides an example of a corrosion product layer that failed after the sample was removed for analysis. With water removal from the surface layer, this layer will crack and sometimes fall apart. As seen in Figure 176, part of the upper layer seems to have fallen into an area where corrosion was undermining the initial corrosion product layer. The area exposed from underneath the layer is considered to be a mixed iron carbonate – iron sulfide from EDS analysis.

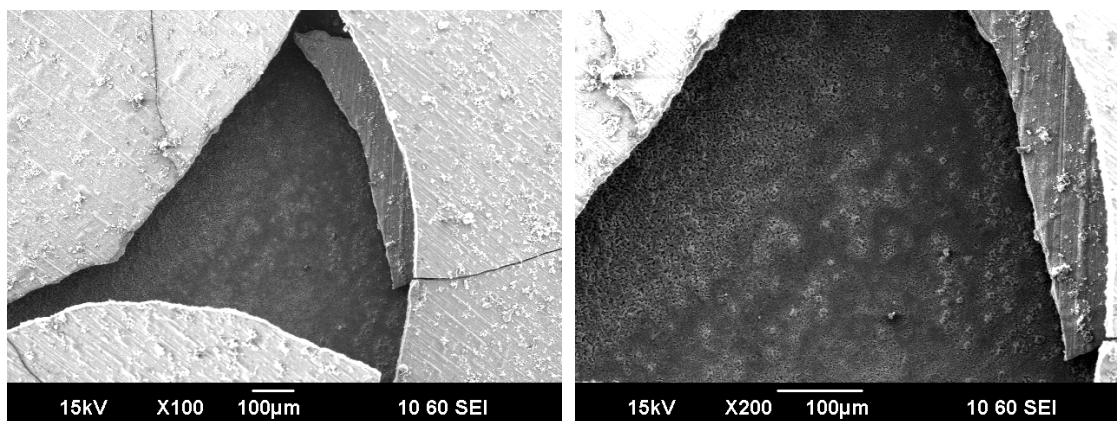


Figure 176. Layer failure (ex situ); polish marks visible on corrosion product layer.

Analysis of the sample removed from multiphase flow after 7 days, shows the surface to be covered with dark corrosion product with some areas of damage in the upper left quadrant, as seen in Figure 177 (left image). IFM analysis shows the difference in height from the metal substrate to the top of the corrosion product layer to be about

45 μm which is much larger than the predicted 23 μm (Figure 167); the difference in the predicted vs. measured corrosion product layer values could be caused by the surface being lifted in the undermining corrosion mechanism or could be influenced by the true porosity of the corrosion product layer. When the corrosion product layer was removed, Figure 177 (far right), a localized area of corrosion was observed with a maximum depth measured by the IFM of 94.6 μm , which over 7 days is equivalent to 4.9 mm/yr. With an overall weight loss corrosion rate measured at 1.1 mm/yr, the pitting ratio of 4.4 indicates that this is a possible location of localized corrosion.

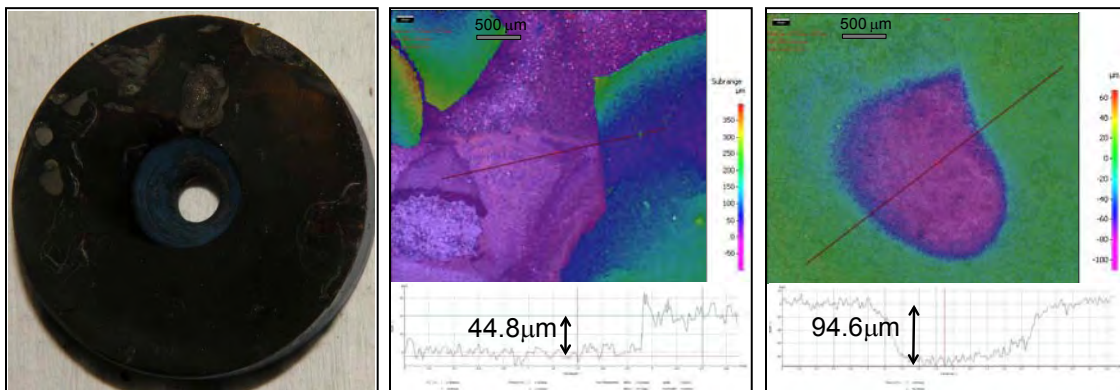


Figure 177. Multiphase flow, 7 days exposure to 40°C; Sample “as removed” on left, IFM image of surface both with the corrosion product layer (middle) and without the corrosion product layer (right).

Localized corrosion observed in two similar cases may have been caused by an inclusion. Figure 178 shows two different weight loss samples taken at different times that have small rounded holes of material lost. This has been seen in this X65 material before in short term tests⁵⁴ and was assumed to be caused by inclusions in the material.

The 82.7 μm pit measured by IFM for the sample at 7 days (Figure 178, left) calculates to be a 4.4 mm/yr penetration rate and compared to the general weight loss of 1.1 mm/yr on that same sample gives a pitting ratio of 4. But the 105.6 μm pit for the sample at 14 days (Figure 178, right) calculates to be a 2.8 mm/yr penetration rate and compared to the general weight loss of 0.97 mm/yr for that same sample only gives a pitting ratio of 2.8. From the similarity in the two sites and the retardation in the pit penetration rate with time, it is thought these locations would have formed very quickly after exposure to the corrosion conditions, but did not propagate with time.

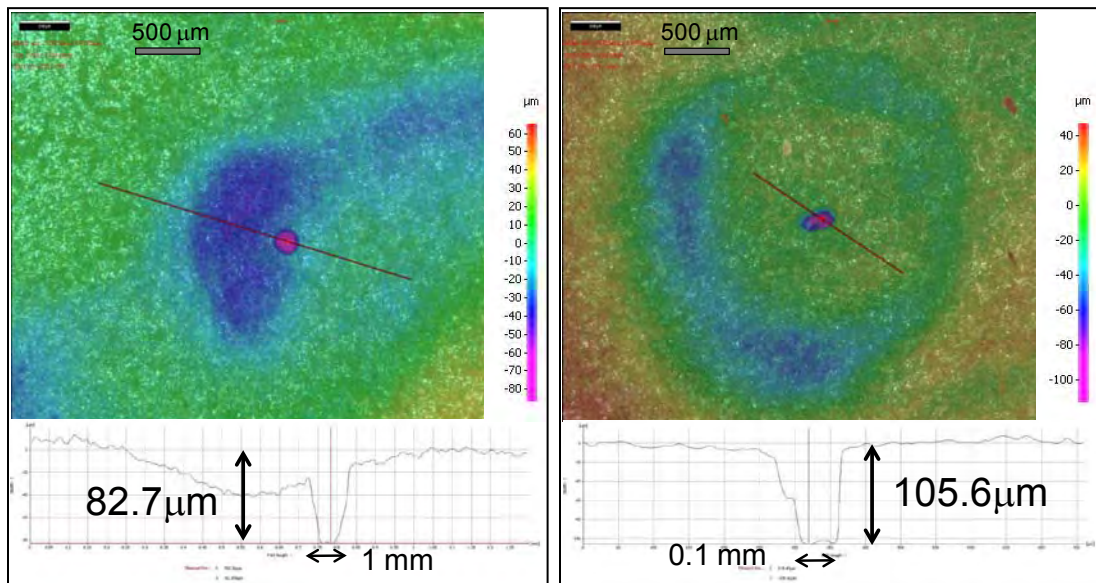


Figure 178. Similar areas of corrosion initiation at 7 days (left) and at 14 days (right) exposure to conditions 40°C, pH 5, $p\text{CO}_2 = 2.8$ bar, $p\text{H}_2\text{S} = 100$ mbar, 1 wt% NaCl solution.

Corrosion product layer at 21 days (Multiphase Flow).

Figure 179 through Figure 184 show examples of the corrosion product surface features found on the weight loss sample taken after 21 days of exposure to the multiphase flow test conditions at 40°C. The broken surface features seen on the left hand image of Figure 179 are confirmed to still have the original polish marks, seen in the right hand image, but also seemed to have been covering underlying or undermining corrosion which would also explain the cracking and failure of this layer after ex situ removal of the water layer within the layer structure.

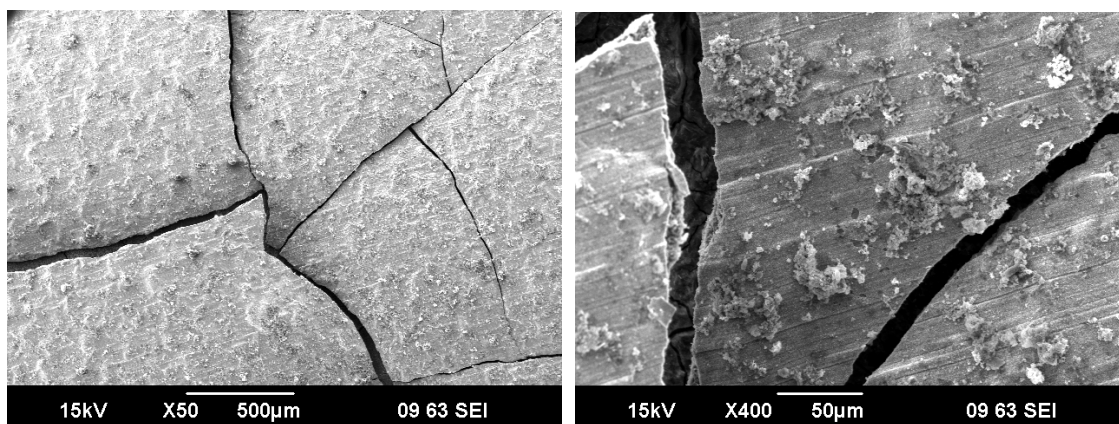


Figure 179. Corrosion product layer fractured after drying procedures showing a top layer that was intact in many areas with polish marks still visible. 21 days, 40°C, pH 5, pCO₂ = 2.8 bar, pH₂S = 100 mbar, 1 wt% NaCl solution

Analysis of the sample removed from multiphase flow after 21 days, shows the surface to be covered with dark corrosion product with some areas of damage as seen in Figure 180 (left image). IFM analysis shows the difference in height from the metal substrate to the top of the corrosion product layer to be about 245µm which is much

larger than the predicted $32\mu\text{m}$ (Figure 167); the difference in the predicted vs. measured corrosion product layer values could be caused by the surface being lifted in the undermining corrosion mechanism or could be influenced by the true porosity of the corrosion product layer. When the corrosion product layer was removed, Figure 180 (far right), minimal areas of corrosion were observed and the maximum depth of penetration measured by the IFM of $69.7\mu\text{m}$ is equivalent to 1.2 mm/yr over the 21 day exposure. With an overall weight loss corrosion rate measured at 0.74 mm/yr , the pitting ratio of 1.6 indicates that this is not localized corrosion.

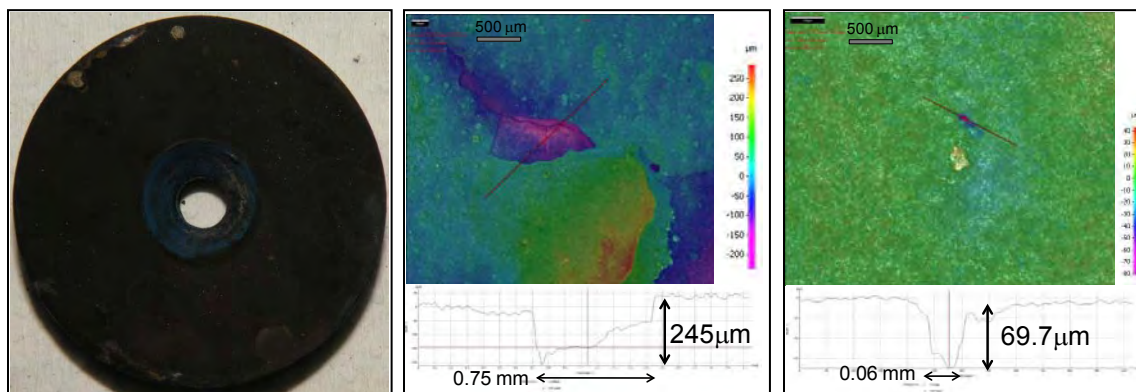


Figure 180. Multiphase flow, 21 days exposure to 40°C ; Sample “as removed” on left, IFM image of surface both with the corrosion product layer (middle) and without the corrosion product layer (right).

An SEM image (Figure 181, left) taken from a different region shows a surface layer failure thought to have occurred during the analysis procedures from the fact that EDS analysis of the area within the failed zones was not found to always have a sulfide component.

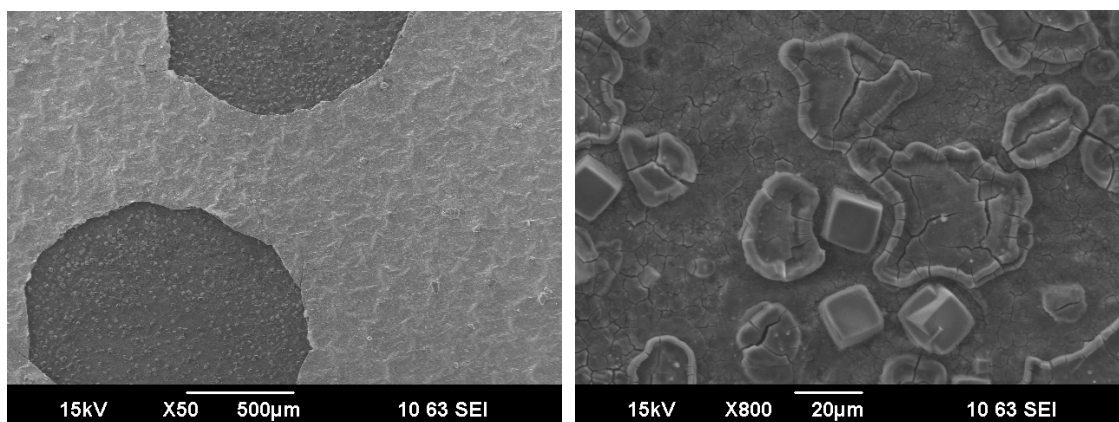


Figure 181. Surface layer failure assumed to occur ex situ (left) and magnified image of the area that would have been under that failed layer (right) indicates iron carbonate growth occurred beneath an iron sulfide layer. Multiphase flow, 21 days, 40°C, pH 5, $p\text{CO}_2 = 2.8$ bar, $p\text{H}_2\text{S} = 100$ mbar, 1 wt% NaCl solution.

A higher magnification image inside the area where the top layer was lost (Figure 181, right) shows a mixture of shapes and crystal types. EDS analysis of a nicely twinned crystal, Figure 182, show it to be an iron carbonate crystal.

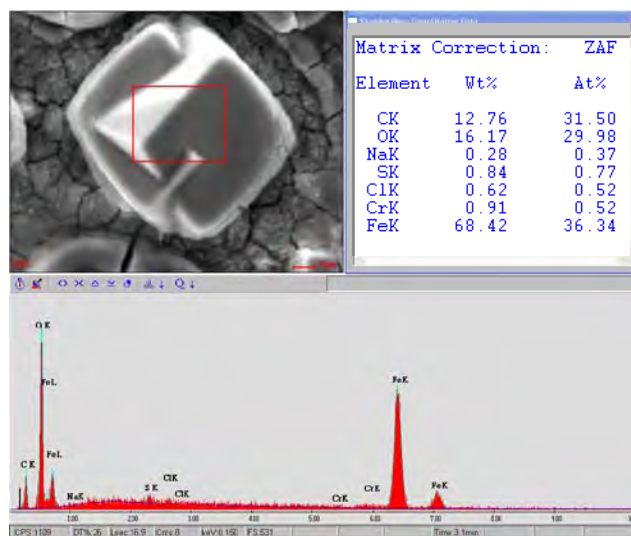


Figure 182. EDS analysis of crystal structure found in area under failed surface layer (Figure 181) shows only components consistent with iron carbonate. Multiphase flow, 21 days, 40°C, pH 5, $p\text{CO}_2 = 2.8$ bar, $p\text{H}_2\text{S} = 100$ mbar, 1 wt% NaCl solution.

Multiple cross section images were stitched together to provide a better picture of the undermining corrosion and uplifting of the corrosion product layer observed for this sample (Figure 183). The length of the lifted layer area is 4.8mm with a height of 350 μ m.

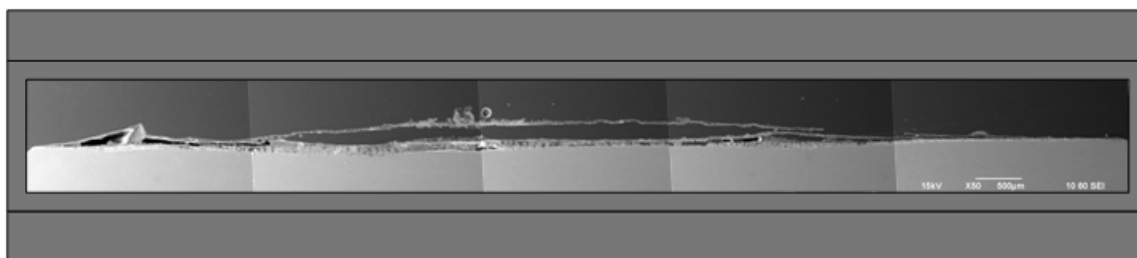


Figure 183. Cross section showing corrosion occurring underneath a thin corrosion product layer (lifted). Multiphase flow, 21 days, 40°C, pH 5, pCO₂ = 2.8 bar, pH₂S = 100 mbar, 1 wt% NaCl solution.

Analysis of several locations has shown that the corrosion product underneath an uplifted layer has a different composition than a corrosion product with direct contact to the bulk solution. This is an indication that species concentrations within the uplifted areas are different than the bulk species concentrations, confirming the uplifted sections of the corrosion product layer are isolating the areas underneath. EDS analysis of two such locations (Figure 184, right side vs. left side) found in close proximity show an increased amount of iron sulfides in the corrosion product with direct contact to the bulk conditions and a mixed (iron carbonate – iron sulfide) corrosion product under the isolating layer. The corrosion product under the uplifted layer also seems to show a

higher ratio of alloying elements to iron indicating that this area could have also lost ferrous ions to the corrosion process.

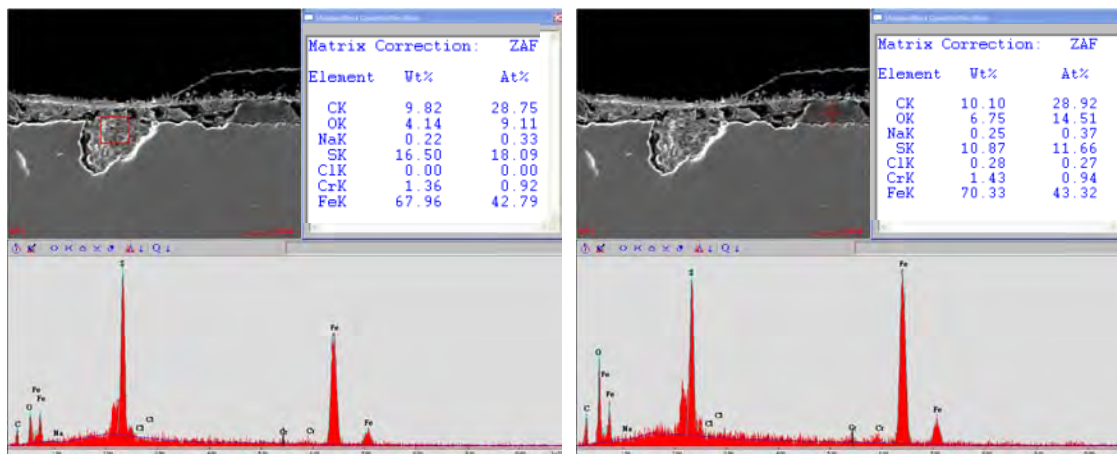


Figure 184. EDS analysis shows lower sulfur content underneath the “lifted” thin layer. Multiphase flow, 21 days, 40°C, pH 5, pCO₂ = 2.8 bar, pH₂S = 100 mbar, 1 wt% NaCl solution.

Conclusions Related to Corrosion Product Layer Development)

At 25°C, the indications of the original surface features (polish marks) were still visible for every time exposure tested (7, 14, & 21 days) in both single phase and multiphase although the corrosion product layer was observed to increase in mass with time:

- 7 day sample: 50 to 70 mg, 9-12 μm depth
- 14 day sample: 100 to 110 mg, 16-18 μm depth
- 21 day sample: 130 to 190 mg, 23-32 μm depth

A mixed corrosion product (FeS / FeCO₃) was found in both single phase and multiphase flow and no samples at 25°C met the criteria for localized corrosion.

At 40°C, the indications of the original surface features (polish marks) were visible in both single phase and multiphase at 7 days, but were not seen on 14 day or 21 day samples. Attributes of a mixed corrosion product (FeS / FeCO₃) were found in both single phase and multiphase flow samples. In these conditions, the corrosion product layer also increased in mass with time:

- 7 day sample: 50 to 90 mg, 8-15 mm depth
- 14 day sample: 80 to 180 mg, 12-29 mm depth
- 21 day sample: 80 to 120 mg, 14-20 mm depth

Under the conditions tested at 40°C, there was possible localized corrosion ONLY in the short term.

The lower temperatures (25°C and 40°C) slowed the kinetics of corrosion, but did not increase the localized effect of H₂S corrosion, since general corrosion rates were measured from 0.8 to 2 mm/yr for both single phase and multiphase flow regimes and both areas had similar values measured for localized corrosion. Every experiment below pH 6.0 has confirmed that a thin corrosion product layer forms on a mild steel surface when exposed to a system containing pH₂S and from the current set of data seems to be independent of temperature, pH₂S, pCO₂, or sodium chloride concentration; although the thin corrosion product layer retards corrosion, it is not protective.

Observations of original surface features (polish marks) in micron thick corrosion product layers indicate that a thin corrosion product layer formed first, but allowed corrosion to continue underneath. Localized corrosion initiation was observed where a

breakdown of the thin corrosion layer occurred. These breakdowns were observed in the experiments at pH 6 where a growth of the corrosion product layer occurred above the site where there was localized corrosion. They were also observed in experiments at pH 4 and pH 5 where the mechanism of undermining corrosion related to the initial layer caused collapse of the corrosion product layer.

Effect of the Presence of Acetic Acid

Introduction

Using the current research experience of 30 day experiments in a CO₂ / H₂S environment in the large scale flow loop and literature review from CO₂ / HAc testing in small scale glass cells as a basis for testing,⁵⁵ an experiment was completed in the H₂S system in order to establish if the addition of 100 ppm free acetic acid (HAc) would propagate localized corrosion.

Experimental Observations

Experiment 15: 60°C, pCO₂ = 7.7 bar, pH₂S = 0.010 bar, pH 6.0, 1wt% NaCl, 100 ppm

Free HAc

Introduction

This experiment ran for a total of 20 days with an exchange of weight loss samples and injection of acetic acid after 10 days as reflected in Table 28. The results show that localized corrosion was developed after 10 days exposure in both single phase

and multiphase flow, but localized corrosion was not enhanced by the addition of 100 ppm free HAc. This experiment did confirm that localized corrosion can be reproduced on X65 material in separate experiments at partial pressures of 0.010 bar p_{H_2S} and 7.7 bar p_{CO_2} for a solution of 1 wt% NaCl adjusted to pH 6 at 60°C.

Table 28. Exp 15. Controlled Parameters for Effect of 100 ppm Free HAc.

Parameter	Description	
Temperature	60.7 ± 0.1 °C	
p_{CO_2}	7.7 ± 0.4 bar	
p_{H_2S}	0.010 ± 0.002 bar	
pH	6.0 ± 0.5	
Solution	1 wt% NaCl	
Free HAc	0	100 ppm
Ionic strength	0.26 ± 0.01	0.29 ± 0.003
[Fe ⁺⁺] (ppm)	0.4 ± 0.28	0.09 ± 0.02
S(FeCO ₃)	1.7 ± 1.2	0.5 ± 0.1
S(FeS)	25.1 ± 23.0	6.0 ± 1.3
S(FeS)/S(FeCO ₃)	13.3 ± 4.0	11.5 ± 1.4

Results and Discussion

Six WL samples were used in the experiment. The first two were used to show the initial corrosion product and likelihood of localized corrosion after 10 days exposure and two more were inserted for the remainder of the experiment. Twenty four hours after the new samples had been inserted, pure glacial acetic acid was injected into the large scale system from a nitrogen purged and pressurized vessel. The injection point is downstream from the upstream multiphase test section and all WL samples. The injected acid would flow over the downstream multiphase test section, so samples were not used in this area.

Due to the large amount of fluid in the system (350 gallons), the pH shift due to the addition of 2.0 liters was approximately 0.1 pH. The system was then adjusted back to pH 6.0 by addition of 50 wt% NaOH purged with nitrogen. The stability of the system conditions can be seen in Figure 185.

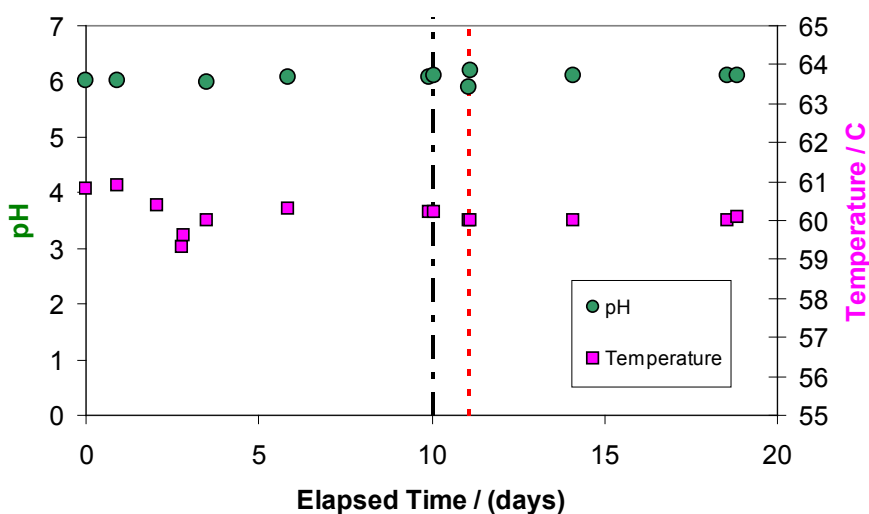


Figure 185. Measured test parameters: pH and Temperature for 21 days, 60°C, pH 6, $p\text{CO}_2 = 7.7$ bar, $p\text{H}_2\text{S} = 10$ mbar, 1 wt% NaCl solution with 100 ppm free acetic acid added at day 10.

Although the system conditions remained relatively stable for the entire experiment, the addition of free acetic acid greatly influenced the electrochemical measurements. The corrosion rate and corrosion potential shown in Figure 186 dramatically changed after the introduction of acetic acid. The effect of adding the free acetic acid created an unstable environment for electrochemical measurements during the first 24 hours after the addition (no recorded data between dotted lines).

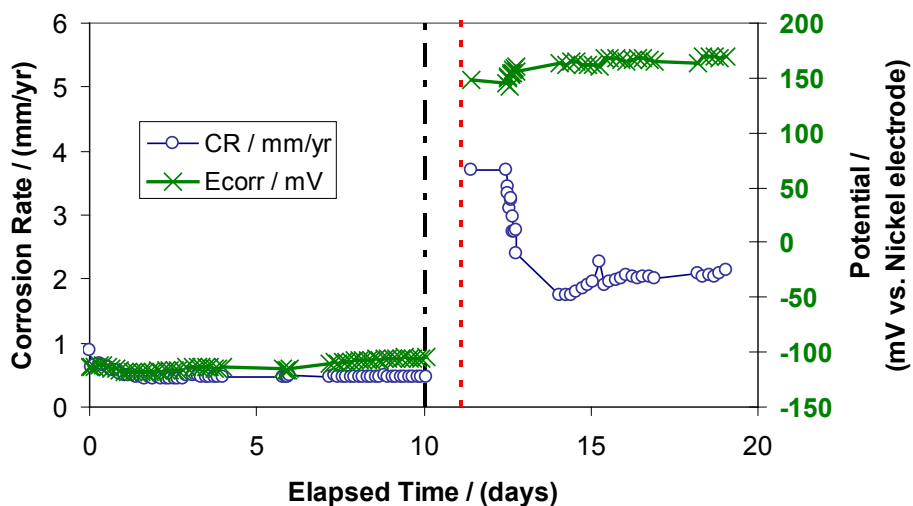


Figure 186. Measured test parameters: corrosion rate and corrosion potential for 60°C, pH 6, $p\text{CO}_2 = 7.7$ bar, $p\text{H}_2\text{S} = 10$ mbar, 1 wt% NaCl solution with 100 ppm free acetic acid added at day 10.

One WL sample from each of the two test sections was removed after the first 10 days of exposure to the system to provide a baseline, or starting point, for further comparisons. These coupons are shown for the single phase and multiphase test sections in Figure 187 and Figure 188, respectively.

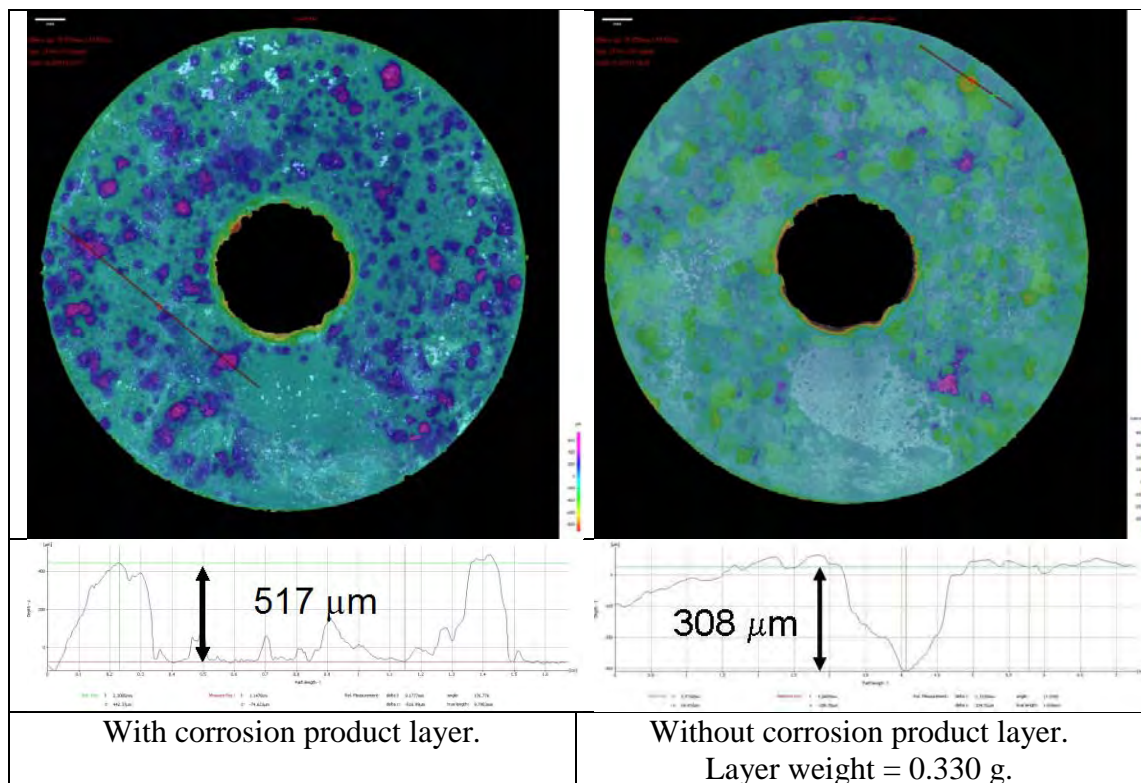


Figure 187. WL coupon after 10 days exposure to conditions in single phase flow.

Corrosion product topography is shown to be related to localized events of corrosion. A comparison of the corrosion product layer topographies by IFM (left side of each figure) shows the maximum depth or growth on the surface to be $517\mu\text{m}$ in single phase versus $214\mu\text{m}$ in multiphase. The difference in the surface topography is assumed to be caused by the turbulence of the flow regime where the growth occurred, but there are underlying differences as well. Although the general corrosion rates are considered to be the same (Table 29: 2.3 mm/yr vs. 1.8 mm/yr), the localized corrosion rates are different by a factor of 2 with the greatest penetration rate of 11 mm/yr found in single phase.

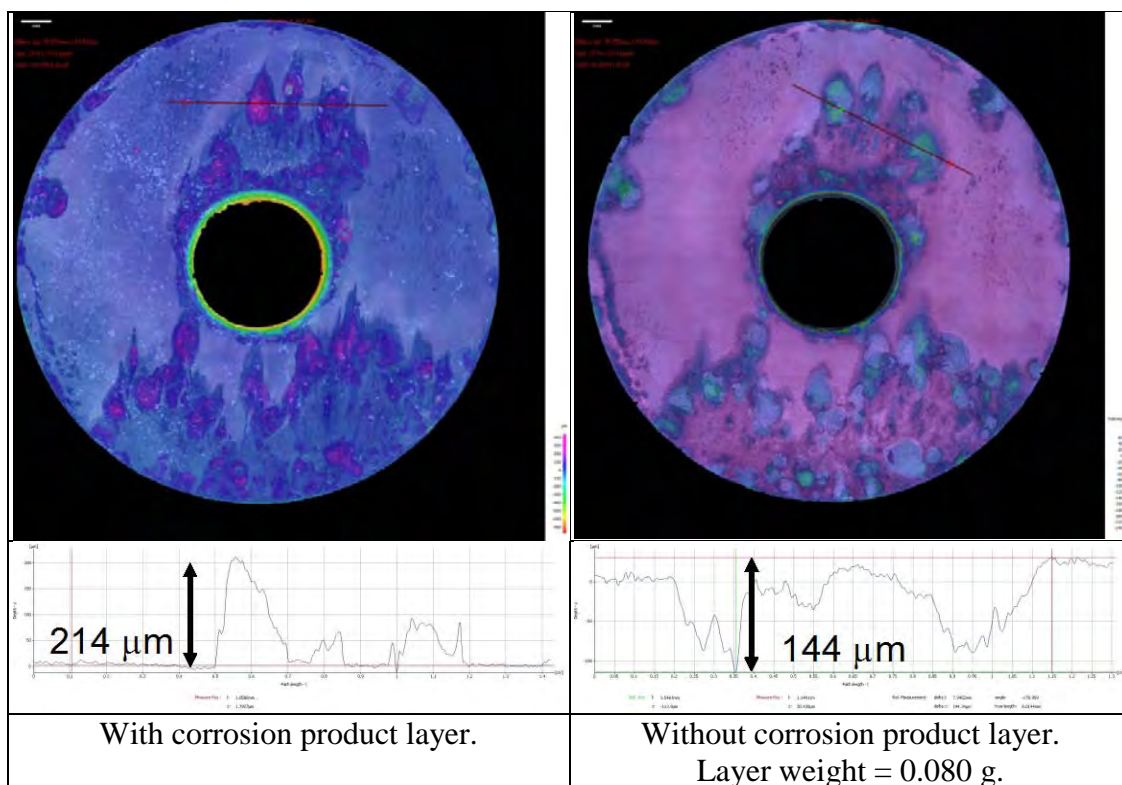


Figure 188. WL samples after 10 days exposure to initial conditions in multiphase flow.

From analysis with the IFM, it can be observed that the deepest location of attack measured (left side of each figure) is also related to the thickest location of corrosion product layer (right side of each figure). This relationship seems like it should be expected, but may not be observed under different water chemistry conditions. The author also believes this phenomenon has not been reported because a good method of analysis to correlate corrosion product layer with surface corrosion was not readily available in the past.

Table 29. Weight Loss Data Before and After Addition of 100 ppm Free HAc.

After 10 days, before exposure to HAc	After 20 days, exposure for full test	After 10 days, exposure to HAc
Single Phase General corrosion rate: 2.3 mm/yr Localized corrosion rate: 11 mm/yr Pitting ratio: 4.8	Single Phase General corrosion rate: 1.3 mm/yr Localized corrosion rate: 9.4 mm/yr Pitting ratio: 7.3	Single Phase General corrosion rate: 0.6 mm/yr Localized corrosion rate: 3.0 mm/yr Pitting ratio: 5
Multiphase General corrosion rate: 1.8 mm/yr Localized corrosion rate: 5.2 mm/yr Pitting ratio: 2.9	Multiphase General corrosion rate: 0.44 mm/yr Localized corrosion rate: 0 mm/yr Pitting ratio: n/a	Multiphase General corrosion rate: >2 mm/yr Localized corrosion rate: 8.9 mm/yr Pitting ratio: ~4.5

Surface analysis was also completed with the SEM/EDS system on the sample retrieved from single phase. Figure 189 shows a sulfide rich surface whether analysis is done on the entire surface or on individual surface morphological features. This occurred for all corrosion product layer analysis conducted normal to the coupon surface.

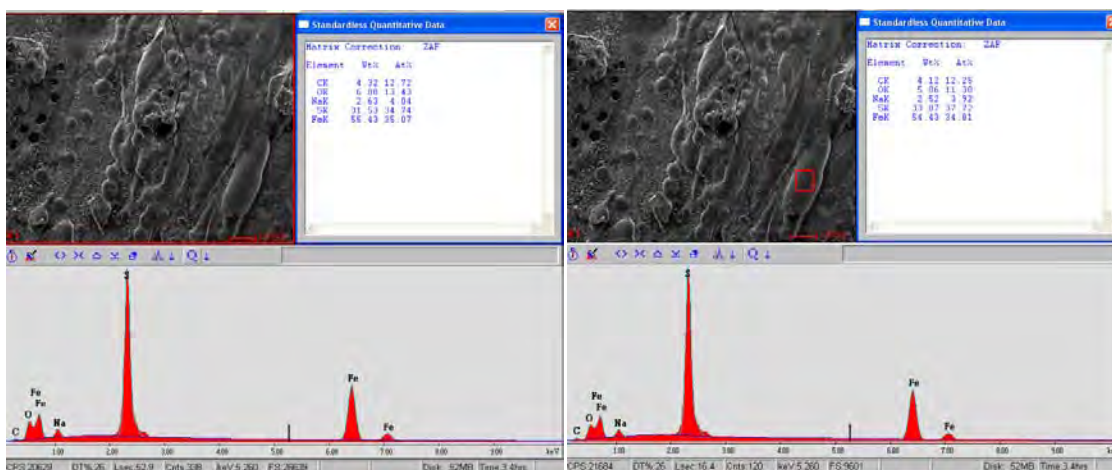


Figure 189. EDS analysis of the single phase coupon exposed for 10 days shows a sulfide dominant layer (left) that is also repeatable for each of the various shaped surface morphologies (right).

Two new WL samples were introduced to the H₂S system after the first two were removed. One WL sample placed in each of the two test sections; single phase and multiphase. The WL samples were allowed to pre-corrode for 24 hours before the addition of acetic acid. These coupons are shown for the single phase and multiphase test sections in Figure 190 and Figure 191, respectively.

The IFM analysis here also shows more corrosion product layer developed in single phase flow, but, in this case, a greater localized corrosion was measured on the multiphase flow WL coupon. Figure 190 shows the deepest localized corrosion to be 115 μm , which is a 4.3 mm/yr penetration rate. As compared to the general corrosion of 0.6 mm/yr, this is a pitting ratio of 6.5 and is considered to be localized corrosion.

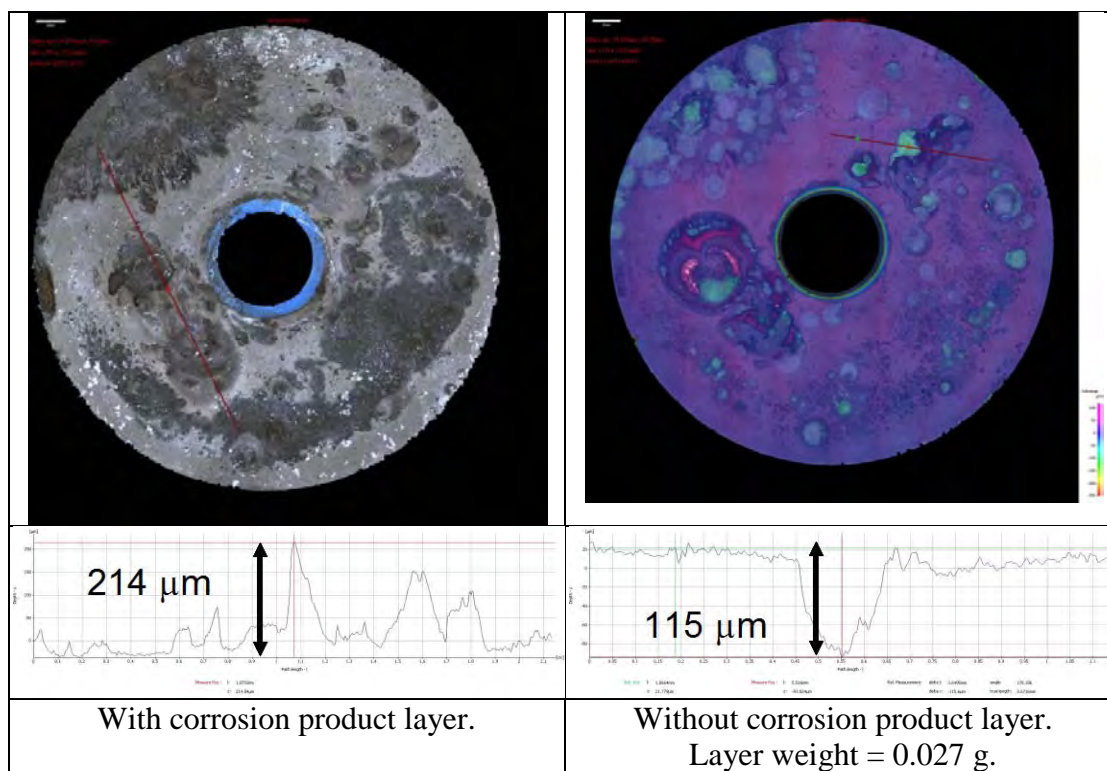


Figure 190. WL coupon after 10 days exposure to conditions with HAc in single phase flow.

Figure 191 shows the WL coupon from multiphase flow before and after layer removal. The “wedge” or half moon shaped image shown here is because the other half of this coupon was used for cross-sectional analysis. Although the variation in layer topography is an order of magnitude less than in single phase flow (29 μm compared to 214 μm), there was more localized corrosion observed in multiphase flow both in quantity and depth of locations. This half of the WL coupon from multiphase flow shows a 244 μm localized depth which translates into a value of 9.1 mm/yr penetration rate compared to the general corrosion of 1.5 mm/yr. This translates to a pitting ratio of 5.0.

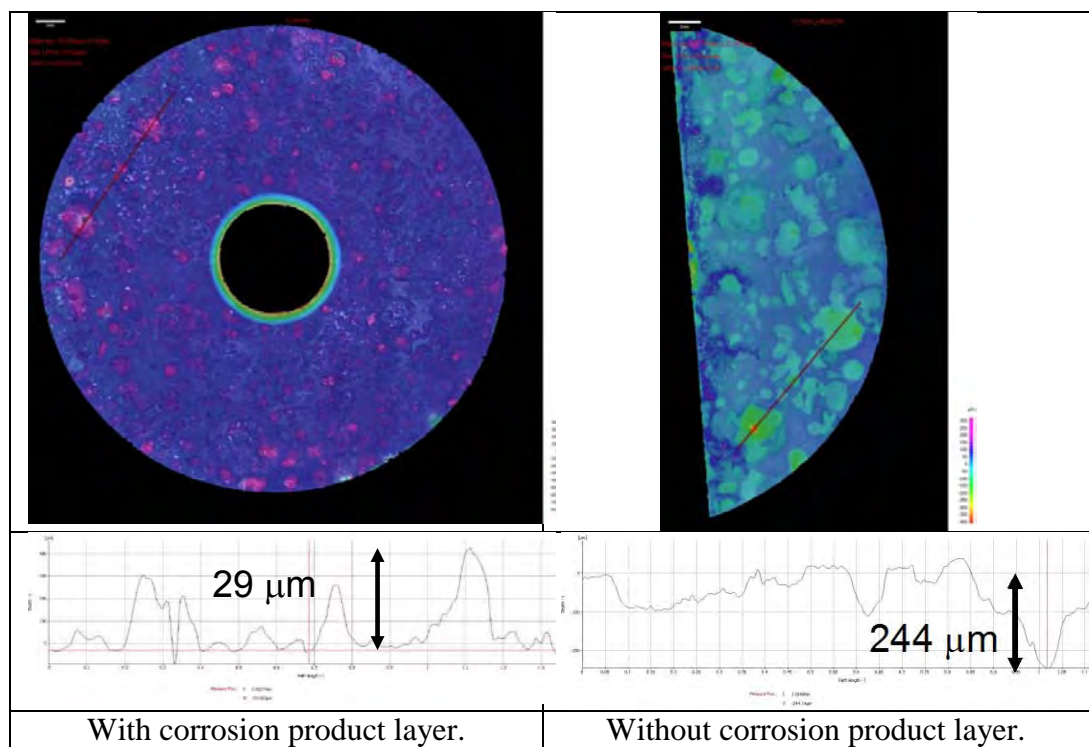


Figure 191. WL coupon after 10 days exposure to conditions with HAc in multiphase flow.

The cross section of this multiphase coupon is shown in Figure 192. Several locations of pitting type corrosion were found in the cross sectional analysis, but the one shown in Figure 192 is the largest cross sectional depth found at 170 μm or a 6.4 mm/yr penetration rate. EDS analysis does show a decrease in the sulfide content of the corrosion product within the pit. This phenomenon was investigated for the WL coupon exposed for 20 days.

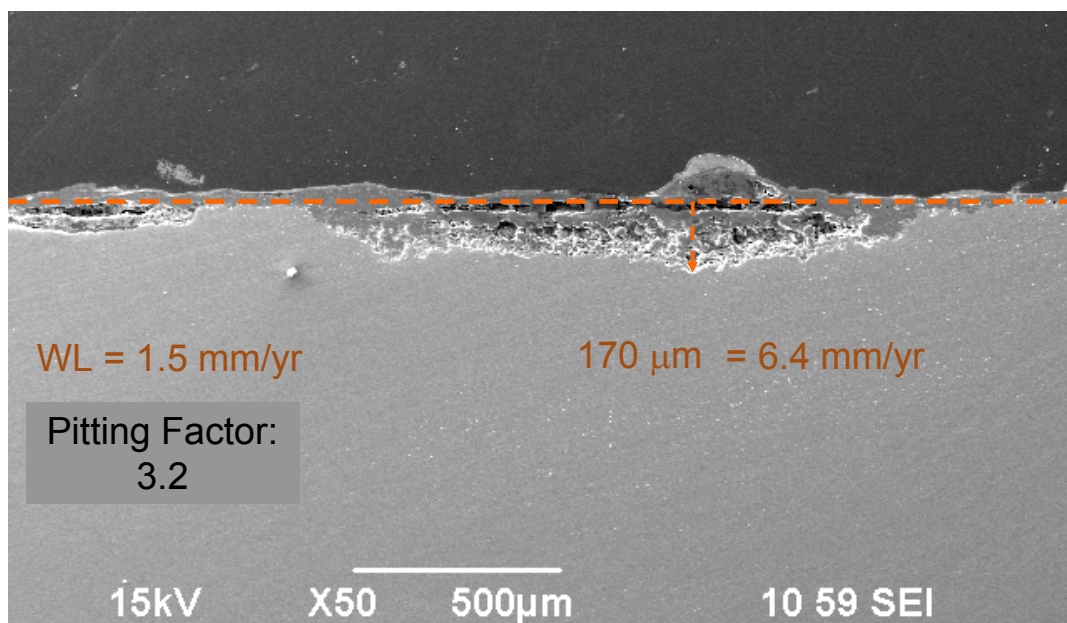


Figure 192. WL coupon after 10 days exposure to conditions with HAc in multiphase flow. Cross section with corrosion product layer.

Three WL samples remained in the H₂S system throughout the entire 20 day test period. Two were in single phase flow and one was in multiphase flow. Since localized corrosion was prominent on most of the WL samples, this experiment did not provide evidence that the addition of 100 ppm free acetic acid affected the initiation or propagation of localized corrosion. It did support the fact that the conditions defined for this experiment provide an environment with a high probability of initiation and propagation of localized corrosion.

Both of the WL coupons from single phase flow over the 20 day experiment have the largest topographical peaks in the corrosion product layer observed. The WL coupon fully analyzed by IFM, coupon “A,” shows an 867 μm topographical peak in Figure 193.

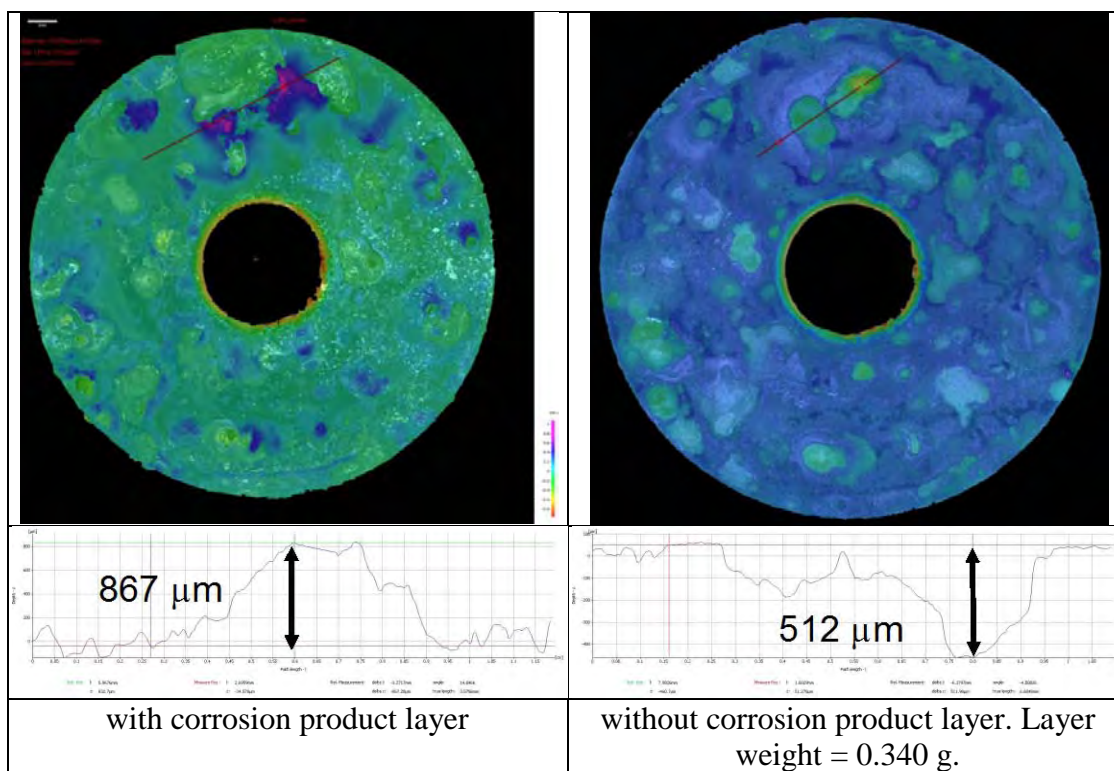


Figure 193. WL coupon “A” after 20 days exposure to the full test conditions in single phase flow.

This excess corrosion product layer was also directly related to the deepest localized corrosion location observed in this experiment. After removal of the corrosion product layer, the deepest pit is measured at 512 μm in depth. This localized event calculates to be a 9.4 mm/yr penetration rate which is more than 6 times larger than the general corrosion rate measured at 1.3 mm/yr. In Figure 194, the WL coupon used for cross sectional measurements, coupon “B,” shows a similar topographical peak of 905 μm and the deepest localized attack found on the remaining wedge after cross section analysis is 155 μm or a penetration rate of 2.9 mm/yr.

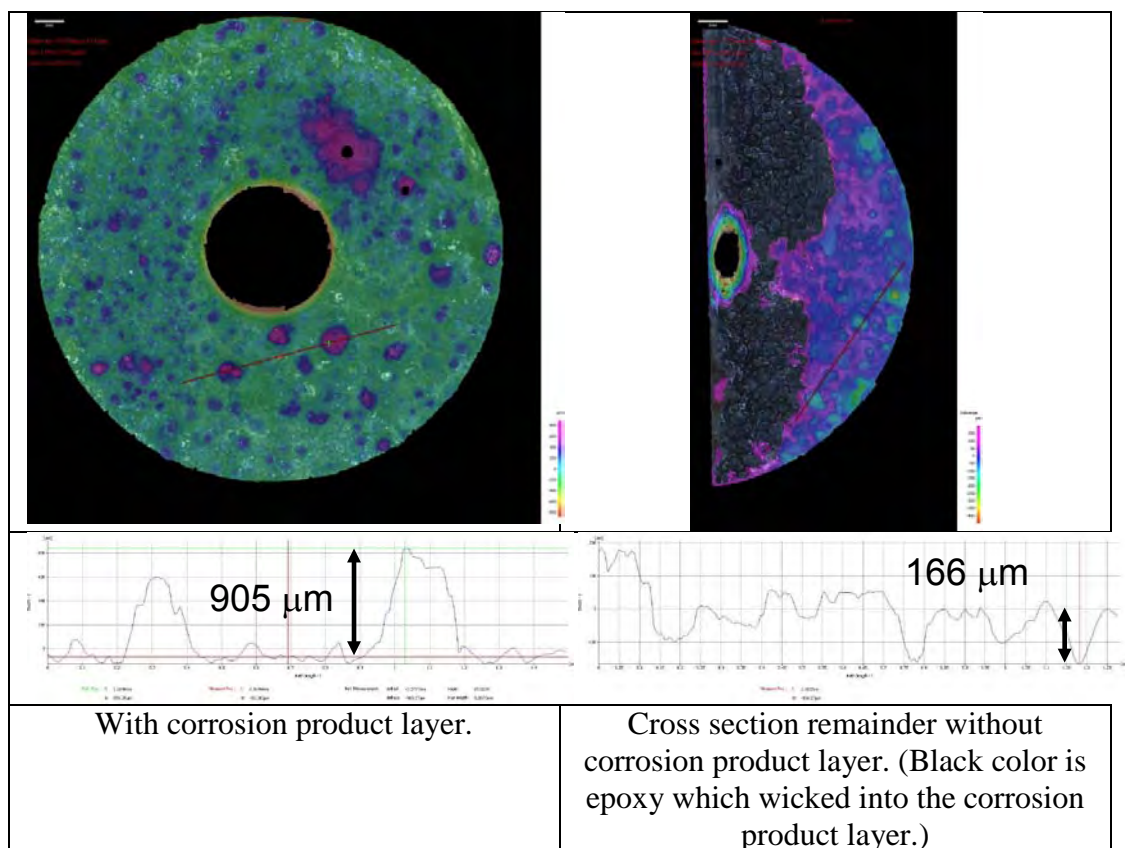


Figure 194. WL coupon “B” after 20 days exposure to the full test conditions in single phase flow.

The full cross section of this coupon shows numerous (8) localized corrosion locations. The deepest localized corrosion location found in this cross section is shown in Figure 195. At 374 μm , the penetration rate is 6.9 mm/yr. This would be considered to be similar to what was found on coupon “A” since a cross sectional analysis is not able to determine a true maximum pit depth.

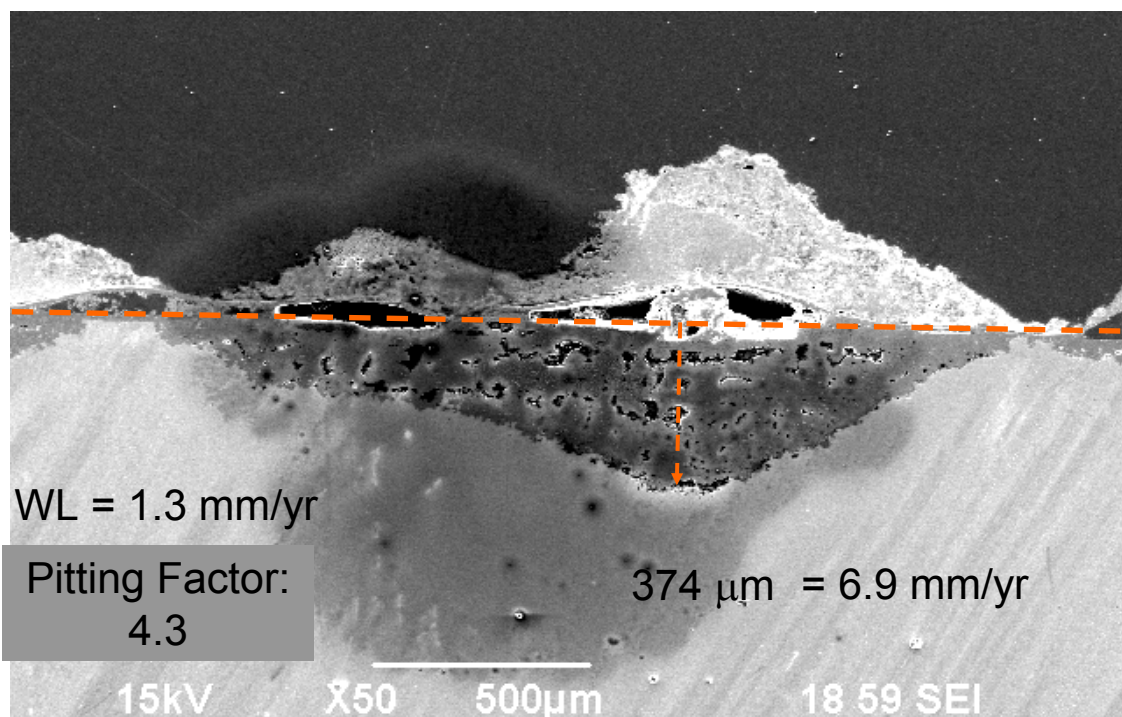


Figure 195. WL coupon after 20 days exposure to conditions with HAC in single phase flow. Cross section with corrosion product layer.

EDS spot analysis is shown in Figure 196, Figure 197, and Figure 198 for three different spots on the same cross section location. The peak in the EDS spectrum left of sulfur (S) is for the gold (Au) sputter coating on the cross-section sample. This peak is not added into the analysis as it is not part of the experimental conditions and would alter the quantitative values for comparison in the upper right hand side of each EDS spectrum analysis.

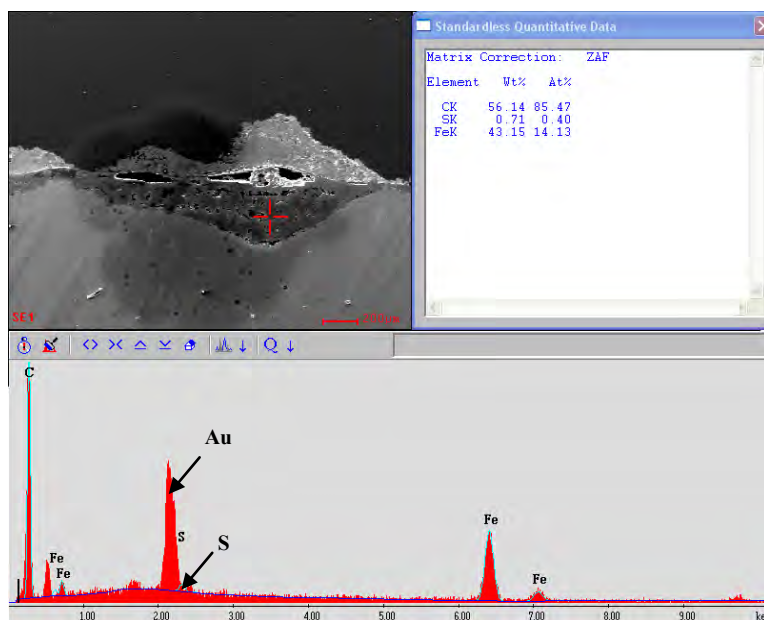


Figure 196. EDS analysis of localized corrosion found in cross section of WL coupon after 20 days exposure to conditions with HAC in single phase flow; material below original surface.

These three figures show that the corrosion product composition within the pit is different than the corrosion product layer above the pit. For this pit, locations above the original coupon surface (orange dotted line, Figure 195) have at least a magnitude greater concentration of sulfides than locations below the original surface. Figure 196 shows a 21 Atomic% of sulfide and Figure 197 shows a 7 Atomic% of sulfide for the corrosion product layer while Figure 198 only shows a 0.4 Atomic% of sulfide within the pit.

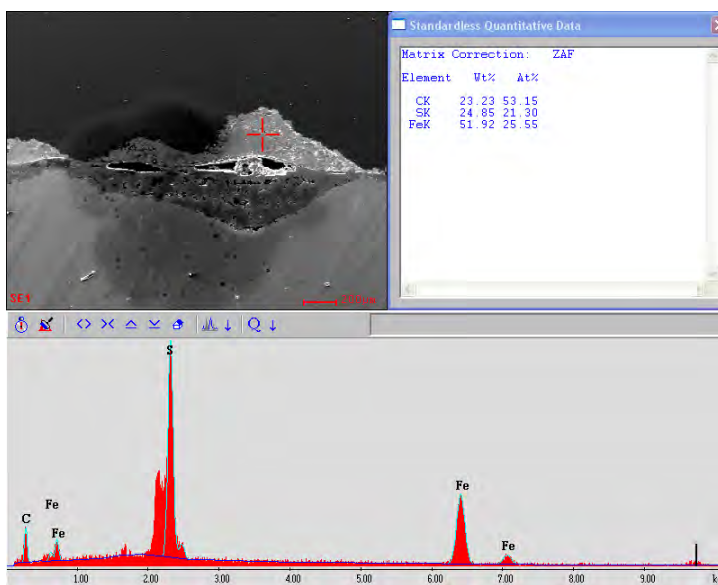


Figure 197. EDS analysis of localized corrosion found in cross section of WL coupon after 20 days exposure to conditions with HAc in single phase flow; material above original surface.

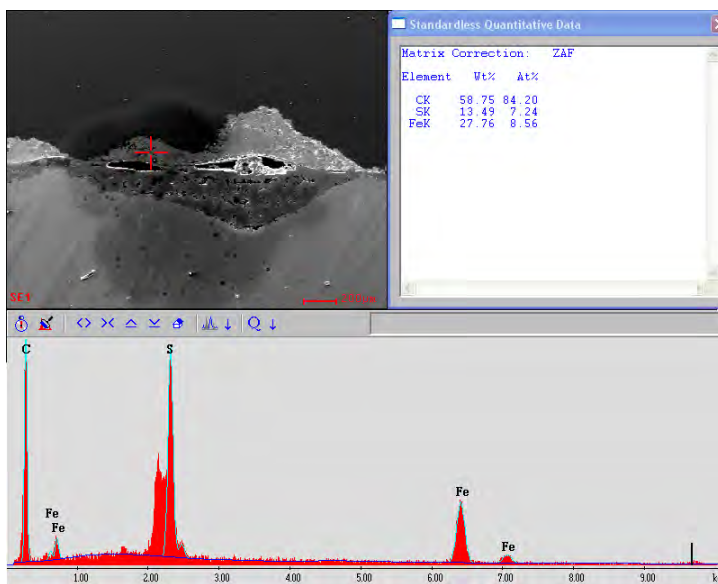


Figure 198. EDS analysis of localized corrosion found in cross section of WL coupon after 20 days exposure to conditions with HAc in single phase flow; material above original surface.

With a concentration of 1000 ppm H₂S in the gas phase and 7.7 bar pCO₂, the total sulfides in the bulk solution ($[\text{H}_2\text{S}]_{(\text{aq})} + [\text{HS}^-] + [\text{S}^{2-}]$) are only 0.7 mM (7×10^{-4} M) and the total carbonate concentration ($[\text{CO}_2]_{(\text{aq})} + [\text{H}_2\text{CO}_3] + [\text{HCO}_3^-] + [\text{CO}_3^{2-}]$) is 213 mM (213×10^{-3} M). With 300 times less concentration in the bulk solution, the corrosion product layer is dominated by sulfides due to the very fast reaction kinetics between hydrogen sulfide $[\text{H}_2\text{S}]_{(\text{aq})}$ and the bisulfide ion $[\text{HS}^-]$ with Fe and $[\text{Fe}^{2+}]$. The corrosion mechanism that would cause a smaller concentration of sulfides within the pit is not yet understood, but it has been shown that the partial pressure of CO₂ plays a role in developing localized corrosion under these conditions. This will be under further review.

The WL coupon from multiphase flow during the same period of time is dramatically different. As can be seen in Figure 199, this WL coupon did not experience excessive corrosion or localized attack. At 0.44 mm/yr general corrosion rate, this is the lowest rate observed for all coupons tested in this experiment. Minimal variation was measured in the topography of the surface layer and, consequently, the layer weight was only measured at 0.019 grams. Under these test conditions it indicates that if no corrosion product layer is developed, there was no location for initiation of a localized event. This multiphase WL coupon provides proof that a corrosion product layer large enough to become a barrier to mass transfer is necessary to develop a galvanic cell and propagate localized corrosion.

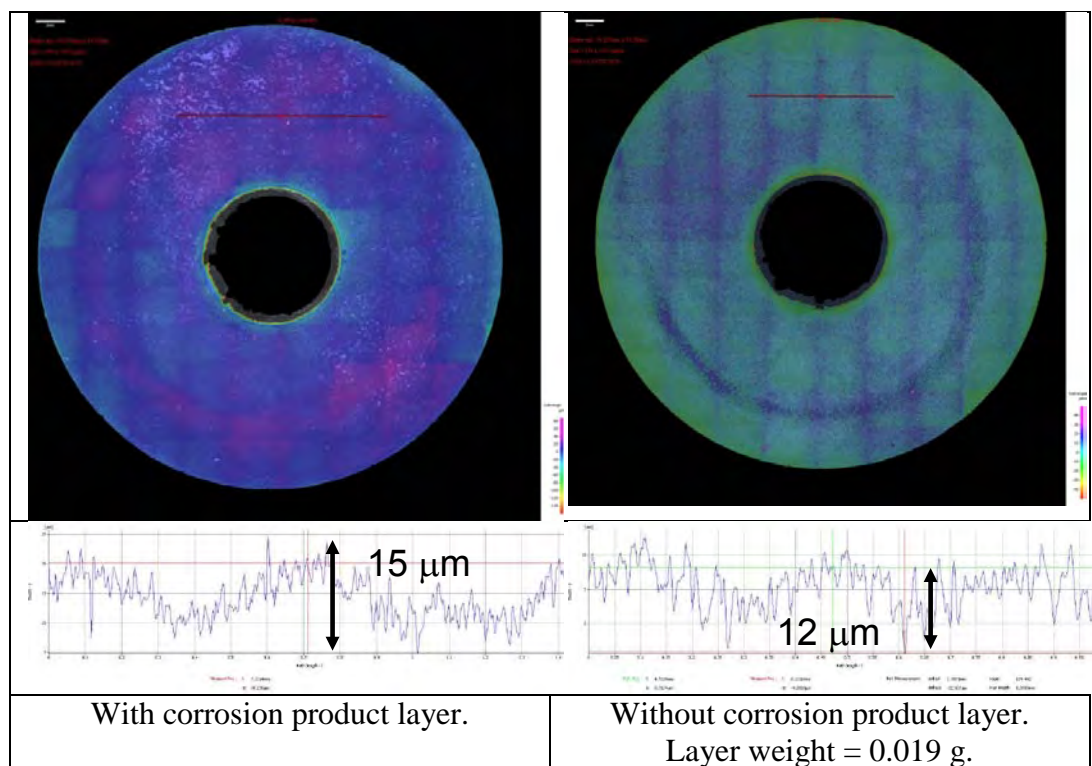


Figure 199. WL coupon after 20 days exposure to the full test conditions in multiphase flow.

A comparison of corrosion rates measured by the WL coupons is found in Figure 200. As stated previously, in this current experiment 6 out of 7 coupons indicated localized corrosion. This occurred in the absence and presence of acetic acid. In a previous 30 day experiment under the same starting conditions, but without acetic acid, only one coupon developed localized corrosion. Since this experiment had an overall higher likelihood of localized corrosion both before and after the addition of HAC and in both single phase and multiphase, no conclusions can be determined for the addition of 100 ppm free HAC. Even a comparison of propagation rates by pitting ratio in Figure 201 does not provide any trend related to time or the addition of HAC.

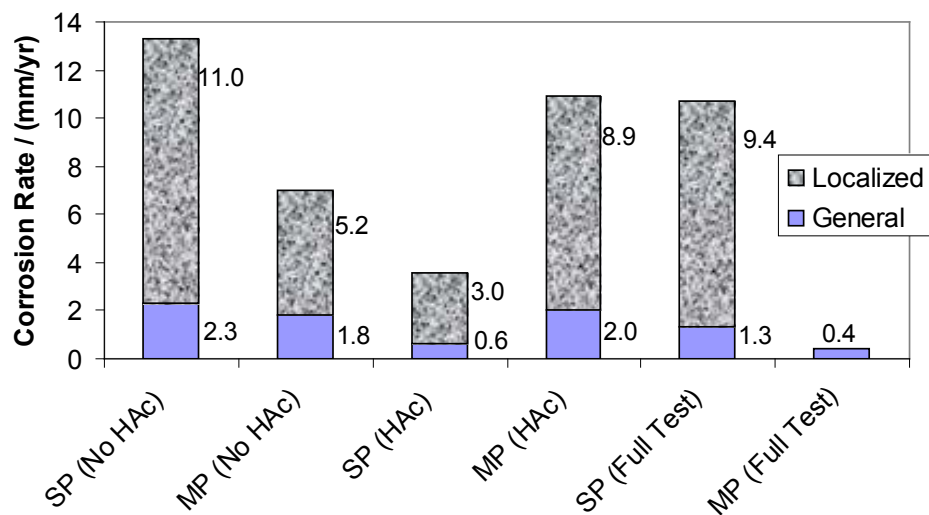


Figure 200. WL corrosion rate data comparison for all coupons from single phase (SP), multiphase (MP), first 10 days (No HAc), second 10 days (HAc), and full test.

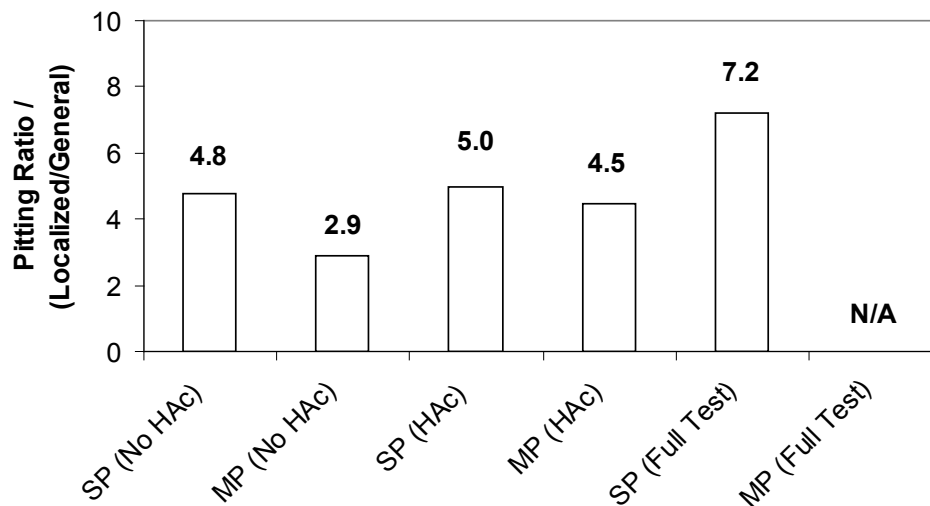


Figure 201. WL pitting ratio comparison for all coupons from single phase (SP), multiphase (MP), first 10 days (No HAc), second 10 days (HAc), and full test.

Conclusion Related to the Presence of Acetic Acid

The likelihood of localized corrosion developed after 10 days exposure was not affected by the addition of 100 ppm free acetic acid. Since localized corrosion was prominent on most of the WL samples, this experiment did not provide evidence that the addition of 100 ppm free acetic acid affected the initiation or propagation of localized corrosion.

CHAPTER 5: PREDICTION OF LOCALIZED CORROSION

The development of a model to calculate the likelihood of localized corrosion must be supported by an understanding of the parameters of interest. After reviewing a descriptive list of the experimental parameters (Table 30), a review of the relationship of parameters used to the understanding of the mechanisms involved in the corrosion process is provided as justification for their use in determining the likelihood of localized corrosion. Then the prediction model for localized corrosion will be presented and verification shown.

Experimental Data Set

The set of experimental parameters and results from 11 of the test cases were used to define the likelihood of localized corrosion. The minimum, maximum, mean, and standard deviation of independent and dependent variables are listed in Table 30. The analysis of variance (ANOVA) for this dataset is located in “Appendix A: ANOVA of Dataset .” From review of this parameter ANOVA, the sample location and exposure time were removed from further analysis because of low confidence levels, indicated by F statistic significance values. The low confidence levels for these parameters indicated that the likelihood of localized corrosion related to either of the two parameters was simply due to chance. Although some correlation to the partial pressures of CO₂ and H₂S was indicated by the ANOVA, the solution concentrations of [H₂CO₃]+[HCO₃⁻] and

$[H_2S]+[HS^-]$ were used instead since they are directly related to the corrosion reaction as proton, $[H^+]$, donors.

Table 30. Descriptive Statistics of H_2S/CO_2 Sample Data Set (N = 78)

Parameter	Units	Minimum	Maximum	Mean	Std. Dev.
Independent variables					
Temperature	Kelvin	298.15	333.15	325.7	12.2
Solution pH		4	6	5.24	.59
Ionic Strength	mol/L	.17	1.7	.55	.67
Sample Location	Up/Dn	0	1	--	--
Exposure Time	day	6.86	14.23	30.9	6.31
pCO ₂	bar	2.7	7.7	5.8	2.4
$[H_2CO_3] + [HCO_3^-]$	mol/L	1.26×10^{-4}	3.59×10^{-4}	2.88×10^{-4}	9.19×10^{-5}
S(FeCO ₃)		.0001	8.29	1.68	2.9
pH ₂ S	bar	.0010	.10	.026	.038
$[H_2S]+[HS^-]$	mol/L	2.36×10^{-10}	1.60×10^{-8}	3.90×10^{-9}	5.03×10^{-9}
S(FeS)		.059	585.95	114.17	213.6
Dependent variable					
Measured Maximum Pitting Ratio		.00	24.2	2.25	3.8

Relationship of Parameters to the Likelihood of Localized Corrosion

Relationship to Saturation values

It is understood that localized corrosion cannot occur in under-saturated solutions without some type of initiator, but there is only an indirect relationship between over-saturated solutions and localized corrosion. If the saturation values are greater than 1, then precipitation of iron sulfide and/or iron carbonate is possible which can lead to the development of a galvanic cell under the right environmental conditions. The saturation values are an important step as they are needed to calculate the precipitation rates of iron

carbonate and iron sulfide. The prediction model for the likelihood of localized corrosion takes into account the temperature of the system and the saturation values of both iron sulfide and iron carbonate. Although temperature is treated as an independent variable, it is also used in the equations of solubility products for both iron sulfide and iron carbonate which may account for the lower coefficients calculated for the saturation values. An interaction parameter was also defined as the product of the saturation values which will be low or negative when the system is undersaturated with respect to iron carbonate and/or iron sulfide, but will be positive when both are above saturation and will increase in magnitude when the values are both highly supersaturated. This is a direct indication of the scaling tendency of the system and observations have shown more localized corrosion occurs due to imperfections in the growth of the corrosion product layer.

Relationship to Ionic strength

A change in ionic strength is understood to have an effect on iron carbonate precipitation, but not as much is known about its effect on iron sulfide corrosion products. In the current experiments, an increase in the ionic strength of the solution (by an increase in sodium chloride concentration) from 0.26 to 1.8 did not have much effect on the general corrosion rate, but was found to increase metal loss underneath the corrosion product layer indicating an increased likelihood toward localized corrosion. When considering a porous corrosion product layer, an increased ionic strength would decrease iron carbonate precipitation within the corrosion product layer and near the

metal surface, thus allowing more metal loss under the corrosion product layer (undermining). Ionic strength is thought to be a significant indicator for the likelihood of localized corrosion.

Relationship to pH

The pH of the solution has a direct influence on the development of the corrosion product layer and therefore has a strong influence on the likelihood for localized corrosion. But it seems the relationship is based on the 'type' of localized corrosion that would occur. At pH 4, iron carbonate is always under-saturated, so localized corrosion is related to thickness and failures of the iron sulfide layer developed. At pH 6 and above, the iron sulfide saturation value can become quite high with just a small concentration of ferrous ions, so precipitation of iron sulfide on top of the corrosion product layer was always observed. At pH 5, the corrosion product layer developed does not have much of a precipitation layer on top of the initial corrosion product layer and the localized corrosion locations underneath the corrosion product layer are usually filled, not empty. The likelihood for localized corrosion is higher in a pH 6 solution than for either pH 5 or pH 4 solutions, so a dramatic increase in the likelihood for localized corrosion is related to precipitation on top of the initial corrosion product layer. By using the bulk solution saturation value or bulk solution precipitation rate, when a large amount of surface precipitation is indicated by these values, the likelihood for localized corrosion would increase by a factor of 2 to 3 (Figure 93). The solution pH is a strong indicator for the

prediction of localized corrosion as it is directly related to the corrosion product layer that will form on the metal surface.

Relationship to decrease in pCO_2

A decrease in partial pressure of CO_2 would be expected to decrease the amount of $[H_2CO_3]$ and $[HCO_3^-]$ available for diffusion through the corrosion product layer which would change the water chemistry conditions that could occur within the corrosion product layer. In the comparison between Experiment 8 and Experiment 10, the decrease in the partial pressure of CO_2 increased the likelihood of developing localized corrosion, but also included an increase in the solution pH. The presence of iron carbonate as a recognizable species in the corrosion product layer was thought to have some relationship to the likelihood of localized corrosion, but a simple comparison over the 8 experiments in Table 31 does not show any obvious correlation between the visual presence of iron carbonate and measured localized corrosion.

Table 31. Environmental conditions for eight experiments at 1 wt% NaCl that involve a change in $p\text{CO}_2$ for comparison.

Exp #	$p\text{CO}_2$ (bar)	$p\text{H}_2\text{S}$ (bar)	Temp (°C)	pH	Localized Corrosion?	FeCO_3 Crystal structure observed?
Exp 3	7.7	0.0012	60	6	Yes ($\text{PR} \geq 5$)	No
Exp 4	7.7	0.010	60	6	Maybe ($3 \leq \text{PR} < 5$)	Yes
Exp 7	7.7	0.001	60	5	No ($\text{PR} < 3$)	No
Exp 8	7.7	0.010	60	5	No ($\text{PR} < 3$)	Yes
Exp 10	2.7	0.010	60	6	Yes ($\text{PR} \geq 5$)	Yes
Exp 11	2.9	0.004	40	5	Yes ($\text{PR} \geq 5$)	No
Exp 13	2.8	0.10	25	5	No ($\text{PR} < 3$)	No
Exp 14	2.8	0.13	40	5	Maybe ($3 \leq \text{PR} < 5$)	Yes

This is an indication that the use of the solution concentrations of $[\text{H}_2\text{CO}_3] + [\text{HCO}_3^-]$ and $[\text{H}_2\text{S}] + [\text{HS}^-]$ have more significance than the partial pressures of the acid gases since these values will also be related to the temperature and pH of the environment.

Relationship to temperature

The effect of temperature on the likelihood of localized corrosion should be related to the kinetics of precipitation which will be related to the porosity of the corrosion product layer. With a lower temperature, the initial corrosion product layer would be expected to be more porous since the adsorption equation is a function of temperature and the precipitation reaction equations are a function of temperature. This was observed to provide a more uniform, general corrosion with less localized corrosion as no localized corrosion was seen at 25°C. The temperature parameter will have an influence on both the initial corrosion rate (determined through the adsorption reaction)

and on the corrosion product layer (related to precipitation rate equations). The temperature is also expected to be strongly related to the likelihood of localized corrosion.

Relationship to acetic acid

In this series of tests, acetic acid was not fully tested over many parameters, but was just added in one experiment to observe if the results achieved were as expected. It is understood from previous experience that the addition of acetic acid has proven to be equivalent to the addition of another cathodic reaction in the corrosion of mild steel and does not have a synergistic effect with either CO₂ corrosion or H₂S corrosion. With this understanding in mind, the addition of acetic acid will change the ionic strength of the solution and provide another species that can diffuse through the corrosion product layer to increase the corrosion rate. The relationship of the presence of acetic acid to the likelihood of localized corrosion may be related to the effect it has on the precipitation rate of iron carbonate near the metal surface after diffusion through the corrosion product layer. Since there was not enough empirical data to add this parameter directly to the correlation for the likelihood of localized corrosion, it is assumed to influence the ionic strength. Further studies are necessary with acetic acid when defining the growth and diffusion of species through a corrosion product layer.

Analysis of the Data Set

In order to gain a visual understanding of the dataset, the test conditions were adjusted by arbitrary factors and arranged on an arbitrary y-axis so the parameters could be visually compared. A comparison of the independent variables (Figure 202) shows that there are three nominal categorical parameters (temperature, pH, ionic strength) and the remaining covariates must be considered as continuous variables (carbonic acid, bicarbonate, aqueous hydrogen sulfide, and bisulfide concentrations).

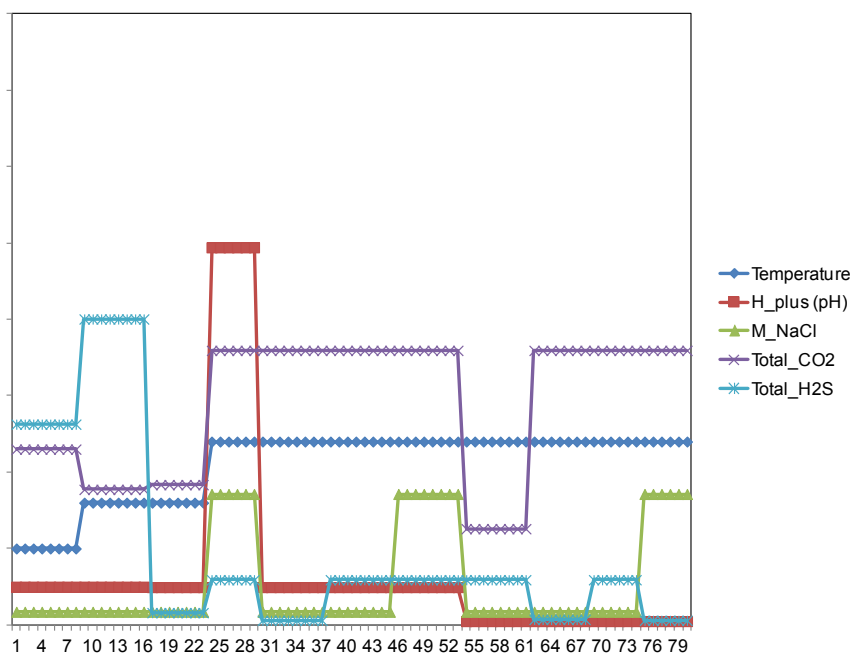


Figure 202. Environmental parameters plotted on an arbitrary axis for 80 analyzed weight loss samples (x-axis) sorted by temperature, pH, and sodium chloride concentration (M_NaCl represents ionic strength, Total_CO₂ represents the sum of [H₂CO₃]+[HCO₃⁻], Total_H₂S represents the sum of [H₂S]_{aq}+[HS⁻].

The only dependent variable is the pitting ratio which is a comparison of localized corrosion penetration rate to the general corrosion measured for the weight loss samples, so this was used to determine the likelihood of localized corrosion. As can be seen in Figure 203, the pitting ratio does show a relationship to the changes in the water chemistry parameters, so a set of linear equations was tested as the first step in modeling to gain a better understanding of the input variables required in the model.

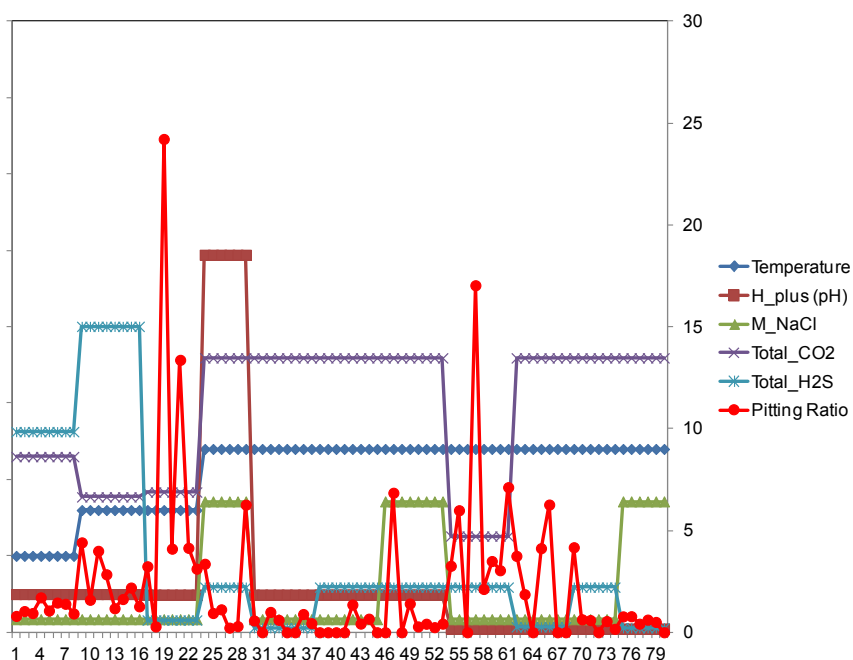


Figure 203. Addition of Pitting Ratio data to the environmental parameter set.

The pitting ratio (PR) was converted into a likelihood value by using the definition previously given in Chapter 3. There were 5 to 8 samples in each experiment that were analyzed for localized corrosion and weight loss for the 11 experimental datasets used in the analysis. The value for the likelihood of localized corrosion was

calculated based on the number of samples in each dataset that experienced localized corrosion ($PR \geq 5$) or showed an increased risk for localized attack ($3 \leq PR < 5$). Each sample that experienced localized corrosion was given a risk factor of 100% while the samples that had an increased risk for localized corrosion were given a risk factor of 50%. The values determined for the likelihood of localized corrosion for each set of parameters tested are shown in Table 32 sorted with respect to temperature, pH, sodium chloride concentration, pCO_2 , and pH_2S with the visual representation of the full dataset shown in Figure 204.

Table 32. Determination of Likelihood of Localized Corrosion from Sample Analysis

Temp. (°C)	pH	[NaCl] (M)	pCO_2 (bar)	pH_2S (bar)	PR < 3	$3 < PR < 5$	PR > 5	Sample Count	Likelihood of Localized Corrosion
25	5	1	2.8	0.1000	8	0	0	8	0.0%
40	5	1	2.8	0.1000	6	2	0	8	12.5%
40	5	1	2.9	0.0040	1	4	2	7	57.1%
60	4	10	7.7	0.0100	4	1	1	6	25.0%
60	5	1	7.7	0.0010	8	0	0	8	0.0%
60	5	1	7.7	0.0100	8	0	0	8	0.0%
60	5	10	7.7	0.0100	7	0	1	8	12.5%
60	6	1	2.7	0.0100	2	3	3	8	56.3%
60	6	1	7.7	0.0012	4	2	1	7	28.6%
60	6	1	7.7	0.0100	4	1	0	5	10.0%
60	6	10	7.7	0.0010	5	0	0	5	0.0%
Totals:					57	13	8	78	

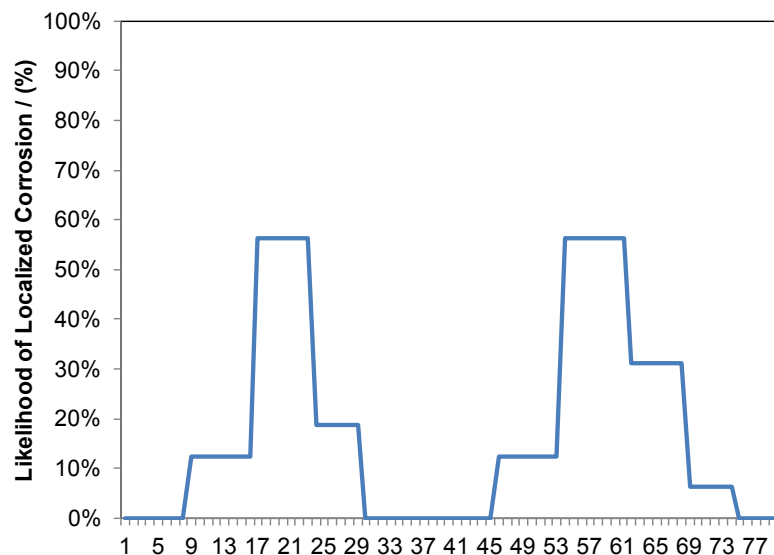


Figure 204. Likelihood of localized corrosion sorted with respect to temperature, pH, sodium chloride concentration, $p\text{CO}_2$, and $p\text{H}_2\text{S}$.

Prediction Model for Localized Corrosion

A solution was determined using the technique of Gaussian elimination in MATLAB using the environmental conditions of the 11 datasets to calculate the likelihood of localized corrosion. The set of 78 homogeneous equations were solved according to Equation (34):

$$a_1x_1 + a_2x_2 + \cdots + a_nx_n = p_1 \quad (34)$$

where a = parameter coefficient,

x = parameter value, and

p is the unique solution.

The parameters used for the solution of Equation (34) are based on the chemical, electrochemical, and precipitation reactions reviewed in Chapter 3 with tested

experimental conditions focused on elucidation of possible interactions between parameters. The results are shown in Table 33.

Table 33. Definition of parameters used for correlation with calculated coefficients.

Parameter Title	Coefficient (a)	Sensitivity	Parameter definition (x)
Temperature	-1.94	± 0.016 ($\pm 1.1\%$)	T_K
pH	59.45	± 1.1 ($\pm 1.5\%$)	pH
Carbonate concentration	-99.25	± 2.5 ($\pm 2.5\%$)	$\log([H_2CO_3]+[HCO_3^-])$
Sulfide concentration	-31.46	± 1.6 ($\pm 5\%$)	$\log([H_2S]+[HS^-])$
Ionic strength	25.65	± 2.6 ($\pm 10\%$)	I
Iron sulfide saturation	0.11	- - -	S(FeS)
Iron carbonate saturation	0.32	- - -	S(FeCO ₃)
Interaction of saturation values	12.71	± 2.5 ($\pm 20\%$)	$\log(S(FeS)*S(FeCO_3))$

Five of the parameters used in correlation of the data (T_K , pH, I, S(FeS), S(FeCO₃)) were reviewed directly in the research as each play a role in defining the environmental conditions. An indirect effect of CO₂ and H₂S is also expected, so the species in solution that can directly provide protons for the corrosion reaction were used ([H₂CO₃], [HCO₃⁻], [H₂S], [HS⁻]); refer to the section on Calculation of Environmental Conditions. The solubility constants for carbonic acid, bicarbonate ions, aqueous hydrogen sulfide, and bisulfide ions are an exponential function of temperature, the base 10 logarithm of these values are used as the linear transform of the data in order to fit

them in the set of linear equations. An interaction parameter was also necessary to provide an indication of corrosion product layer formation and was provided by using the base 10 logarithm of the product of saturation values. This value will be positive when both saturation values are above 1 (supersaturated conditions for both species), but negative when the system is not dominated by either iron sulfide or iron carbonate precipitation (undersaturated for both species).

Figure 205 shows the comparison between measured and predicted likelihood for localized corrosion using these datasets with good correlation between over-prediction and under-prediction of the likelihood of localized corrosion. Direct comparison of the likelihood values calculated can be seen in Figure 206 for the 11 datasets. The raw data of pitting ratio for each of the 78 samples is also shown in comparison to the measured and calculated likelihood for localized corrosion in Figure 207.

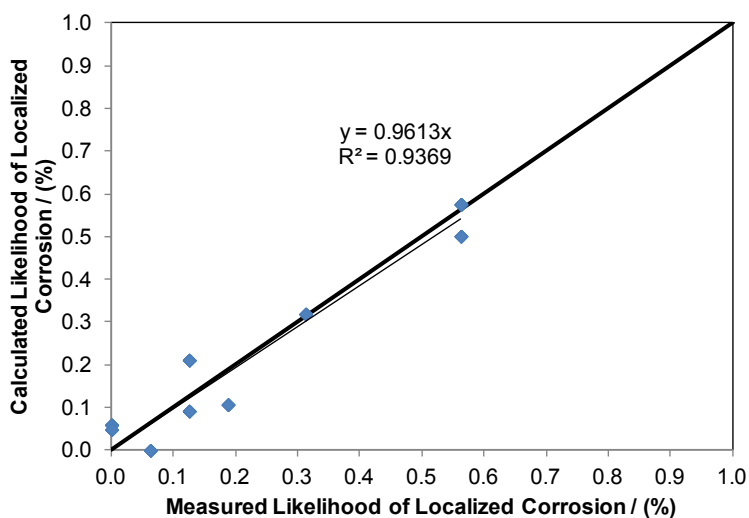


Figure 205. Correlation between measured and calculated values for likelihood for localized corrosion.

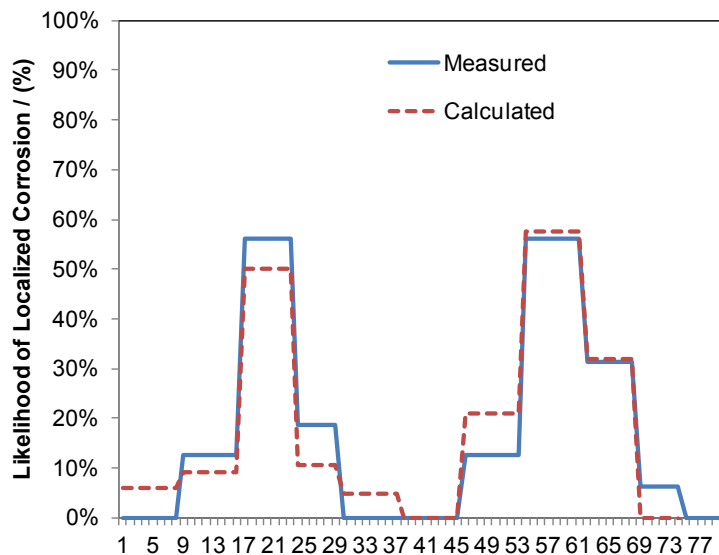


Figure 206. Direct comparison of measured and calculated likelihood for localized corrosion under the tested conditions.

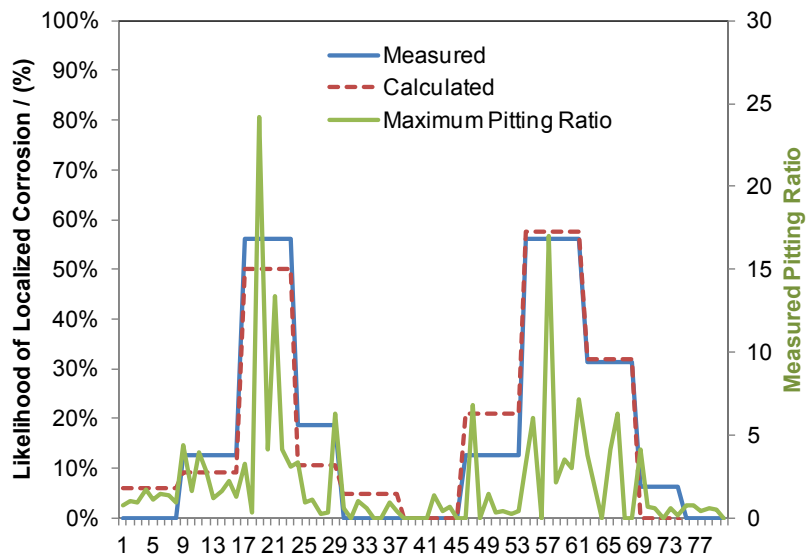


Figure 207. Comparison of the measured maximum pitting ratio for 78 test samples to the measured and calculated values for likelihood of localized corrosion.

In order to identify which variables are more important in the calculation of the likelihood of localized corrosion, a qualitative review of the parameters was done to determine their sensitivity to change. The sensitivity of each of the parameter coefficients in Table 33 was tested through comparison of the calculated value to the measured value of the Likelihood of Localized Corrosion while varying that specific parameter. The maximum difference between the measured and calculated values for the likelihood of localized corrosion in Figure 206 is less than 9%. In order to determine a value for sensitivity, the maximum difference was not allowed to exceed 15% while changing each specific variable. The results are shown as an uncertainty and a percent change for each coefficient.

A comparison of the coefficient sensitivity values in Table 33 shows which parameters are more sensitive to change. The model is most sensitive to changes in the coefficients for temperature and pH, where changes from 1% to 2% change the output of the model by more than 15%. The coefficients for the concentrations of carbonates and sulfides in solution affect the outcome of the model if they are varied by 2.5% to 5%, which shows that these variables are also highly significant in the calculation of the model. The values of uncertainty for iron carbonate saturation and iron sulfide saturation coefficients were not calculated because they are used in the interaction parameter and would not be varied independently. And the coefficient for the interaction of the saturation values is the least sensitive parameter which is an indication that the degree of

saturation is not as important as having both iron carbonate and iron sulfide saturated in solution.

It must be understood that the form of Equation (34) does not have any intrinsic boundaries, so some must be imposed. Values calculated for the likelihood of localized corrosion are valid in the range from 0 to 100%. The magnitudes of calculated values that exceed the 0 to 100% range do not have any justifiable meaning and should be limited to these boundary values.

Verification of Model

Comparisons of the model for the likelihood of localized corrosion to other published literature are necessary to check the validity of the model. The difficulty was in finding the results from other research that related to the parameter set and confirmed that localized corrosion was observed. Two papers from IFE, Norway, and one paper from ICMT, USA, are used to provide the data comparison. In the first two cases, the ferrous ion concentration was not provided. Since the calculation of the likelihood of localized corrosion depends upon the saturation values for iron sulfide and iron carbonate, a concentration of ferrous ions in solution needs to be assumed.

The research done at the Institute for Energy Technology in Norway was conducted in a single phase flow loop in experiments related to sour glycolic corrosion (glycol is used to prevent hydrate formation in the H₂S containing fields of the North Sea). Two separate research papers were found that both report observation of localized

corrosion as defined in Table 34. The first three experiments were conducted with a pH change during the experiment to determine target pH values to be used in pH-stabilization techniques in the sour gas pipelines. All three experiments were carried out at 0.6 bar pCO₂ and just over 1 bar pH₂S.

Table 34. Referenced Research from IFE, Norway

Parameter	Description			
Given Values	1	2	3	4
Reference	[56] Table 3	[56] Table 4	[56] Table 5	[57] Table 4
Test duration (days)	27	26	42 - 60	55
Temperature	20°C	60°C	60°C	60°C
pCO ₂ (bar)	0.6	0.6	0.6	5
pH ₂ S (bar)	1.1	1.3	1.4	0.5
pH	5.5 - 6.5	5.5 - 6.5	4 - 6.5	5
Solution (wt% NaCl)	1	1	0.1	0.82
MEG	50%	50%	0	50%
Final corr. Rate LPR (mm/yr)	0.1 - 0.092	1.2 - 0.20	0.004 - 0.01	0.085 - 0.098
Max. Pit depth (µm)	---	---	50	235 - 300
Max. Local Corr. Rate (mm/yr)	0.31-0.34	2.7-1.9	0.3	---
Pitting Ratio	0.9 - 3.5 (localized?)	2.5 - 10 (localized)	30 (localized)	18.3 - 20.3 (localized)
Calculated Values for Model				
[Fe ⁺⁺] (ppm)	1 - 5	1 - 2	0 - 10	15 - 20
Likelihood of localized corrosion	38 - 100%	85% - 100%	100%	0.5 - 20%
Data and Model both agree on localized corrosion?	Yes	Yes	Yes	Not Well

The first of these experiments at 20°C had an LPR final corrosion rate of approximately 0.1 mm/yr and a maximum pit penetration rate of 0.34 mm/yr which can be used to calculate a pitting ratio just greater than 3. According to the definition of Localized Corrosion provided in Chapter 3, this may not be an indication of localized corrosion. The outcome of the model for the likelihood of localized corrosion is sensitive to the amount of ferrous ions in solution since the calculation relies on the saturation values for iron carbonate and iron sulfide. For this case at 20°C, testing the model with ferrous ion concentrations show that even with 1 ppm $[\text{Fe}^{++}]$ the likelihood of localized corrosion is 38% at pH 5.5 while any $[\text{Fe}^{++}]$ above 5 ppm should have a 100% chance of localized corrosion. The second and third experiments reported in Table 34 at 60°C have pitting ratios greater than 5 and are considered to have confirmation of localized corrosion. For the second experiment, any concentration of $[\text{Fe}^{++}] > 1$ used in the calculation returned a 100% likelihood of localized corrosion. For the third experiment, no localized corrosion would be expected to form at pH 4 (the beginning of the experiment), but with the increase of pH to pH 5.5 and pH 6.5, localized corrosion with a pitting ratio of 30 was observed. The likelihood of localized corrosion agreed with a 100% chance of localized corrosion expected. The fourth experiment in Table 34, also at 60°C, but with a much higher pCO_2 and pH_2S , had an experimentally observed pitting ratio of approximately 20 which is confirmed localized corrosion. The calculation for likelihood of localized corrosion shows that a concentration from 15 to 20 ppm $[\text{Fe}^{++}]$

would increase the likelihood of localized corrosion from 0.5% up to a 20% chance for localized corrosion.

The research done at the ICMT was done in the same flow loop as the experiments conducted in the data set for the model. The three referenced experiments shown in Table 35 were completed as part of a Top-of-the-Line Corrosion (TLC) study that used a stratified flow regime for these samples and did not add sodium chloride (NaCl) to the solution since it would not impact the results of TLC. Testing was conducted at 70°C for 21 days, but no localized corrosion was observed on the samples taken from the bottom of the line. Calculation of the likelihood of localized corrosion shows a discrepancy with experimental results for the case with 0.004 bar pH_2S since the model does predict a slight increase in the likelihood of localized corrosion when the amount of sulfide species in solution is limited, but notice that with $\text{S}(\text{FeS}) > 1$ there is an increased risk for localized corrosion.

Table 35. Referenced Research from ICMT, USA (NACE 2007)

Parameter	Description		
Given Values	5	6	7
Reference	[58]	[58]	[58]
Test duration	21 days	21 days	21 days
Temperature	70°C	70°C	70°C
pCO ₂	2 bar	2 bar	2 bar
pH ₂ S	0.004 bar	0.07	0.13
pH	4.2-4.7	4.3 – 4.5	4 – 4.4
Solution	0 wt% NaCl	0 wt% NaCl	0 wt% NaCl
[Fe ⁺⁺] (ppm)	8 - 18	9 – 20	6.5 – 26
S(FeCO ₃)	0.2	0.06	0.1
S(FeS)	2	11	43
Calculated Values for Model			
Likelihood of localized corrosion	20.7%	0%	0%
Data and Model both agree on localized corrosion?	Not well	Yes	Yes

Since the model for likelihood of localized corrosion was in agreement with over 70% of the seven experiments found in published literature, the model is considered acceptable in its current form.

CHAPTER 6: DISCUSSION AND CONCLUSIONS

Introduction

Localized corrosion is understood to be related to a failure of the corrosion product layer to maintain a uniform coverage on the metal surface, but definition of these *failure mechanisms* for localized corrosion has not yet been defined. A review of the current knowledge of H₂S/CO₂ corrosion product growth mechanisms shows what assumptions have been made, what new understanding can be added to the model, and what important research topics need attention in the near future.

Discussion

Initial Corrosion Product Layer

When a bare metal surface is exposed to an environment with H₂S present, the general corrosion rate may immediately decrease by approximately 80%. Analysis has shown⁴ this layer is very thin and not visible to the naked eye. This *initial adsorbed layer* of iron sulfide (FeS) on a metal surface has been referred to as providing a “retardation of the charge transfer reaction” and is modeled by a Langmuir type adsorption isotherm⁴:

$$1 - \theta_{H_2S} = \frac{1}{1 + K_{a/d} c_{H_2S}} \quad (35)$$

where $K_{a/d}$ is the adsorption /desorption constant for sulfide species.

The *initial surface coverage* by this adsorbed layer of FeS is understood to be a function of temperature and $[H_2S]_{(aq)}$ (which are generically captured by the current model) and directly influences the corrosion rate by retardation of the anodic reaction (less surface area available for iron dissolution). Although the current model adequately captures the effect of the initial corrosion product layer when H_2S is present, there is current research underway to better define the mechanisms of H_2S with the metal substrate. ⁶ The current model is accepted as is for this discussion.

Corrosion Product Layer Growth

In addition to the initial corrosion product layer of FeS, the thickness of the corrosion product layer is known to increase with time and the *growth of the layer* is currently modeled by Sun ⁵ as a simple linear expression with respect to the calculated corrosion rate. Although this is a valid first step in modeling this phenomenon, it requires modification to include the mechanisms of corrosion product formation in order to capture the likelihood of localized corrosion.

Current ⁵ corrosion product layer model:

When H_2S is present in the water chemistry, an iron sulfide layer is immediately formed which decreases the corrosion rate. This corrosion product layer acts as a mass transfer diffusion boundary between the solution and the metal surface where all cathodic

and anodic reactions occur. As the corrosion product layer increases in size, the diffusion path to the surface becomes more difficult, decreasing effective species diffusion rates, which subsequently decreases the general corrosion rate. The current⁵ corrosion product growth model also contains a simple linear expression (Equation (1)) with respect to the calculated corrosion rate (CR) to calculate the scale damage rate (SDR). The scale damage rate is a model of an observed mechanism of spalling, or loss of the surface layer nearest to the bulk solution, and acts to limit the overall depth of the corrosion product layer. In the current⁵ model, the corrosion product layer formation in an H₂S/CO₂ environment continues to have iron sulfide as the first layer on the steel surface and iron carbonate may co-precipitate with iron sulfide in the outer corrosion product layers.⁵ This model was a landmark achievement in corrosion prediction as it was the first mechanistic model of sour corrosion and has provided the basis for developing a better understanding of sour corrosion mechanisms.

Basis for changing the current⁵ model:

Experiments reviewed within this document show observations of iron carbonate crystals (Experiment 8 & Experiment 10) beneath a distinct iron sulfide corrosion product layer and iron carbonate composition by EDS (Experiments 3, 4, & 14) without the presence of sulfides in the bottom of pitting corrosion. Because the current⁵ model for the corrosion product layer formation in an H₂S/CO₂ environment⁵ does not capture this phenomenon, new mechanisms need to be added to the overall mechanistic model. What

was not taken into account in the current ⁵ model was the reality of precipitation / dissolution reactions occurring within the corrosion product layer in relation to the flux of species from the bulk solution to the metal surface and vice versa. The additional precipitation that would occur could eliminate Equation (1) and provide a prediction of the composition of the corrosion product layer closer to what is observed.

Progress toward updating the current ⁵ model:

There are a few research projects being conducted at the ICMT for determining the mechanisms of sour corrosion and a couple of these are associated with better understanding of the corrosion product layer. Below are five research areas associated with the growth of the corrosion product layer that require more investigation. (These still should not be considered as all inclusive, but are assumptions toward new research directions.) Two of these research areas currently have research projects and previous research on the chemical and electrochemical reactions will suffice for now, but two topics related to reactions in the corrosion product layer are needed. The model for the growth of the corrosion product layer should include:

- Chemical and electrochemical reactions
- Reactions on the bulk solution side of the layer
- Reactions within the layer
- Reactions near the metal substrate
- Types of iron sulfides

This goal of this discussion is to provide a hypothesis for future research on the growth mechanisms of a mixed iron sulfide iron carbonate corrosion product layer.

Proposed corrosion product layer model:

The thickness of the iron sulfide corrosion product layer is known to increase over time as a function of temperature and $p\text{H}_2\text{S}$, but the rate at which this occurs is not known. The current ⁵ model maintains the initial corrosion product layer by direct reduction of H_2S , but further growth should include a mass balance for the loss of ferrous ions. Ferrous ions will be consumed in the direct reaction with H_2S , in the precipitation of iron sulfide and in the precipitation of iron carbonate in the corrosion product layer and in the bulk solution.

In Figure 208 to Figure 210, a variation in the concentration of species through a developing corrosion product layer include: “[sulfides]” which are hydrogen sulfide [H_2S], bisulfide ions [HS^-], and sulfide species [S^{2-}]; “[carbonates]” which are aqueous carbon dioxide [CO_2], carbonic acid [H_2CO_3], bicarbonate ions [HCO_3^-], and carbonate ions [CO_3^{2-}]; and “ferrous ions” or [Fe^{2+}].

Hypothesis for a Thin Corrosion Product Layer

Diffusion of all species through the initial and subsequent mackinawite layers to the substrate below is possible because of its sheet like structure which contains trapped

water molecules.¹⁹ The concentrations of each species that reach the substrate are dependent upon the concentrations on the bulk surface side of the corrosion product layer, their respective diffusion rates, the thickness of the layer, and the precipitation rates for iron sulfide and iron carbonate. The boundary conditions will change during the development of the corrosion product layer and are visually shown in Figure 208 through Figure 210. At the corrosion product interface with the metal surface, the H₂S-Fe reaction is very fast so $[\text{sulfides}]_{(\text{surface})} = 0$; at the bulk solution side of the corrosion product $[\text{sulfides}]_{(\text{bulk})}$ are defined by water chemistry calculations; and in between these two locations, $[\text{sulfides}]$ should be defined by a non-linear diffusion equation that includes the H₂S-Fe reaction in the corrosion product layer.

At the corrosion product interface with the metal surface, $[\text{Fe}^{2+}]$ is at the maximum concentration which decreases as it migrates through the corrosion product by reacting to form iron sulfides before it reaches the interface with the bulk solution where $[\text{Fe}^{2+}] \neq 0$. In the first example of a relatively thin corrosion product, $[\text{sulfides}]$ reach the surface of the metal to directly react with the metal substrate. For a thin corrosion product layer, $[\text{carbonates}]$ remain near equilibrium concentration across the thin corrosion product layer as the consumption of $[\text{Fe}^{2+}]$ keeps $S(\text{FeCO}_3) \ll 1$. A graphic representation of this hypothesis is shown for a thin corrosion product layer, approximately 25% of its final depth at equilibrium with the environmental conditions in Figure 208. An example of this type of corrosion product can be seen in Figure 27 where an X65 sample developed a uniform corrosion product layer with a thickness of 28 to 30

μm after 30 days exposure to a system at 60°C , 7.7 bar pCO_2 , 0.12 mbar pH_2S in multiphase flow.

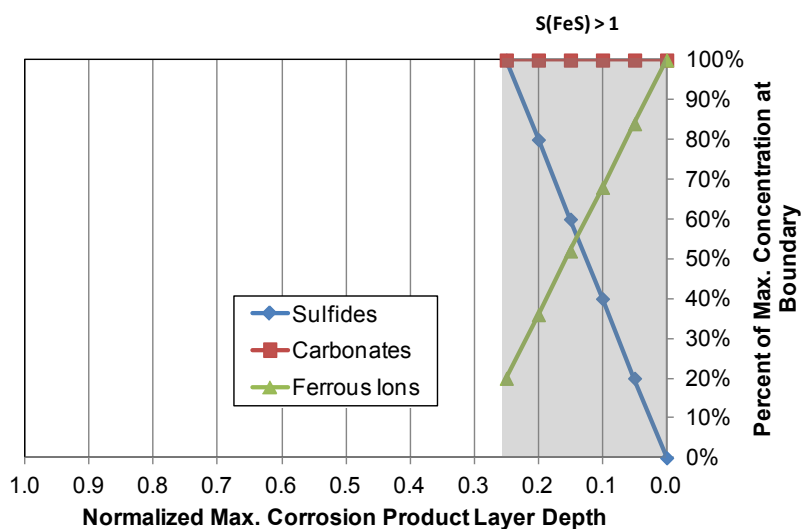


Figure 208. Graphic representation of the concentration of species as diffused through an initial corrosion product layer in an $\text{H}_2\text{S}/\text{CO}_2$ environment that is 25% of its final thickness.

Hypothesis for a Growing Corrosion Product Layer

Observations that the corrosion product layer near the bulk solution has a higher sulfide content in EDS scans supports the fact that the reaction between [sulfides] and $[\text{Fe}^{2+}]$ is the dominant reaction in this system based on the fast kinetics of the reaction. But [sulfides] can only affect the corrosion product layer to a certain depth until it has been depleted by reaction with emerging $[\text{Fe}^{2+}]$ as it diffuses through the layer. As the corrosion product layer grows, [sulfides] that diffuse through will be fully depleted before reaching the metal substrate.

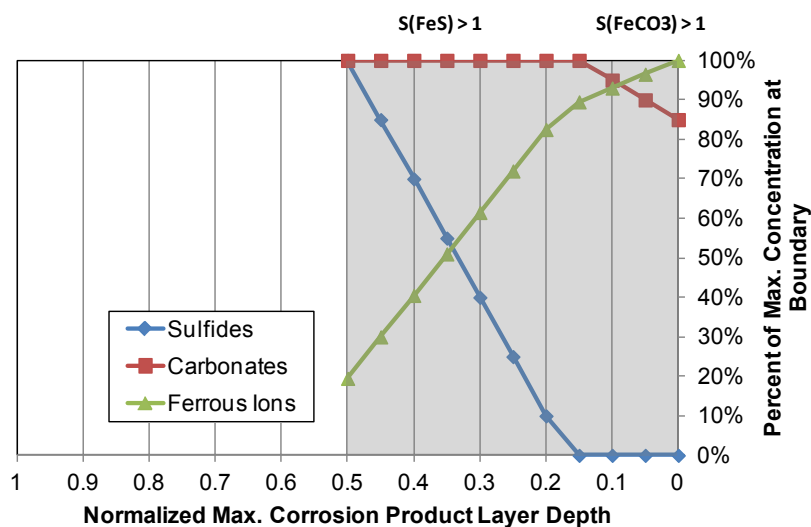


Figure 209. Graphic representation of the concentration of species, $[\text{H}_2\text{S}]_{(\text{aq})}$, $[\text{H}_2\text{CO}_3]$, and $[\text{Fe}^{2+}]$, as diffused through an initial corrosion product layer in an $\text{H}_2\text{S}/\text{CO}_2$ environment that is only 50% of its final thickness.

This will allow iron carbonate formation within the corrosion product layer when $S(\text{FeCO}_3) > 1$ as in Figure 209. An example of this type of corrosion product can be seen in Figure 49 where the upper crust of the corrosion product layer is damaged and reveals an underlying surface morphology similar to an iron carbonate precipitate.

Hypothesis for a Mature Corrosion Product Layer

With continued loss of $[\text{Fe}^{2+}]$ through the corrosion product layers into the bulk solution, the voids left in the iron carbide structure (Fe_3C) near the metal substrate will eventually be filled with FeCO_3 due to the lack of [sulfides]. Figure 210 shows a hypothetical situation where [sulfides] are consumed as it diffuses through the first half

of the corrosion product layer allowing consumption of [carbonates] through dissociation and precipitation of FeCO_3 . An example of this was observed experimentally as can be seen in Figure 46 where different compositions of the layer were determined by EDS.

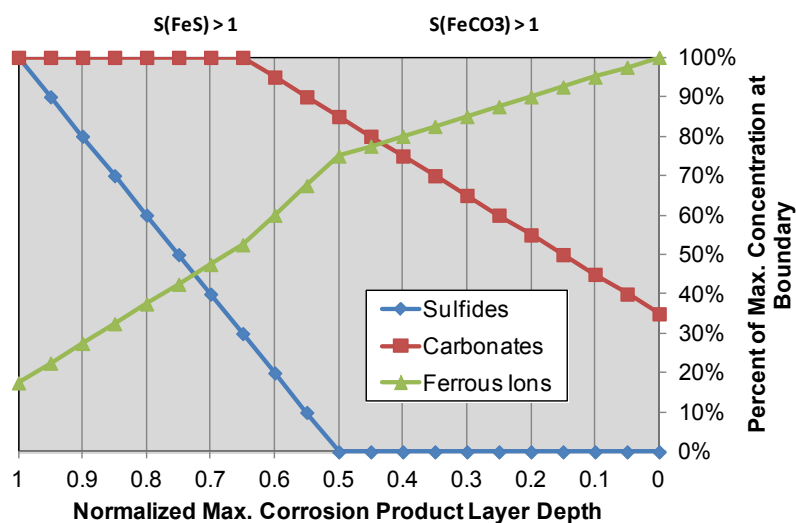


Figure 210. Graphic representation of the concentration of species, $[\text{H}_2\text{S}]_{(\text{aq})}$, $[\text{H}_2\text{CO}_3]$, and $[\text{Fe}^{2+}]$, as diffused through a corrosion product layer in an $\text{H}_2\text{S}/\text{CO}_2$ environment that is fully developed.

The assumptions in the example show the [sulfides] with $[\text{Fe}^{2+}]$ reaction is dominant. When the [sulfides] are depleted during the diffusion through the corrosion product layer, then [carbonates] are allowed the ‘time’ required to dissociate and react with the ferrous ions to precipitate iron carbonate; otherwise there is not enough $[\text{Fe}^{2+}]$ for $\text{S}(\text{FeCO}_3)$ to be greater than 1. The observation that the original surface finish (polish marks) remain visible on the corrosion product layer for extended periods of time, especially at pH 4 and pH 5, indicates that subsequent corrosion product must develop

under the initial corrosion product layer. Because iron sulfide is a semiconductor, cathodic reactions can occur on the bulk solution side of the corrosion product layer to provide the electrons necessary for the anodic dissolution of iron that is occurring on the metal substrate side of the corrosion product layer. The anodic dissolution of iron releases ferrous ions which will be in higher concentrations underneath the mackinawite layer and will diffuse toward the bulk solution. The sulfide species have a higher concentration in the bulk solution and will diffuse toward the metal substrate through the mackinawite layer. Since the reaction between [sulfides] and $[\text{Fe}^{2+}]$ is dominant, iron sulfide will fill in the area where the two meet in the diffusion process.

Initiation Mechanisms for Localized Corrosion

Diffusion and reaction of species within the corrosion product layer are necessary to provide the basis for localized corrosion initiation. Any defect that will occur within the corrosion product layer can be the driving force that increases the likelihood for localized corrosion through failure of the coverage effect provided by the direct reaction of H_2S and iron. The research results provided in this dissertation show examples of these defects in the corrosion product layer and show the relationship to the water chemistry conditions which provide the species for diffusion through the layer and the temperature which directly influences the reaction and precipitation rates. Progress in related research areas is currently underway with two Ph.D. graduate studies focused on the reactions of iron sulfides at the metal substrate and understanding the types of iron sulfides formed.

Additional studies related to defining the corrosion product layer are necessary to complete the full mechanistic model related to sour corrosion and localized corrosion.

Conclusions

The likelihood for localized corrosion in an H₂S/CO₂ environment was defined for conditions related to oil and gas industry pipelines which operate under slightly sour conditions as listed in Table 2. Parameters with the most influence on the likelihood of localized corrosion in these environments are the bulk solution pH, concentrations of carbonates, concentration of sulfides, and the ionic strength of the solution. The remaining parameters required for the relationship to corrosion product layer formation include temperature and saturation values for both iron sulfide and iron carbonate.

From experiments focused on the relationship of localized corrosion to saturation values of iron carbonate and iron sulfide, an interaction parameter was defined as a direct indication of the scaling tendency of the system where observations have shown more localized corrosion occurs in relation to corrosion product layer growth. The pH is a very important parameter related to localized corrosion because the solution pH directly affects the ‘type’ of localized corrosion that would occur. The effect of temperature on the likelihood of localized corrosion directly affects the kinetics of precipitation and the porosity of the corrosion product layer. Ionic strength is a significant indicator for the likelihood of localized corrosion because an increase in ionic strength directly affects the iron carbonate saturation value and may cause more metal loss under the corrosion

product layer (undermining). And it was also observed that a decrease in partial pressure of CO₂ decreases the amount of carbonates available for diffusion through the corrosion product layer which will change the water chemistry conditions that could occur within the corrosion product layer. A calculation for the likelihood of localized corrosion is provided for the range of parameters tested. The current understanding toward the relationship of these parameters to the likelihood of localized corrosion was reviewed and used as a basis to provide hypotheses on the growth of the corrosion product layer under these environmental conditions.

Future work

Indications of further research areas needed for review are provided in the context of the dissertation. These include:

1. Additional studies related to defining the corrosion product layer are necessary to complete the full mechanistic model related to sour corrosion and localized corrosion. These include:
 - a. Reactions of iron sulfides at the metal substrate,
 - b. Reactions on the bulk solution side of the corrosion product layer,
 - c. Reactions within the corrosion product layer,
 - d. Formation of iron sulfides in the corrosion product layer, and
 - e. Review the breakdown of the passive layer by chlorides to determine if they play a role in the initiation of localized corrosion.

2. Expansion of the operational parameters used in this study to cover higher or lower values of temperature, $p\text{CO}_2$, and $p\text{H}_2\text{S}$ as observed in field conditions related to the upstream oil and gas industry are necessary to expand the current model of the likelihood of localized corrosion.

REFERENCES

1. Sun, Y., Localized Corrosion in Horizontal Wet Gas Flow, Ohio University, PhD dissertation, June 2003.
2. Han, J., Yang, Y., Brown, B., Nešić, S., Electrochemical Investigation of Localized CO₂ Corrosion on Mild Steel. Corrosion/2007, paper No. 07323, (Houston, TX: NACE, 2007).
3. Brown, B., "H₂S Multiphase Flow Loop: CO₂ Corrosion in the Presence of Trace Amounts of Hydrogen Sulfide," Ohio University, MSChE Thesis, November 2004.
4. Lee, K. J., A Mechanistic Modeling of CO₂ Corrosion of Mild Steel in the Presence of H₂S, Ohio University, PhD dissertation, November 2004.
5. Sun, W., Kinetics of Iron Carbonate and Iron Sulfide Scale Formation in CO₂/H₂S Corrosion, Ohio University, PhD dissertation, November 2006.
6. Zheng, Y., Brown, B., Nešić, S., "Electrochemical Study and Modeling of H₂S Corrosion of Mild Steel," NACE Corrosion 2013, paper no. 2406.
7. Crolet, J.L., and Bonis, M.R., How to Pressurize Autoclaves for Corrosion Testing Under Carbon Dioxide and Hydrogen Sulfide Pressure, Corrosion, Vol. 56, No. 2, pp167-182, February 2000.
8. Eden, B., Laycock, P. J., and Fielder, M., "Oilfield Reservoir Souring, Health and Safety Executive, Offshore Technology Report," Crown publishing, 1993, ISBN 0-7176-0637-6.

9. Shrier, L. L., R. A. Jarman, and G. T. Burstein. "Corrosion, Vol. 1." Butterworth-Heinemann (1994).
10. Roberge, P. R. "Corrosion Engineering, Principles and Practice" McGraw Hill (2008).
11. Sastri, V.S., G. Edward, and M. Elboudjaini. "Corrosion Prevention and Protection, Practical Solutions" John Wiley & Sons, Ltd (2007).
12. Kvarekval, J., "The Influence of Small Amounts of H₂S on CO₂ Corrosion of Iron and Carbon Steel," EUROCORR '97, Trondheim, Norway.
13. Sun, W., Nešić, S., Papavinisam, S., Kinetics of Iron Sulfide and Mixed Sulfide/Carbonate Scale Precipitation in CO₂/H₂S Corrosion, NACE Corrosion 2006, paper no. 06644.
14. Sun, W., Nešić, S., A Mechanistic Model of H₂S Corrosion of Mild Steel, NACE Corrosion 2007, paper no. 07655.
15. Smith, S.N. and Joosten, M.W., "Corrosion of Carbon Steel by H₂S in CO₂ Containing Oilfield Environments," Corrosion 2006, Paper 06115.
16. Brown, B., Nešić, S., CO₂/H₂S Corrosion under Scale Forming Conditions, NACE Corrosion 2005, paper no. 05625.
17. Brown, B., Young, D., Nešić, S., Localized Corrosion in an H₂S/CO₂ Environment, Paper #2704, 17th International Corrosion Congress, Las Vegas, NV, October 6-10, 2008.

18. Lee, K. J., Nešić, S., The Effect of Trace Amount of H₂S on CO₂ Corrosion Investigated by EIS Technique, NACE Corrosion 2005, paper no. 05630.
19. Wolthers, M.; Van der Gaast, S.J., Rickard, D., The Structure of Disordered Mackinawite, American Mineralogist, 2003, 88(11), 2007-2015.
20. Zhao, J.M., Wei, Z., Zuo, Y., Zhao, X.H., Effects of some ions on ion-selectivity of ferrous sulfide layer, J. of App. Electrochemistry, (35), pp267-271, 2005
21. Lide, David, R., Editor-in-Chief, "CRC Handbook of Chemistry and Physics", 84th Edition, section 12 (Properties of Solids), pages 14 – 16.
22. Szklarska-Smialowska, Z., Mechanism of pit nucleation by electrical breakdown of the passive layer, Corrosion Science, (44), pp 1143-1149, 2002.
23. Videm, K., and Kvarekval, J., Corrosion of Carbon Steel in CO₂ Saturated Aqueous Solutions Containing Small Amounts of H₂S, NACE CORROSION/94, Paper No. 12, 1994.
24. Ikeda, A., Ueda, M., and Mukai, S., Influence of Environmental Factors on Corrosion in CO₂ Source Well, Advances in CO₂ Corrosion, Vol. 2, pp.1-22, NACE, 1985.
25. Valdes, A., Case, R, Ramirez, M., and Ruiz, A., The Effect of Small Amounts of H₂S on CO₂ Corrosion of a Carbon Steel, Paper No. 22, CORROSION/98.
26. Jepson, W.P., and R.E. Taylor, Slug Flow and Its Transitions in Large-Diameter Horizontal Pipes, Int. J. Multiphase Flow, Vol. 19, pp411-420, 1993.

27. Brown, B., Schubert, A., "The Design and Development of a Large-Scale Multiphase Flow Loop for the Study of Corrosion in Sour Gas Environments," NACE Corrosion 2002, paper no. 02502, NACE International, Houston, TX.
28. International Organization for Standardization (ISO/TC 67, Working Group 7), "Petroleum and natural gas industries: Materials for use in H₂S-containing environments in oil and gas production," NACE MR0175/ISO 15156, 2007, Table A.2.
29. Bockris, J.O.M., Drazic, D., and Despic, A.R., *Electrochimica Acta*, 4 (1961): p.325
30. Nešić, S., Postlethwaite, J., and Olsen, S., An Electrochemical Model for Prediction of CO₂ Corrosion, CORROSION/95, paper no.131
31. Nordsveen, M., Nešić, S., Nyborg, R., Stangeland, A., A Mechanistic Model for Carbon Dioxide Corrosion of Mild Steel in the Presence of Protective Iron Carbonate Layers – Part 1: Theory and Verification, *Corrosion*, May 2003, vol. 59, no. 5, pp 443 – 456.
32. Remita, E., Tribollet, B., Sutter, E., Vivier, V., Ropital, F., and Kittel, J., "Hydrogen evolution in aqueous solutions containing dissolved CO₂: Quantitative contribution of the buffering effect," *Corrosion Science*, vol. 50, pp. 1433-1440, 2008.

33. Pots, B. F. M., John, R.C., Improvements on de-Waard Milliams Corrosion Prediction and Applications to Corrosion Management, Paper #02235, CORROSION/2002.
34. Sun, W., Nešić, S., Young, D., Woolam, R., “Equilibrium expressions related to the solubility of the sour corrosion product mackinawite”, *Ind. Eng. Chem. Res.* 2008, Vol.47, 1738-1742.
35. Benning, L.G., Wilkin, R.T., Barnes, H.L., Reaction pathways in the Fe-S system below 100°C, *Chemical Geology*, v. 167, 2000, pp25-51
36. Geochemist’s Workbench, Aqueous Solutions LLC, 60 Hazelwood Drive, Champaign, IL, 61820, USA (2012)
37. Ning, J., Zheng, Y., Young, D., Brown, B., Nešić, S., “A Thermodynamic Study of Hydrogen Sulfide Corrosion of Mild Steel,” *NACE Corrosion 2013*, paper no. 2462.
38. Tanupabrungrun, T., Brown, B., Young, D., and Nešić, S., “Construction and verification of Pourbaix diagram for CO₂ corrosion of mild steel valid up to 250°C,” *NACE Corrosion /2012 Conference*, paper no. C2012-0001418, Salt Lake City, Utah, 2012
39. OLI Stream Analyzer, OLI Systems Inc, 108 American Road, Morris Plains, New Jersey, 07950, USA (2012)
40. Fishtik, I., “Thermodynamic Stability Relations in Redox Systems,” *Environmental Science & Technology*, 2006, 40 (6), pp 1902-1910

41. Dyskin, A.V., Hu, X., Sahouryeh, E., Editors, "Structural Integrity and Fracture," p 437, copyright 2002 Swets & Zeitlinger B.V., Lisse, The Netherlands, ISBN 90 5809 513 4.
42. Wang, J.Q., Atrens, A., Cousens, D.R., Kinaev, N., "Microstructure of X52 and X65 pipeline steels," *Journal of Materials Science*, 34 (1999) pp. 1721-1728.
43. Specification, A. P. I. "5L, Specification for Line Pipe." Edition March (2004).
44. Certified Test Report, ICM001-03-10-24383-1, Laboratory Testing, Inc., 2331 Topaz Drive, Hatfield, PA, 19440 (10/16/2003).
45. Hernandez, S., "Technical Report – API 5L X65 Evaluation," Internal report for Institute for Corrosion and Multiphase Technology, Ohio University, October 27, 2003.
46. Choi, Y., Choo, W.Y., Kwon, D., "Analysis of mechanical property distribution in multiphase ultra-fine-grained steels by nanoindentation," *Scripta Materilia*, 45 (2001) pp. 1401-1406.
47. Abbade, N. P., Crnkovic, S.J., "Sand-water slurry erosion of API 5L X65 pipe steel as quenched from inter critical temperature," *Tribology International*, 33 (2000) pp. 811-816.
48. Chevron Corporation, Energy Technology Company, FE - MEE - Corrosion Lab, 3901 Briarpark Dr., WP117, Houston, TX 77042 U.S.A.
49. ASTM G1 – 81, (Section 7), "Standard Practice for Preparing, Cleaning, and Evaluating Corrosion Test Specimens," *Proceedings of the Symposium on*

Laboratory Corrosion Tests and Standards, G. S. Haynes, R. Balboian, editors, pp. 505-510, 1983.

50. Smith, S.N., Brown, B., and Sun, W., Corrosion in Higher H₂S Concentrations and Moderate Temperatures, NACE CORROSION 2011, paper no. 11081, Houston, TX.
51. Fang, H., Brown, B., and Nešić, S., “Sodium Chloride Concentration Effects on General CO₂ Corrosion Mechanisms,” Corrosion Mar 2013, Vol. 69, No. 3 (March 2013) pp. 297-302
52. Fang, H., Brown, B., and Nešić, S., “Effects of Sodium Chloride Concentration on Mild Steel Corrosion in Slightly Sour Environments,” Corrosion Jan 2011, Vol. 67, No. 1 (January 2011) pp. 015001-1-015001-12.
53. Zipperian, D., SiC Abrasive Grinding Applications, Pace Technologies – Metallographic Technical Newsletters, Vol. 1, Issue 2, November 2002, <http://www.metallographic.com/Newsletters/SIC-newsletter2.PDF> (6/23/2013).
54. Fang, H., “Localized H₂S Attack at High Salt Concentration,” Corrosion Center JIP, Advisory Board Meeting, ICMT, Athens, OH, October 2007.
55. Fajardo, V., “The Effect of Undissociated Acetic Acid on the Integrity of Iron Carbonate Layer,” CC JIP Advisory Board Meeting, Oct. 2007
56. Kvarekval, J., Dugstad, A., “Pitting Corrosion in CO₂/H₂S Glycol Solutions under Flowing Conditions,” NACE Corrosion 2005, paper no. 054631.

57. Kvarekval, J., "Corrosion Layer Breakdown and Localized Corrosion in CO₂/H₂S Environments," NACE Corrosion 2012, paper no. C2012-0001537.
58. Singer, M., Brown, B., Camacho, A., Nešić, S., "Combined Effect of CO₂, H₂S, and Acetic Acid on Bottom of the Line Corrosion," NACE Corrosion 2007, paper no. 07661.

APPENDIX A: ANOVA OF DATASET

		Sum of Squares	df	Mean Square	F	Sig.
Kelvin	Between Groups	2790.628	6	465.105	3.797	.002
	Within Groups	8696.552	71	122.487		
	Total	11487.179	77			
Nominal Location	Between Groups	.291	6	.048	.187	.980
	Within Groups	18.389	71	.259		
	Total	18.679	77			
Time_LMH	Between Groups	.150	6	.025	.032	1.000
	Within Groups	55.389	71	.780		
	Total	55.538	77			
Ionic Strength	Between Groups	14.831	6	2.472	9.065	.000
	Within Groups	19.361	71	.273		
	Total	34.191	77			
Solution pH	Between Groups	22.234	6	3.706	63.583	.000
	Within Groups	4.138	71	.058		
	Total	26.372	77			
Log_Total_CO2	Between Groups	1.509	6	.251	30.085	.000
	Within Groups	.593	71	.008		
	Total	2.102	77			
Log_Total_H2S	Between Groups	11.334	6	1.889	7.884	.000
	Within Groups	17.011	71	.240		
	Total	28.346	77			
Saturation value for Iron Sulfide	Between Groups	3495641.893	6	582606.982	2557.330	.000
	Within Groups	16175.111	71	227.818		
	Total	3511817.004	77			
Saturation value for Iron Carbonate	Between Groups	657.905	6	109.651	4789.770	.000
	Within Groups	1.625	71	.023		
	Total	659.530	77			
pCO2	Between Groups	214.102	6	35.684	10.775	.000
	Within Groups	235.132	71	3.312		
	Total	449.235	77			
pH2S	Between Groups	.027	6	.004	3.682	.003
	Within Groups	.086	71	.001		
	Total	.112	77			

APPENDIX B. NACE 2002 CONFERENCE PAPER NO. 02502

Reproduced by permission from NACE International, Houston, TX. All rights reserved.

Paper 02502 presented at CORROSION/2002, Denver, Co. ©NACE International 2002.

111 Form: Permission Page 12 Date: 11/19/2013 4:00:53 PM

NACE International
 1440 South Loop West
 Houston, TX 77002
 Tel: 281-226-2276
 Fax: 281-226-2279

**Permission to Publish
 NACE International
 Copyrighted Paper/Article**

Date: 11-11-13

Name: Bruce Brown Title: Assoc. Dir. of Operations, ICAAT, OU

Company (Publisher): OHIO University

Address: 342 W. Spalding St., Athens, OH 45701

Tel: (740) 593-0683 Fax: (740) 593-9949

Email: Bruce.Brown@ohio.edu

Publication Media: Check the applicable box:
 Magazine/Journal (Periodical) PHD Dissertation Book Appendix
 Web Site URL (Web Site) Ohio University Thesis/Dissertation, Open Access

Circle the source: Materials Performance CORROSION Conference Paper Standards
 Paper/Article Title: The Design and Development of a Large-Scale Multiphase Flow Loop for the Study of Corrosion in "Work" Conference Paper No./Year: 02502/2002
 Author: Bruce B. Brown, A. Schabert, A. Srinivasan

NACE International ("NACE") hereby grants to "Publisher" the right to publish the Work using the Publication Media elected above. To the extent the Publication Media is a Periodical, the publication right is limited to publication in the specific issue identified above or the Periodical identified above and this right shall automatically terminate upon the date of issue of the particular issue of the Periodical, whether or not such Work is actually published. To the extent the Publication Media is a Web Site, the publication right is limited to publication of the specific Web Site identified above. Any right granted herein is a limited, non-transferable, non-exclusive right. No other rights in the Work are granted herein. The Publisher agrees to hold NACE harmless and indemnify NACE against any and all legal action and expenses arising out of the Publisher's use and selling of NACE content.

Notwithstanding the foregoing, Publisher may still wish to publish the Work in a manner necessary to accommodate the style and size requirements of the specific publisher so long as the published Work shall appear in the Publication medium substantially similar to the original Work. Any such permitted use or modification shall remain the liability of the original author.

Publisher shall obtain a copy of the original Work directly from NACE International and shall not utilize copies of the Work from other sources, including the author(s). Publisher shall indicate on the published version of the Work the names of all authors listed on the original Work.

The Publisher shall include the following applicable Copyright notices with any publication of the Work:

A. Conference Paper
 Reproduced with permission from NACE International, Houston, TX. All rights reserved. Paper NUMBER
 presented at CORROSION/YEAR, City, State. © NACE International YEAR.

B. Magazine/Journal Article
 Reproduced with permission from NACE International, Houston, TX. All rights reserved. Published in the MONTH, YEAR issue of JOURNAL, © NACE International YEAR.

C. Standards
 STANDARDS/TECHNICAL COMMITTEE REPORT NAME. © NACE International YEAR. All rights reserved
 by NACE. Reproduced with permission. NACE standards are revised periodically. Users are cautioned to
 obtain the latest edition, extension or an updated version of the standard may be necessary.

* Modifications to Permission: Other necessary wording can be used, but must be approved by NACE in writing in
 advance.

As between NACE and Publisher, Publisher acknowledges that NACE owns all rights in the Work. Publisher shall not be entitled
 to any compensation for its efforts in promoting the Work.

THE WORK IS PROVIDED "AS IS." ALL EXPRESS OR IMPLIED WARRANTIES, CONDITIONS, REPRESENTATIONS OR
 WARRANTIES, INCLUDING ANY IMPLIED WARRANTY OF MERCHANTABILITY OR FITNESS FOR A PARTICULAR
 PURPOSE, ARE DISCLAIMED.

Permissions/Publishing/NACE.org (A000)
 The fee codes required by CIP FullBase are shown. For more information, visit <http://www.cip.com>

1111 Form: Release Page 20 Date: 11/19/2013 4:00:53 PM

PURPOSE OR CONDITIONS OF ACCURACY, COMPLETENESS OR QUALITY AND THOSE ARISING BY STATUTE OR OTHERWISE IN LAW, ARE HEREBY DISCLAIMED.

IF NO EVENT WILL NACE BE LIABLE FOR ANY DIRECT, INDIRECT, PUNITIVE, SPECIAL, INCIDENTAL OR CONSEQUENTIAL DAMAGES IN CONNECTION WITH OR RELATED TO THIS AGREEMENT (INCLUDING LOSS OF PROFITS, USE, DATA, OR OTHER ECONOMIC ADVANTAGES, PERFORMANCE, OR PROFITS).

This Agreement and the rights granted herein may be terminated immediately by NACE upon breach of this Agreement by Publisher. Unless earlier terminated, this Agreement and the rights granted herein will automatically terminate 6 months from the date set forth above. If the Work has not been published within that time period, a new Agreement must be obtained.

Publisher may not, directly or indirectly, sell, assign, sublicense, lease, rent, distribute, or otherwise transfer this Agreement or any rights granted herein, without the prior written consent of NACE.

If any provision of this Agreement is found to be unenforceable, that this Agreement shall be deemed to be amended by modifying such provision to the extent necessary to make it legal and enforceable while preserving its intent. This remainder of the Agreement shall not be affected by such modification.

This Agreement does not create, and shall not be construed to create, any employment, joint venture or partnership, relationship between the parties. No officer, employee, agent, or vessel or independent contractor of either party shall at any time be deemed to be an employee, servant, agent or contractor of any other party for any purpose whatsoever.

This Agreement shall be governed by, and construed and enforced in accordance with, the laws of the State of Texas, without regard to the choice of law provisions of that State.

This Agreement shall only be effective if signed by authorized representatives of both parties. This Agreement constitutes the entire agreement between the parties with respect to the subject matter of this Agreement. Any change, modification or waiver hereof must be in writing and signed by authorized representatives of both parties.

Other Terms & Conditions:

Publisher hereby requests permission to publish the paper/article described above and agrees to comply with all Terms and Conditions listed above.

Request submitted by:
Bruce Brown
 Printed Name
Assoc. Dir. of Operations ICAAT, OU
 Title
 Signature
 Date

Request approved by NACE:
Brenda Nitz
 Printed Name
Books Coordinator
 Title
Brenda Nitz
 Signature
11-19-2013
 Date

Request agreed to by:
Bruce Brown
 Local Author Printed Name
Assoc. Dir. of Operations, ICAAT, OU
 Local Author Title
Bruce Brown
 Local Author Signature
11-19-2013
 Date

Permissions/Publishing/NACE.org (A000)
 This fee was located by CIP FullBase for access. For more information, visit <http://www.cip.com>

Paper No.
02502

CORROSION 2002

**THE DESIGN AND DEVELOPMENT OF A LARGE-SCALE, MULTIPHASE FLOW LOOP
FOR THE STUDY OF CORROSION IN SOUR GAS ENVIRONMENTS.**

Bruce Brown and Al Schubert
Institute for Corrosion and Multiphase Technology
Ohio University
Athens, Ohio 45701

ABSTRACT

A state-of-the-art laboratory flow loop has been researched, designed, and developed to study the corrosive effects of sour gas in multiphase flow. This unique system is housed in an environmentally isolated, explosion-proof area providing a safe location where an operator can study the effects of a single parametric change on corrosion. This report describes the fluid pumping system, the flow monitoring system, the corrosion monitoring methods, and safety systems associated with the new experimental loop. Initial baseline testing of the entire system consisted of slug flow and full-pipe flow regimes in seawater and the resulting effect on corrosion rates under partial pressures of CO₂.

keywords: system design, sour system, slightly sour, multiphase flow, safety systems, CO₂ corrosion.

INTRODUCTION

CO₂ and H₂S content in produced fluids constitute a very corrosive environment that has been studied extensively in glass cells and autoclaves since the early 1970's, but little research work has been completed to model corrosion in slug flow of a sour system. Under various multiphase conditions, the slug flow regime has been shown to increase the corrosion damage to pipelines^{1,2}. High velocity slugs are very turbulent with the existence of pulses of entrained bubbles in the mixing zone behind the front of the slug. These pulses of bubbles impact the pipe wall and collapse causing a cavitation-type effect, leading to increased corrosion rates in slug flow³.

Copyright

©2002 by NACE International. Requests for permission to publish this manuscript in any form, in part or in whole must be in writing to NACE International, Publications Division, 1440 South Creek Drive, Houston, Texas 77084-4906. The material presented and the views expressed in this paper are solely those of the author(s) and not necessarily endorsed by the Association. Printed in U.S.A.

H₂S-related corrosion is a topic of great concern due to the increased oil and gas production technology that allows deeper wells producing more corrosive fluids and longer transmission lines. Longer transmission lines of multiphase fluids over various terrains provide opportune environments for slug flow regimes. In the presence of H₂S, acidity of the corrosive media is a parameter known to play a determining role in the cracking phenomena (SWC, SSC, SCC) of low alloy steels as well as stainless steel and must be accurately evaluated⁴. Corrosion in the presence of H₂S has resulted in the formation of an iron sulfide film that decelerated the corrosion rate at temperatures between 20°C and 60°C⁵. A similar film was seen at low concentrations of H₂S in a brine containing CO₂ and acted as a corrosion film that greatly decreased the corrosion rates in 2-liter glass cells⁶. The addition of hydrogen sulfide to a corrosive system contained in a bubble cell or other small volume test apparatus provides information necessary for characterizing the reactions and by-products of the corrosion process. However, this information fails to show the mechanical action of the flow regime on the scale or corrosion product film. Sour gas corrosion research has been limited to small-scale studies, which do not provide an adequate environment for the simulation of corrosion in multiphase slug flow.

Current laboratory research associated with sour gas is conducted in autoclaves because of the ability to reproduce the wellhead temperature and pressure conditions; some even have circulatory pumps to achieve better mass transfer in the corrosion process. Srinivasan⁷ describes an autoclave system developed to simulate fluid flow induced corrosion in CO₂/H₂S systems. This small-scale system provides an adequate environment for reproducing the corrosive constituents and wall shear stress effects, but lacks the size for development of certain flow regimes. Studies such as Pargeter⁸ have provided valuable information on maximum permissible hardness levels for welded steels at risk of sulfide stress corrosion cracking, but he did have some concerns that the 16:1 solution volume to sample surface area was small and resulted in a higher contamination of the aqueous environment not seen in a production environment.

Concern over the construction of larger and more complicated flow loops was voiced by Nestic⁹. His study compares the hydrodynamic parameters in two different flow geometries, rotating cylinder and pipe flow, on the corrosion rate of low carbon steel in CO₂ environments. This information is used to transfer data from one laboratory scale flow-corrosion system (rotating cylinder) to another (pipe flow) and ultimately to field conditions. But his concern that “building larger and more complicated loops closer in scale to production pipelines means admitting that we do not know what goes on in our processes” is misleading. Our understanding of what goes on in the corrosion processes has reached a point that a larger system is necessary to fill in gaps of information not possible in smaller systems and provide another confirmation step to the transfer of data from small-scale conditions to field conditions.

Jepson and Taylor¹⁰ found that, in order to mimic the mechanisms observed in large diameter pipelines, test facility pipeline should be above 7.5 cm in diameter. The advantage of large diameter research is the ability to produce repeatable flow regime phenomena similar to that of pipelines in field operations. Multiphase flow pattern reproduction in a controlled environment provides researchers with an opportunity to study corrosion and corrosion control mechanisms.

The greatest concern when developing a system involving hazardous materials is the amount of safety consciousness that must be focused on the project. Srinivasan⁷ stated that H₂S related corrosion has not been studied extensively in the laboratory due to the difficulty of working with H₂S, but the

need for understanding CO₂/H₂S corrosion has grown with the advent of deeper and more corrosive production systems. Corrosion studies in an H₂S/CO₂ environment could involve hydrogen sulfide concentrations in the gas phase of the system above the 100ppm value that is reported by the Occupational Safety and Health Association (OSHA) to be "immediately dangerous to life and health" (IDLH). The current testing program for the system involves the effects of low concentrations of H₂S from 3ppm to 500ppm in the gas phase. The higher gas concentration means that systems must be put in place for personal and public safety. Using the proper materials of construction, installing hazardous gas sensors, purchasing personal protective equipment, and installing a gas removal system were the first steps to the physical control of the hazard while safety training, safety committees, and technical meetings provide the hazard awareness necessary during operations. The multiphase flow system must be developed of a suitable material with a procedure to maintain system integrity. The test parameters of the multiphase system must be stable and repeatable for each test run and should reflect field conditions as much as possible.

Safety consciousness began in the design phase with construction of a special environmentally closed room to house the multiphase flow loop and progressed to safety training. The major wetted portions of the loop were made of Hastelloy C-276 (UNS No. N10276) and ultrasound testing was completed in multiple locations before wetting the system with any materials to provide a baseline measurement for wall thickness and continuity. A combustion system was designed to evacuate the contaminated room air volume through a furnace to convert the H₂S to SO₂. The combustion system is automated to activate at 10ppm H₂S, which is the current threshold limit value (TLV) set by OSHA. Addition of pure hydrogen sulfide to the system was used because it is less sensitive to the filling rate and the influence of temperature stability can be controlled¹¹. The two hydrogen sulfide system operators attended an H₂S instruction program that follows the ANSI Z390.1 - 1995 Hydrogen Sulfide Training Standard. This OSHA training course provided the knowledge required for teaching others how to work safely in the field with and around hydrogen sulfide. A certified course on hydrogen sulfide safety was taught to the others at the Institute. The effect of the training was to include all personnel at the Institute in the goal of maintaining a safe environment and providing multiple perspectives on safety strategies. Weekly technical meetings and bi-weekly safety committee meetings provide the necessary information transfer for the entire facility. System operation and measurements will be conducted from a location outside the environmental room with the "buddy system" in place for any excursions into the room when hydrogen sulfide is present.

In respect to the culmination of research work done in carbon dioxide corrosion, research on the effect of mixtures of carbon dioxide and hydrogen sulfide on corrosion is relatively new with no information available under slug flow conditions. Research information is desperately needed in this area. This information is used to better define corrosion rate models, which, in turn, predict corrosion rates under various conditions helping engineers to design better methods of corrosion control in the field. Laboratory simulation of corrosive environments has brought information from wheel tests, glass cell experiments, autoclave experiments, and flow loop studies. Each has its own place. Models developed for the simulation of flow are also used to enhance corrosion prediction. Providing research conditions in flow regimes that cannot be established in small-scale testing will aid the cause and help to modify existing corrosion prediction models for increased accuracy.

With all these factors, the development of a large-scale research system capable of reproducing conditions of a sour gas environment was absolutely necessary. Few such rigs exist. This report

describes the systems developed for the operation of a closed-loop, large-scale, sour-gas, multiphase flow loop for corrosion research data collection.

SYSTEM DESIGN

Schematic Interpretation

The basic design of a system relies on the requirement to provide a fully developed flow and repeatable conditions in a test area for corrosion testing. This is accomplished by moving quantitative amounts of liquid and gas to a mixing point, allowing enough pipe length for fully developed flow from that mix, and providing an area for insertion or connection of instruments for measurement in a closed system. Figure 1 is the piping and instrumentation diagram for the multiphase research system built to study corrosion under sour gas conditions. This schematic representation shows the H₂S system to be a closed system using three pumps, two test sections, one tank, and one heat exchanger.

The Pumping System

The liquid pump (P1) and gas pump (P2) are both progressive cavity pumps. Progressive cavity pumps were chosen because of their ability to move multiphase mixtures and provide positive-displacement flow qualities under most conditions. These progressive-cavity pumps use a double-helix design stator made of nitrile in the outer shell with a single helix rotor that is chrome-plated stainless steel. The liquid pump (P1) has a 50 horsepower (Hp) motor with a 4.93 to 1 step down ratio from motor speed to rotor speed. Calculation of the flow rate, as shown in Equation 1, is based upon manufacturer calibrated rotor-stator combinations that provide a specific volume per 100 revolutions.

$$MotorRPM \left(\frac{1 RotorRotation}{4.93 MotorRotations} \right) \left(\frac{115 gal}{100 RotorRotations} \right) \left(\frac{1 m^3}{264.2 gal} \right) \left(\frac{31.2 m PipeLength}{1 m^3 PipeVolume} \right) \left(\frac{min}{60 sec} \right) = m/s \quad (1)$$

Pump P1 provides a 0.5-2.5 m/s liquid flow rate in linear response to the 200-1000 RPM motor speed as calculated from Equation 1. These values were calibrated against an ultrasonic flow meter as shown in Figure 2. The gas pump (P2) has a 150 Hp motor with a 5.68 to 1 step down ratio from motor speed to rotor speed with the same operating techniques as P1. The third pump (P3) is a positive displacement gear pump that provides a percentage of the total liquid flow added to the gas pump (P2) to provide a lubricating seal required in moving the gas phase. Pump P3 provides a 0-114 lpm (0-30 gpm) in response to 0-1725 RPM change in motor speed. The volumetric flow from P3 is subtracted from the volumetric flow determined from the rotational speed of P2 to provide the gas volumetric flow rate.

Physical Characteristics

The H₂S system is 95 ft (29 m) long by 12 ft (3.6 m) wide by 9.6 ft (2.9 m) high at its highest point in the gas pump suction line from the top of the tank. Two test sections are named "Upstream" and "Downstream" because of their location within the system in relation to the mixing point. The tank is a gas-liquid separation device with a diffusion plate located just under the return stream. The

heat exchanger was a necessary addition from previous experience in obtaining high gas velocities because P2 will add excess heat to the system that must be removed. All piping is made of N10276 because of its ability to withstand this type of a "wetted" corrosive environment better than other alloys. The pump rotors, pump suction, and pump discharge housings are made of 316L stainless steel.

The Upstream test section is located 9 m (354 in.) downstream from the gas-liquid mixing point and 1.2 m (48 in.) upstream from the first 90-degree bend. This location is 88 pipe diameters downstream from the turbulent gas-liquid mixing point and 12 pipe diameters upstream from the 90-degree bend. The Downstream test section is 130 pipe diameters from the second 90-degree bend and 24 pipe diameters from the tank entrance. These are both acceptable locations for achieving fully developed flow.

Each test section has numerous ports. Figure 3 shows a diagram of the test section where fluid flow is from the left to the right. Ports A, D, E, and F are used in differential pressure drop relationships for determining the flow pattern. Each of these ports is a 1" (2.54 cm) flange and pipe welded into position with a 1/8" (0.3175 cm) hole through the pipe wall. Ports B and C are the insertion points for electrical resistance (ER) and linear polarization (LPR) probes; each having a 1.5" (3.8 cm) opening for insertion of a 1.25" (3.175 cm) flush probe element. Each of these has a 2" N10276 ball valve to provide for mounting and inserting the probe into the pipe wall while the system is under pressure. Port G is similar in design to port A, but port H has a 1" (2.54 cm) opening into the pipeline from its 1" flange. Ports G and H are used for different purposes in the upstream and downstream locations. The Downstream test section uses these two locations for a thermocouple and pH probe, respectively, for measuring a temperature compensated pH. The Upstream test section uses these two locations for gas injection and a pressure measurement location downstream of Valve #1.

Technical grade gases are added through a 316L stainless steel (UNS No. S31603) tubing and valve system shown in Figure 4 as the "Gas Mix Panel." Stainless steel has excellent corrosion resistance to dry hydrogen sulfide gas, which is the most corrosive of gases to be used. The last valve before entering the system ("Main") and the associated tubing to the system is made of N10276 because they will be exposed to "wetted" hydrogen sulfide gas.

Combustion System

The purpose of this system is to oxidize H_2S or CH_4 should it need to be vented from the pressure vessel in a controlled manner, or in the event of a gas leak. A combustion chamber system of gas incineration was chosen for this process because only colorless flue gas will exhaust from the stack. Primary air for combustion will be drawn from outside while the secondary air for combustion will be drawn from the environmental chamber where the H_2S System is located. The combustion system can be activated by a manual switch or by a signal from a calibrated, fixed gas sensor. There are eight (8) H_2S gas sensors and four (4) CH_4 sensors placed about the test cell and there is a ventilation system that provides an exit route for hazardous gases to safely exit the room. Should one or more of the gas sensors be exposed to more than 10ppm H_2S or 50% Lower Explosive Limit (LEL) CH_4 concentrations, the exhaust blower will remove the air from the test cell and route it through the combustion system.

The hazardous gas monitors provide a 4 – 20 mA output in relation to a 0 – 100 ppm concentration of H₂S or to a 0 – 100% lower explosive limit (LEL) of methane (CH₄). The output of each H₂S sensor is sent through a 243-ohm resistor where 0 ppm will give 0.9720 volts and 100 ppm will give 4.86 volts. A 10 ppm concentration would therefore be equivalent to 1.3608 volts ($1.3608 = 0.9720 + 10 * 0.03888$). The output of each CH₄ sensor is also sent through a 243-ohm resistor where 0% LEL will give 0.9720 volts and 100% will give 4.86 volts. The 50% LEL set point is equivalent to 2.916 volts ($2.916 = 0.9720 + 50 * 0.03888$).

Located outside the test cell, the control box for the combustion system contains five circuit boards. Three of these boards all have the same signal comparators. Each of the signal comparators has hysteresis. For example, the H₂S sensor comparators are set to go high at 1.3608 V, but will not return to a low until the input signal is less than 1 volt. The outputs of all comparators are logically “OR’d” together so that any single sensor will turn on the system if its output exceeds 1.3608 V. The other two circuit boards within the control box contain the combustion system interface and the power supplies.

Three H₂S monitors are located within 6” (15.24 cm) of the floor, one is located in the H₂S gas storage cabinet, and two are located 15’ (5 m) off the ground. All are set to trigger an alarm system for any concentration of H₂S over 10ppm. H₂S has a density greater than air (1.189) and will concentrate in low-lying areas, but, if mixed with a less dense gas, the buoyant effect could lift the hydrogen sulfide gas. Three CH₄ monitors are all located at the 15’ (5 m) level due to the lighter density of the gas.

The ventilation system within the room is comprised of 4” PVC in three flow lines that converge into a 6” PVC manifold and a liquid containment box. A 4” carbon steel pipeline entering the box from outside the building, leads the gas through a combustion system before being released from a stack, 20 feet above ground level. The ventilation system can be activated by a manual switch and is automatically activated as part of the combustion system. A portable hood is also available from the ventilation system to draw gases that escape during probe insertion away from the user.

System Operation

When using multiple gases in a test procedure, the gases are to be added to the system based upon partial pressure. The Gas Mix panel is designed for injection order of the lowest partial pressure gas to the highest partial pressure gas (ie. H₂S, CH₄, CO₂, N₂) and to use the higher partial pressure gases to purge the Gas Mix panel tubing lines into the system. It should be noted from Figure 4 that nitrogen gas has the longest path through the tubing to the system input. The last valve on the tubing string, after the “Main” valve is the “Vent” valve, which is used to exhaust the contents of the Gas Mix Panel out to the combustion system by using nitrogen or carbon dioxide as a purge gas.

Liquid velocities are measured/calibrated by using an ultrasonic flow meter. For non-diverted flow in the main 4” flow line, a calibration curve was established between the motor RPM and the flow rate for the liquid progressive cavity pump. If lower flow velocities are required, a 2” flow diversion line and recycle valve can be used and flow measured with an ultrasonic flow meter on the smaller line. Valves #3, #4, and #5 from Figure 1 are used in this process. The progressive cavity pump for the gas flow is capable of moving 3 m/s to 10 m/s gas directly with only the addition of

lubrication fluid (pump #2) and calculations from the rotational speed of the gas pump (pump#1). Gas flow rates lower than 3 m/s begin to show signs of pulses from the progressive cavities. Partial closure of valve #1 can produce gas flow rates in the test section as high as 20 m/s. This partial closure of valve #1 alters the gas flow by changing the area between the exit of pump #1 and valve #1 into a storage vessel and gas flow rate in the main flow line (v_2) is calculated by the ideal gas law comparison.

$$v_2 = P_2 / P_1 v_1 \quad (2)$$

Where: P_2 = pressure downstream of valve #1,
 P_1 = pressure upstream of valve #1, and
 v_1 = velocity or volumetric flow rate upstream of valve #1.

SAFETY AND DESIGN CONSIDERATIONS

When using hazardous gases, many safety considerations must be taken into account during the initial design phase of a research facility. System location, piping and instrumentation, safety systems, and operational procedures are four of the core considerations during construction. Each of these topics will be discussed as it pertains to the sour-gas multiphase flow loop located at Ohio University.

System Location

The sour-gas system is located in a 100 ft (30 m) long by 20 ft (6 m) wide by 25 ft (7.6 m) high isolated room. The two doors connecting the room to the main laboratory area each have a 21" x 24" (0.53m x 0.61m) reinforced window for viewing the full room without entering. A full opening garage door on the east wall has windows for viewing and allows forklift access into the room, although the system must be shut down and dismantled before entry, there is enough room for drums to be transferred into or out of the room from that access. A total of five doors allow exiting the room without locks, but each door requires a key to re-enter. If needed, an eye wash station and two fire extinguishers are within the room. An additional eyewash station and fire extinguisher are located nearby within the main laboratory. A combustion system for conversion of H_2S to SO_2 is located in close proximity outside the southwestern wall. A release of H_2S within the test cell will be detected by at least one of eight H_2S monitors located close to the floor since H_2S is heavier than air ($\rho_{H_2S} = 1.182$). Assuming a perfect dispersion of H_2S along the floor, a gas release within the room would be detected before more than 1/1000 lb (0.45 g) was released. When 10ppm H_2S is detected, the ventilation and combustion system will automatically switch on and draw the gas-air mixture from the room; the ventilation and combustion systems remain on until the concentration detected by any one sensor is less than 10 ppm. An audible alarm also sounds throughout the main laboratory when H_2S is detected.

Building Location

Since H_2S is a toxic gas, the location of the building with respect to the community and the amount of release possible is of concern. The possibility of a release of the total 2.2 kg (1.0 lb) of H_2S onsite was also considered for its impact on the community. Using the room volume of $1133m^3$

(40,000ft³) and assuming the 0.16 m³/s (340 CFM) room evacuation fan can exchange the room air in 2 hours, a catastrophic spill of 2.2kg of H₂S onsite would result in a release rate (Q) of 6.3x10⁻⁵ kg/s. If the level of concern for hydrogen sulfide exposure is 0.042ppm, the concentration distance can be calculated as a hazard distance. The hazard distance is the maximum dispersion distance in which ground-level chemical concentrations of the plume centerline exceed the specified exposure levels. This concentration as a function of release rate, wind speed, and effective stack height is shown in Equation 3¹²:

$$C = \frac{Q}{\pi\sigma_y\sigma_zU} \exp\left[-0.5\left(\frac{H}{\sigma_z}\right)^2\right] \quad (3)$$

Where: C = ground-level ambient concentration, g/m³
 Q = toxic release rate, g/s
 σ_y = crosswind dispersion coefficient, m
 σ_z = vertical dispersion coefficient, m
 U = mean wind speed at the stack height, m
 H = effective stack height, m

Through regression analysis and choice of the worst-case conditions (having rural locations within 500 m of the release and a minimal wind turbulence), calculation of the hazard distance as related to release rate and ground-level concentration is shown in Equation 4.

$$HD = 6200 f_h f_U \left(\frac{Q}{C}\right) \quad (4)$$

Where: HD = hazard distance, m
 Q = toxic release rate, kg/s
 C = ground-level ambient concentration or level of concern, mg/m³

Correction factor for height of dispersion, H

$$f_h = 1.07 - 0.0086H \quad (5)$$

Correction factor for wind speed, U

$$f_U = 2.80U^{-0.64} \quad (6)$$

Using Equations 4, 5, & 6 to calculate the concentration gradient through a linear distance from the release point, Figure 5 shows the acceptable exposure limit of hydrogen sulfide is reached within 5 meters from the point of the release at ground level.

If there is a release of H_2S greater than 10ppm within the hydrogen sulfide test area, the wall-mounted sensors will automatically turn on the room air evacuation fan and the combustion system. If the previous assumption of 2.2 kg of H_2S released within 2 hours holds true, then complete combustion of 2.2 kg of H_2S in 2 hours would produce 22.4×10^{-5} kg/s of SO_2 . Also considered a hazardous gas, the use of Equations 4, 5, & 6 to calculate the concentration gradient of sulfur dioxide through a linear distance from the release point provides a more acceptable result than the release of hydrogen sulfide. An acceptable limit of 0.8ppm SO_2 as set by the State of Ohio is reached within 2 meters of the point of the release at ground level as shown in Figure 6.

With corrosion testing beginning with low ratios of H_2S/CO_2 , it is possible to maintain a low inventory of hydrogen sulfide. The low inventory of less than 2.2 kg H_2S provides that even under catastrophic release conditions, the public vicinity surrounding the test cell will be unaffected.

Piping and Instrumentation Diagram

The system is made up of three "positive-displacement" pumps that calibrate linearly against rpm. Progressive cavity pumps are used for the main liquid and gas movement and a gear pump is used for the liquid lubrication feed to the gas pump. Since a minimal amount of compression transpires from the inlet to the outlet of a progressive cavity pump, it can be ideally considered a multiphase transport pump. Since valves are located at the discharge of the pumps (Figure 1: V1, V3, V4, & V5), over pressure control (OPC) circuits must also be installed to sense the pressure at the discharge and shut down the pumps if a maximum set pressure is attained. Each OPC is set for a maximum pressure much larger than the operating pressures, but lower than maximum possible pressures. For operating ranges of 0.27MPa (25 psig) to 1.5MPa (200 psig), the OPC is set for 3.45MPa (500psig). A fault caused by an overpressure condition at the outlet of the pump will immediately shut the pump motor controller off. If an overpressure condition exists at the outlet of the pump when it shuts off, the progressive cavity pump in the off condition is free to rotate to come to equilibrium and will reverse direction to feed the high pressure back to the suction.

A rupture disk is located in the gas phase at the top of the gas/liquid separation tank. The 2" Teflon lined, stainless steel, rupture disk is set at 1000 psi with the understanding that failure can occur between 70 to 100% of this burst pressure in a pulsating system. Failure of the rupture disk would send gas and fluid down a 2" pipeline to the liquid containment box connected directly to the combustion system. Any hydrogen sulfide gas concentration above 10ppm released from the system will actuate one of two fixed sensors within the box and automatically turn on the combustion system.

Operation of the Flow Loop

A closed system design is used to minimize the amount of products that are used and to help maintain chemical equilibrium. The operational order of each system of the flow loop is very important from the aspect of safety and experimental repeatability.

The system is cleaned in between each experiment and, before filling with the test solution, the system is tested for cleanliness. To do this, the system is filled with tap water and operated for 20 to 30 minutes. A sample is drawn and tested against an unused tap water sample in a tensiometer for determination if any oils or surfactants exist.

The current procedure in use is:

1. An ASTM sea salt mixture is added to de-ionized water to create the test solution as it is filled into the system under ambient temperature and pressure.
2. All valves are checked for proper orientation. The valves on the base of the tank are checked after introduction of the ASTM salt water to make sure the valve from the bottom of the tank to the gear pump suction is open while the valve used to add the solution is closed. Valve 1, 2, & 3 from Figure 1 should be open.
3. The heating system is then turned on and set for 60°C.
4. Two hydraulic pumps are then started that pressure mechanical seals on the rotating shafts of the progressive cavity pumps. These mechanical seals maintain a set differential pressure above the pump suction pressure through a differential pressure feedback mechanism known as a Tascom[®] valve. Both of these valves are currently set to maintain approximately 25 to 40 psi differential pressure. The positive differential pressure across the mechanical seal provides a safety that leakage through the seal will occur into the system, so that H₂S will not be lost to the hydraulic pumps.
5. CO₂ is then used to purge the gas cap of the system of oxygen by flowing through the stagnant system and out valve #6, Figure 1. After a 20-minute purge, valve #6 is closed while the CO₂ is still entering the system and the fluid flow pumps are turned on.
6. The fluid flow pumps are turned on in order. First the gear pump, then the liquid pump, and finally the gas pump. RPM settings to provide 1.0m/s Vsl and 3.5m/s Vsg are used to create a turbulent slug flow to aid in the deoxygenating process.
7. After the system reaches 25 psig (0.27MPa), the CO₂ flow is stopped and the system allowed to circulate.
8. The CO₂ gas pressure is released and replaced numerous times at 30-minute intervals while heating and circulating in order to deoxygenate the fluid.
9. After deoxygenation is complete, the pumps are set to the predetermined flow rates and the system allowed to come to temperature equilibrium overnight.
10. Corrosion studies begin the next day by retesting oxygen content, iron content, and pH before insertion of the probes. If H₂S is to be used, it is added at this point, allowed time to come to equilibrium, and the gas phase tested through the portable gas analyzer.
11. When hazardous gases are in use, the "buddy system" will *ALWAYS* be used requiring that an observer be outside the room during any necessary excursion into the test area.

Operation of the Combustion System

The status of any sensor can be observed from the front panel of the control box in the operator area. In the upper left hand corner is the 'power on/off' switch. When all systems are in working order and the monitors do not detect gas in the test cell, all lights on the panel will be green. Along the bottom of the front panel is the sensor status /sensor test switches. With all these switches in the down position, all sensors are activated.

In the center of the front panel are 4 switches labeled SW1, SW2, SW3, and SW4. These allow the user to override the logic circuits to test the various parts of the system. Above these switches are 4 LEDs that indicate the status of the various parts of the system. SW1 tests the siren. SW2 tests the combustion system. SW3 tests the combustion blower. SW4 tests the exhaust blower. If the combustion system is tested, the combustion blower indicator light along with the combustion system light will turn red because the combustion system requires the blower in order to operate correctly.

At the upper right is a manual override switch. This can be used to turn on the combustion system when a controlled venting of the pressure vessel is needed. Once activated, one 340 CFM fan draws air from the H₂S environmental room and mixes it with another 340 CFM fan providing ambient air for combustion. A differential pressure switch is activated which allows natural gas to enter the flow and a spark plug provides the necessary ignition.

EXPERIMENTATION

Set-up

The current operating procedure was used up to step 9, so the system would be ready for probe insertion. The test matrix is shown in Table 1. Two electrical resistance (ER) probes, one linear polarization probe, and one set of four coupons was used for each test, but only results for ER probes will be provided in this report.

Flow Regime

From empirical data¹³, relationships between gas velocity, film Froude number, and slug frequency were estimated. Table 2 and 3 show the data for each liquid velocity tested by Wilkens and the linear relationship calculated for Froude number and slug frequency. From this information, the gas velocity was calculated from the given liquid velocity to provide a Froude 6 slug flow at 0.45MPa. The measurement of slug frequency would provide the assurance of the attained flow regime.

The hydrogen sulfide system uses a closed circulatory system that maintains environmental equilibrium while separating and re-mixing the gas and liquid phases. The re-mixing of the flows to provide the desired flow pattern is based upon the volumetric flow rates of three pumps. But changes in the total pressure produce changes in flow densities and interfacial tension between the phases, which, in turn, alters the slug frequencies as shown in Figure 7. The volumetric flow rates used in the following testing were based upon Froude 6 slug flow at 0.45MPa for each liquid velocity (i.e. 0.5, 1.0, and 1.5 m/s), but by maintaining constant volumetric flows, this flow regime changed with total pressure.

Results

Comparison to previous testing shows the trends in the measured corrosion rate to be as expected. The corrosion rate increases with an increase in liquid velocity and also increases with an increase in pressure of CO₂. Slug frequency is investigated and is shown to decrease with an increase in system pressure, although this seems to have a negligible effect on the corrosion rate.

As seen in Figure 8, previous work^{14,15} done at the Institute for Corrosion and Multiphase Technology provided corrosion rate information for a Froude 6 stationary slug under specific multiphase flow conditions. It was assumed that the trends in measured corrosion rates would be similar between a stationary slug system and a moving slug system with changes apparent in overall corrosion rate. Figure 9 shows the measured corrosion rates in slug flow for the three different liquid velocities of 0.5, 1.0, and 1.5 m/s.

Compared to the stationary slug corrosion rates of Figure 8, corrosion rate values measured for the moving slug environment were approximately one-quarter (1/4) of those measured for the stationary slug environment. Figure 9 shows an increasing corrosion rate at each mixture velocity for increases in CO₂ pressure. Figure 10 shows increasing corrosion rates at each pressure for increasing liquid velocities. A stationary slug provides a highly turbulent zone with high relative corrosion rates. On the other hand, a moving slug environment has an associated slug frequency that lowers the amount of time that the turbulent zone is in contact with the corrosion measurement instrument. Corrosion rates produced in a moving slug environment would thus be lower due to intermittent turbulence designated by slug frequency instead of the constant exposure to turbulence of a stationary slug.

CONCLUSIONS

1. Large systems are a necessary addition to the large array of testing systems available to the research community. They provide flow patterns not possible in smaller systems.
2. Use of progressive cavity pumps for multiphase flow studies is feasible and the pumps are easily calibrated for use in the laboratory.
3. Gas flow rates larger than the volumetric flow capacity of the progressive cavity pump are possible by using a pipe segment at the output of the pump as a reservoir to hold a volume of gas. The output of this pipe segment uses a pressure drop across a valve to increase flow rate while the input from the pump continually supplies the excess gas to the reservoir.
4. Initial corrosion testing with low ratios of H₂S to CO₂ total pressure makes it possible to maintain a low inventory of hydrogen sulfide, providing that, even under catastrophic release conditions, the public vicinity surrounding the test cell will be unaffected.
5. Since changes in pressure alter the moving slug flow pattern, there is a need to choose a better "marker" than volumetric flow for repeatable conditions. Namely, for constant slug frequency, each coupon would experience similar time effects of turbulence under different total pressures.

6. CO₂ corrosion rate trends under moving slug conditions are similar to CO₂ corrosion rate trends of previous testing.

REFERENCES

1. Sun, J.Y., and Jepson, W.P., "Slug Flow Characteristics and Their Effect on Corrosion Rates in Horizontal Oil and Gas Pipelines," SPE, Paper No. 24787, Washington, D.C., 1992.
2. Zhou, X., "Experimental study of Corrosion Rate and Slug Flow Characteristics in Horizontal, Multiphase Pipelines," NACE International Annual Conference and Exhibition, Paper No. 92081, Nashville, TN, April 1992.
3. Gopal, M., Kaul, A., and Jepson, W. P., "Mechanisms Contributing to Enhanced Corrosion in Three Phase Slug Flow in Horizontal Pipes," NACE CORROSION/95, Paper No. 105, 1995.
4. Crolet, J.L., and Bonis, M.R., "pH measurements under high pressures of CO₂ and H₂S", Advances in CO₂ Corrosion, Vol. 2, CORROSION/85, 1985.
5. A.Ikeda et al., "Influence of Environmental Factors on Corrosion in CO₂ Wells," Advances in CO₂ Corrosion, Vol.2, pp.1-22, NACE, 1985.
6. Videm, K., and Kvarekval, J., "Corrosion of Carbon Steel in CO₂ Saturated Aqueous Solutions Containing Small Amounts of H₂S," NACE CORROSION/94, Paper No. 12, 1994.
7. Srinivansan, S., and Kane, R. D., "Experimental Simulation of Multiphase CO₂/H₂S Systems," Paper No. 14, Corrosion/99.
8. Pargeter, R. J., "The Effect of Low H₂S Concentrations on Welded Steels," NACE CORROSION/2000, Paper No. 143, 2000.
9. Nesic, S., Solvi, G. T., and Enerhaug, J. "Comparison of the Rotating Cylinder and Pipe Flow Tests for Flow Sensitive CO₂ Corrosion," NACE CORROSION/95, Paper No. 130, 1995.
10. Jepson, W.P., and R.E. Taylor, "Slug Flow and Its Transitions in Large-Diameter Horizontal Pipes," Int. J. Multiphase Flow, Vol. 19, pp411-420, 1993.
11. Crolet, J.L., and Bonis, M.R., "How to Pressurize Autoclaves for Corrosion Testing Under Carbon Dioxide and Hydrogen Sulfide Pressure," Corrosion, Vol. 56, No. 2, pp167-182, February 2000.
12. Kumar, A., "Estimate Dispersion for Accidental Releases in Rural Areas," Chemical Engineering, Vol. 106, No. 7, pp91-94, July 1999.
13. Wilkens, R. J., "Prediction of the Flow Regime Transitions in High Pressure, Large Diameter, Inclined Multiphase Pipelines," Ph.D. dissertation, Russ College of Engineering, Ohio University, June 1997.

14. Vuppu, A.K., "Study of Carbon Dioxide Corrosion of Carbon Steel Pipes in Multiphase Systems," Thesis presented to the Russ College of Engineering and Technology, August 1994.
15. Jepson, W.P. and Bhongale, S., "Effect of Pressure, Temperature, and Oil Composition on Corrosion Rate in Horizontal Multiphase Slug Flow," NACE Middle East Conference, Paper No. 96006, Bahrain, February 1996.

TABLES

Table 1.
Multiphase Baseline Corrosion Test Matrix

Temperature	60°C
Fluid	100% ASTM Seawater
Flow Regime	Slug Flow, Froude 6
Vsl	0.5, 1.0, & 1.5 m/s
CO ₂ Pressure	0.27, 0.45, & 0.79 MPa
Calculated Vsg	3.3, 3.5, & 4.9 m/s, respectfully

Table 2.
Froude Number Correlation for 100% Saltwater, 0.45MPa, horizontal multiphase flow.

Vsl (m/s)	Vsg (m/s)	film Froude No.	Fr. No. vs. Vsg	R ²
0.5	1.4	2.1	Fr. = 2.33(Vsg) - 1.67	0.975
	3.3	5.7		
	5.1	9.5		
	7.5	17.8		
	10.3	19.6		
	13.6	31.3		
1.0	1.3	2.1	Fr. = 2.23(Vsg) - 1.75	0.993
	3.4	5.3		
	4.9	8		
	7.8	16.1		
	9.3	19.1		
	12.2	25.5		
1.5	1.7	2.8	Fr. = 2.14(Vsg) - 1.65	0.989
	3.4	5.1		
	5.6	9.3		
	8.1	15.9		
	9.1	18.6		
	10.3	20.1		

Table 3.
Slug Frequency Correlation for 100% Saltwater, 0.79MPa, horizontal multiphase flow.

Vsl (m/s)	Vsg (m/s)	Fv (min ⁻¹)	Fv vs. Vsg	R ²
0.5	1.3	16	$Fv = 2.07(Vsg) + 17.2$	0.95
	3.3	8		
	5.6	6		
	7.6	2		
1.0	8.3	0	$Fv = 1.59(Vsg) + 20.8$	0.92
	1.2	20		
	3.5	14		
	5.1	12		
1.5	7.4	10	$Fv = 3.94(Vsg) + 29.6$	0.94
	1.2	26		
	3.4	14		
	5.3	10		

FIGURES

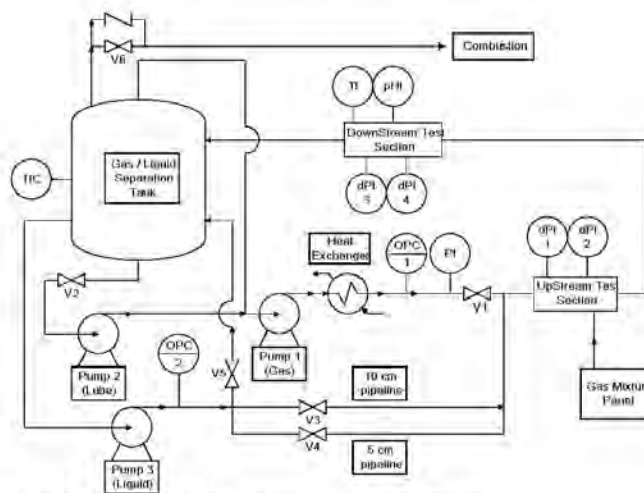


Figure 1. Schematic diagram of Multiphase flow loop (P&ID).

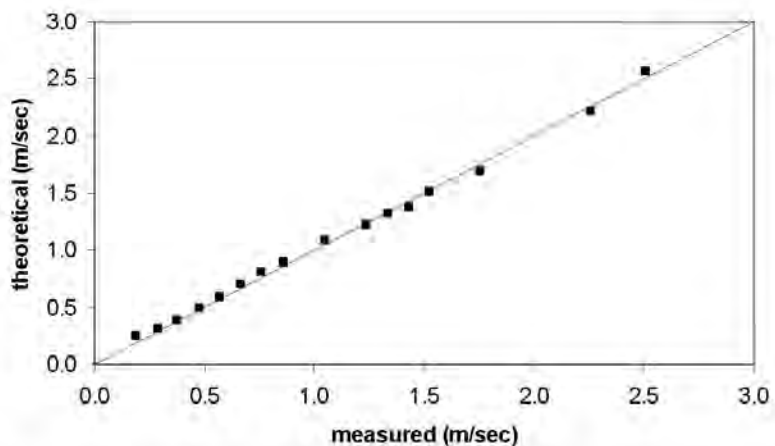


Figure 2. Comparison of Theoretical to Empirical Liquid Pump Flow Rate

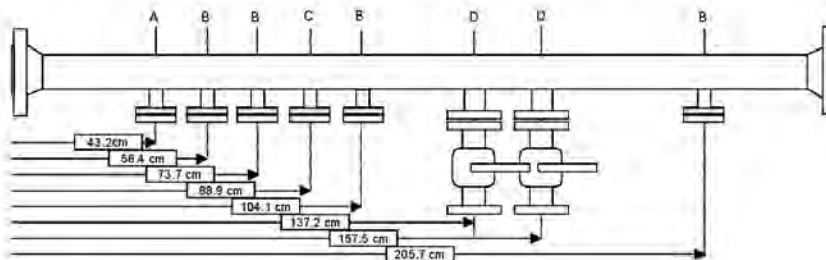


Figure 3. Test Section Layout.

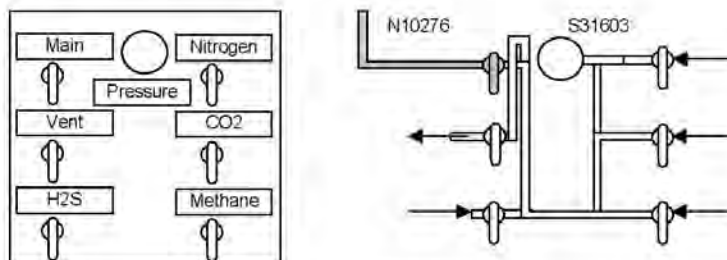


Figure 4. Gas mixture panel and tubing configuration.

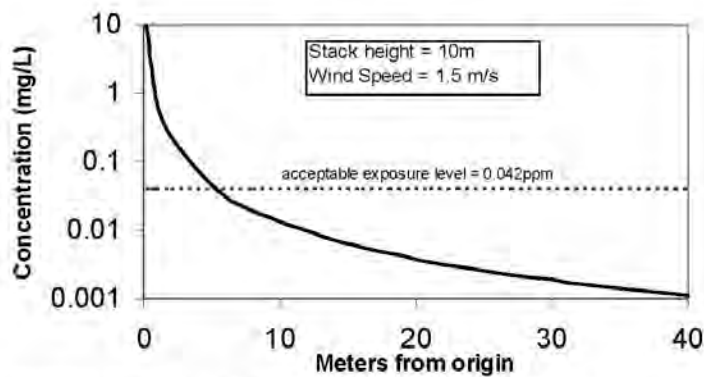


Figure 5. Concentration vs. Distance from Release Point for Hydrogen Sulfide gas.

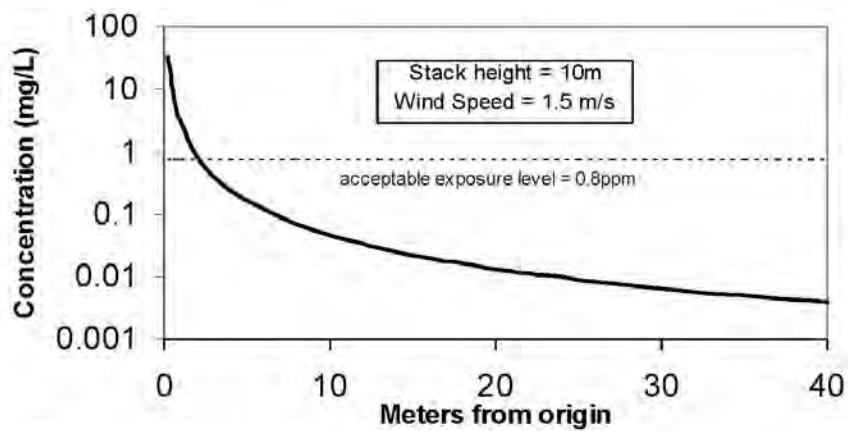


Figure 6. Concentration vs. Distance from Release Point for Sulfur Dioxide gas

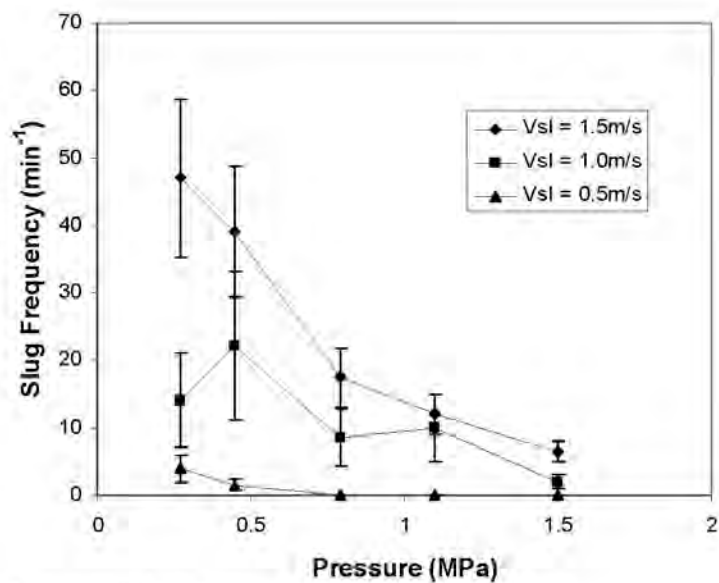


Figure 7. Decrease in Slug Frequency with Increase in Total Pressure.

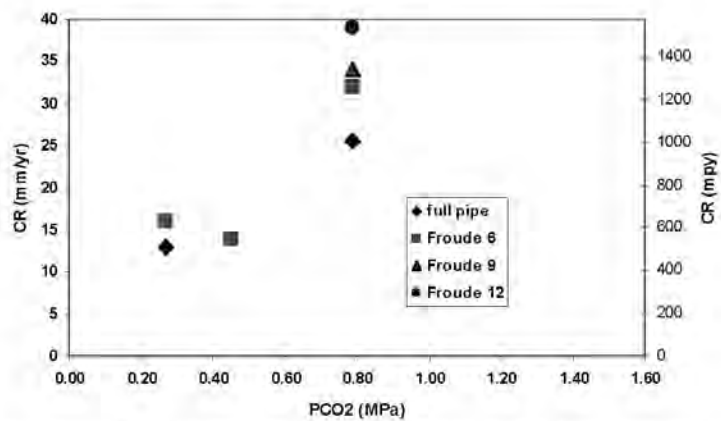


Figure 8. Corrosion Rate in "Standing Slug" Multiphase flow, CO₂ & 100% Seawater, 60°C (Vuppu, 1994) (Jepson and Bohngale, 1996)

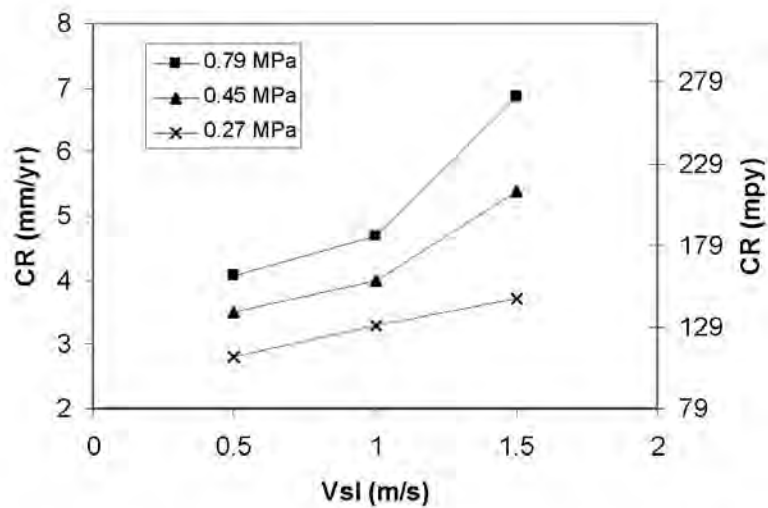


Figure 9. Corrosion Rate in "Moving Slug" Multiphase flow, CO₂ & 100% Seawater, 60°C.

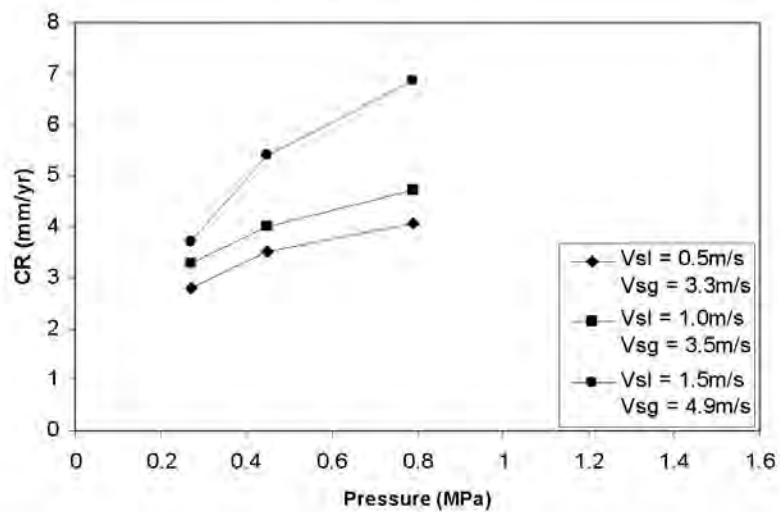


Figure 10. Corrosion Rate From Change in Vsl, Fr. 6 @ 0.45MPa, CO₂ & 100% Seawater, 60°C.



Thesis and Dissertation Services